MECHANISTIC UNDERSTANDING OF DISSOLUTION OF AMORPHOUS SOLID DISPERSIONS

by

Sugandha Saboo

A Dissertation

Submitted to the Faculty of Purdue University

In Partial Fulfillment of the Requirements for the degree of

Doctor of Philosophy

Department of Industrial and Physical Pharmacy

West Lafayette, Indiana

May 2020

THE PURDUE UNIVERSITY GRADUATE SCHOOL
STATEMENT OF COMMITTEE APPROVAL

Dr. Lynne S. Taylor, Chair

Department of Industrial and Physical Pharmacy

Dr. Stephen R. Byrn

Department of Industrial and Physical Pharmacy

Dr. Qi (Tony) Zhou

Department of Industrial and Physical Pharmacy

Dr. Stephen P. Beaudoin

Department of Chemical Engineering

Dr. Umesh S. Kestur

Bristol-Myers Squibb

Approved by:

Dr. Rodolfo Pinal

To my loving parents and husband

ACKNOWLEDGMENTS

TABLE OF CONTENTS

7

LIST OF TABLES

LIST OF FIGURES

13

17

ABSTRACT

As amorphous solid dispersions (ASDs) are more widely employed as a formulation strategy for poorly water-soluble drugs, there is a pressing need to increase the drug loading in these formulations. The drug loading is typically kept low to obtain the desired drug release rate, but often results in large or even multiple dosage units, which is undesirable from a patient compliance perspective. We have identified the cause of this conundrum to be the drug loading dependent dissolution mechanism of ASDs. At low drug loadings, the dissolution rate of ASDs is polymer-controlled, while at high drug loadings, the dissolution rate is drug-controlled and considerably slower. This phenomenon is most pronounced for ASDs with hydrophilic polymers, such as poly (vinylpyrrolidone-co-vinyl acetate) (PVPVA) and the change in dissolution mechanism from being polymer-controlled to drug-controlled has been attributed to water-induced amorphous-amorphous phase separation (AAPS) in higher drug loading ASD matrices of hydrophilic polymers. The drug loading limit for this switch has been found to be dependent on drug properties as well as drug-polymer interactions. Interestingly, drug-polymer hydrogen bonding interaction has been found to be detrimental and decrease the drug loading limit for polymer-controlled release while drug log P did not have any impact on this limit. Variable dissolution temperature studies indicated a detrimental impact on the polymer-controlled drug loading limit when the drug-rich phase (of phase separated ASD matrix) exists in a glassy state. ASDs with relatively hydrophobic polymers, such as hypromellose acetate succinate (HPMCAS), have been found to be polymer-controlled up to higher drug loadings. The mechanistic understanding obtained in this body of work can thus be adopted to develop strategies enabling ASD formulations with optimized performance and improved drug loading.

CHAPTER 1. INTRODUCTION

1.1 Research significance, specific aims and hypotheses

1.1.1 Research significance – originality and potential impact

The number of poorly water soluble compounds in the developmental pipeline has been increasing. This increase results from drug discovery strategies, including the increasing complexity of drug targets, exploitation of hydrophobic interactions with target receptors and use of non-aqueous solvents to initially dissolve drugs for use in high throughput screening of new chemical entities (NMEs).[1] As solubility is essential for *in vivo* dissolution and oral bioavailability, this has led to a challenging situation resulting in the concomitant development of various enabling formulation strategies to mitigate the solubility limitations of these NMEs.[2] Strategies to overcome drug solubility issues can be divided into two broad categories. First are solubilizing strategies, for example, surfactants, cyclodextrins, etc. which lead to an increase in the equilibrium crystalline solubility of the compounds.[3] The second category is supersaturating strategies, which includes amorphous solid dispersions, cocrystals, etc.[4, 5] which do not enhance the drug crystalline solubility, but generate concentrations in excess of crystalline solubility leading to supersaturated solutions.

Amongst these strategies, amorphous solid dispersions (ASDs) are finding increasing utility as a solubility enabling formulation strategy. There have been a number of amorphous solid dispersion-based drug products reaching the market in the past two decades.[6] However, the promise that this approach has shown in terms of bioavailability advantage has not yet been fully utilized and the number of marketed products is certainly not proportional to the immense potential of this strategy. To widely employ this formulation strategy, there are new frontiers in ASD design that need to be advanced. One of the most important is the drug:polymer ratio paradigm. Low drug loading is a primary constraint in ASD formulation design[7, 8] and is often necessary for reasons, such as, maintaining the amorphous form of drug in the ASD matrix, enhancing the rate of drug release and also achieving and sustaining the supersaturation upon dissolution. The drug:polymer ratio in the ASD is, of course, an important practical consideration for all but the most potent compounds from a manufacturing standpoint and may result in large or even multiple dosage units, which is

undesirable from a patient compliance perspective and can provide a marketing disadvantage. Therefore, in order to use ASDs more broadly as an enabling strategy for poorly water soluble compounds, there is a need to increase the drug loading, while still achieving the desired dissolution advantages of ASDs.

Unfortunately, the mechanism of drug release from ASDs is not well understood. *A priori* knowledge in this regard is that there are two regimens that often exists in ASD dissolution as a function of drug loading. At low drug loadings, the ASD dissolution has been found to be polymer controlled[9-12] (dictated by physicochemical properties of the polymer) while at high drug loadings, drug-controlled dissolution has been reported[13, 14] (governed by physicochemical properties of the drug). There is limited knowledge on what causes this switch from a polymer-controlled to a drug-controlled regimen and no predictability exists regarding the drug loading at which this switch happens for a particular drug-polymer system. An interplay between both drug and polymer properties is likely to play a role in this switch. Therefore, various experimental approaches employed in this study attempt to address this knowledge gap by probing the underlying mechanism of ASD dissolution process and understanding the extent to which the ASD dissolution profile can be manipulated through formulation. A goal of this study thus is to probe the mechanism of drug release as a function of drug loading, drug properties (log P, crystallization tendency, hydrogen bonding capacity, glass transition temperature (T_g), etc.) and polymer type, specifically, for commercially used common polymers, such as, hypromellose acetate succinate (HPMCAS), hypromellose (HPMC) or poly (vinylpyrrolidone-co-vinyl acetate) (PVPVA). The interplay between drug and polymer properties will also be explored in terms of phase behavior during dissolution and drug-polymer interactions. Mechanistic understanding of the link between compound properties and release rates from given polymeric systems will lead to better formulation design and less trial and error experimentation. Identification of important drug properties to enable informed polymer selection is an expected outcome. The mechanistic understanding gained can then be utilized to develop alternative formulation strategies to optimize drug loading in ASDs.

Since studying the effect of solid-state phase behavior of ASDs during dissolution is one of the aims of this study, a prerequisite is to develop an analytical method to screen (im)miscibility of

ASD formulations upon contact with water. The successful application of ASD is based on an important underlying assumption of homogeneity or miscibility of drug and polymer at a molecular level in the ASD matrix. Miscibility of ASDs has been found to be an issue that can impact stability as well as the dissolution performance of ASDs.[15-17] Phase separation of ASDs can result from crystallization of drug in the polymeric matrix or it can be phase separation with both drug and polymer retaining their amorphous forms. The latter type of phase separation is termed amorphous-amorphous phase separation (AAPS).[18, 19] Conventional analytical techniques available to evaluate the miscibility of ASDs are reasonable for detecting crystallinity in the ASD matrix but suffer from a range of issues in detecting the AAPS phenomenon, namely, lack of drug-polymer specificity, inability to detect small-sized phase separated domains, interference from water, tedious sample preparation and problematic data interpretation. Thus, an additional goal of this study was to establish confocal fluorescence microscopy as a new approach to differentiate drug-rich and polymer-rich regions in an ASD matrix which has undergone AAPS and to utilize it to gain mechanistic insight into water-induced AAPS during dissolution.

1.1.2   Specific aims and Hypotheses

Specific aim 1

- Demonstrate the utility of confocal fluorescence microscopy as a screening tool for water-induced AAPS.

Hypothesis:

- Hydrophobic environment sensitive fluorescent probes will preferentially partition into the drug-rich phase and hydrophilic fluorescent probes will preferentially partition into the hydrophilic polymer-rich phase enabling simultaneous contrast imaging for drug and polymer-specific regions in phase separated ASD matrices.

Specific aim 2

- Elucidate relationships between drug log P, phase behavior during dissolution, and ASD release rate as a function of drug loading when formulated with poly (vinylpyrrolidone-co-vinyl acetate) (PVPVA).

Hypotheses:

- Differences in supersaturation achieved by dissolution of ASDs formulated with a hydrophilic polymer, like PVPVA, depend on the congruent (simultaneous) or incongruent release (different release rate) of ASD components, resulting from competing kinetics between phase separation upon hydration and dissolution of components from the ASD matrix.

- A PVPVA ASD with a more hydrophobic drug will have an increased tendency for water-induced AAPS and will show congruent release behavior during dissolution only up to a lower drug loading as compared to an ASD with a more hydrophilic drug.

Specific aim 3

- Elucidate the impact of drug-polymer hydrogen bonding interaction, surface crystallization and glass transition on the ASD release rate as a function of drug loading when formulated with poly (vinylpyrrolidone-co-vinyl acetate) (PVPVA).

Hypotheses:

- Strong interactions between drug and polymer (such as hydrogen bonding) in ASDs will result in polymer-controlled release up to higher drug loadings as compared to drug-polymer combinations with weak interactions. Thus, drug-polymer combinations with stronger interactions will result in superior dissolution performance.

- Fast crystallizing compounds with rapid matrix crystallization prior to release will show poor release rates.

- ASDs in the glassy state (when the dissolution temperature is below glass transition temperature) will show poor release rates due to reduced molecular mobility.

Specific aim 4

- Elucidate relationship between polymer hydrophobicity and ASD release mechanism as a function of drug loading.

Hypothesis:

- Hydrophobic polymers will shift the boundary between polymer-controlled and drug-controlled release to higher drug loadings due to less water absorption and reduced tendency of water-induced AAPS in the dissolving ASD matrix.

1.2   Background

1.2.1   Solubility advantage of amorphous solids

The fundamental difference between amorphous and crystalline solids is that amorphous solids lack the three dimensional ordered arrangement of a crystalline lattice. The solubilization process of a crystal can be divided into two parts: first, disruption of the crystal lattice, wherein intermolecular bonds in a crystal are broken down into its individual components (molecules) and the second part is where these individual components (molecules) interact with the aqueous medium to give a solution. This process is analogous to heating the crystal to its melting point and converting it into a liquid, followed by mixing with a solvent as shown in Fig. 1.1.
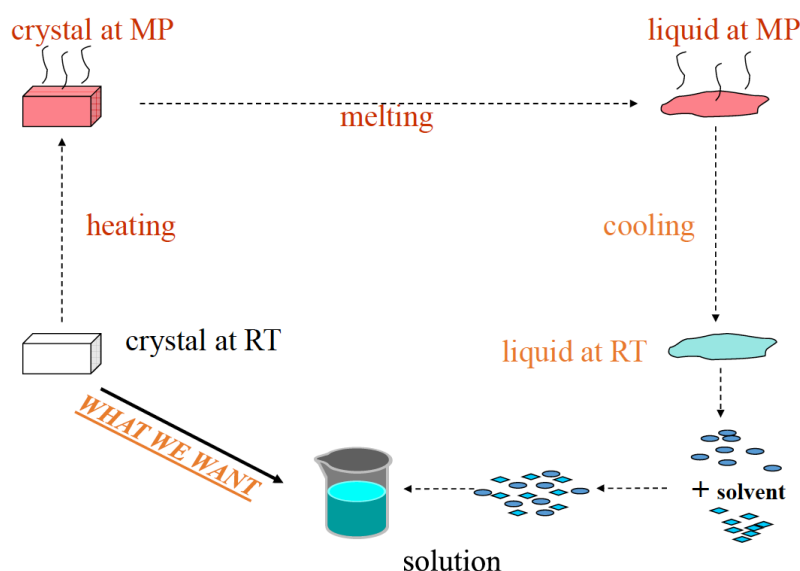
Figure 1.1 shows the solubilization process of a crystalline API into solution. Analogy is shown between melting of a crystal and dissolution process. (Figure courtesy: IPPH 580 lecture notes)

The solubility of a crystalline solute in a solvent can be predicted by the equation 1:[20]

$$\ln x = \frac{\Delta H_f}{R}\left[\frac{1}{T_m} - \frac{1}{T}\right] \qquad (1.)$$

24

where x is the mole fraction solubility, ΔH_f is the enthalpy of fusion (J/mol), T_m is the melting temperature of crystal (K), T is the temperature (K) and R is the gas constant (8.314 J/mol.K^{-1}). Equation 1 pertains to ideal solids when there is no interaction between the solute and the solvent. However, this is not typically the case and to account for non-ideality in systems, i.e., solute-solvent interactions, an activity coefficient (γ) is incorporated into the solubility equation to obtain equation 2:

$$\ln x = \frac{\Delta H_f}{R}\left[\frac{1}{T_m} - \frac{1}{T}\right] - \ln \gamma \qquad (2.)$$

where ΔH_f term represents the energy required to break down the crystalline lattice and $\ln \gamma$ accounts for the interactions between solute and solvent molecules.

When dissolving amorphous solids in an aqueous medium, there is no need to supply energy to break down the crystalline lattice and the only step in the dissolution of amorphous solids is the interaction of the amorphous solid with the aqueous medium. This forms the basis of solubility enhancement obtained with amorphous solids. Equation 2 also implies that the higher the crystal lattice energy barrier, the higher the theoretical amorphous solubility advantage over the crystalline form. The solubility of the amorphous form can be predicted from the experimentally determined crystalline solubility and the free energy difference between amorphous and crystalline forms, as expressed by the following equation:[21]

$$\Delta G = RT \ln \frac{a_{amorphous}}{a_{crystalline}} \simeq RT \ln \frac{c_{amorphous}}{c_{crystalline}} \qquad (3.)$$

where a is the activity of the solute in saturated solution (mol/L), c is the solubility (mol/L), R is the gas constant (8.314 J/mol.K^{-1}) and T is the temperature (K). When in dilute solution where activity coefficients are approximately unity, the activity, a, can be assumed to be equal to the concentration, c, in an aqueous solution. From equation 3, the larger the free energy difference, the higher the potential solubility enhancement by the amorphous form. The free energy difference between amorphous solids and crystals can be estimated using the equation 4, derived by Hoffman:[22]

$$\Delta G = \frac{\Delta H_f (T_m - T)T}{T_m^2} \qquad (4.)$$

where ΔH_f is the melting enthalpy (J/mol), T_m is the melting temperature (K) and T is the experimental temperature (K). The amorphous form has been found to provide a several fold increase in aqueous solubility over the crystalline form.[22] However, a larger free energy difference translates to a greater thermodynamic force for crystallization.

1.2.2 Amorphous solid dispersions (ASDs)

As mentioned above, the solubility advantage of amorphous solids can be easily negated by crystallization, therefore, an amorphous drug is molecularly dispersed into second component, i.e., a polymer to inhibit crystallization in order to formulate an amorphous solid dispersion. One of the earliest definitions of solid dispersion was given by Choiu and Reigelman[23] as, "the dispersion of one or more active ingredients in an inert matrix or carrier in solid state prepared by melting (fusion), solvent or melting-solvent method". Although this earlier definition included even crystalline active ingredients, it is important to note that the focus of the literature review and research presented here is solely on "amorphous solid dispersions" where drug is dispersed in the amorphous state in the polymeric matrix, at least initially.

Thermodynamics of drug- polymer miscibility

In order to derive advantages from amorphous solid dispersions, drug-polymer miscibility is a prerequisite. The thermodynamics of drug-polymer miscibility can be understood by Flory-Huggins theory as given by the following equation:

$$\Delta G_m = \Delta H_m - T\Delta S_m = RT \left[\chi \Phi_D \Phi_P + \Phi_D ln\Phi_D + \frac{\Phi_P}{P} ln\Phi_P \right] \qquad (5.)$$

where ΔG_m represents the free energy of mixing, Φ_D is the volume fraction of drug, Φ_P is the volume fraction of polymer, P is the degree of polymerization of polymer, χ is the Flory-Huggins

interaction parameter, T is the temperature (K) and R is the gas constant (8.314 J/mol.K^{-1}). The first term in equation 5 represents the enthalpic contribution (ΔH_m) to free energy and the last two terms represents the entropic contribution to free energy of the system ($-T\Delta S_m$). Figure 1.2 shows hypothetical plots between free energy, enthalpy and entropy contributions to the free energy versus volume fraction of polymer for three different scenarios: total miscibility, total immiscibility and partial miscibility of a hypothetical amorphous solid dispersion system.[24, 25]
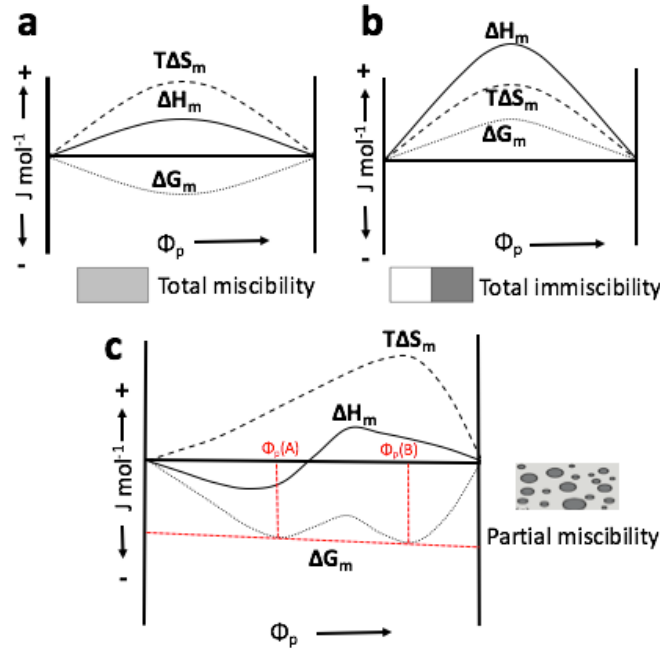
Figure 1.2 Schematic representation of free energy (ΔG_m), enthalpic (ΔH_m) and entropic contribution ($-T\Delta S_m$) to free energy as a function of polymer volume fraction (ϕ_p) for a hypothetical ASD with total miscibility (a), total immiscibility (b) and partial miscibility (c). $\phi_p(A)$ and $\phi_p(B)$ represents the volume fractions of polymer in two phases of a partially miscible system.

Some amorphous solid dispersions are characterized by free energy diagrams of the type shown in Fig. 1.2 (c). The thermodynamics of phase separation of this partially miscible system is discussed herein in some detail. The schematic shown in Fig. 1.3 shows the free energy of mixing (ΔG_{mix}) versus volume fraction of polymer (ϕ_p) curve for a partially miscible system which can be divided into three regions, I, II and III.

Figure 1.3 Free energy versus composition (polymer volume fraction) for a partially miscible amorphous solid dispersion. Adapted from ref.[24].

Region I corresponds to the stable region where the drug-polymer system will remain miscible. Taking a hypothetical point A on the curve, shown in region I, if we draw a tie line perpendicular to line joining points A and A', a line with the ends a' and a'' lying on the curve (referred as a tie line) is obtained. It can be seen that free energy of the miscible system will always be lower than the free energy of the phase separated system. Therefore, region I is called the stable region where phase separation will not occur and the system will remain miscible. A similar analysis of region III considering a point B, which can potentially phase separate into points b' and b'', reveals that the free energy of the phase separated compositions will be lower than the original point B. Therefore, in region III, the system is unstable and will tend to undergo phase separation.[24, 25]

In region II, consider a point C which will phase separate to c' and c'' as shown in Fig. 1.3. In this case, the free energy of the phase separated system will be higher than the miscible composition at point C. Thus, the system will not phase separate and remain miscible. However, if the system at point C is able to gain sufficient energy to overcome the energy barrier that exists towards phase separation, then it will phase separate to points S and T since the total free energy of the system will be less than the original composition at C. Thus, region II is the metastable region of the given free energy diagram where a system can be locally stable but will phase separate if sufficient activation energy is provided.[24, 25]

28

Preparation methods and impact of processing conditions on miscibility

The two most commonly employed amorphous solid dispersion manufacturing methods at commercial scale are: spray drying (SD) and hot melt extrusion (HME). The former is a solvent evaporation approach while latter is a melting (fusion) method. Since these are two entirely different methods to prepare ASDs, it is not surprising that differences in the properties and dissolution performance of ASDs produced using SD and HME have been observed.[26] The following sections discuss important processing factors that may impact ASD properties using each of these methods, particularly, the impact of solvents in the SD approach and the impact of temperature during HME.

Impact of solvents

Solvent choice in a spray died amorphous solid dispersion may impact phase behavior, extent of surface enrichment and dissolution properties of amorphous solid dispersions. The choice of solvent has both thermodynamic and kinetic implications for ASDs.

Thermodynamic implications. For ternary systems containing drug (*D*), polymer (*P*) and solvent (*S*), which describe, for example, spray drying feed solutions for amorphous solid dispersions, an extended version of the Flory- Huggins equation can be written as following:[27]

$$\Delta G_m = RT[n_D ln\Phi_D + n_P ln\Phi_P + n_S ln\Phi_S + n_S \Phi_D \chi_{SD} + n_S \Phi_P \chi_{SP} \qquad (6.)$$
$$+ n_D \Phi_P \chi_{DP}]$$

where ΔG_m is the free energy of mixing, *R* is the gas constant, *T* is the temperature, *n* is the number of moles, Φ is the volume fraction and χ is the interaction parameter. The first three terms in the equation 6 comprise of favorable entropic interactions while the last three terms represent enthalpic contributions, where $\chi_{DP} = 0$ can be assumed for a system in which drug and polymer do not interact and undergo athermal mixing. In this instance, the remaining two terms, χ_{SP} and χ_{SD}, will determine the enthalpic contribution. It has been established that the larger the difference in the interaction parameters between solvent and individual solutes (drug and polymer in this case), the greater is the probability for the system to phase separate. This effect is known as the delta chi

effect.[28, 29] Mathematically, the difference in interaction parameters or the so called delta chi effect is expressed as following: $|\Delta\chi| = |\chi_{SP} - \chi_{SD}|$.

The above theory can be applied to amorphous solid dispersions as follows: the spray drying solvent can be a good or bad solvent for the drug and/or polymer and determines the phase behavior of ASDs. Different spray drying solvents have been found to result in particles with different stability and dissolution properties. A study by Obaidi et al attributed the differences in the ASD properties to different degree of interactions of the polymer with the solvent (or a combination).[30] Similar observation can be found in other literature studies.[26]

Kinetic implications. Surface enrichment of either drug or polymer during spray drying of ASDs is one of the kinetic implications of the choice of spray drying solvent. Surface enrichment results from competing kinetics and imbalance between drying kinetics and molecular diffusivity of ASD components. The Peclet number (P_{ei}) is a common parameter to quantify the relative extent of these two processes and is defined as follows:[31]

$$P_{ei} = \frac{k}{8D_i} \tag{7.}$$

where k is the evaporation rate of the solvent and D is the diffusivity of individual components of interest (either drug or polymer). It is intuitive from the equation that a high Peclet number will result in surface enrichment of the component of interest and vice versa. Surface enrichment of drug on spray dried ASD particles can be particularly detrimental to ASD stability and dissolution because it can render the amorphous drug more prone to crystallization due to reduced polymer concentration and, moreover, surface crystallization kinetics can be faster than bulk crystallization.[32]

In addition to the Peclet number, surface enrichment as well as phase separation of ASD components can arise from precipitation of one of the components during the drying process. As drying proceeds, the ASD components start to concentrate in the dissolving solvent and owing to a differential solubility of drug and polymer in the solvent, the lower solubility component might precipitate. The situation can be more complex if the spray drying solvent is a mixture of solvents.

If the solvent mixture is azeotropic, then the relative ratio of solvents will remain the same throughout the drying process. But if the solvent mixture is zeotropic, then the relative ratio of solvents is likely to change during the drying process because the solvent with high vapor pressure or lower boiling point will evaporate faster,[33] and depending on the relative solubility of drug and polymer in the higher mass fraction of the solvent with higher boiling point or lower vapor pressure, one of the components will precipitate. In spite of the challenges associated with spray drying as a technique for manufacturing ASDs, it is indispensable for thermolabile drugs and polymers that cannot be easily extruded.

Impact of temperature on drug- polymer miscibility

The free energy versus composition profile shown in Fig. 1.3 corresponds to a particular temperature, T. Similar profiles at various temperatures can be obtained and a temperature versus composition profile as shown in Fig. 1.4 can be derived with the following derivation for two distinct curves: binodal and spinodal.
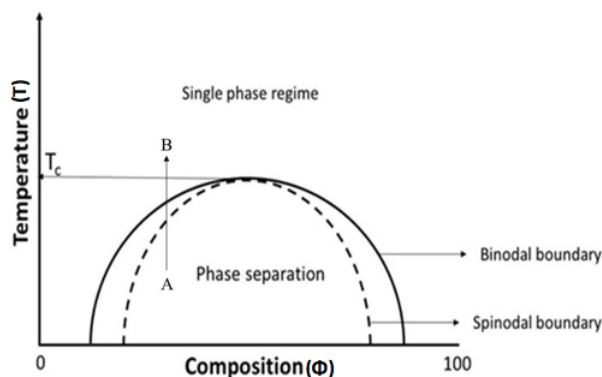
Figure 1.4 Temperature versus composition diagram for an amorphous solid dispersion. T_c is the critical temperature and the path A to B shows the phase transition from phase separated to miscible system upon increase in temperature at a particular composition.[34]

i. Binodal curve: It is also known as the coexistence curve. It is derived from a free energy versus composition curve by plotting all the pairs of "common tangent points" at various temperatures fulfilling the following criteria: a pair of common tangent points at compositions ϕ' and ϕ'' should fulfill equality criteria of $\left(\frac{\partial \Delta G_m}{\partial \phi}\right)_{\phi=\phi'} = \left(\frac{\partial \Delta G_m}{\partial \phi}\right)_{\phi=\phi''}$.[35]

ii. Spinodal curve: The spinodal curve is derived by plotting all the inflection points from a free energy versus composition curve at various temperatures into temperature versus composition plot. Inflection points are determined by equating the second derivative of the free energy to zero: $\frac{\partial^2 \Delta G_m}{\partial^2 \phi} = 0$.[35]

The region surrounded by spinodal boundaries is the unstable region and any composition and temperature combination lying in this region will undergo phase separation. The region between the binodal and spinodal boundaries is the metastable region where the system can be phase separated or mixed depending on its free energy state in response to external disturbances. In Fig. 1.4, the uppermost point on the binodal/ spinodal curve corresponds to critical temperature (T_c), it is that temperature beyond which system exists in the form of a single phase miscible system at any composition as long as it does not degrade. A representation of this phase transition is shown in Fig. 1.4 where if the starting conditions of a phase separated ASD corresponds to point A, and if we increase the temperature of the system from A to B, then at some point, the ASD is going to be miscible. The same principle is utilized in hot melt extrusion for ASD manufacturing, where a blended mixture of drug and polymer is heated close to T_c while passing through an assembly of screws to obtain a single phase miscible system which is later cooled down and milled to the desired particle size. The cooling step kinetically traps the single phase ASD system and the ASD remains miscible unless the kinetic barrier to phase separation is overcome due to external factors, for instance, increased mobility due to absorption of water at high RH conditions.[34, 35]

1.2.3 Dissolution advantage of amorphous solid dispersions

The thermodynamic solubility of the drug is the solubility of the most stable crystalline form of the drug when crystalline drug is in equilibrium with the medium. Amorphous solubility, on the other hand, is the maximum solution concentration that can be attained by dissolving an amorphous solid into the dissolution medium where an amorphous solid attains a metastable equilibrium with the dissolution medium. Since the amorphous form has higher solubility than the crystalline form, supersaturation can be created by dissolving amorphous solids, which means that the solution concentration is higher than the crystalline solubility. The supersaturation ratio (*S*) is generally

determined by taking a ratio of the activity of the solute in solution (*a*) to the activity of the crystalline state (*a_eq*) from the following relationship:[36]

$$S = \frac{a}{a_{eq}} \approx \frac{c}{c_{eq}} \tag{8.}$$

For the dilute solutions in simple media, this relationship can be approximated by substituting activity by concentration. c is the drug concentration in the supersaturated solution and c_{eq} is the equilibrium crystalline solubility.

Supersaturation generated by dissolution of amorphous solids, even though significant, can be short-lived due to the thermodynamic driving force towards crystallization as shown in Fig. 1.5 as the 'spring' effect. It is evident that the supersaturation generated from dissolution of the amorphous form does not last long and the concentration quickly drops back towards the equilibrium solubility of the crystalline form. The dissolution advantage obtained from amorphous solid dispersions is not only derived from the solubility advantage of the amorphous form but also because the drug is able to remain in the supersaturated state for an extended period of time as compared to the dissolution of the amorphous form of the drug alone. The typical dissolution profile of ASDs, is often described in terms of 'spring and parachute' effect as shown in Fig. 1.5.[37] The 'spring' effect is the initial surge in concentration achieved due to the higher solubility of amorphous form in ASD as well as contributions from the increased wettability due to the presence of hydrophilic polymers. The 'parachute' effect is the sustained supersaturation due to the crystallization inhibition effect of polymers. Polymers inhibit crystallization in the dissolving ASD matrix, from the dissolved drug in the solution as well as from colloidal drug-rich aggregates, which have been reported to generate upon ASD dissolution once the drug concentrations exceeds the amorphous solubility. A more detailed description of the role of polymers in ASD dissolution in provided in next sub-section.
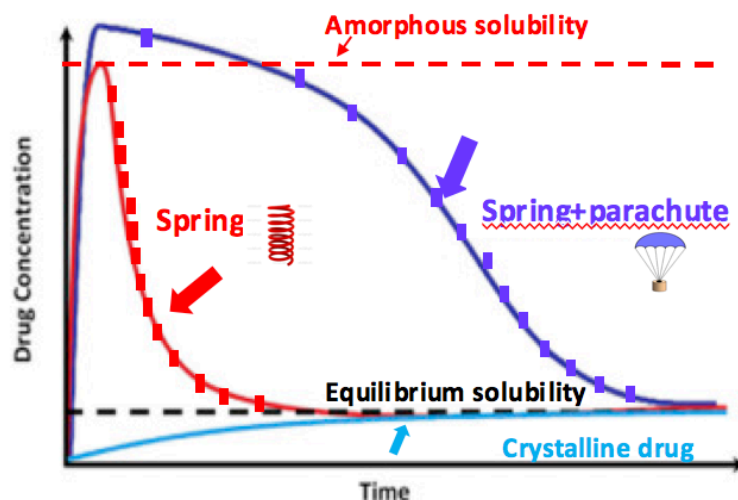
Figure 1.5 Graphical illustration of spring and parachute effect during ASD dissolution (purple curve). The representative profiles for amorphous drug dissolution (red curve) and crystalline drug dissolution (cyan blue curve) are also shown. Adapted from ref.[37].

The dissolution advantage of amorphous solid dispersions is two-fold: they not only increase the rate and extent of dissolution but also help in increasing drug flux through the intestinal membrane.[38] Thus, the dissolution advantage of ASD formulations does translate into a bioavailability advantage. To give a statistically significant conclusion, a review by Newman et al. showed that amorphous solid dispersions improved bioavailability in 82% of the total surveyed 40 studies from literature.[39]

Role of polymer in ASDs

There are two distinct purposes for adding a polymer to an ASD: crystallization inhibition and improved dissolution.

Crystallization inhibition

Fig. 1.6 represents a schematic showing crystallization inhibition mechanisms of polymers in ASDs.[40] Since the amorphous form has higher free energy as compared to the stable crystalline form, there is always a thermodynamic driving force towards crystallization. When polymer is added to prepare amorphous solid dispersions, there are two main ways in which a polymer can inhibit crystallization.

First, mobility is decreased in the presence of a high T_g polymer, increasing the kinetic barrier and making it more difficult for amorphous drug to crystallize. The T_gs of polymers are typically higher than the drug T_g, and the T_g of the ASD is thus higher than that of the amorphous drug. The increase in T_g is one mechanism by which the kinetic barrier for transformation from amorphous to crystalline form is increased.[41, 42] Another mechanism is the decrease in molecular mobility due to the presence of specific interactions between amorphous drug and polymer in an ASD, such as hydrogen bonding.[43]

Second, when the drug and polymer are mixed, and because of favorable interactions, the free energy of the system is decreased.[44] Therefore, the driving force towards crystallization is lower as compared to pure amorphous drug. Thermodynamically, energetically favorable interactions, such as, hydrogen bonding, therefore can also result in decrease in crystallization tendency.[45, 46]
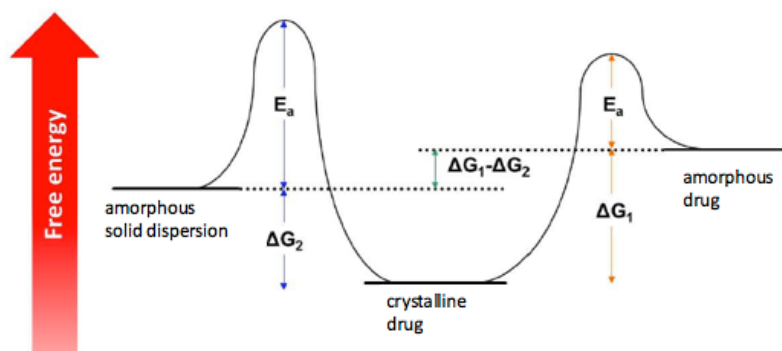
Figure 1.6 Schematic with hypothetical free energy diagram showing the relative free energy states of amorphous drug, crystalline drug and amorphous solid dispersion. E_a represents the activation energy barrier for crystallization and ΔG represents the free energy difference.[40]

Improved dissolution

Most of the polymers used in amorphous solid dispersions are hydrophilic in nature, and therefore, during dissolution they impart increased wettability to the overall ASD formulation giving enhanced dissolution properties to ASDs.

1.2.4 Models for dissolution kinetics of ASDs

As dissolution rate enhancement is one of the most important advantages of amorphous solid dispersions over conventional dosage forms, the mechanisms by which the dissolution rate is improved have been an area of interest and various dissolution models governing the dissolution rate enhancements have been proposed. While no single model proposed to date fully describes all the scenarios with respect to dissolution of solid dispersions, these models enhance our understanding of factors underpinning the dissolution advantage of solid dispersions in some instances. Since elucidating the mechanism of dissolution of ASDs and proposing predictive models is one of the goals of this research, it is imperative to review the current state of knowledge and models developed thus far.

The very first expression for dissolution rate of a pure substance in a medium was given by Noyes along with Whitney, yielding the well-known 'Noyes-Whitney equation' in 1897.[47] The relation is given by:

$$\frac{dm}{dt} = \frac{AD}{h}(C_S - C_b) \qquad (9.)$$

where dm/dt is the solute dissolution rate, t is time, A represents surface area of the solute particle, D is the diffusion coefficient, h is the thickness of the diffusion layer, and C_s and C_b represents the concentration on the particle surface (saturation solubility) and in the bulk solvent/ solution, respectively. Since amorphous solid dispersions are a two component systems, the mathematical models outlined by Higuchi for the dissolution of binary mixtures were the first to be applied to amorphous solid dispersions.[48] According to Higuchi's model, both components of a dissolving binary mixture will follow Noyes-Whitney kinetics initially until the solid-liquid interface at the dissolving front gets depleted in the more rapidly dissolving component. As per the model, after time t, three scenarios may occur for a mixture of component A and B as shown in Fig. 1.7:
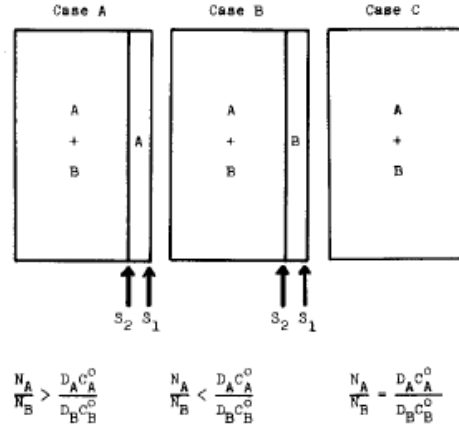
C_A° and C_B° are the respective saturation solubilities of A and B
N_A and N_B are the respective amounts of A and B in the mixture
D_A and D_B are the respective diffusion coefficients of A and B
$S_2 - S_1$ is the thickness of the concentrated layer on the surface

Figure 1.7 Schematic representation of the dissolution model as proposed by Higuchi.[48]

Case A: Component A dominates dissolving surface

Case B: Component B dominates dissolving surface

Case C: Both components co-dissolve in proportion to their initial concentrations

The model provides a good explanation as well as mathematically models the dissolution kinetics for high drug loading ASDs. More specifically, the water soluble polymer depletes at the dissolving front owing to its fast dissolution kinetics compared to the hydrophobic drug leaving behind a porous drug-rich layer which acts as an additional barrier retarding the dissolution of the remainder of the undissolved ASD. Thus, the dissolution of the interfacial drug-rich layer becomes the rate limiting step and the dissolution rate is drug controlled. The mathematical derivation as per this model gives following dissolution rates for drug and polymer:

Drug dissolution rate:
$$G_d = \frac{D_d C_d}{h}$$
(10.)

Polymer dissolution rate:
$$G_p = \frac{N_p G_d}{N_d}$$
(11.)

Here, G_d and G_p are the surface normalized dissolution rates of drug and polymer, respectively. N_d and N_p are the respective amounts of drug and polymer in the mixture. D_d is the diffusion coefficient of drug, C_d is the particle surface (saturation) concentration of drug and h is the thickness of the diffusion layer.

While the aforementioned Higuchi model is applicable at high drug loadings, the model is less tenable for lower drug loadings or higher polymer loadings, where sufficient amount of drug is not present to form a drug-rich layer during the dissolution process. In this scenario, Corrigan proposed that polymer dissolves unhindered by the presence of a drug-rich layer and carries molecularly dispersed drug along with it.[9, 10] The ASD dissolution in such cases is polymer controlled and drug dissolution rate is proportional to polymer dissolution rate and ratio of drug and polymer in the ASD mixture as given by following equation:

$$G_d = \frac{N_d G_p}{N_p} \qquad (12.)$$

However, while polymer controlled dissolution is the more common observation at low drug loadings, there have been number of papers where drug properties (particle size, physical form, etc.) had an influence over dissolution profiles at low drug loadings suggesting that there might be other mechanisms playing a role in those cases.[13, 14] It is to be noted that these observations were based on PEG or xylitol based solid dispersions and to what extent these findings are applicable to amorphous solid dispersions remain debatable. Nevertheless, thereafter Craig came up with a unifying model for these dual observations and proposed that both drug-controlled and polymer-controlled dissolution "may be facets of essentially the same process".[7] The model was based on the following premise: there is a highly concentrated polymer layer at the dissolving front of ASDs through which the drug passes before releasing into the dissolution medium. Based on the solubility of the drug in this concentrated polymer layer. There may be two scenarios as depicted in Fig. 1.8.
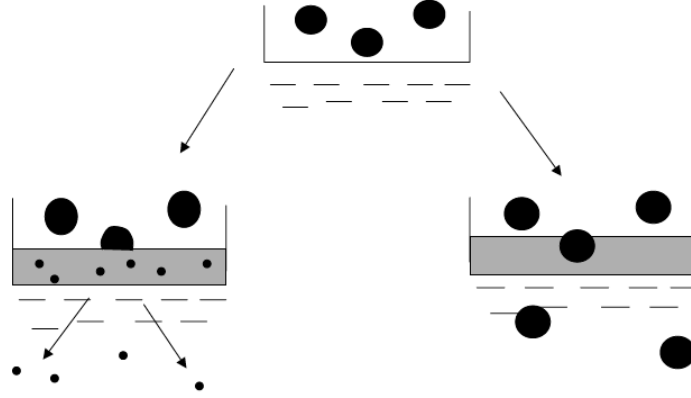
Figure 1.8 Schematic representation of two mechanisms of drug release from solid dispersions: carrier controlled dissolution (a) and drug controlled dissolution (b).[7]

In case (a), the drug, owing to its higher solubility in the polymer-rich layer becomes molecularly dispersed and thereafter, drug diffusion out of the viscous polymer layer is very slow per the Stokes-Einstein equation:

$$D = \frac{kT}{6\pi\eta r} \tag{13.}$$

where k is the Boltzmann constant, η is the viscosity and r is the radius of the diffusing molecule. The rate limiting step to dissolution then becomes the polymer dissolution governed by Eq. (4.) In case (b), the drug solubility in the polymer is limited, thus drug particles remain intact in the polymer layer and consequently, get released in the dissolution medium intact. The dissolution is rendered drug-controlled and depends on drug properties, such as, size, physical form, etc. Craig also derived a mathematical expression for drug-controlled release as given below:

$$G_d = \frac{3D_d \, (C_s - C_b)R^2 x t}{r^4} \int_{t=0}^{t=t} G_p \, dt \tag{14.}$$

where, r is the radius of a drug particle, R is the radius of dissolving surface, x is the weight fraction of drug in ASD. This model explains the dependence of drug release on drug particle size and non-linearity of the dissolution profiles for drug-controlled release formulations.

In spite of these different dissolution models for ASDs, predictability of drug-controlled versus polymer-controlled release remain debatable. Craig discussed examples where the application of his proposed model may not be straightforward.

- Faster dissolution hydrodynamics may favor drug-controlled dissolution by enhancing the rate of polymer dissolution into the bulk in relation to drug dissolution into the diffusion layer.
- Change in drug physical form (e.g. size reduction) may change the mechanism by altering the dissolution kinetics into the diffusion layer.
- The process may not always be one of two extremes, there may be a case of two simultaneous mechanisms of dissolution, e.g. the drug particles may partially dissolve in the diffusion layer before being released intact.

Thus with these aforementioned proposed dissolution models, the dissolution performance of ASDs can't be predicted with certainty currently and ASD formulation design thus remains largely empirical. These models however provide preliminary understanding and lay a foundation for future work towards understanding the mechanism of dissolution of amorphous solid dispersions, which is the scope of this study.

1.2.5   Phase transformations of ASDs

Fig. 1.9 summarizes the plausible phase transformations of an ASD in the ASD matrix via three different routes, i.e., preparation method, during stability or dissolution and in the solution state during dissolution. The following sections provide a detailed description of both solid-state and solution-state phase transformations of ASDs.
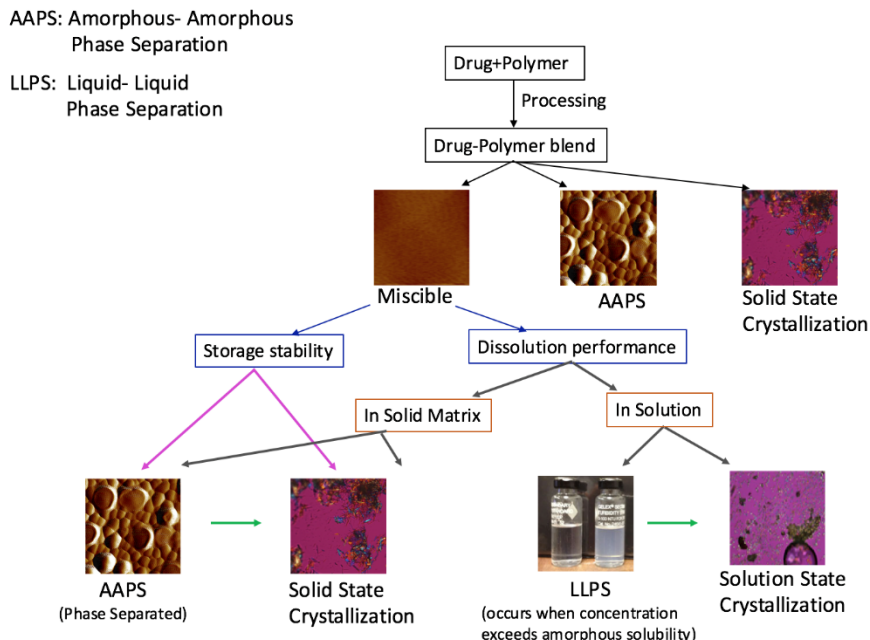
Figure 1.9 Plausible phase transformations of an ASD.

Solid state phase transformations

In the solid state, ideally an ASD system is completely miscible, i.e., a molecular dispersion of drug and polymer. The immiscibility of ASDs can result from direct crystallization of drug in the polymeric matrix or it can be a phase separation with both drug and polymer retaining their amorphous forms. The latter type of phase separation is termed amorphous-amorphous phase separation (AAPS).[49] AAPS can also be a precursor to crystallization since phase separated drug-rich regions have increased propensity towards crystallization.[50]

Crystallization

Crystallization can be divided into two different processes, nucleation and crystal growth.

Nucleation. Nucleation refers to the generation of small nuclei or embryos which later grow into crystals. It involves the formation of new phase capable of independent existence. The process of nucleation can be further divided into two types: primary nucleation and secondary nucleation. Primary nucleation involves formation of a nucleus when there are no existing crystals present while secondary nucleation involves nucleation in the presence of existing crystal seeds. Primary

nucleation can be further of two types: homogenous nucleation and heterogeneous nucleation. Homogeneous nucleation is a phenomenon where nucleation is spontaneous as a result of disturbances in the system without any role of foreign surfaces. Heterogeneous nucleation, on the other hand, is induced due to the presence of foreign surfaces, such as vessel walls, dust particles, impurities, etc. Classical nucleation theory (CNT) is the first account explaining the mechanism of nucleation, while more recently two-step nucleation theory has been proposed to overcome the shortcomings of classical nucleation theory (CNT).[51]

i. *Classical Nucleation theory (CNT).* Classical Nucleation Theory (CNT) is the simplest explanation of the nucleation process. According to this theory,[52] the process of nucleation is favored after a certain critical radius (r_c) is achieved for a nucleus, at which the total free energy of system (ΔG) reaches a maximum, followed by a decrease as shown in Fig. 1.10.[51] The kinetic part of this theory gives the steady-state rate of nucleation (J), which is equal to number of nuclei formed per unit time per unit volume and is given by the following equation:

$$J = A \exp\left(-\frac{\Delta G_{crit}}{kT}\right) \qquad (15.)$$

where k is the Boltzmann's constant and A is the pre-exponential factor. The kinetics of nucleation is related to rate of attachment of molecules, and thus depends on molecular mobility. Since molecular mobility changes rapidly with temperature, the temperature dependence of the pre-exponential factor (A) also needs to be taken into account and can play a significant role in nucleation rate.
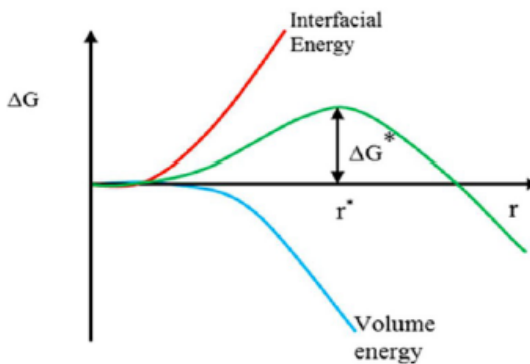
Figure 1.10 Graphical representation of dependence of nucleation barrier (ΔG*) on the radius r as per classical nucleation theory.[51]

ii. *Two-Step Nucleation Theory.* Per two step nucleation theory, there is an additional intermediate phase before the formation of the nucleus. The first step is the formation of a highly disordered liquid droplet. When the crystalline nucleus inside the droplet obtains a certain critical size, the free energy decreases and consequently the nucleation rate increases. Thus, the first step in nucleation is the formation of highly disordered sufficient sized cluster of solute molecules followed by the second step of reorganization of that cluster into an ordered structure. In two step nucleation theory, organization time of lattice structures, i.e., the second step is the rate-determining step as reorganization of cluster is a higher energy barrier process.[53]

Crystal growth. Once a stable nucleus has formed, crystal growth happens by transfer of molecules from the bulk to the surface of the nucleus.[52] Various theories have been proposed to explain the mechanism of crystal growth and it is considered to be a complex phenomenon. As per Jackson's work[54] on crystal growth rate determination, both molecular mobility (kinetic factor) and free energy difference between amorphous & crystalline form (thermodynamic driving force) determine the overall crystal growth rate. As these two factors depend oppositely on temperature, various studies have shown that crystal growth initially increases and then decreases with supercooling resulting in a bell shaped curve with a maximum lying somewhere between melting temperature (T_m) and glass transition temperature (T_g).[55, 56] A schematic illustrating the rates of nucleation, crystal growth and overall crystallization as a function of temperature for undercooled melts is shown in Fig. 1.11.
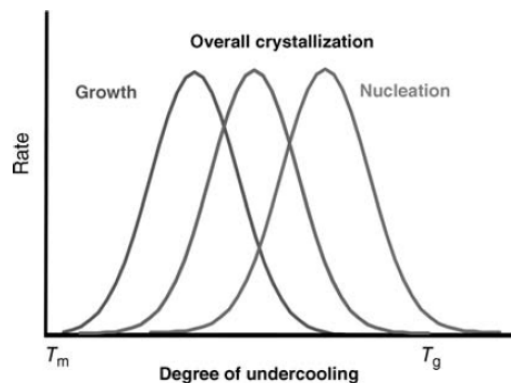
Figure 1.11 Schematic illustration of dependence of rates of nucleation, crystal growth and overall crystallization as a function of temperature.[57]

Amorphous-amorphous phase separation

Amorphous-amorphous phase separation where ASDs are phase separated into drug-rich and polymer-rich phases can be caused by processing conditions as reviewed in section 1.2.2. Thus, the focus of this section is on another important route by which AAPS can occur, i.e., water-induced AAPS. The presence of water during processing, storage at high relative humidity as well as during dissolution can result in water-induced AAPS. The mechanism by which water-induced AAPS can occur can be classified into two routes: kinetic and thermodynamic.

Kinetic route. Moisture absorption into ASDs is a known issue, firstly, due to the greater tendency of water sorption by amorphous drugs (due to their disordered structure) as compared to crystalline drugs and, additionally, due to presence of hydrophilic polymers in the ASDs. Water, due to its low T_g (135K) has a plasticization effect and can lower the overall T_g of an ASD.[58] Every 1% water absorbed can lower the T_g of the system by approximately 10°C,[59] based on the well-known Gordon-Taylor equation given in equation 16.[42] This equation reasonably estimates the T_g decrease of amorphous solid dispersions following water sorption in a number of cases.[60] The decreased T_g results in enhanced mobility in the ASD matrix which can lead to amorphous-amorphous phase separation followed by crystallization or even direct crystallization in some cases.

$$T_g^{mix} = \frac{[(w_1 T_{g1}) + (Kw_2 T_{g2})]}{[w_1 + (Kw_2)]} \qquad (16.)$$

where subscripts 1 and 2 represent the two different components, T_g^{mix} is the glass transition temperature of the mixture, T_{g1} and T_{g2} are the glass transition temperatures of component 1 and 2, respectively, and w_1 and w_2 are weight fractions of component 1 and 2, respectively. K in above equation can be found using the following equation, where ρ_1 and ρ_2 are densities of component 1 and 2, respectively:

$$K = \frac{T_{g1}\rho_1}{T_{g2}\rho_2} \tag{17.}$$

Thermodynamic route. Amorphous-amorphous phase separation can have thermodynamic origin which can be understood by rewriting the Flory-Huggins equation for ternary systems (equation 6) with water as the solvent.

$$\Delta G_m = RT[n_D ln\Phi_D + n_P ln\Phi_P + n_w ln\Phi_w + n_w \Phi_D \chi_{wD} + n_w \Phi_P \chi_{wP} \\ + n_D \Phi_P \chi_{DP}] \tag{18.}$$

'w' here stands for water and rest all abbreviations remain the same as described for equation 6. It is evident from equation 18 that miscibility of an ASD system after the water is introduced into it would depend on the relative strengths of interactions between drug-polymer, drug-water and polymer-water, which is accounted in the equation in terms of the Flory-Huggins interaction parameter, χ. For instance, owing to increased hydrophilicity of polymer, it is reasonable to speculate that polymer-water interactions are stronger than drug-water interactions or drug-polymer interactions, and that the system may phase separate due to "$\Delta\chi$ effect". A study done by Rumondor et al. found that a less hydrophobic API, minimal hygroscopicity of the polymer and stronger drug-polymer interactions are important factors that provide resistance against water-induced amorphous-amorphous phase separation.[61]

Solution-state phase transformations

A supersaturated solution generated upon dissolution of amorphous solid dispersions can undergo various phase transformations depending on the extent of supersaturation. Fig. 1.12 shows a

concentration versus temperature phase diagram for a hypothetical system.[62] Supersaturation at the crystalline solubility is unity and as the concentration exceeds its crystalline solubility, the supersaturation is greater than 1. In zone I in Figure 1.12, the system is supersaturated and the crystal growth of already existing crystals can happen but there is insufficient driving force to overcome the nucleation barrier and no spontaneous nucleation or nucleation in presence of crystal seeds can happen. As the concentration increases into zone II, nucleation can occur in the presence of crystal seeds but primary nucleation cannot happen. Zone I and II are together referred to as the metastable zone and the concentration range in this region is referred as metastable zone width. It is possible to obtain supersaturated solutions in this zone and crystallization can be inhibited using different additives. The more labile zone which is prone to spontaneous nucleation is the zone III, where the concentration exceeds than that of metastable zone. At a certain concentration beyond the metastable zone in zone III and if crystallization does not happen, there will be a point in the phase diagram where the concentration will reach the amorphous solubility beyond which solution will undergo liquid-liquid phase separation (LLPS).[63] LLPS, also known as oiling out, is a phenomenon where the system will phase separate into a solute-rich and solvent-rich phase. When LLPS occurs during dissolution of amorphous solid dispersions, nano-sized, drug-rich colloidal aggregates are formed in the solution, while the free drug concentration in the solution remains at the amorphous solubility. The phenomenon of LLPS is discussed in detail in the next section. It should be noted that beyond the amorphous solubility, supersaturated solution can undergo LLPS or crystallization depending on the competing kinetics between the two. Crystallization in this zone can happen either directly from the solution or also from the colloidal aggregates formed.
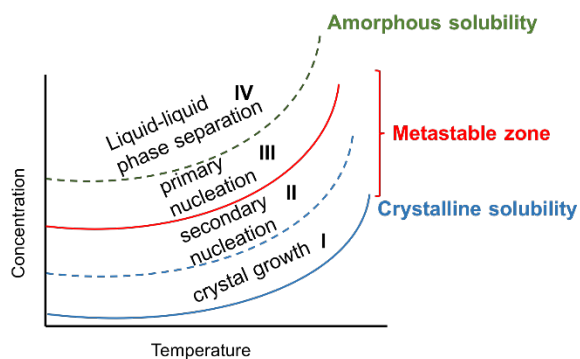
Figure 1.12 Concentration versus temperature phase diagram for a hypothetical solution. Adapted from ref.62.

Liquid-liquid phase separation

The free energy versus composition phase diagram, as shown in Figure 1.3 for partially miscible ASDs, can also be applied to partially miscible liquids and can be used to describe LLPS as shown in Fig. 1.13.[64] Here the two liquids considered, water (*W*) and amorphous drug (*D*), exhibit a miscibility gap. x_{DW} and x_{WD} are binodal points which represent the composition of two phases that phase separates when the system undergoes LLPS for any compositions falling between x_{DW} and x_{WD}. The drug-rich aggregates formed will have a composition corresponding to x_{DW} while the water-rich phase will have x_{WD} as the composition. The composition of the water-rich phase thus formed, corresponds to amorphous solubility of the drug. The compositions between the binodal and spinodal points is termed the metastable region where formation of a new liquid phase occurs through nucleation and growth, while LLPS occurs spontaneously for compositions between the spinodal points. The chemical potentials of two phases at LLPS are the same as shown by the tie line in the figure.
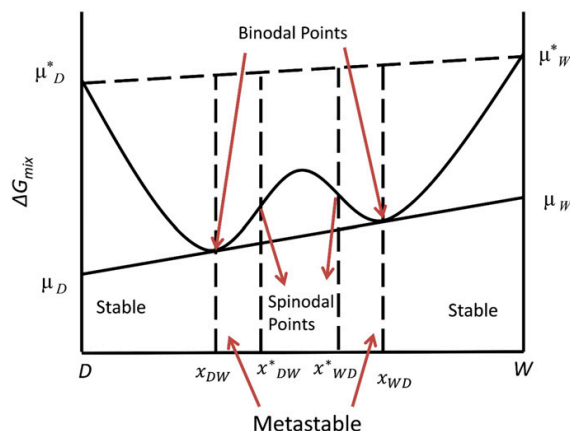
Figure 1.13 Free energy versus composition phase diagram for two liquids with a miscibility gap. The liquids here are amorphous drug and water. D stands for amorphous drug and W stands for water.[64]

In a study by Ilevbare and Taylor for eight different compounds, it was experimentally and conceptually demonstrated that the LLPS onset concentration for an amorphous drug coincides with the amorphous solubility in aqueous solutions.[63] In another study by Raina et al, flux measurements in a side-by-side diffusion cell were performed for a series of nominal concentrations added to the donor cell.[65] The receiver cell drug concentrations were measured over time to determine diffusive flux (J_D) as per following equation:

$$J_D = \frac{dm}{Adt} = \frac{Da}{h\gamma_m} \qquad \text{(19.)}$$

where $\frac{dm}{dt}$ is the rate of mass transfer, A is the surface area available for mass transfer, D is the diffusion coefficient of the drug molecule, h is the diffusion layer thickness, a is the thermodynamic activity in the donor cell and γ_m is the activity coefficient of the drug in the membrane. As supersaturation in true thermodynamic terms is defined by the activity ratio of drug in amorphous form with respect to crystalline form, flux measurements depending on the activity of the solute in the donor compartment give a true measure of supersaturation. As shown in Fig. 1.14, an increase in concentration of drug in the donor cell results in a concomitant increase in the flux in the receiver cell until a maximum supersaturation is achieved, i.e., at the amorphous solubility, beyond which activity of the solute remains constant. It also means that LLPS and amorphous solubility is the maximum limit of supersaturation and activity of an amorphous drug. The occurrence of LLPS is considered pivotal from an *in vivo* perspective as the drug-rich phase helps replenish the free drug concentration in the dissolution medium as the drug diffuses across the membrane and it does so until all the colloidal nanodroplets dissolve in this manner thereby increasing the timeframe for the maximum achievable activity or mass flow with potential *in vivo* bioavailability enhancement effect.[65, 66] This phenomenon can be demonstrated from Fig. 1.15, where the thermodynamic activity (as determined from the flux) remains constant over time for a system undergoing LLPS while it decreases with time for a system undergoing crystallization.
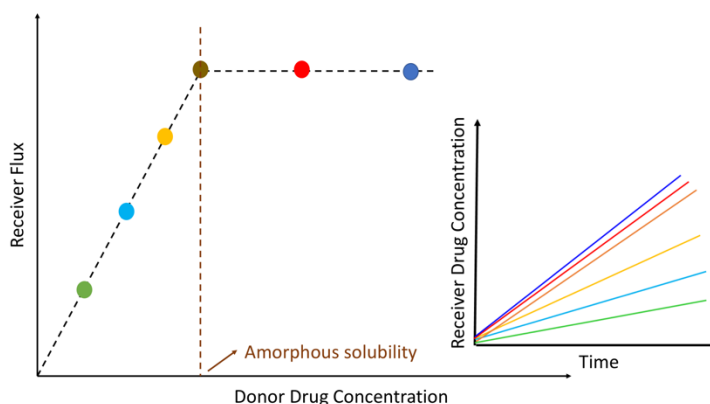
Figure 1.14 Schematic showing the increase in receiver flux as a function of drug concentration in donor compartment in a side by side diffusion cell. The amorphous solubility is the limiting donor concentration above which the receiver flux remains constant.
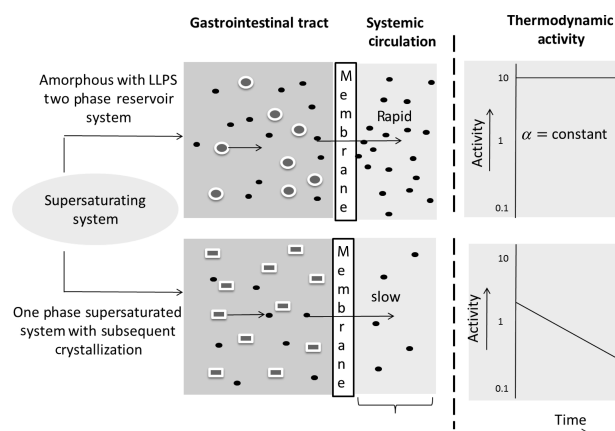
Figure 1.15 Comparison of mass transfer and activity over time for system undergoing LLPS versus crystallization.[65]

1.3   Overview of content in different chapters

Table 1.1 Summary of content included in different chapters

Chapter number	Summary of content
1.	• The fundamental aspects of solubility advantage of amorphous solids, ASDs, solid and solution-state phase transformations associated with ASDs, namely, AAPS and LLPS, literature-based dissolution kinetics models, nucleation and crystal growth were discussed.
2.	• A new confocal fluorescence microscopy-based method was developed to study drug-polymer miscibility in an ASD. • Drug-specific and polymer-specific fluorescent dyes enabled simultaneous visualization of drug-rich and polymer-rich phases in a phase-separated ASD film. • Water-induced AAPS was observed upon high RH/ bulk water exposure during preparation, storage and dissolution for the model miconazole-poly (vinylpyrrolidone-co-vinyl acetate) ASD.

Table 1.1 continued

3.	• Liquid-liquid phase separation occurred only at low drug loadings when drug and polymer released congruently from an ASD.
	• Limit of congruency (LoC) for PVPVA ASDs was independent of drug log P.
	• Congruent release occurred when dissolution rate was faster than the phase separation kinetics.
	• A distinct drug-rich porous interface was observed on the partially dissolved incongruently releasing ASD tablet surface.
4.	• Contrary to our initial hypothesis, ASDs with drug-polymer hydrogen bonding interaction showed lower LoC as compared to the non-hydrogen bonding analogue ASDs.
	• Surface crystallization led to incongruent release at longer time points for ASDs with relatively fast crystallizer drug.
	• Variable temperature dissolution studies suggested that ASDs with a higher wet T_g relative to the dissolution temperature are detrimental to the dissolution performance.
5.	• Drug and polymer release of felodipine ASDs with five diverse polymers were studied.
	• Hydrophilic polymers, namely, PVP, PVPVA and HPMC showed lower LoC ($\leq$15% drug loading) with sudden decline in release rates above LoC.
	• Hydrophobic polymers, namely, HPMCAS and EUDS showed higher LoC (>50% drug loading).
	• Within congruent regimen (at low drug loadings), hydrophilic polymers, PVP and PVPVA, outperformed relatively hydrophobic polymers with regards to drug dissolution rates.

CHAPTER 2. WATER INDUCED PHASE SEPARATION OF MICONAZOLE-POLY (VINYLPYRROLIDONE-CO-VINYL ACETATE) AMORPHOUS SOLID DISPERSIONS: INSIGHTS WITH CONFOCAL FLUORESCENCE MICROSCOPY

2.1 Abstract

The aim of this study was to evaluate the utility of confocal fluorescence microscopy (CFM) to study the water-induced phase separation of miconazole-poly (vinylpyrrolidone-co-vinyl acetate) (mico-PVPVA) amorphous solid dispersions (ASDs), induced during preparation, upon storage at high relative humidity (RH) and during dissolution. Different fluorescent dyes were added to drug-polymer films and the location of the dyes was evaluated using CFM. Orthogonal techniques, in particular atomic force microscopy (AFM) coupled with nanoscale infrared spectroscopy (AFM-nanoIR), were used to provide additional analysis of the drug-polymer blends. The initial miscibility of mico-PVPVA ASDs prepared under low humidity conditions was confirmed by AFM-nanoIR. CFM enabled rapid identification of drug-rich and polymer-rich phases in phase separated films prepared under high humidity conditions. The identity of drug- and polymer-rich domains was confirmed using AFM-nanoIR imaging and localized IR spectroscopy, together with Lorentz contact resonance (LCR) measurements. The CFM technique was then utilized successfully to further investigate phase separation in mico-PVPVA films exposed to high RH storage and to visualize phase separation dynamics following film immersion in buffer. CFM is thus a promising new approach to study the phase behavior of ASDs, utilizing drug and polymer specific dyes to visualize the evolution of heterogeneity in films exposed to water.

2.2 Introduction

Many of the new compounds emerging from pharmaceutical pipelines have low solubility and dissolution rates.[67] There are many solubility and dissolution enabling technologies available to address this issue.[2] Amongst them, using the amorphous form of drug, molecularly dispersed in a

polymeric matrix, producing a system commonly referred to as an amorphous solid dispersion (ASD), has proven to be a highly effective and viable formulation strategy to improve solubility and in turn, bioavailability of poorly soluble drug candidates.[4, 39]

The successful application of ASD is based on an important underlying assumption of homogeneity or miscibility of the drug and polymer at a molecular level in the ASD matrix. Lack of homogeneity in ASDs has been found to be of issue that can impact stability as well as the dissolution performance of ASDs. If the polymer is not homogeneously mixed with the drug, or phase separation has occurred resulting in drug-rich and drug-lean domains, the role of the polymer as a crystallization inhibitor is undermined.[15-17] Phase separation in the solid ASD matrix can result from either crystallization of drug or demixing with both drug and polymer retaining their amorphous nature. The latter phenomenon is termed as amorphous-amorphous phase separation (AAPS). AAPS has been found to be a precursor to crystallization as the resultant drug-rich phase has increased propensity towards crystallization due to the lower local polymer concentration.[68] Crystallization, in turn, can be expected to negate the solubility advantage of the amorphous formulation.[69] AAPS can occur during manufacturing,[70] as a result of environmental moisture absorbed during storage [68, 71] or in presence of bulk water introduced into the matrix during the dissolution process.[18]

Conventional analytical techniques, such as differential scanning calorimetry (DSC) and X-ray diffraction (XRD), are useful for detecting crystallinity in the ASD matrix, but it may be challenging to detect AAPS using these approaches. DSC, for instance, can fail to detect phase separation due to its non-isothermal nature which can lead to remixing during heating,[70] and is inherently limited for systems with a domain size of less than 30 nm.[72] XRD is most suited for analyzing systems with long-range order, and research is still underway to extract interpretable information from complex amorphous systems such as ASDs. Microscopic and surface analysis techniques, such as atomic force microscopy and electron microscopies (scanning and transmission) have nano-scale spatial resolution but lack chemical specificity to differentiate drug and polymer.[73, 74] Infrared (IR) and Raman spectroscopy can provide useful chemical information about miscibility based on the presence of intermolecular interactions [50, 75] but data interpretation can be complex and not all systems are suitable to this type of analysis. Due to aforementioned

challenges encountered with many conventional analytical methods, there continues to be interest in new approaches to evaluate ASD miscibility.[76]

An emerging analytical approach for miscibility evaluation involves fluorescence-based methods, both steady-state fluorescence spectroscopy and fluorescence microscopy.[18, 34, 77, 78] Both techniques require a fluorophore for successful application. ASDs of drugs which are autofluorescent have been investigated using this approach[78] while for non-fluorescent systems, extrinsic environment sensitive fluorescent probes have been used to monitor phase separation.[18, 34, 77] Fluorescence microscopy, utilizing external fluorescent probes, is a promising approach for visualizing phase separation in ASDs, but is an un-optimized technique. To date, most studies have focused on staining the drug-rich phase by incorporating a hydrophobic dye that preferentially interacts with the drug. However, in the biological sciences, it is common to employ multiple dyes, chosen to stain specific structures. This approach is also feasible for drug-polymer systems since the polymer is typically more hydrophilic than the drug.[79] The objectives of this study were two-fold. First, to investigate confocal microscopy as a tool to probe miscibility in drug-polymer ASD films by employing fluorescent dyes with different affinities for drug and polymer. Second, to evaluate the evolution of microstructure in ASD films following water-induced AAPS occurring during preparation, storage at high relative humidity and during dissolution. The model drug-polymer system used was miconazole-poly (vinylpyrrolidone-co-vinyl acetate) (mico-PVPVA); the miscibility of this model system has been found to vary depending on the preparation method used (spray drying versus hot melt extrusion) and stresses involved (compression pressure, dwell time, etc.).[80-82] It was hypothesized that the simultaneous contrast imaging of drug-rich and polymer-rich domains could be achieved by utilizing two fluorescent probes, added to the ASD matrix; a hydrophobic fluorescent probe which selectively partitions into the drug-rich phase, and a second hydrophilic probe which preferentially associates with polymer-rich phase. After screening several dyes, prodan and rhodamine-6G (R6G) were selected as drug-specific and polymer-specific dyes, respectively. An orthogonal technique, atomic force microscopy (AFM) coupled with infrared (IR) spectroscopy (AFM-nanoIR) and Lorentz contact resonance (LCR) measurements (AFM-LCR) was used to confirm the results obtained from confocal fluorescence microscopy.[77]

2.3 Materials

Miconazole (mico) was purchased from ChemShuttle (Jiangsu, China). Methanol and dichloromethane were procured from Macron chemicals (NJ, U.S.A.). Prodan was obtained from AnaSpec Inc. (CA, U.S.A.). 5-(4,6-dichlorotriazinyl) aminofluorescein (5-DTAF) and Alexa Fluor®488 were procured from ThermoFisher Scientific (CA, U.S.A.), while fluorescein, pyrene, nile red, fluorescein isothiocyanate (FITC) and rhodamine 6G (R6G) were obtained from Sigma-Aldrich Co. (MO, U.S.A.). Kollidon VA 64 (PVPVA) was supplied by the BASF Corporation (Ludwigshafen, Germany). The chemical structures of model drug and polymer along with selected fluorescent probes are given in Figure 2.1.
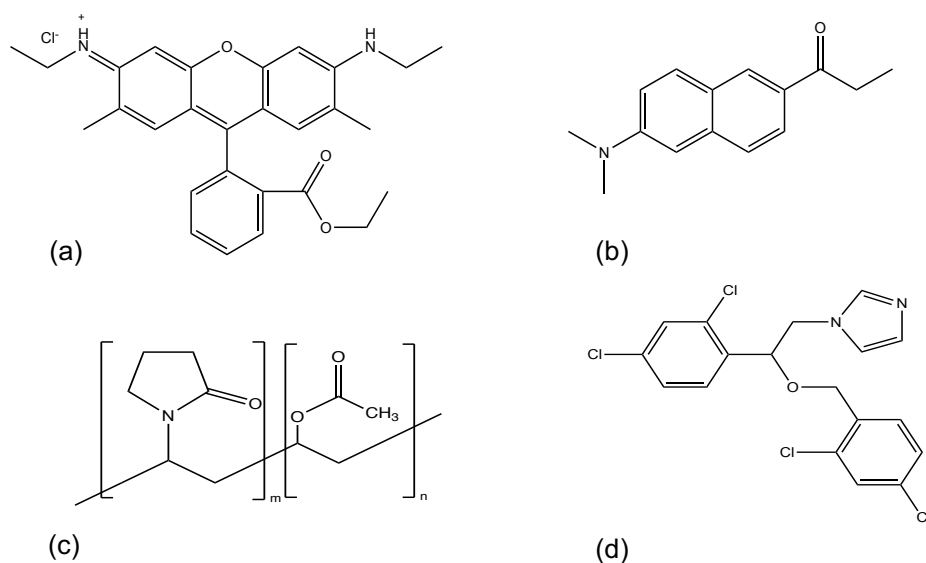
Figure 2.1 Structures of the compounds used. Rhodamine-6-G (R6G) (a), prodan (b), poly (vinylpyrrolidone-co-vinyl acetate) (PVPVA) (c) and miconazole (d).

2.4 Methods

2.4.1 Preparation of drug-polymer films

Thin films of pure amorphous mico, pure PVPVA and mico-PVPVA ASDs at 50:50 w/w ratio were prepared by dissolving the solids (50 mg/mL) in a 50:50 v/v methanol:dichloromethane mixture, followed by spin coating. Two sets of each solution were prepared. The first set was used for AFM analysis, whereas fluorescent probes were added to the second set at an individual concentration of 0.01% w/v (100 µg/mL). A two-stage spin coater KW-4A (Chemat Technology Inc., Northridge, CA) was used to prepare films at 500 and 3,000 rpm for 6 and 30 s,

respectively. The substrate and the amount of sample used for spin coating varied depending on the analytical technique used. For AFM studies, the volume was 15 µL, deposited on a ZnS substrate (Model: SM-nIR2-Flat-5, Anasys Instruments, Inc., Santa Barbara, CA); for bulk IR spectroscopy, 50 µL was deposited on a KRS-5 substrate (Harrick Scientific Corporation, NY), and for fluorescence microscopy, 100 µL sample was added to a quartz slide (1" x 1", 1 mm thick, Ted Pella Inc., Redding, CA). Films were prepared at either "low" or "high" RH conditions. Low RH conditions were achieved by placing the spin coater in a glove box purged with dry nitrogen gas where an RH of 20% was achieved. High RH conditions were achieved by spin coating in the ambient lab condition where the RH was recorded for each film and was found to vary between 45-60%. All films were dried overnight under vacuum before conducting further studies. Films produced in this manner were estimated to be around 300 nm thick based on AFM height measurements.

2.4.2 Storage stability of miscible films at high relative humidity

ASD films prepared at low RH were stored in a desiccator maintained at 75% RH using a saturated salt solution of NaCl. The films were evaluated after 1, 2, 3, 7, and 28 days using CFM and AFM imaging.

2.4.3 Phase behavior of miscible films during buffer immersion

In order to mimic the impact of dissolution on the phase behavior of initially miscible ASD films, films were immersed in pH 6.8 100 mM phosphate buffer for time periods of 5, 10, 20, and 30 min, rapidly dried and then evaluated using confocal fluorescence microscopy. Only the 30 min time point sample was analyzed using AFM topographical and nano-IR imaging.

2.4.4 Selection of fluorescent probes for confocal fluorescence microscopy (CFM)

To determine if the fluorescent probes preferentially stained the drug or polymer-rich phase, phase separated ASD films of 50:50 w/w mico-PVPVA were prepared at high RH as described above, adding individual fluorescent probes. Films were then imaged using fluorescence microscopy to determine the location of the probe. An additional criterion in selecting probes was photobleaching tendency. To evaluate this, three consecutive fluorescence images, with a constant exposure time of 500 ms and no lag time, were

taken and qualitatively checked for deterioration of fluorescence intensity over time. For probe screening, fluorescence images were obtained using a wide field fluorescence microscope (Olympus BX-51, Olympus, NY). Other criteria considered for selection of fluorescent probes were the availability of excitation laser lines and corresponding emission filters for the confocal fluorescence microscope utilized (Nikon A1 confocal microscope, Melville, NY), spectral distance between a pair of drug-specific and polymer- specific dyes and, lastly, the cost of fluorescent probes.

2.4.5 Atomic force microscopy (AFM) topographical imaging

AFM topographical imaging was performed using a nanoIR2 AFM-IR instrument (Anasys Instruments, Inc., Santa Barbara, CA). A contact mode NIR2 probe (model: PR-EX-NIR2, Anasys Instruments, Inc., Santa Barbara, CA), was used to collect images. The image acquisition time was 8.5 min with a scan rate of 0.5 Hz and an x and y resolution of 256 points. The scan area was chosen based on the lateral extent of phase separation. For instance, 50 μm x 50 μm scan area was used to visualize the phase separation during buffer immersion studies as compared to 5 μm x 5 μm for preparation-induced phase separation and 10 μm x 10 μm for storage-induced phase separation. Analysis Studio software (version: 3.12, Anasys Instruments, Inc., Santa Barbara, CA) was used to collect and process topographical images. The image flattening function was used for topographical images.

2.4.6 Bulk IR spectroscopy

Thin films of pure amorphous mico and PVPVA were prepared on KRS-5 substrates by the spin coating method described above. A Bruker Vertex 70 FTIR spectrophotometer (Bruker, Billerica, MA) was used to collect spectra. 128 scans in transmission mode were co-averaged for both background and samples over a spectral range of 1200-1800 cm^{-1} with a 4 cm^{-1} resolution. OPUS software (version: 7.2, Bruker Optik GmbH, Ettlingen, Germany) was used to collect and analyze the IR spectra.

2.4.7 Nanoscale IR (nano-IR) spectroscopy and imaging

A nanoIR2 AFM-IR instrument (Anasys Instruments, Inc., Santa Barbara, CA) with Analysis Studio software (version: 3.12, Anasys Instruments, Inc., Santa Barbara, CA) was used to collect

localized mid-IR spectra and IR images, at nanoscale resolution, in contact mode, with NIR2 probes (Model: PR-EX-NIR2, Anasys Instruments, Inc., Santa Barbara, CA). AFM-IR is a technique which combines the nanoscale resolution of an AFM with a tunable pulsed IR laser source for chemical specificity. When the wavelength of the incident light corresponds to an absorption band, the sample absorbs energy and thermal expansion occurs causing the AFM cantilever in contact mode with the sample to oscillate. By recording the characteristic decay in the amplitude of oscillations as a function of time, the "ringdown" of the cantilever is recorded. The second harmonic mode of cantilever oscillation with a frequency center of 200 kHz and a frequency window of 50 kHz was chosen for recording "ringdown" signal in this case. The information about amplitudes and frequencies of oscillations can be extracted by applying Fourier transformation techniques, where the amplitude of this "ringdown" is proportional to the absorption of the sample. A local absorption spectrum (absorption versus wavenumber) is generated by measuring this "ringdown" over a wide range of wavenumbers [83]. The IR laser source was optimized and tuned at 1590 cm^{-1} for miconazole and 1679 cm^{-1} for PVPVA for chemical imaging. Details on IR optimization can be found in Li et al [77]. Background calibration and data collection for AFM-IR spectra were performed over 1200−1800 cm^{-1} with a co-average of 256 scans, at a data point spacing of 4 cm^{-1}. The acquisition time for IR spectra was 2.5 min. A co-average of 8 scans was used for AFM-IR chemical imaging, with a scan rate of 0.1 Hz, and X and Y resolution of 256 points. The IR image acquisition time was 42.7 min. All spectra represent the co-average of 3 scans smoothed using a Savitzky-Golay function.

2.4.8 Lorentz contact resonance (LCR) measurements

Lorentz Contact Resonance AFM (LCR-AFM) enables compositional mapping of phases based on their different viscoelastic properties and can discriminate phases based on localized nanomechanical spectra [84]. Oscillations are induced in an AFM probe by an oscillating Lorentz force, which is a force generated by the interaction of an AC current passing through the probe in presence of a magnetic field focused near the probe [85]. The amplitude and resonance frequency of the oscillating probe depends on the mechanical properties of the material in contact with the AFM tip. By scanning the sample surface at a certain frequency, the oscillation amplitude as a function of position generates LCR images that reflect compositional differences based on the relative stiff-

ness of each phase. By conducting frequency sweeps over a wide range at a particular position, localized mechanical spectra of the surface in contact with the probe can be obtained.[77, 84, 86]

A Thermalever probe (Model: EXP-AN2-300, Anasys Instruments Inc., Santa Barbara, CA) together with a LCR magnet was used to perform frequency sweeps and collect LCR images. An AFM height scan was performed prior to LCR measurements in order to place the probe at a position of interest for subsequent collection of localized mechanical spectra. An AC voltage drive strength of 50% was used for conducting LCR sweeps in the frequency range of 1 kHz to 1000 kHz, at a sweep rate of 100 kHz/s. The data collection rate was 200 points/s. LCR images were obtained by driving the AFM cantilever to a contact frequency that is sensitive to differences based on contact stiffness of different regions in the sample. To identify drug-rich regions in phase separated films, the thermalever probe was driven to a drive frequency of 113.8 kHz corresponding to first flexural peak (first large peak) of the mechanical spectrum of pure miconazole. When the contact frequency of both the region of interest and the probe is the same, bright areas in the LCR amplitude image correspond to a drug-rich phase. The same is true for polymer-rich phases at a drive frequency of 112.6 kHz, which corresponds to first flexural peak of the pure polymer mechanical spectrum. An x and y resolution of 256 points, with a scan rate of 0.5 Hz was utilized. The LCR image acquisition time was about 8.5 min.

2.4.9   Confocal fluorescence microscope imaging

Confocal fluorescence imaging of ASD films was performed with a Nikon A1 Confocal Fluorescence Microscope (Melville, NY, USA). A 60X oil-immersion objective lens with a numerical aperture of 1.49 was used. The ASD films analyzed contained two fluorescent probes, prodan (relatively hydrophobic) for drug specificity and R6G (relatively hydrophilic) for polymer specificity. Prodan was excited with a laser at 407 nm, and emission was collected using a 425-475 nm filter. R6G was excited with a laser at 561 nm and emission was collected with a 570-620 nm filter. Nikon NIS-Elements AR software (version: 4.20.01) was used for image collection at 1024 x 1024 pixels with the optical resolution of 0.07 μ/pixel. The subtract white function was utilized in the software to improve the color saturation of the image and remove background effects. Certain images were further processed using the levels adjustment tool in Photoshop CC (Adobe

Systems Incorporated, San Jose, CA) to enhance the contrast between discrete and continuous phases. Care was taken not to clip any pixels so that underlying spatial information remains intact.

2.4.10 Preparation of bulk amorphous solid dispersions

Powdered ASD of 50:50 mico:PVPVA were prepared by dissolving the solids (50 mg/mL) in a 50:50 v/v methanol:dichloromethane mixture followed by rotary evaporation in a Buchi Rotavapor-R (New Castle, DE) equipped with Yamato BM-200 water bath at 45°C under reduced pressure. The ASD powder thus obtained were dried under vacuum overnight prior to determination of the glass transition temperature (T_g). To evaluate the impact of water on T_g, around 10 mg of powder was equilibrated at 75 or 100% RH using a SGA-100 symmetric vapor sorption analyzer (VTI Corp, Hialeah, FL) at 25°C to control RH. Samples were considered equilibrated when there was less than 0.01% weight change in 5 min with a maximum equilibration time of 180 min.

2.4.11 Differential scanning calorimetry (DSC)

T_g analysis on the ASD powder was performed using a TA Q2000 DSC equipped with a refrigerated cooling accessory (RCS) (TA Instruments, New Castle, DE). Approximately 3-5 mg of the ASD powder (a sample dried under vacuum overnight, and samples post equilibration at 75%RH and 100% RH) were placed in hermetically sealed Tzero aluminium pans and heated at rate of 2°C/ min from -40 °C up to 120 °C with modulation of 1 °C every 60s. In an additional experiment, the vacuum dried sample was subjected to isothermal heating at 100°C for 60 min, cooled and reanalyzed as described above.

2.5   Results

2.5.1   Impact of preparation method

AFM topographical imaging and localized IR spectroscopy

AFM has been widely used to evaluate miscibility in ASDs [73, 77, 87, 88] and was therefore used to initially characterize the miconazole-PVPVA system. AFM height images of spin coated films of pure drug and polymer are shown in Fig. 2.2A. The films are smooth with no discernable surface

features. Reference spectra were obtained from these films using the nano-IR system with results shown in Fig. 2.2B. Miconazole is characterized by a peak at 1590 cm^{-1} while PVPVA shows a characteristic peak at 1679 cm^{-1}. The peak at 1590 cm^{-1} in the miconazole spectrum arises from the conjugated aromatic ring stretching whereas the peak at 1679 cm^{-1} in the PVPVA spectrum is due to stretching of the carbonyl group of the pyrrolidone monomer [89]. The spectra obtained using the nano-IR show good agreement with bulk transmission IR spectra obtained on a standard FTIR instrument (Fig. 2.3). The 50:50 miconazole:PVPVA film prepared at 20% RH also presents a smooth topography (Fig. 2.4A), suggesting that the drug and polymer are miscible; previous studies on phase separated drug-polymer systems typically show the presence topographical features corresponding to drug-rich and polymer-rich domains [34, 77, 87]. IR mapping across this film yielded identical spectra (Fig. 2.4B) at each analysis point, indicating that the film is chemically homogeneous at the resolution of the nano-IR system, which is around 100nm [90]. The resultant spectra show peaks characteristic of both the polymer and the drug and thus suggest that films prepared at low RH are miscible.

In contrast, spin coating at a RH of 60% leads to the formation of discrete, circular domains which formed pits, with a depth of around 200-400 nm, in the continuous phase (Fig. 2.5A). Localized IR spectra were collected from the continuous and discrete phases with results shown in Fig. 2.5B. Both drug and polymer specific peaks were present in each phase indicating either that the system is partially miscible, and/or as a result of spectral mixing vertically throughout the penetrable thickness of the sample or horizontally between two domains closer than the spatial resolution limit of the instrument or some combination of both factors [77, 91]. As the intensity of localized IR spectra is dependent on sample thickness, i.e., height features, comparison of the relative peak heights of normalized spectra provides a better comparison of the chemical composition of the different phases. For the phase separated films, the relative peak height of the characteristic drug peak at 1590 cm^{-1} is higher for the discrete phase as compared to continuous phase, whereas the relative peak height of the polymer specific peak at 1679 cm^{-1} is higher in the continuous phase as compared to discrete phase (Fig. 2.5B). This indicates that the discrete phase is miconazole-rich, whereas the continuous phase is PVPVA-rich (Fig. 2.6).
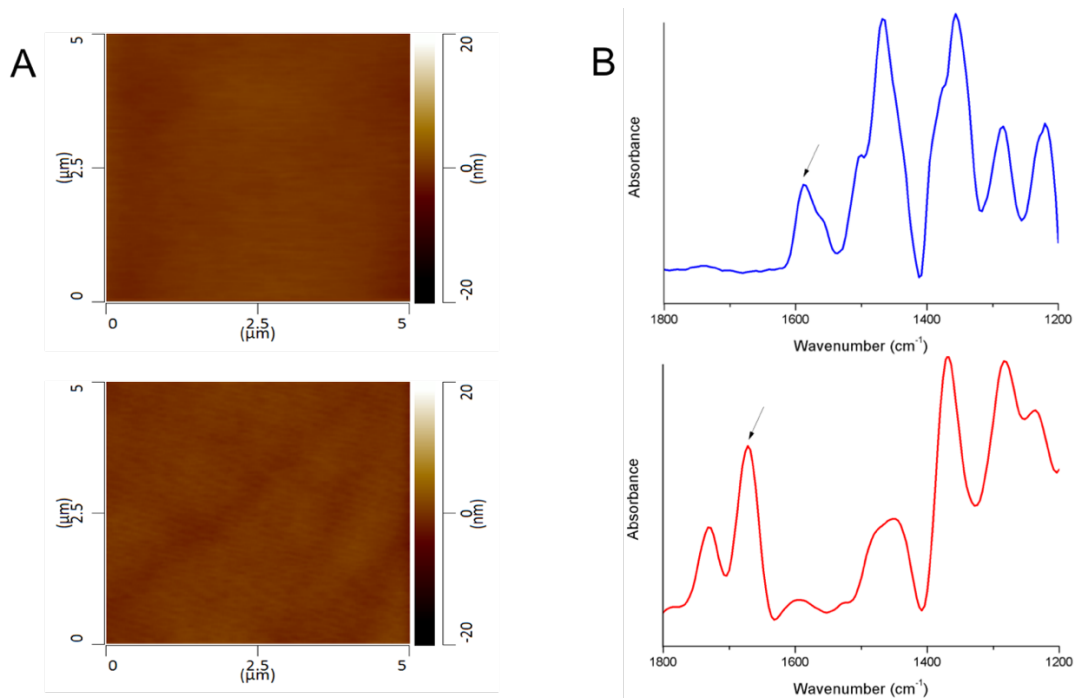
Figure 2.2 (A.) AFM topographical image of pure miconazole (top) and pure PVPVA (bottom) (B.) IR spectra (1200-1800 cm^{-1}) obtained from spin-coated films of pure miconazole (top) and pure PVPVA (bottom) (n=3). Arrows indicate drug and polymer specific peaks used for subsequent imaging.
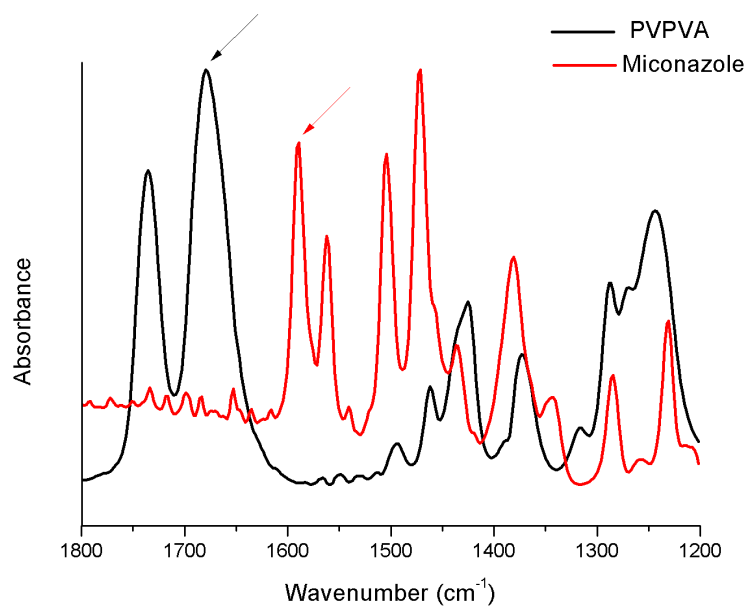
Figure 2.3 Bulk IR spectra (1800-1200 cm^{-1}) of pure miconazole (red) and pure PVPVA (black). Amorphous miconazole peak at 1590 cm^{-1} (indicated by arrow) was used to differentiate drug-rich phase while PVPVA peak at 1679 cm^{-1} (indicated by arrow) was used to differentiate polymer-rich phase.
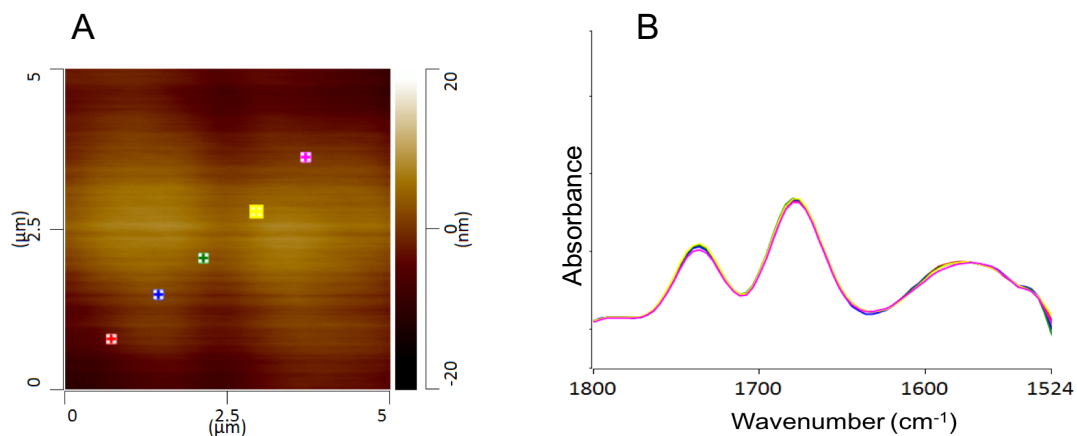
Figure 2.4 (A.) AFM topographical image of miscible 50:50 mico:PVPVA film prepared at 20% RH (B.) IR spectra for region of interest (1524-1800 cm^{-1}) obtained from spin-coated miscible film of 50:50 mico:PVPVA ASD.
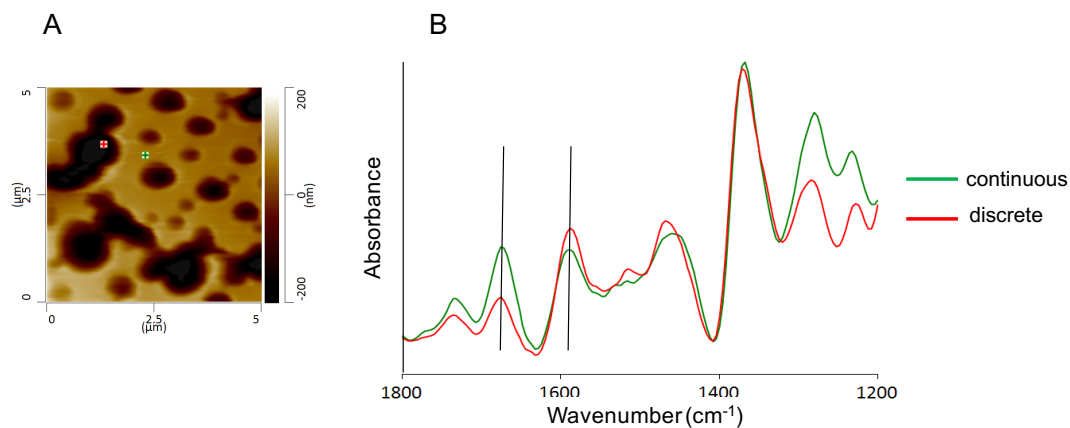
Figure 2.5 (A.) AFM topographical image of 50:50 mico:PVPVA phase separated film prepared at 60% RH (B.) IR spectra (1200-1800 cm^{-1}) obtained from discrete (red marker) and continuous (green marker) phases of phase separated film of 50:50 mico:PVPVA ASD (n=3).
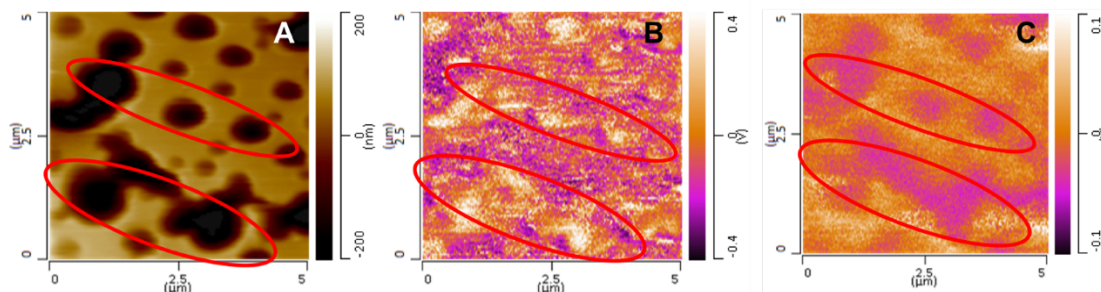
Figure 2.6 (A.) AFM topographical image of phase separated 50:50 mico:PVPVA film prepared at 60% RH (B.) Chemical mapping image at drug-specific 1590 cm^{-1} peak (C.) Chemical mapping image at polymer-specific 1679 cm^{-1} peak (areas shown by red ellipses highlight registry between topographical and chemical features)

AFM-IR imaging

To further investigate the chemical composition of the discrete and continuous phases, chemical mapping was performed at two wavelengths, 1590 cm^{-1} for drug specificity and 1679 cm^{-1} for polymer specificity. The resultant AFM IR chemical images which correspond to the topographical image shown in Fig. 2.6A for the phase separated 50:50 mico:PVPVA system are shown in Fig. 2.6B-C. It is apparent that the discrete phases have higher absorption when excited at the drug specific wavelength (1590 cm^{-1}) confirming that this is the drug-rich phase, whereas, the continuous phase exhibits much lower absorption. When the excitation wavelength is changed to be specific for the polymer absorption peak at 1679 cm^{-1}, the continuous phase now shows a higher absorption as compared to the discrete phase.

Lorentz Contact Resonance (LCR) imaging

Compositional differences of phase separated films were also studied based on their mechanical properties via Lorentz contact resonance measurements [77, 92, 93]. The mechanical spectra of pure drug and pure polymer are shown in Fig. 2.7. The first large peak, also known as the first flexural resonance mode, is considered to be most sensitive to differences in the stiffness of compositionally different phases, providing the maximum contrast during mechanical mapping. It was found that PVPVA's first flexural resonance mode was at slightly lower frequency (112.6 kHz) as compared to miconazole (113.8 kHz) indicating that PVPVA is softer than miconazole, enabling contrast imaging through LCR sweeps throughout the scan area based on stiffness differences. Thus scanning at a contact resonance frequency of 113.8 kHz highlights drug-rich regions, while when the contact resonance frequency was set at 112.6 kHz, the polymer-rich phase provides a higher signal. Results are summarized in Fig. 2.8, and the images further support the supposition that the discrete domains are drug-rich and the continuous phase is polymer rich.
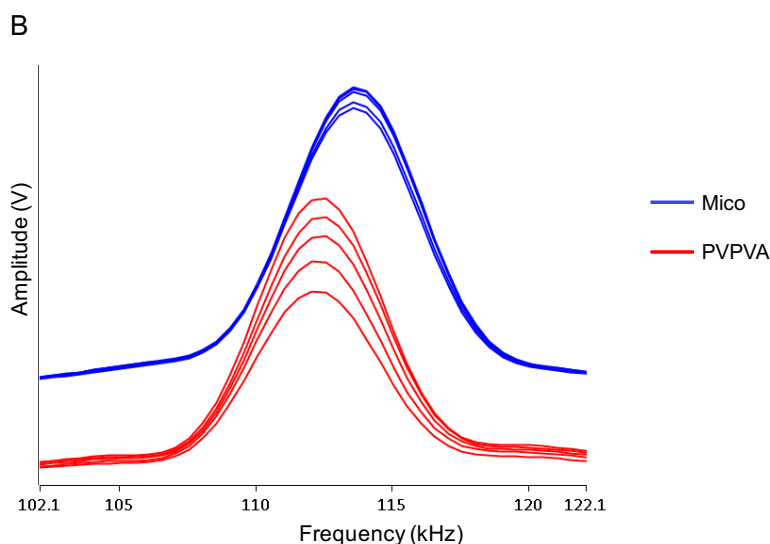
Figure 2.7 LCR mechanical spectra of pure miconazole (blue) and pure PVPVA (red): (A) Extended frequency range (B) Low frequency region (5 different spectra).
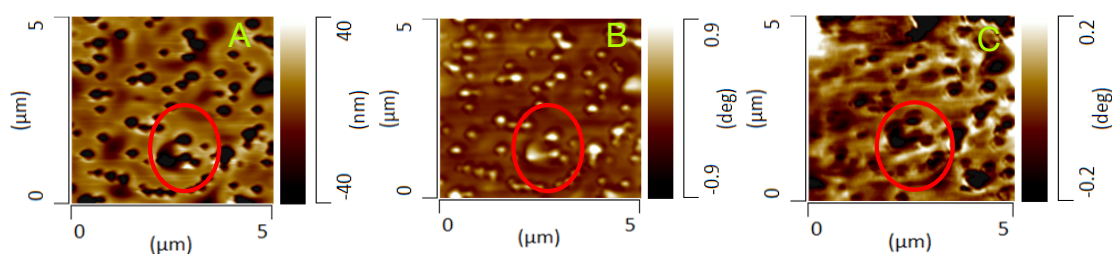
Figure 2.8 (A.) AFM topographical image of phase-separated 50:50 mico:PVPVA film prepared at 45% RH (B.) LCR mapping image at 113.8 kHz frequency which is drug-specific. The drug-rich areas are indicated by the lighter region in the image (C.) LCR image at 112.6 kHz frequency which is polymer-specific. The polymer-rich areas are indicated by the lighter regions in the image (areas highlighted by red ellipses highlight registry between topographic and mechanical features)

Confocal fluorescence microscopy (CFM)

Selection of Fluorescent Probes

Fluorescent probes were screened for drug or polymer specificity based on their staining of discrete or continuous phases present in phase separated films (Table A1, Appendix A). It was found that relatively hydrophobic probes (based on unionized state and higher log P values), namely prodan, pyrene and Nile red, were drug-specific, staining the discrete domains. Fluorescein and its derivatives, fluorescein isothiocyanate (FITC) and 5-(4,6-dichlorotriazinyl) aminofluorescein (5-DTAF), were also somewhat surprisingly found to be drug specific, staining the discrete phase in

spite of being relatively hydrophilic due to the presence of an ionizable carboxylate group [94, 95]. Other hydrophilic dyes studied were rhodamine-6G (cationic) and Alexa Fluor®488 (anionic) [96], both of which were found to be polymer specific. Results of drug/ polymer specificity of the various fluorescent probes studied are summarized in Table 2.1.

Pyrene, Nile red, as well as fluorescein and its derivatives were found to undergo photobleaching and were therefore considered less desirable for imaging purposes [97]. Further, based on the available laser lines on the confocal microscope (Table 1), pyrene (excitation maximum of 350nm and emission maximum between 380-400 nm) was eliminated as a potential dye [98]. Next, in order to avoid spectral mixing or cross-talk between channels, the fluorescent probe pair (drug and polymer specific) needs to have different photochemical properties to avoid crossover of their excitation or emission spectra which could lead to imaging artifacts [99]. After taking these factors into consideration, as well as the probe cost, prodan and rhodamine-6G were selected as suitable dyes to attempt selective staining of drug and polymer domains in phase separated films.

Table 2.1 Summary of drug/polymer specificity, presence/absence of photo-bleaching, available excitation laser line wavelength and emission filter wavelength range of Nikon A1 confocal fluorescence microscope for different fluorescent probes used in this study for screening.

	Drug specific	Polymer specific	Photo-bleaching	Excitation laser line (nm)	Emission Filter (nm)
Pyrene	✓	✗	✓	Not available	Not available
Nile red	✓	✗	✓	561	570-620
Prodan	✓	✗	✗	407	425-475
Fluorescein	✓	✗	✓	488	500-550
FITC	✓	✗	✓	488	500-550
5-DTAF	✓	✗	✓	488	500-550
R6G	✗	✓	✗	561	570-620
Alexa Fluor®488	✗	✓	✗	488	500-550

CFM imaging

Films containing both R6G and prodan and prepared at low RH (20%) were homogeneous in terms of fluorescence intensity showing blue and red emission when prodan and R6G were excited respectively and a purple color when the images were combined (Fig. 2.9). Thus the probes are able to uniformly distribute within the miscible film, and the fluorescence emission of each probe can be independently collected.

In phase separated films, prepared at 60% RH, the probes showed remarkably different affinities for the drug-rich and polymer-rich domains resulting in heterogeneity in the fluorescence intensity observed for each probe. The drug-rich phase appears as approximately circular domains that are stained blue by prodan (Fig. 2.10A). The polymer forms the continuous phase and is stained red by R6G (Fig. 2.10B). Combining the images yields Fig. 2.10C.

Differential scanning calorimetry

Modulated DSC measurement of T_g is commonly utilized to study miscibility of ASDs, wherein a single glass transition event is typically considered an indication of homogenous, single phased ASD. A single midpoint T_g value of 26°C was observed for 50:50 mico:PVPVA ASD dispersion prepared by rotary evaporation, consistent with a miscible system. The midpoint T_g values for pure miconazole and pure PVPVA alone were 0 and 107°C, respectively.
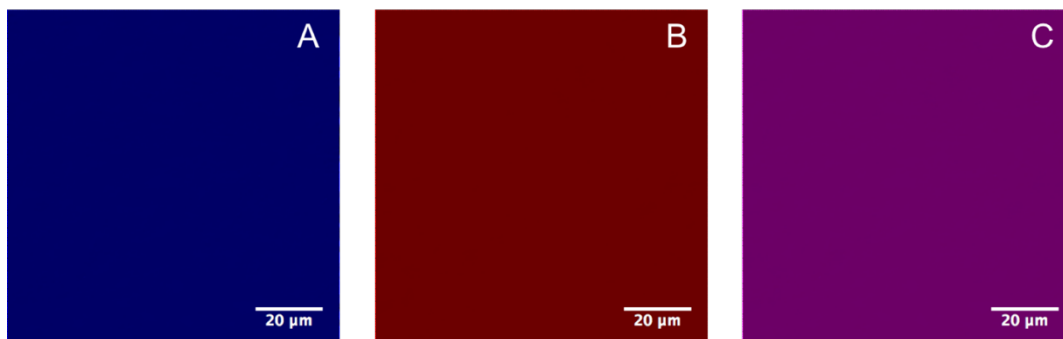
Figure 2.9 Confocal microscopy images of 50:50 mico:PVPVA miscible film prepared at 20% RH: excited at 407 nm (prodan-specific excitation) (A), 561 nm (rhodamine 6G-specific excitation) (B) and both 407 nm and 561 nm (C). Homogenous fluorescence intensity confirms the miscibility of the system.
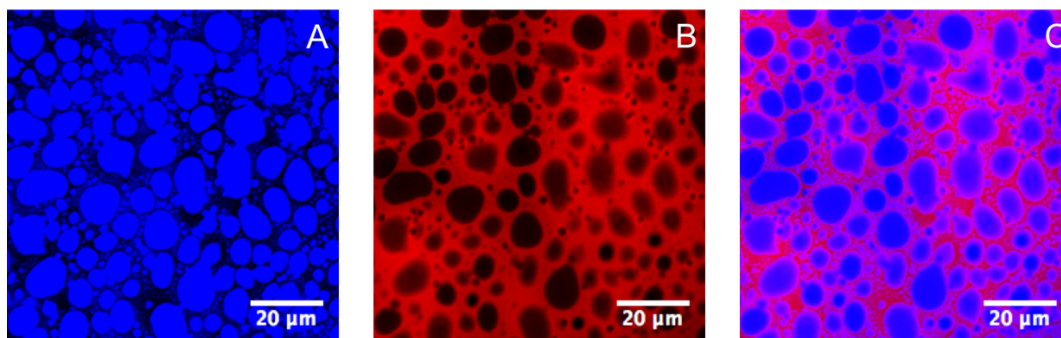
Figure 2.10 Confocal microscopy images of 50:50 mico:PVPVA phase separated films prepared at 60% RH: excited at 407 nm (prodan-specific excitation) (A), 561 nm (rhodamine 6G-specific excitation) (B) and both 407 nm and 561 nm (C). Discrete phase is drug-rich and is shown in (A), continuous phase is polymer-rich and is shown in (B) and combined image showing the distribution of drug- and polymer-rich phases is shown in (C).

2.5.2 Storage-induced phase separation

To evaluate the impact of high RH storage on miscibility, a film was prepared at low RH to ensure the initial miscibility and then stored at 75% RH, RT. After storage for 7 days, phase separation could be observed based on confocal fluorescence imaging (Fig. 2.11) and AFM topography/IR imaging as summarized in Fig. 2.12. As with phase separation occurring during preparation, the drug-rich phase forms discrete domains embedded in a polymer-rich continuous phase. No further phase changes in morphology for storage times of up to 4 weeks were observed. The powdered miscible ASD sample equilibrated at 75%RH was also found to have two midpoint Tgs during DSC analysis, at 10 and 48°C, indicating phase separation into drug-rich and polymer-rich phases, respectively.
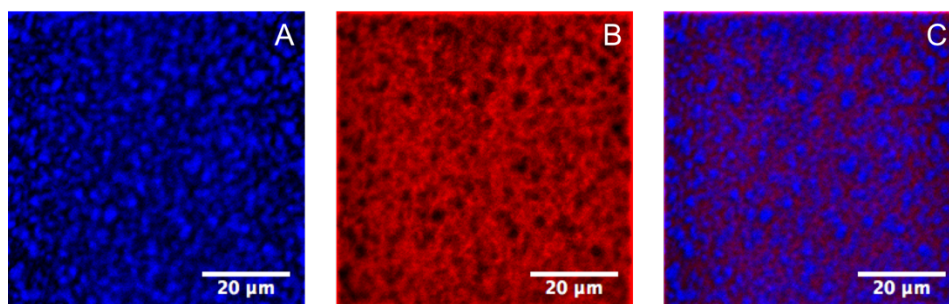
Figure 2.11 Phase separated 50:50 mico:PVPVA film after 1 week storage at 75% RH excited at a prodan-specific wavelength of 407 nm (A), at a rhodamine 6G-specific wavelength of 561 nm (B) and both 407 nm and 561 nm (C). Discrete phase is drug-rich and is shown in (A), continuous phase is polymer-rich and is shown in (B) and combined image showing the distribution of drug- and polymer-rich phases is shown in (C).
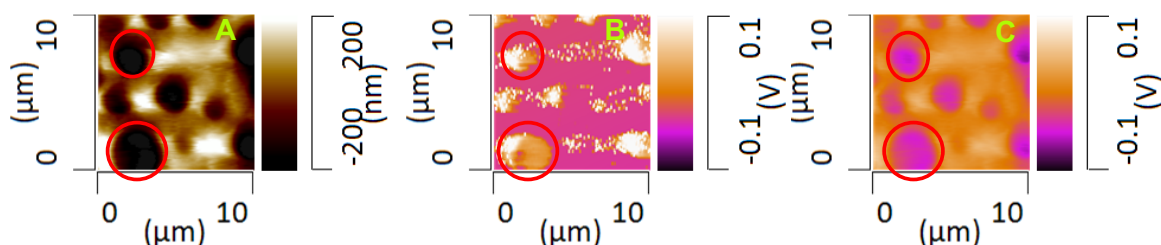
Figure 2.12 Initially miscible 50:50 mico:PVPVA film after 1 week storage at 75% RH indicating that phase separation occurred. (A.) AFM topographical image (B.) Chemical mapping image at drug-specific 1590 cm^{-1} peak (C.) Chemical mapping image at polymer-specific 1679 cm^{-1} peak (areas highlighted by red ellipses highlight registry between topographic and chemical features).

2.5.3   Impact of buffer immersion

During dissolution, the ASD matrix will rapidly hydrate and absorption of water is anticipated to induce phase separation in susceptible systems. It is analytically challenging to evaluate phase separation occurring in the matrix during this process, and it was of great interest to determine if CFM analysis could yield insights into this phenomenon. Following buffer immersion of initially miscible films containing both prodan and R6G for different times, phase separation could be clearly observed, based on the redistribution of the dyes into different regions of the film, as shown in Fig. 2.13. The presence of miconazole in one phase, and polymer in the other phase was confirmed by AFM topographical imaging and nano-IR imaging as shown in Fig. 2.14 and 2.15, respectively, for the 30 min immersion sample. Initially, from the CFM images, it appears that the polymer forms a discrete phase embedded in a drug-rich matrix. However, with time the morphology evolves and the phases appear more bi-continuous.   For the 30 min immersion film, AFM topography measurements showed bi-continuous morphology different from the discrete domains embedded in a continuous phase observed for the films described previously (phase separation induced during preparation or on high RH storage). Furthermore, for the immersed samples, the higher height features corresponded to the drug-rich phase and lower height features to the polymer-rich phase. This is most likely because of a faster dissolution rate of the polymer-rich phase relative to the drug-rich phase after the initial phase separation occurred. Following equilibration at 100%RH, the ASD powder showed two T_g events were at -5 and 68°C (midpoint values) presumably corresponding to drug- rich and polymer- rich phases, respectively.
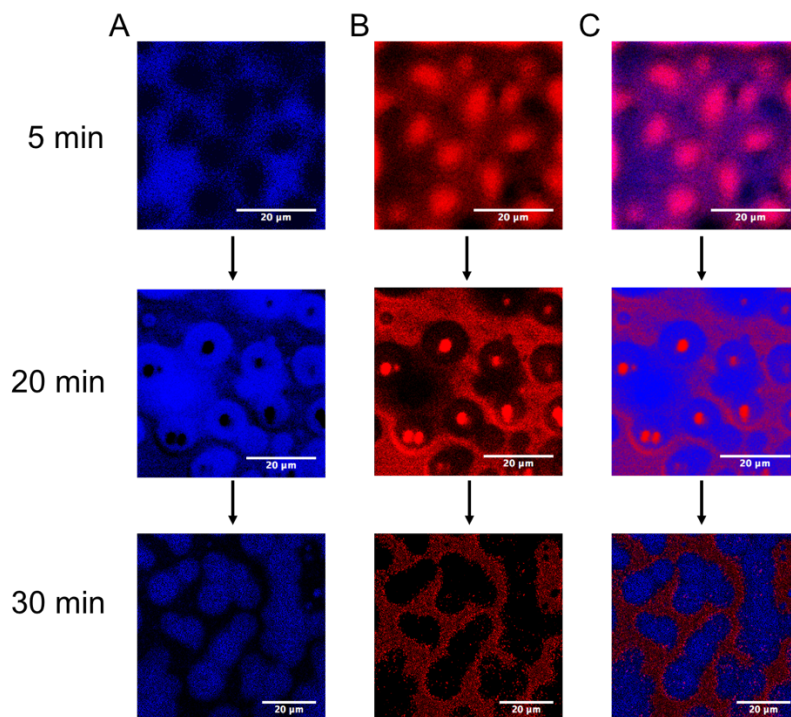
Figure 2.13 Evolution of morphology of an initially miscible 50:50 mico:PVPVA film as phase separation proceeds at 5, 20, and 30 min of pH 6.8 phosphate buffer immersion. Samples excited at a prodan-specific wavelength of 407 nm (A), R6G-specific wavelength of 561 nm (B) and both 407 nm and 561 nm (C). Discrete phase is drug-rich as shown in (A), continuous phase is polymer-rich as shown in (B) and combined image showing the distribution of drug- and polymer-rich phases is shown in (C).
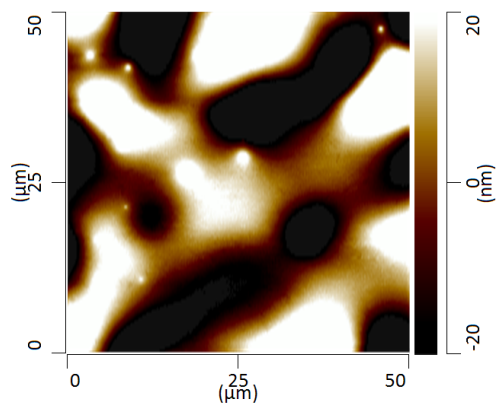
Figure 2.14 AFM topographical image of phase separated 50:50 mico:PVPVA film showing bi-continuous morphology after 30 min of pH 6.8 phosphate buffer immersion.
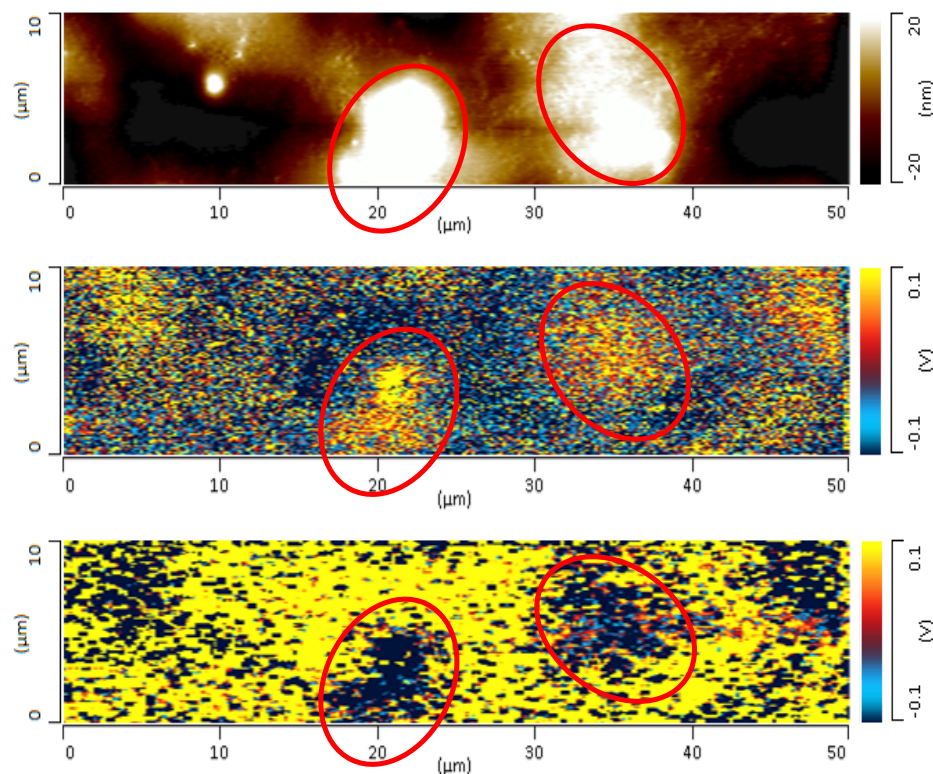
Figure 2.15 Phase separated 50:50 mico:PVPVA film after 30 min of pH 6.8 phosphate buffer immersion. From top to bottom: AFM topographical image, chemical mapping image at drug-specific 1590 cm^{-1} peak and chemical mapping image at polymer-specific 1679 cm^{-1} peak (areas highlighted by red ellipses highlight registry between topographic and chemical features)

2.6   Discussion

With the increasing utilization of ASD formulations in commercial products, there is considerable interest in gaining more fundamental understanding of the phase behavior and microstructure of drug-polymer blends. Intimate mixing between drug and polymer at a molecular level is considered essential for optimized performance, in particular in terms of inhibition of drug crystallization during storage and dissolution. Drug-polymer demixing is a poorly understood phenomenon, rendered difficult to study by the detection challenges inherent to many analytical approaches. Studies have shown that drug-polymer demixing can be induced during ASD formation if water is present in the solvent during processing. This occurs because water is an anti-solvent for the drug and can thus lead to phase separation for certain drug-polymer combinations during ASD formation.[93] Likewise, there is abundance of polymer literature demonstrating that

the presence of an anti-solvent for one of the polymers leads to phase separation or formation of microstructures in the polymer blends.[29, 100, 101] Water can also be absorbed into the ASD during storage, and it has been demonstrated that some drug-polymer systems are highly susceptible to water-induced amorphous-amorphous phase separation upon high RH storage, while other systems are quite stable.[61, 102-104] Very recently, it has been also noted that very rapid phase separation can occur within seconds during the hydration stage of dissolution.[18] All of these studies demonstrate the potentially deleterious impact of water, but were performed on different drug-polymer systems and a systematic comparison of the impact of water, introduced at different stages e.g. during formation, storage and hydration, on the resultant drug-polymer phase behavior and microstructure is necessary to gain greater insight. It is intuitive that, if a particular system is susceptible to phase separation upon exposure to water during one route, water will likely have deleterious consequences when introduced via an alternative route. However, given the different thermodynamics and mobilities, the evolution of the microstructure may differ considerably.

The confocal fluorescence microscopy technique developed herein enables us to visualize the phase behavior of the individual components in a variety of different situations, by selectively staining drug-rich and polymer-rich phases with dyes exhibiting different affinities for the ASD components. This new approach garners its precedent from the polymer literature. Here, two separate fluorescent probes have been utilized in combination, whereby the individual probes show a preference for one of the two polymers in the blend, thereby enabling study of polymer gradients in phase separated blend.[27, 105] The selection of drug-specific and polymer-specific fluorescent probes applies classical principles of fluorescent staining[106]; a hydrophobic phase is stained with a hydrophobic probe and a hydrophilic phase with a hydrophilic probe. This principle worked well when applied to the drug-polymer system studied herein. Many fluorescent probes are inherently hydrophobic due to the presence of multiple aromatic rings and high molecular weights, and thereby preferentially stain the drug, as demonstrated for pyrene, Nile red and prodan. In contrast, the charged dyes, cationic rhodamine 6G and anionic Alexa Fluor®488, stained the polymer. The only non-predictable observation was that fluorescein, typically considered a hydrophilic probe due to presence of ionizable carboxylate group, showed a preference for the drug-rich phase. This preference may arise due to the weakly basic nature of miconazole leading to specific interactions with the acidic fluorescein. Given that confocal fluorescence microscopy enables fast sample

71

analysis (<1 min), as well as straightforward sample preparation and data interpretation, it is a useful addition to the toolbox of analytical methods for miscibility assessment, bearing in mind that the theoretical lower resolution limit for discrete domains is estimated to be ~ 150 nm calculated based on the Abbe diffraction limit of a microscope, ~0.5 λ/NA, wherein λ is the wavelength of the light (prodan's excitation wavelength, 407nm) and NA is the numerical aperture of the lens (1.49).[107] This technique also has shown evidence of versatility for different drug-polymer systems; itraconazole-hydroxypropyl methylcellulose ASDs were noted to be phase separated based on staining and analysis with the confocal fluorescence microscopy with results confirmed by solid state nuclear magnetic resonance spectroscopy.[108]

2.6.1 Insights into water-induced AAPS

The method developed herein enabled rapid assessment of miconazole:PVPVA miscibility under different conditions. It has been reported previously that at drug loadings greater than 20%, miconazole:PVPVA ASDs prepared by spray drying were phase separated,[81] while dispersions prepared by hot melt extrusion showed better mixing and a single glass transition event.[80] Our observations on the preparation of high drug loading miconazole ASDs via solvent evaporation perhaps provide some insight into factors that might be important in influencing the miscibility of the resultant ASD. It is clear that if exposure to water is minimized during ASD formation (low RH conditions), that a miscible film can be obtained (Fig. 2.4A and 2.9). In contrast, exposure to moderate RH conditions during film formation leads to the formation of discrete, miconazole-rich domains with a size range from submicron to few microns. The formation of discrete drug domains embedded in a polymer-rich continuous phase indicates that the phase separation may occur via a nucleation and growth mechanism.[109] The ability of water to induce phase separation is further confirmed by exposing an initially miscible film to high RH, with the subsequent formation of discrete and continuous domains. Thus, PVPVA and miconazole, as a binary system, do not appear to be inherently immiscible. Rather, the phase separation is induced by the presence of water, which is an antisolvent for the hydrophobic miconazole. During amorphous amorphous phase separation upon exposure to high RH, the question is often raised about the role of water. Thus, does water simply enhance molecular mobility[42] in a kinetically trapped system in which phase separation is already thermodynamically favored to occur, or is it the alteration in the thermodynamics of the ASD system, the so called delta chi effect,[29, 101] due to change in

composition upon absorption of water that results in the phase separation? Considering that, during the film formation process via solvent evaporation at low and high RH, mobility is likely to be high in both instances due to the presence of the solvent, evidence is provided for the thermodynamic role of water in inducing phase separation. Furthermore, annealing an ASD at 100°C, which is approximately 75°C above the T_g of a 50:50 dispersion, did not lead to a system with two T_gs after cooling and rescanning (data not shown). Thus, even after providing sufficient mobility to a single phase mico:PVPVA ASD, the system remained miscible. This suggests that mobility is not the sole criterion required for phase separation. This conjecture is consistent with the observation that ASDs produced by melt extrusion are miscible and also that remixing of phase separated miconazole:PVPVA ASDs can be induced during compression.[80][81]

The observed phase separation during exposure to bulk water is also consistent with water changing the thermodynamic properties of the system and inducing phase separation. Thus the absorption of water by the film following immersion leads to the rapid formation of drug-rich and polymer–rich regions that undergo considerable rearrangement for longer immersion times. The length scale of phase separation becomes quite large in the immersed films, and the higher height of the drug-rich domains relative to the polymer-rich regions suggests that PVPVA is dissolving faster than the drug. Thus the immersed films show a much coarser microstructure than the films exposed to high RH. The phase behavior of initially miscible ASDs during dissolution may well be of great importance in terms of impacting the drug release rate. Therefore, analytical approaches such as the CFM method described herein, are likely to be of great importance when comparing the performance of different ASD formulations.

2.7 Conclusion

Confocal fluorescence microscopy, in combination with drug- and polymer-specific fluorescent dyes has been implemented as a rapid and informative technique to evaluate the homogeneity of drug-polymer blends produced using solvent evaporation techniques. Miconazole:PVPVA dispersions were found to be miscible and homogeneous when prepared at low RH conditions. Exposure to water during film formation, storage or dissolution led to rapid phase separation and an inhomogeneous distribution of drug and polymer. Discrete drug-rich domains could be stained by the dye, prodan, while the polymer-rich phase was stained by rhodamine R6G. The identity of

different domains was confirmed using nanoscale infrared spectroscopy measurements. Confocal fluorescence microscopy, in combination with exogenous dyes with differing specificities for drug and polymer, thus offers a useful approach to evaluate drug-polymer homogeneity and will ultimately be useful to improve understanding and optimize the formulation of amorphous solid dispersions.

CHAPTER 3. CONGRUENT RELEASE OF DRUG AND POLYMER: A "SWEET SPOT" IN THE DISSOLUTION OF AMORPHOUS SOLID DISPERSIONS

3.1   Abstract

Liquid-liquid phase separation (LLPS) occurs following amorphous solid dispersion (ASD) dissolution when the drug concentration exceeds the "amorphous solubility", and is emerging as an important characteristic of formulations that may enhance the oral bioavailability of poorly soluble drugs. The purpose of this research was to identify criteria that impact the rate and extent of drug release and hence the occurrence or not of LLPS upon ASD dissolution. Specifically, the effect of drug log P, phase behavior of the hydrated but undissolved ASD matrix and the relative dissolution rates of drug and polymer were studied as a function of drug loading, using nilvadipine (Nil) (ClogP=3.04) and cilnidipine (Cil) (ClogP=5.54) as model drugs. The model polymer was poly (vinylpyrrolidone-co-vinyl acetate) (PVPVA). Nil-PVPVA and Cil-PVPVA ASDs with different drug loadings were prepared. Surface area normalized dissolution rates of both the drug and the polymer from ASD tablets were studied. At a similar and relatively low drug loading (<20% w/w drug), dissolution of both Nil-PVPVA and Cil-PVPVA ASDs was found to switch from rapid, congruent (i.e., simultaneous) release of drug and polymer to incongruent release with slow release of drug. Only ASDs showing congruent release underwent LLPS, with the formation of amorphous drug-rich aggregates (~300nm). Scanning electron microscopy (SEM) and micro-computed tomography (micro-CT) showed the presence of characteristic "pits" on the surface of partially dissolved, incongruently releasing ASD tablets. These most likely arise due to faster polymer release in comparison to drug, whereby the drug-rich composition around these pits was confirmed by energy-dispersive X-ray (EDX) analysis and the surface drug enrichment on the compacts was confirmed by X-ray photoelectron spectroscopy (XPS). This study demonstrates two important findings, firstly, a link between congruent release of drug and polymer and the occurrence of LLPS and secondly, the switch between congruent and incongruent release of drug

and polymer is a result of competitive kinetics between phase separation and the release rate of ASD components with minimal influence from drug hydrophobicity for two structural analogues.

3.2   Introduction

Amorphous solid dispersions (ASDs) are finding increasing utility as a solubility enabling formulation strategy. An ASD is a system in which the amorphous form of a drug is molecularly dispersed in a hydrophilic polymeric matrix. The dissolution advantages of ASDs are at least two-fold.[37] First, a supersaturated solution is generated by dissolution of the higher energy amorphous form of the drug. Second, by choosing a polymer that is an effective crystallization inhibitor, the supersaturation generated upon dissolution can be maintained for a biologically relevant time period. Further, it has been noted recently that some ASDs, typically those with a low drug loading, dissolve to a concentration higher than the amorphous solubility of the drug leading to liquid-liquid phase separation (LLPS).[26, 110] When LLPS occurs, a new amorphous colloidal drug-rich phase is formed that coexists with the aqueous phase which contains a drug concentration equivalent to the amorphous solubility.[63] The occurrence of LLPS is considered beneficial from an *in vivo* perspective as the drug-rich phase replenishes the free drug concentration in the aqueous phase as drug is absorbed across the gastrointestinal epithelium. This reservoir effect will continue, maintaining the supersaturation at a level corresponding to the amorphous solubility of the drug, and hence maximizing the membrane flux, until all of the colloidal drug dissolves [64-66, 111].

There have been a number of amorphous solid dispersion-based drug products reaching the market in the past two decades.[112] However, for this formulation strategy to be more widely employed, there are several challenges that need to be overcome. One of the most important of these is the drug:polymer ratio paradigm. Low drug loading ASDs are often necessary to achieve good drug release and the desired *in vivo* exposure following oral dosing.[7, 8, 26, 110] On the other hand, low drug loading formulations lead to large dosage forms for all but the more potent compounds, which is undesirable from a patient compliance perspective and can provide a marketing disadvantage. Therefore, in order to use ASDs more broadly as an enabling strategy for poorly water-soluble compounds, there is a need to gain mechanistic understanding of the factors that impact drug release, and the design parameters that can be manipulated to ensure a high degree of supersaturation, and the formation of colloidal drug-rich species that can promote *in vivo* oral

absorption. If deciphered, this information can be of great value for ASD formulation design and optimization aimed at achieving higher drug loadings.

There have been previous attempts to understand ASD dissolution mechanisms. Two dissolution regimens are often observed. At low drug loadings, dissolution has been found to be polymer controlled,[9, 10, 113, 114] while at high drug loadings, drug-controlled dissolution has been reported.[14, 115] This picture is likely to be oversimplified, and there is limited knowledge of factors that influence the switch from polymer-controlled to drug-controlled regimens, in particular the drug loading at which this switch will occur for a particular drug-polymer system. The interplay between drug and polymer properties is likely to influence the switching point, if observed, and at this point it is unclear if this phenomenon only occurs for certain drug-polymer combinations or is a more general phenomenon. Thus, several studies have shown the influence of polymer-type and drug-polymer interactions/phase behavior on the ASD dissolution performance,[116-120] whereby the results have been found to be highly drug-specific. Qian *et al.*[121] attempted to study multiple factors but clear trends remain elusive. Therefore, there is a need for further studies to evaluate key drug and polymer properties that may impact ASD dissolution performance. A major distinguishing property between drug and polymer in an ASD is their hydrophobicity differential. While poorly water-soluble drugs tend to be highly lipophilic, the water-soluble polymers used in ASDs are comparatively hydrophilic. One way to study the effect of this differential is to vary the hydrophobicity (or hydrophilicity) of one of the components, either drug or polymer and study the impact on the dissolution performance of the ASD. Herein, the effect of drug hydrophobicity on drug release as a function of drug loading was investigated using two model drugs, nilvadipine (Nil) (ClogP = 3.04) and cilnidipine (Cil) (ClogP = 5.54), which differ in their log P values by 2.5 units. Otherwise, these compounds are structural analogs (Fig. 3.1) from the same therapeutic class and have a high degree of chemical similarity, are non-ionizing and have a relatively low crystallization tendency enabling easier study of the release rate. The model polymer used was poly (vinylpyrrolidone-co-vinyl acetate) (PVPVA), which has been widely used in commercial ASD formulations prepared with both hot melt extrusion and spray drying and can be considered a hydrophilic polymer.

The hypotheses to be tested in this study were two-fold. First, that congruent (i.e., simultaneous) release of drug and polymer from ASDs results in superior dissolution performance when using the hydrophilic polymer, PVPVA. Second, ASDs with the more hydrophobic drug will exhibit congruent release for a lower range of drug loadings than ASDs formulated with the less hydrophobic drug. ASDs were prepared at different drug loadings, and surface normalized release rates of both drug and polymer were determined. Phase behavior and microstructural characterization of partially dissolved ASD tablets were evaluated using surface analytical and imaging techniques. Further, the elemental composition of partially dissolved tablet surfaces was also studied. The presence or absence of drug-rich nano-sized aggregates following ASD dissolution was confirmed and, if present, size information was obtained.

3.3   Materials

Nilvadipine (Nil) was purchased from ChemShuttle (Jiangsu, China). Cilnidipine (Cil) was purchased from Euroasia Chemicals Pvt. Ltd. (Mumbai, India). Kollidon VA 64 (PVPVA) was supplied by the BASF Corporation (Ludwigshafen, Germany). The chemical structures of model drug and polymer are given in Fig. 3.1. The medium for all solubility and dissolution studies consisted of 100 mM phosphate buffer, pH 6.8, which was prepared by dissolving 7.037 g of monosodium phosphate monohydrate and 6.956 g sodium phosphate dibasic anhydrous in 1 L of DI water.
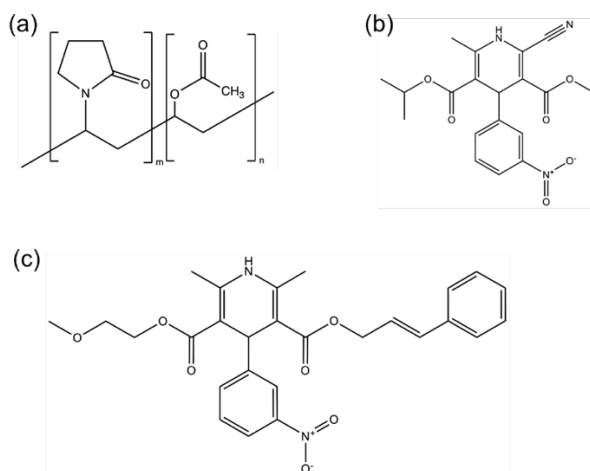
Figure 3.1 Structures of the model drugs and polymer used. Poly (vinylpyrrolidone-co-vinyl acetate) (PVPVA) (a), nilvadipine (Nil) (b) and cilnidipine (Cil) (c).

3.4   Methods

3.4.1   Determination of crystalline and amorphous solubility

Crystalline solubility determination

The equilibrium crystalline solubility of nilvadipine and cilnidipine in 100 mM phosphate buffer was determined by stirring an excess amount of each drug in buffer at 37°C for 48h. The excess solid was separated from saturated solution by ultracentrifugation at 35,000 rpm in an Optima L-100 XP centrifuge (Beckman Coulter, Inc., Brea CA) equipped with a swinging-bucket rotor SW 41Ti for 30 minutes and the drug concentration in the supernatant was analyzed by reverse phase high performance liquid chromatography (RP-HPLC) system (Agilent Technologies, Santa Clara, CA) after appropriate dilution. For nilvadipine, a mobile phase of 50% acetonitrile and 50% water (v/v) at a flowrate of 1 mL/min with an injection volume of 50 μL and ultraviolet (UV) detection wavelength of 240 nm was used. The separation column used was Ascentis Express C18 column (15 cm x 4.6 mm, 5 μm particle size). For cilnidipine, the same parameters were used except the composition of mobile phase was 60% acetonitrile and 40% water (v/v). The crystalline solubilities for both drugs were also determined in the presence of 1 mg/mL PVPVA.

Amorphous solubility determination

The amorphous solubility of nilvadipine was determined in the presence of 50 μg/mL PVPVA (to prevent crystallization during the experiment) as well as 1 mg/mL PVPVA (to evaluate the effect of high concentration of polymer on amorphous solubility) by four methods, namely, UV-extinction, ultracentrifugation, fluorescence spectroscopy and flux measurements. An extensive evaluation of amorphous solubility of cilnidipine was not conducted since the previously reported value of 0.5 ± 0.3 μg/mL[122] was found reproducible in absence and presence of polymer for triplicate samples as determined via ultracentrifugation.

UV extinction

The concentration where a new drug-rich phase appeared was determined by monitoring the increase in extinction at a non-absorbing wavelength. A 0.2-cm path length dip probe attached to an SI photonics 400 UV/vis spectrophotometer (SI photonics, Tuscan, AZ) was used to measure

the scattering at 450 nm where nilvadipine shows no absorption. A scintillation vial containing 15 ml of 100 mM pH 6.8 phosphate buffer in the presence of 50 µg/mL or 1 mg/mL of PVPVA was placed in a water jacketed beaker and stirred at 300 rpm at a temperature of 37°C. A stock solution of nilvadipine in methanol (3 mg/ml) was added to the buffer solution using a syringe pump (Harvard Apparatus, Holliston, MA) at a rate of 50 µL/min. The scattering at 450 nm was monitored every 15 seconds and plotted against the concentration of drug in the vial. The formation of a nilvadipine-rich phase as a result of LLPS resulted in an increase in scattering, and the concentration where this occurred was recorded as amorphous solubility.

Fluorescence spectroscopy

An RF-5301pc spectrofluorophotometer (Shimadzu, Kyoto, Japan) was used to perform fluorescence experiments using 4-Di-2-Asp as an environmentally sensitive fluorescence probe; the emission spectrum and intensity of 4-Di-2-Asp depends on the polarity of the environment.[123] Solutions with different concentrations of nilvadipine were prepared by adding small aliquots of nilvadipine stock solution in methanol (10 mg/mL) to 20 mL of 100mM pH 6.8 phosphate buffer (pre-equilibrated at 37°C) containing 50 µg/mL or 1000 µg/mL of PVPVA and 4-Di-2-Asp at a concentration of 1 µg/ml as an exogenous fluorescent probe. Samples were analyzed in a 1 cm cuvette with an excitation wavelength of 488 nm and the emission spectrum between 500 and 700 nm was recorded, with a 10 nm excitation slitwidth and 3 nm emission slitwidth. The changes in the emission maximum wavelength and intensity were measured as a function of concentration, and the inflection point was recorded as amorphous solubility.

Mass flow measurements

Diffusion studies were performed using a side-by-side diffusion cell (PermeGear Inc., Hellertown, PA) to determine the mass flow of different concentration of nilvadipine across a regenerated cellulose membrane with a molecular weight cutoff of 6-8 kDa. Both compartments contained 34 mL of 100 mM phosphate buffer pH 6.8 at 37°C and 50 µg/mL of PVPVA was added to both donor and receiver sides to prevent crystallization of the drug. Different concentrations of nilvadipine were generated in the donor cell by addition of a small amount of a highly concentrated nilvadipine stock solution, where the final organic solvent concentration was <1% v/v. A control

experiment with 100 µg/mL of nilvadipine donor concentration in the presence of 1 mg/mL of PVPVA on both sides was also performed to check the influence of a high concentration of polymer on mass flow. The increase in the concentration of the drug in the receiver cell was monitored by removing 100 µL of aliquots from the receiver every 10 minutes for 60 minutes and analyzing using HPLC. The slope of the plot of receiver concentration versus time profile was used to determine mass flow after compensating for the volume (34mL).

Ultracentrifugation

For nilvadipine, a supersaturated solution was generated by adding 50 µL of 20 mg/mL of methanolic stock solution to 15 mL of pH 6.8 phosphate buffer (pre-equilibrated at 37°C) containing 50 µg/mL or 1 mg/mL of PVPVA. For cilnidipine, 50 µL of 2 mg/mL of methanolic stock solution was used to generate supersaturation with and without PVPVA (1 mg/mL). The supersaturated solution generated was then ultracentrifuged at 35,000 rpm in an Optima L-100 XP centrifuge (Beckman Coulter, Inc., Brea CA) equipped with a swinging-bucket rotor (SW 41Ti) for 30 minutes. Analysis of the supernatant concentration was performed using HPLC.

3.4.2 Preparation of amorphous solid dispersions (ASDs)

Preparation of powdered ASDs using rotary evaporation (for dissolution studies)

Amorphous solid dispersions of nilvadipine with PVPVA at drug loadings of 5%, 10%, 15% and 20% (w/w) were prepared by solvent evaporation using a rotary evaporator (Buchi Rotavapor-R, New Castle, DE) equipped with Yamato BM-200 water bath at 45°C. Drug and polymer were dissolved in a 1:1 v/v of methanol and dichloromethane at a solid content of 50 mg/mL prior to rotary evaporation. For cilnidipine, an additional drug loading of 25% was also prepared. The resultant ASD powders were dried overnight under vacuum, cryo-milled and sieved (desired particle size of 106-250 µm). All ASDs were confirmed to be crystal free by powder X-ray diffraction (PXRD) and polarized light microscopy (PLM).

Preparation of ASD thin films using spin coating (for confocal fluorescence microscopy)

Thin films of Nil:PVPVA ASDs (10% drug loading) were prepared using a spin coater (Chemat Technology Inc., Northridge, CA). Drug and polymer were dissolved at the desired ratio in a 1:1

v/v methanol:dichloromethane mixture to obtain a final concentration of 50 mg/mL. Fluorescent probes: prodan and rhodamine 6G (R6G) were also added to this stock solution to obtain a concentration of 0.01% w/v for each individual probe. Stock solution (100 μL) was deposited on a quartz slide (1"x1", 1 mm thick, Ted Pella Inc., Redding, CA)., followed by spinning at 500 rpm for 6 s and 3000 rpm for 30 s. Spin coating was performed in a glovebox with a dry nitrogen purge at low RH conditions (below 20% RH) to prevent water vapor induced phase separation during the preparation stage. ASD films prepared in this manner were then dried overnight under vacuum to remove residual solvents before conducting high RH exposure studies

3.4.3   Surface normalized dissolution of nilvadipine and cilnidipine ASD tablets

Surface normalized dissolution (under non-sink conditions w.r.t amorphous solubility) of Nil-PVPVA and Cil-PVPVA ASD tablets was carried out at 37°C using a Wood's intrinsic dissolution rate apparatus (Agilent Technologies, Santa Clara, CA) where only one face of the tablet is exposed to the dissolution medium, maintaining a constant surface area throughout the dissolution experiment. It is assumed that the surface area exposed remained constant throughout the experiment, with a renewed layer of compact presenting itself periodically. Briefly, 100 mg of the ASD powder, prepared by rotary evaporation and cryo-milled to the desired size range (106-250 μm), was tableted in an 8mm die (this gives a tablet of surface area of 0.50 sq. cm) using a hydraulic tablet press at a pressure of 1500 pounds per square inch applied for a minute. The die containing the tablet was mounted on the shaft of the overhead stirrer and then immersed into 100 mL of 100 mM pH 6.8 phosphate buffer in a water jacketed beaker. A stir rate of 100 rpm was used. 2 mL of the dissolution medium was aliquoted at desired time points for up to 2 hours and replaced with fresh buffer. Out of the 2 mL of medium aliquoted, a small aliquot (100 μL) was used as is for drug analysis and the remaining was used for polymer analysis after filtering through 0.2 μm pore sized nylon membrane filter (VWR technologies Radnor, Pennsylvania) and discarding the initial 1 mL of the filtrate. Samples were then analyzed for drug and polymer amount, using RP-HPLC and HPLC-size exclusion chromatography (SEC), respectively. RP-HPLC methods for both nilvadipine and cilnidipine were as discussed above. For PVPVA quantification, a Malvern A3000, Aqueous GPC/ SEC column (300x8mm) was used. The mobile phase constituted of 80% pH 7.4 phosphate buffer saline (PBS) solution and 20% methanol. pH 7.4 PBS solution was prepared by dissolving 1 PBS tablet (Research Products International, Mt. Prospect,

IL) in 100 mL of DI water. The flow rate was kept at 0.5 mL/min. The injection volume was 50 µL and an ultraviolet (UV) detection wavelength of 205 nm was used. The dilutions of the samples were done to match the organic-to-aqueous ratio of the mobile phase. The surface normalized dissolution rates of drug and polymer were calculated by linear regression analysis of the initial linear portions of a plot of percent release versus time.

Crystallization was monitored by powder X-ray diffraction (PXRD) studies performed on compacts at various time points until the end of experiment using a Rigaku Smartlab™ diffractometer (Rigaku Americas, Texas). To further evaluate the compacts, the surface of the tablets was scraped off at intermittent time points during the dissolution process for selected samples and polarized light microscopy (PLM) was used to examine samples for birefringence.

Partially dissolved ASD tablets at different stages of dissolution were examined by micro-computed tomography (micro-CT), scanning electron microscopy (SEM) (with or without energy-dispersive X-ray (EDX) analysis) and X-ray photoelectron spectroscopy (XPS). Specifically, partially dissolved tablets (10 minute time point) for both Nil and Cil- PVPVA ASDs, with drug loadings of 10% and 15% for Nil-PVPVA ASDs and 15% and 20% for Cil-PVPVA ASDs, were analyzed using the aforementioned techniques. Additionally, solution phase behavior was studied using fluorescence spectroscopy, dynamic light scattering (DLS) and nanoparticle tracking analysis (NTA) to analyze the dissolution medium. For fluorescence spectroscopy, 4-Di-2-Asp was added at a concentration of 1 µg/mL in the dissolution medium. Samples were withdrawn from the dissolution medium at approximately the one hour time point for all three analyses.

3.4.4 Humidity exposure studies

In order to study the influence of water-induced amorphous-amorphous phase separation (AAPS) on an initially congruently releasing system, Nil:PVPVA 10:90 ASD tablets were exposed to 97% RH for 12 hours and surface normalized dissolution studies as described above were performed. SEM images were taken of the tablet surface exposed to high humidity in order to study microstructural surface changes arising from humidity exposure.

Nil:PVPVA 10:90 ASD thin films were also exposed to 97% RH conditions for 12 hours. The films were evaluated using confocal fluorescence microscopy (CFM) imaging.

3.4.5 Solution phase behavior during surface normalized dissolution of nilvadipine and cilnidipine ASD tablets

Fluorescence spectroscopy

A 2 mL aliquot was extracted and analyzed using an RF-5301pc spectrofluorophotometer (Shimadzu, Kyoto, Japan) in a 1 cm cuvette. The excitation wavelength was 488 nm and the emission spectrum was recorded from 500 to 700 nm. The excitation slit width was 10 nm and emission slitwidth was 1.5 nm.

Nanoparticle Tracking Analysis (NTA)

1 mL of the solution was withdrawn and analyzed using a NanoSight LM-10 from Malvern Instruments (West borough, MA) equipped with a nanoparticle tracking analysis software. The LM10 is equipped with a green laser (75 mW, 532 nm) which was used as a light source and a temperature controlled flow-through cell which was controlled at 37°C. Samples were visualized via a 20x magnification microscope objective and a video sequence was recorded for 30s. NTA tracks individual particles and calculate their hydrodynamic diameter based on the Stokes-Einstein equation.

Dynamic Light Scattering (DLS)

2 mL of the dissolution medium was characterized by DLS (Malvern Zetasizer ZS®, Worchestershire, UK) for size determination of the generated nanoparticles. A 173° backscatter detector was used and the measurement settings were set to "auto" on the Malvern Zetasizer® software. 1 cm pathlength disposable cuvettes from VWR (West Chester, Pennsylvania) were used and all the experiments were performed at 37°C. The average particle size (d_{50}, volume median diameter) and the polydispersity index (PDI) were recorded for each measurement.

3.4.6 Microstructural characterization and elemental composition analysis of partially dissolved or humidity exposed ASD tablet surfaces

X-ray Micro Computed Tomography (micro-CT)

The partially dissolved tablets were mounted on a Styrofoam holder and analyzed using a SkyScan 1272 high-resolution micro-CT scanner (Bruker microCT, Kontich, Belgium). The X-ray tube was set to 60kV and the beam was filtered with a 0.25 mm aluminum filter. The samples were imaged at a 3.0 μm isotropic pixel size and two-dimensional projections were collected corresponding to a 180° rotation of the entire tablet with steps of 0.1° (4 images were averaged per position). The subsequent reconstructions were done using NRecon (Bruker, v1.6.9.8) where appropriate corrections to reduce beam hardening and ring artifacts were applied. After reconstruction, individual 2D slices were viewed and recorded through *Dataviewer* software.

Scanning Electron Microscopy (SEM)

SEM images of partially dissolved tablet surfaces or a tablet surface exposed to high humidity were taken using a Nova nanoSEM field emission scanning electron microscope (FEI Company, Hillsboro, Oregon). Tablets were fixed on aluminum stubs using double sided carbon tape, sputter-coated with platinum for 60 s and imaged using an Everhart-Thornley detector. A high resolution through-the-lens detector (TLD) was also used to obtain high magnification scans (>20,000) for a few samples. Scanning was completed at spot size of 3 nm, 10 kV beam energy and ~5 mm working distance.

In order to confirm the elemental composition of features seen on partially dissolved tablets, energy dispersive X-ray (EDX) analysis was additionally performed on a Nil:PVPVA 15:85 tablet using the aforementioned FEI Nova nanoSEM field emission SEM equipped with an Oxford EDX silicon drift detector (SDD, X-Max^N 80 mm^2). For EDX analysis, a spot size of 3 nm, 5 kV beam energy and ~10 mm working distance was used. Quantitative estimate of the elemental analysis was performed using the AZtec software package (Oxford Instruments) utilizing a standardless analysis based on the Cliff-Lorimer method.

X-ray photoelectron spectroscopy (XPS)

XPS data were obtained with a Kratos Axis Ultra DLD spectrometer (Kratos Analytical Inc., Manchester, UK) using monochromic Al Kα radiation (1486.6 eV) at constant pass energy (PE) of 20 and 160 eV for high-resolution and survey spectra acquisition, respectively. A commercial Kratos charge neutralizer was used to neutralize the surface charge of non-conducting tablet surface during data acquisition and to achieve better resolution. The instrument resolution for a PE of 20 eV is about 0.35 eV. Binding energy (BE) values were referenced to the Fermi edge and the BE scale was calibrated using Au $4f_{7/2}$ = 84.0 eV and Cu $2p_{3/2}$ = 932.67 eV. Tablets were placed on a stainless steel sample holder bar using a double-sided sticking Cu tape with surface of interest facing upwards. All XPS spectra were analyzed with *CasaXPS* software (www.casaxps.com). Charge correction was performed prior to data analysis by setting the C–C component of the C 1s peak at BE of 284.8 eV. The atomic concentrations of the elements in the near-surface region (~10 nm) was estimated after Shirley or Tougaard background subtraction. Curve fitting was performed using model peak shapes for O 1s, N 1s and C 1s obtained from materials alone (nilvadipine, cilnidipine and PVPVA) to determine the relative composition of drug and polymer on the ASD tablet surface before and after dissolution for incongruently releasing ASD formulations (Nil:PVPVA 15:85 and Cil:PVPVA 20:80). As control experiments, XPS analysis was also performed on the tablet surface before and after dissolution on two of the congruently releasing ASD formulations (Nil:PVPVA 10:90 and Cil:PVPVA 15:85). 3-5 spots were measured for each sample.

3.4.7 Confocal fluorescence microscopy (CFM) imaging

Nil:PVPVA (10% drug loading) ASD films containing two fluorescent probes, prodan and R6G, as is and exposed to 97%RH for 12 hours were analyzed using a Nikon A1 confocal microscope (Melville, NY, USA) to gain visual insight into the phase separation behavior. The expectation is that the less polar probe (prodan) will partition into drug-rich phase in contrast to the more polar probe (R6G), which will partition into the polymer-rich phase in the event of phase separation. The detailed methodology of CFM imaging on such samples is as described previously.[19]

3.4.8 Powder dissolution of nilvadipine and cilnidipine ASDs

Dissolution of milled and sized powdered ASDs of nilvadipine and cilnidipine was conducted in 50 mL of 100 mM pH 6.8 phosphate buffer in a water jacketed beaker at 37°C under constant agitation using a magnetic stir bar at 300 rpm. The purpose of conducting powder dissolution experiments was to confirm that the rank ordering and dissolution performance of ASD formulations, as seen with surface normalized dissolution, were not influenced by specific hydrodynamics of dissolution, but were a result of the inherent properties of the formulation under study here (drug hydrophobicity and drug loading). For all dissolution experiments, the nominal drug concentration (for both nilvadipine and cilnidipine) was kept constant at 100 µg/mL, i.e., a total concentration of 100 µg/mL of the drug will be obtained if all of the drug is released from the ASD. A 0.2 cm pathlength *in situ* UV probe attached to the SI photonics 400 UV/vis spectrophotometer (SI photonics, Tuscan, AZ) was utilized to monitor nilvadipine concentration in the dissolution medium. Due to excess scattering, the *in situ* UV probe could not be used for cilnidipine systems. Cilnidipine concentrations during ASD dissolution experiments were measured by withdrawing 300 µL of the dissolution medium at predefined time points after filtration using a PTFE syringe filter (4 mm diameter) with a pore diameter of 0.45 µm to remove any undissolved ASD. The volume removed from the dissolution medium was replaced by fresh medium.

3.4.9 Data Analysis

Data are presented as mean ± standard deviation (SD). The statistical analyses were conducted by student's *t*-test or one-way ANOVA followed by Tukey's post hoc test using GraphPad Prism 7.0. A p-value ≤ 0.05 was used to assess statistical significance.

3.4.10 ClogP

The partition coefficients (logP) were calculated using ChemDraw Professional version 18.0 from Perkin Elmer, where ClogP is calculated based on a fragment method algorithm.

3.5 Results

3.5.1 Crystalline and amorphous solubility

The crystalline solubilities of nilvadipine and cilnidipine in 100 mM pH 6.8 phosphate buffer were found to be 1.7 and 0.05 µg/mL, respectively (Table 3.1). The amorphous solubility values of nilvadipine, determined by the four different methods were found to be in good agreement with each other as shown in Table 3.1. For cilnidipine, due to the low value of the amorphous solubility, only the ultracentrifugation method was used. The amorphous solubilities of nilvadipine and cilnidipine were found to be around 31 and 0.6 µg/mL respectively, yielding corresponding amorphous:crystalline solubility ratios of 18 (nilvadipine) and 12 (cilnidipine). The crystalline and amorphous solubility determinations were also performed at high polymer concentration (1 mg/mL PVPVA) and the solubility values were found within the range of values mentioned in Table 3.1 (data not shown) indicating that polymer, at the concentrations used in this study, did not affect the solubility values for nilvadipine and cilnidipine.

Table 3.1 Crystalline and amorphous solubility values for nilvadipine and cilnidipine (values in parentheses represent standard deviations, n=3)

	Nilvadipine	Cilnidipine
Crystalline solubility (µg/mL)	1.7 (0.2)	0.05 (0.0)
		0.03 (0.0)[#]
Amorphous solubility (µg/mL)[*]		
UV extinction	31.9 (2.8)	-
Fluorescence	~ 30	-
Mass flow	~ 30	-
Ultracentrifugation	31.2 (3.3)	0.6 (0.1)
		0.5 (0.3)[#]

- Experiment not performed.
* Amorphous solubility obtained in presence of 50 µg/mL PVPVA for nilvadipine (to prevent crystallization) and without polymer (neat) for cilnidipine (a slow crystallizer).
# literature value obtained from ref.[122].

3.5.2 Surface normalized dissolution rates of drugs, polymer and ASD tablets

Since powder dissolution is impacted by non-uniform and changing surface area, surface normalized dissolution rates were studied to compare ASD formulations across different drugs and drug loadings. No crystallization of the compact was observed by either PXRD or PLM for the duration of the experiments. Figure 3.2 shows the release versus time profiles for selected ASDs, whereby both the polymer and the drug release is shown. Clearly for some systems, drug and polymer release at the same rate, whereas for other ASDs, drug release is much slower than the polymer release. From these data, the surface normalized dissolution rates of drug alone and polymer alone, as well as drug and polymer from different drug loading ASDs can be determined and these are summarized in Tables 3.2 and 3.3. The dissolution rate of amorphous nilvadipine was measured to be 0.002 mg/min/cm^2, while the dissolution rate of amorphous cilnidipine could not be quantified since solution concentrations were below the detection limit of the HPLC analysis. The dissolution rate of PVPVA alone was measured to be 3.49 mg/min/cm^2, approximately 1700 time faster than the dissolution rate of nilvadipine. The dissolution rates of drug and polymer when formulated as an ASD varied between these two extremes. The drug release rates for drug loadings of 5% and 10% for nilvadipine ASDs, and drug loadings of 5%, 10% and 15% for cilnidipine ASDs were found to be similar to the polymer release rate. This suggests that the polymer controls dissolution at low drug loadings. In contrast, the drug release rates for 15% and 20% nilvadipine ASDs were found to be closer to the dissolution rate of the amorphous drug alone, indicating that the amorphous drug controlled the release rate at these drug loadings. It should be noted that polymer release rates are slightly reduced as compared to polymer alone, even in ASDs with low drug loadings that show polymer-controlled dissolution. This has been observed previously [26, 118] and is most likely due to increased hydrophobicity of the formulation in the presence of hydrophobic drug or interactions between drug and polymer resulting in slower polymer dissolution rates. The drug loading at which the release mechanism switches from polymer-controlled to drug-controlled occurs at a similar drug loading for each compound, when the drug loading is normalized to account for the number of moles of each component present (where the average monomer molecular weight was used for the polymer). Thus, the switch occurs between 6 and 9 molar% for nilvadipine and between 7 and 9 molar% for cilnidipine ASDs.
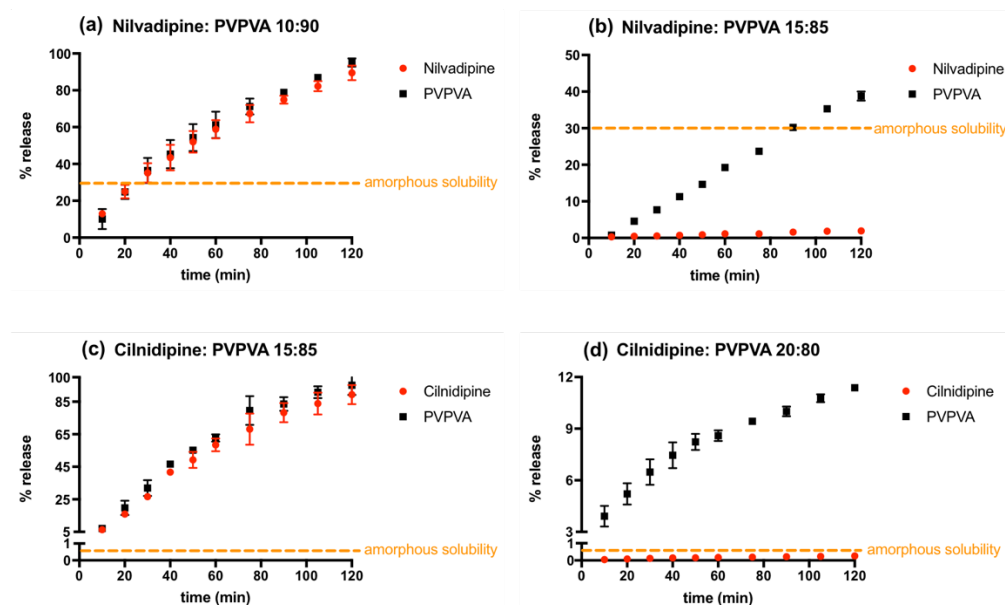
Figure 3.2 Comparison of the dissolution rates of drug and polymer at drug loadings where a switch between polymer-controlled and drug-controlled release is observed: Nil:PVPVA 10:90 (a), Nil:PVPVA 15:85 (b), Cil:PVPVA 15:85 (c) and Cil:PVPVA 20:80 (d). The dashed horizontal line represents amorphous solubility of the drug.

Table 3.2 Summary of the normalized dissolution rates of amorphous nilvadipine and PVPVA alone, and when incorporated into an ASD (mean ± SD, n=3)

Normalized release rate (mg/min/cm^2)*					
Nilvadipine: PVPVA weight ratio (% drug loading by moles)	PVPVA	SD	Nilvadipine	SD	Ratio (PVPVA/Nil)
PVPVA alone	3.49	0.07	N/A	N/A	N/A
05:95 (3%)	2.76	0.25	2.53	0.26	~1
10:90 (6%)	2.35	0.43	2.13	0.41	~1
15:85 (9%)	0.72	0.01	0.035	0.002	~20
20:80 (13%)	0.52	0.06	0.013	0.003	~40
Nilvadipine alone	N/A	N/A	0.002	0.00008	N/A

*The drug and polymer release rates are normalized with respect to their respective contents.

Table 3.3 Summary of the normalized dissolution rates of PVPVA alone and cilnidipine and PVPVA when incorporated into an ASD (mean ± SD, n=3)

Normalized release rate (mg/min/cm^2)*					
Cilnidipine: PVPVA weight ratio (% drug loading by moles)	PVPVA	SD	Cilnidipine	SD	Ratio (PVPVA/Cil)
PVPVA alone	3.49	0.07	N/A	N/A	N/A
05:95 (2%)	2.74	0.24	2.51	0.26	~1
10:90 (4%)	2.41	0.38	2.26	0.31	~1
15:85 (7%)	2.36	0.44	2.18	0.17	~1
20:80 (9%)	0.24	0.01	0.006	0.001	~40
25:75 (12%)	0.21	0.03	0.002	0.0002	~105
Cilnidipine alone	Below quantification limit				

*The drug and polymer release rates are normalized with respect to their respective contents.

Because AAPS in the matrix was suspected to be responsible for the slow drug release, a Nil:PVPVA 10:90 ASD was exposed to high RH (97%) for 12 hours (the compact was in the die during the conditioning period). Exposure to high RH is known to induce phase separation in some ASDs.[18, 19, 124] For the first 15 min of the dissolution experiments on this system, the drug released slowly, and at a much lower rate than that observed for the polymer. Between 15 and 20 min, the surface layer appeared to peel off the tablet, presumably revealing a fresh surface. Drug release was much faster after this point (Figure B1, Appendix B). Data for the first 15 minutes of dissolution for a Nil:PVPVA 10:90 ASD compact with and without exposure to 97% RH is compared in Figure 3, illustrating the dramatic reduction in the drug release following conditioning of the ASD at high RH. Notably, the polymer also releases at a slower rate in the sample exposed to high RH.
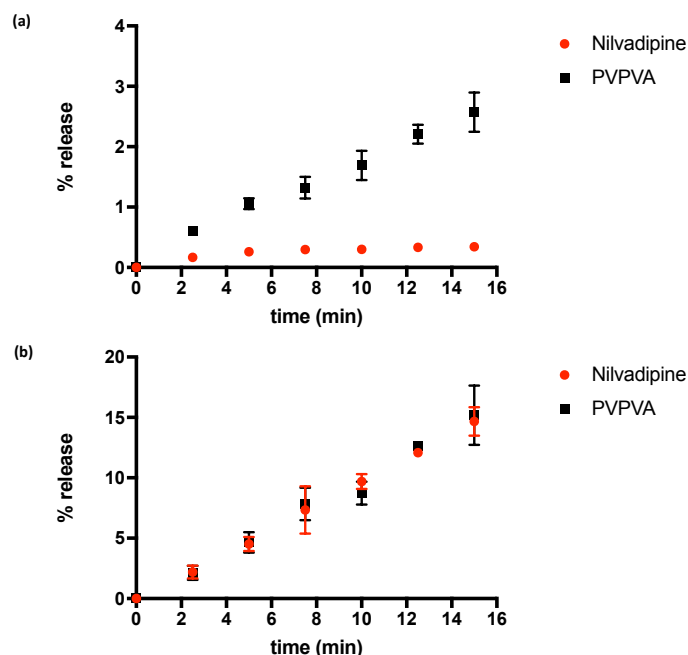
Figure 3.3 Comparing the dissolution rates (mean ± SD, n=3) of drug and polymer from Nil:PVPVA 10:90 ASD tablet surface exposed to 97% RH for 12 hours (a) and 0 hour (control) (b).

3.5.3 Solution phase behavior during surface normalized dissolution of nilvadipine and cilnidipine ASD tablets

Solution phase behavior during ASD tablet dissolution of nilvadipine and cilnidipine ASDs was monitored using orthogonal techniques namely, fluorescence spectroscopy, DLS and NTA.

Fluorescence spectroscopy

4-Di-2-Asp has been previously used as an environment sensitive fluorescent probe to determine the presence of amorphous drug-rich nano-droplets [123]. The emission wavelength and intensity of 4-Di-2-Asp depends on the polarity of its local environment and this property was utilized in this study to determine the occurrence of LLPS during ASD dissolution. In short, the presence of amorphous drug aggregates formed during ASD dissolution will result in partitioning of a hydrophobic fluorescent probe into the drug-rich phase resulting in a blue shift of the emission spectrum with respect to emission spectrum in the dissolution medium (aqueous buffer) with no aggregates. Figure 3.4 shows the normalized fluorescence emission spectra of 4-Di-2-Asp for solutions derived from the dissolution of different drug loading nilvadipine and cilnidipine ASDs. A blue shifted spectrum results for the lower drug loading ASDs, whereas the higher drug loading

dispersions yield a spectrum with a maximum at a higher wavelength. The cutoff was 10-15% for nilvadipine ASDs and 15-20% for cilnidipine ASDs. These results support that the lower drug loading ASDs dissolve to produce drug-rich aggregates, resulting in the probe partitioning into the drug-rich phase resulting in a blue shift of the emission spectrum, consistent with a less polar environment for the probe.
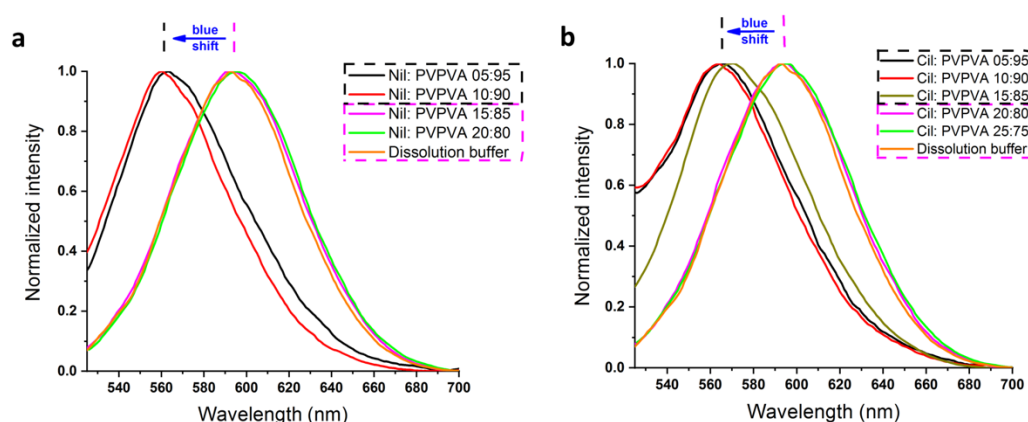
Figure 3.4 Representative fluorescence emission spectrum (with normalized intensity) of 4-Di-2-Asp for: Nil:PVPVA ASDs for different drug:polymer weight ratios (a), and Cil:PVPVA ASDs for different drug:polymer weight ratios (b). The figure shows shorter emission maximum wavelengths of the probe for low drug loading ASDs (05:95 and 10:90 for Nil:PVPVA ASDs; 05:95, 10:90 and 15:85 for Cil:PVPVA ASDs) due to probe partitioning into drug-rich phase as a result of LLPS. The fluorescence emission spectrum of 4-Di-2-Asp in dissolution medium (pH 6.8 buffer) without ASDs is also known as reference.

Dynamic Light Scattering (DLS)

To confirm the presence or absence of colloidal species upon dissolution of nilvadipine and cilnidipine ASDs, samples were withdrawn from the dissolution medium after approximately one hour. DLS analysis of these samples confirmed the presence of nano-sized droplets for 5% and 10% drug loading nilvadipine ASDs, and 5%, 10% and 15% drug loading cilnidipine ASDs and the measured d_{50} values are provided in Table 3.4. The PDI was smaller than 0.2 for these measurements. The trend towards larger sizes with increased drug loading could indicate a lower stability of the nanodroplets to agglomeration under these release conditions,[125, 126] or an impact of drug loading on the formation mechanism (which has not been widely explored and is under debate).[60, 127] No nano-droplets were observed during dissolution of higher drug loading ASDs ($\geq$15% for nilvadipine ASDs and $\geq$20% for cilnidipine ASDs) whereby these systems gave no meaningful DLS results.

Table 3.4 Size of amorphous nano-droplets from ASD tablet dissolution (mean ± SD, n=3).

Drug: Polymer weight ratio	Diameter (nm)	
	Nil: PVPVA	Cil: PVPVA
05:95	237±8	255±1
10:90	246±3	300±2
15:85	None*	366±7
20:80	None*	None*
25:75	N/A	None*

*No meaningful data could be obtained

 N/A- not applicable (drug loading not performed)

Nanoparticle Tracking Analysis (NTA)

Figures 3.5 and 3.6 show representative screenshots from NTA videos acquired on solutions obtained after ASD tablet dissolution. It was observed that dissolution at low drug loadings, i.e., up to 10% for nilvadipine and 15% for cilnidipine ASDs, led to the appearance of scattering centers, consistent with the formation of amorphous nano-droplets. Higher drug loadings (≥15% for nilvadipine ASDs and ≥20% for cilnidipine ASDs) did not show scattering centers. The size distribution of the nano-droplets formed upon dissolution determined using NTA were in a similar range as those determined by DLS measurements (Figure B2, Appendix B).
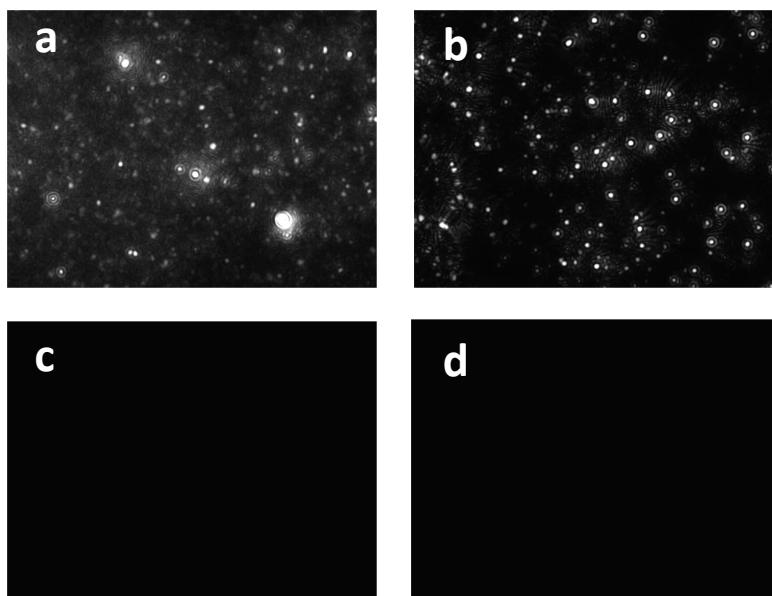
Figure 3.5 NTA scattering images of solutions obtained after dissolution of Nil: PVPVA ASDs with different drug:polymer weight ratios. Nil: PVPVA 05:95 (a), Nil: PVPVA 10:90 (b), Nil: PVPVA 15:85 (c), and Nil: PVPVA 20:80 (d). The bright spots indicate the presence of light scattering species where the field of view is 100 by 80 μm.
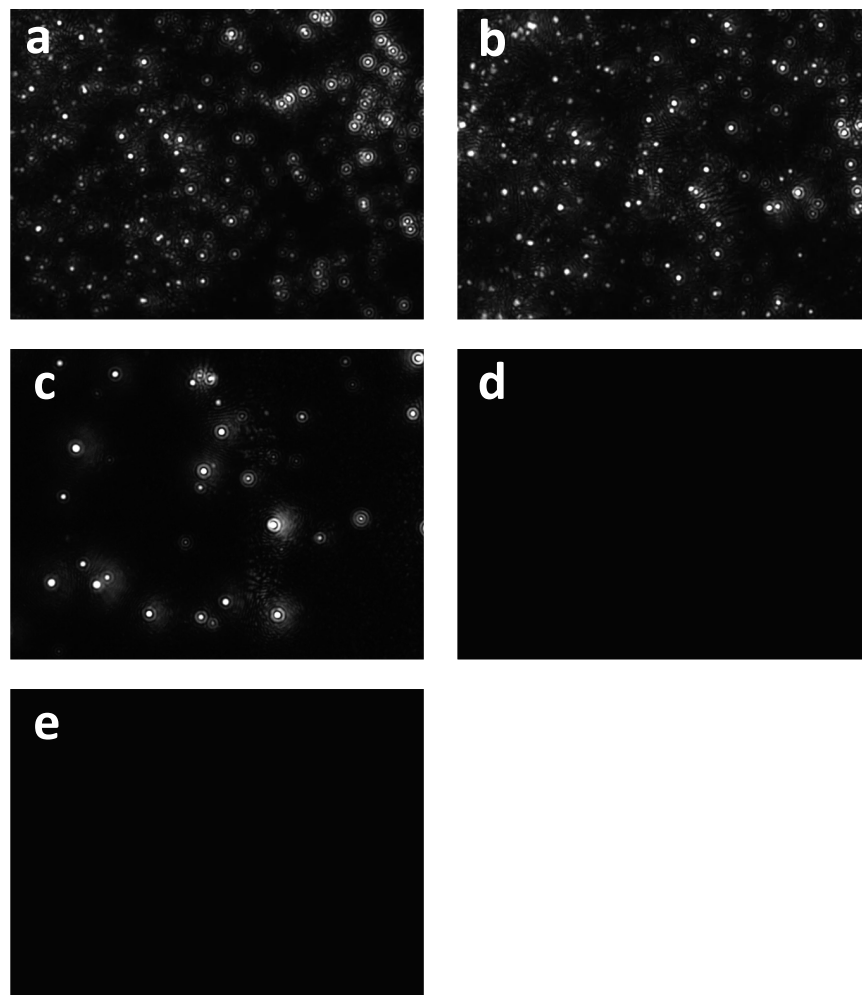
Figure 3.6 NTA scattering images of solutions obtained after dissolution of Cil: PVPVA ASDs with different drug:polymer weight ratios. Cil: PVPVA 05:95 (a), Cil: PVPVA 10:90 (b), Cil: PVPVA 15:85 (c), Cil: PVPVA 20:80 (d), and Cil: PVPVA 25:75 (e). The bright spots indicate light scattering species where the field of view is 100 by 80 μm.

3.5.4 Microstructural characterization and elemental composition analysis of partially dissolved or humidity exposed ASD tablet surfaces

X-ray Micro Computed Tomography (micro-CT)

Interesting differences in the microstructure of the partially dissolved tablets (10 minute time point) on either side of boundary between slow and rapid release of ASD components were observed using micro-CT. The tablets with the lower drug loading exhibited a relatively homogenous internal microstructure devoid of pores (Figure 3.7 (a) and (b)), in stark contrast to tablets with a higher drug loading which had porous microstructure at the interface that had been in contact with

the dissolution medium (Figure 3.7 (c) and (d)) with the porous structure developing within 10 minutes of dissolution. The porous microstructure is consistent with the polymer dissolving faster than the drug leaving behind pores and a higher concentration of drug at the surface. For Nil:PVPVA 15:85 ASD tablets, microCT imaging at successive time points (20 and 30 minutes) was performed in order to visualize the evolution of porous interface (Figure B3, Appendix B). The porosity of the interface increased with time, consistent with the increased loss of polymer at longer time points. Additionally, a network of "channels" developed in the tablet matrix at longer times.
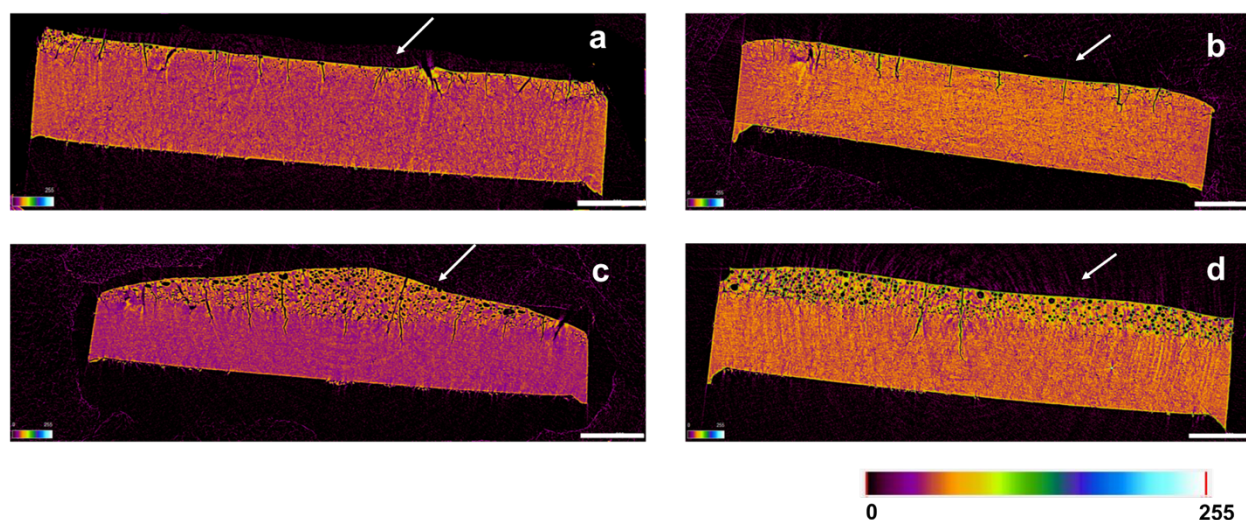
Figure 3.7 x-y cross-section images of partially dissolved tablets (10 minute time point) for Nil:PVPVA 10:90 (a), Cil: PVPVA 15:85 (b), Nil:PVPVA 15:85 (c) and Cil:PVPVA 20:80 (d). The arrow on the images is pointing towards the dissolving face of the tablet. The color scale bar represents the range of density measurement with zero representing the lowest density and 255 representing the highest density measured. Scale bar (in white) is 1 mm.

Scanning Electron Microscopy (SEM)

SEM images of the partially dissolved tablet surface showed surface topography in general agreement with the micro-CT data. A smooth surface was observed for the lower drug loading compacts, while for the higher drug loading system, the surface was rough and had pits, suggestive of faster polymer dissolution, resulting in a drug-enriched surface with rougher topography (note the protrusions in the areas around the holes) as depicted in Figure 3.8. Figure 3.9 is an SEM image of a fractured, partially dissolved Cil:PVPVA 20:80 tablet showing that the holes penetrate into

the interface, and are not merely a surface feature of the tablet, in agreement with the micro-CT cross-sectional images.
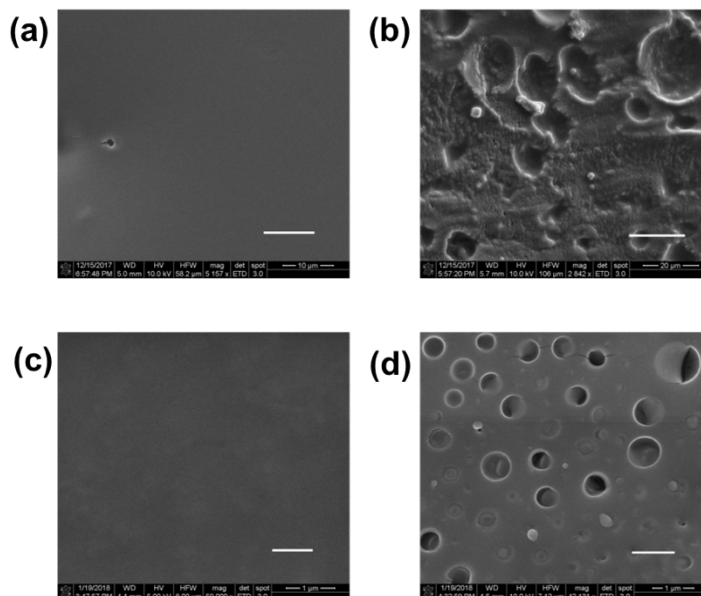
Figure 3.8 SEM images of dissolving tablet surface (10 minute time point) for Nil:PVPVA 10:90 (a), Nil:PVPVA 15:85 (b), Cil:PVPVA 15:85 (c) and Cil:PVPVA 20:80 (d). Scale bar is 10 μm (a), 20 μm (b) and 1 μm (c and d).
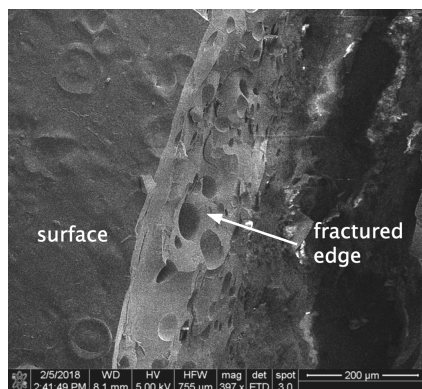
Figure 3.9 SEM image of the surface (left hand side) and the fractured edge (marked by arrow) of a partially dissolved ASD tablet of Cil:PVPVA 20:80 at 10 minute time point.

To investigate the differences in elemental composition, if any, across rough surfaces, EDX analysis was performed for an incongruently releasing Nil:PVPVA 15:85 ASD tablet. The nitrogen and oxygen atomic percentage ratio difference between nilvadipine and PVPVA was utilized to identify drug-rich regions. A similar analysis could not be performed for the Cil:PVPVA 20:80

ASD tablet surface due to a much smaller difference in the nitrogen and oxygen atomic ratio between cilnidipine and PVPVA.

The molecular formula of nilvadipine is $C_{19}H_{19}N_3O_6$; thus, the nitrogen/oxygen (N/O) atomic ratio of the molecule is 0.5, while PVPVA is a copolymer of N-vinyl-2-pyrrolidone and vinylacetate with a molecular formula of $C_{10}H_{15}NO_3$ for the pyrrolidone acetate dimer, and has a lower N/O atomic ratio of ~0.3. It should be noted that the carbon (C) atomic% was deconvoluted from the EDX quantitative analysis to incorporate it in the matrix corrections for N and O atomic%. Figure 3.10a shows a representative image of a depression on the surface of a partially dissolved Nil:PVPVA 15:85 tablet (10 minute time point) with protruding margins around the periphery. The green and red crosses represent the points of EDX spectra collection from inside the hole and at periphery, respectively. As a control, a similar analysis was performed on a Nil:PVPVA 15:85 tablet before dissolution along the diagonal line, as shown in Figure 3.10b. The significant difference in the average N/O atomic% ratio from the smooth regions inside the hole versus protruding regions around the hole (Figure 3.10c) illustrates that protruding regions are drug-rich, and are presumably left behind after faster polymer dissolution, with a N/O atomic% ratio of ~0.5. In contrast, the region inside the hole (N/O atomic% ratio of ~0.35) has less drug and an N/O atomic% ratio similar to the control tablet indicating that dissolution of components is non-uniform across the surface.
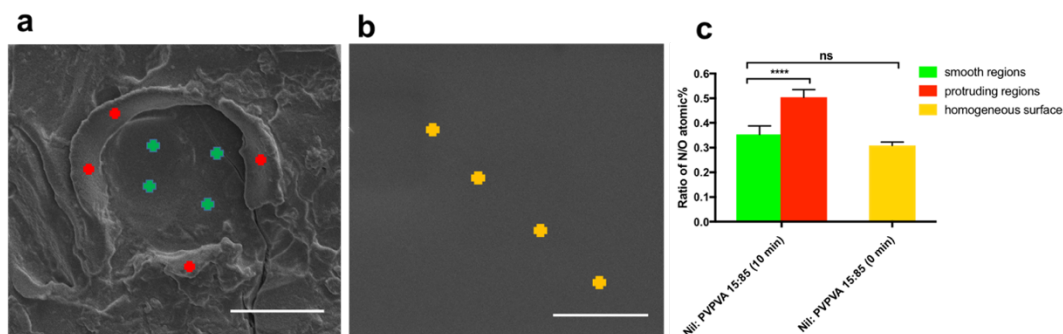
Figure 3.10 (a) A hole on Nil:PVPVA 15:85 partially dissolved tablet (10 minute time point) (green and red crosses represent the points of EDX spectra collection from inside the hole and its protruding peripheral margins, respectively). Scale bar is 50 μm. (b) Nil: PVPVA 15:85 tablet before dissolution (0 minute time point) (yellow crosses represent the points of EDX spectra collection). Scale bar is 50 μm. (c) A plot of the average N/O atomic% ratio (mean±SD, n=4) for points of EDX spectra collection represented in Fig. 10a and 10b. **** $p < 0.0001$ between smooth and protruding regions of Nil:PVPVA 15:85 partially dissolved tablet; [ns] $p > 0.05$ (no significant difference) between smooth regions after dissolution and homogeneous surface before dissolution of Nil:PVPVA 15:85 tablet.

An SEM image (Figure 3.11b) of the Nil:PVPVA 10:90 ASD tablet surface exposed to high RH (97% RH) showed a rough topography, most likely due to water-induced AAPS at the exposed surface. Interestingly, these topographical features were no longer present when SEM imaging was performed on similar humidity exposed ASD tablet after 15 minutes of dissolution (image not shown) indicating the superficial nature of water-induced AAPS, and that it only occurred at the tablet surface, rather than in the bulk.
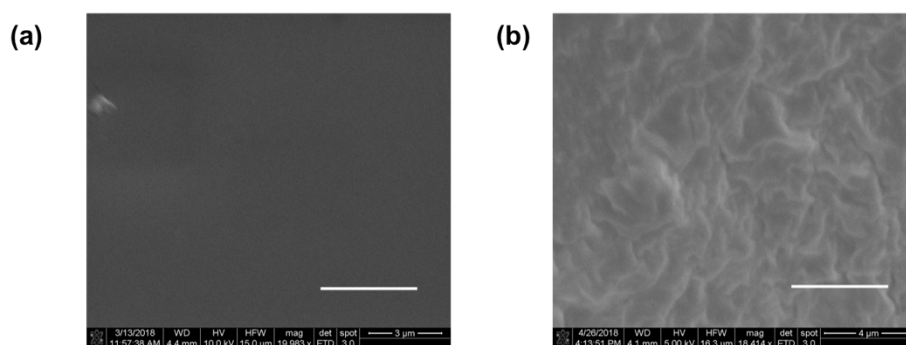
Figure 3.11 SEM image of Nil:PVPVA 10:90 ASD tablet surface initially (a) and after exposure to 97%RH for 12 hours (b). Scale bar is 4 μm.

X-ray photoelectron spectroscopy (XPS)

XPS is an analysis technique capable of providing qualitative and quantitative information about surface chemical composition with a penetration depth of around 10 nm.[128] In this study, XPS was used to evaluate the surface composition of the incongruently releasing ASD tablets (Nil:PVPVA 15:85 and Cil:PVPVA 20:80) before and after dissolution in order to confirm drug enrichment on the tablet surface due to faster polymer release. The relative composition of drug and polymer in these ASDs initially and after 10 minutes of dissolution showed significant drug enrichment of the tablet surface based on a two-sample student's *t*-test for a 5% level of significance (Table 3.5). For example, based on the curve fits of the C1s spectra (Figure B4, Appendix B), a surface drug enrichment of ~60% was observed post dissolution for the Cil:PVPVA 20:80 ASD tablet as compared to the initial ~20% of drug loading. Similarly, for the Nil:PVPVA 15:85 ASD tablet, drug enrichment was ~32% as compared to ~2% prior to dissolution (again based on the C1s spectra curve fitting, Figure B5, Appendix B). It should be noted that for the Nil:PVPVA 15:85 ASD tablet, the initial drug% composition as determined by XPS analysis differs from the theoretical composition (15%) and this could be due to surface polymer enrichment of the initial

99

ASD particles on the outermost surface (ca. 10 nm) as observed previously for other systems.[26,] [129, 130] Nevertheless, surface drug% composition of this formulation after dissolution is higher than prior to dissolution, and more than twice the theoretical composition (15%), demonstrating a substantial extent of drug-enrichment at the surface These results further support the supposition that incongruent release of drug and polymer because of faster polymer dissolution results in the formation of a drug-rich interface. The results for the N1s and O1s peak curve fitting (data not shown) also supported surface drug enrichment. Additionally, based on the C1s peak curve fitting, no significant difference was observed before and after dissolution in the relative composition of drug and polymer for the congruently releasing ASD tablet surfaces (Nil:PVPVA 10:90 and Cil:PVPVA 15:85) (Table B1, Appendix B).

Table 3.5 Surface compositions as measured by XPS (mean ± SD, n≥3) for incongruently releasing ASD tablet formulations (Nil:PVPVA 15:85 and Cil:PVPVA 20:80) before and after dissolution (partially dissolved surface at 10 minute dissolution time point).

ASD tablet composition (dissolution time point)	% surface composition based on XPS (C1s spectra, weight ratio)	
	Drug	PVPVA
Nil:PVPVA 15:85 (0 minute time point)	2±0	98±0
Nil:PVPVA 15:85 (10 minute time point)	32±1[****]	68±1[****]
Cil:PVPVA 20:80 (0 minute time point)	20±1	80±1
Cil:PVPVA 20:80 (10 minute time point)	60±4[****]	40±4[****]

[****]significantly different from corresponding 0 minute time point %drug (or %polymer) surface composition ($p < 0.0001$)

3.5.5 Confocal fluorescence microscopy (CFM) imaging

CFM imaging of ASD films (Nil:PVPVA 10:90) with and without exposure to 97% RH (for 12 hours) confirmed the phase separation of these ASDs upon high humidity exposure and also gave some interesting insights into their phase separation behavior. As established previously, prodan selectively stains the drug-rich phase and R6G selectively stains the polymer-rich phase.[19] The representative CFM images shown in Figure 3.12 show a miscible film prior to exposure with the probes homogeneously distributed (purple for both channels, blue for prodan and red for R6G). After exposure, the drug-rich domains (blue) appear either as filled circles or as rings (the blue rimmed "rings" in Figure 3.12), while the polymer (red) forms the continuous phase, and is also present inside the rings. This observation substantiates the phase behavior pattern of partially

dissolved incongruently releasing ASD tablet formulations as observed through SEM imaging and EDX analysis (pits due to faster polymer dissolution surrounded by a protruding drug-rich phase).
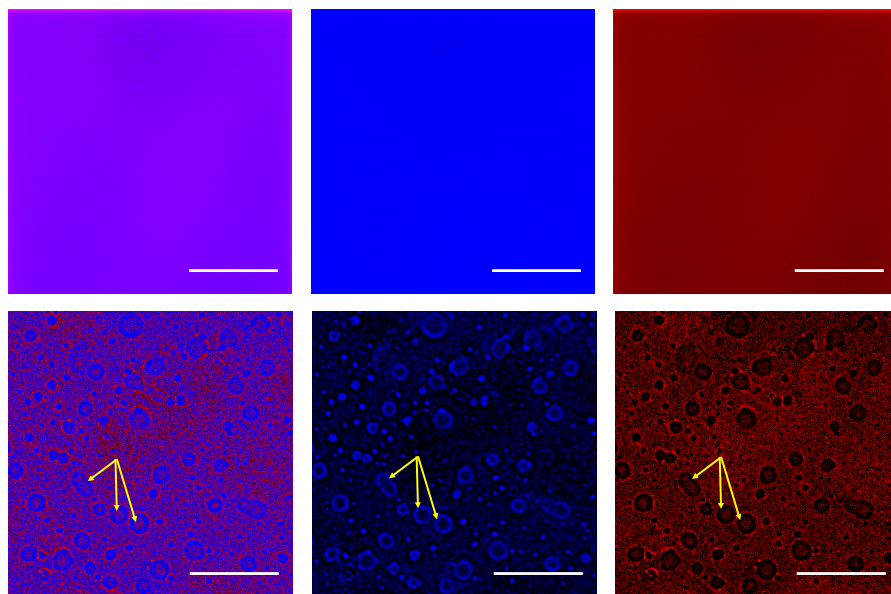
Figure 3.12 Confocal fluorescence microscopy images of Nil:PVPVA 10:90 ASD films. The upper panel represents miscible films prior to high RH exposure with homogenous distribution of prodan (blue in color) and R6G (red in color) probes, whereby the purple panel is the overlay of both probes. The lower panel represents phase separated ASD films upon high RH exposure where Nil-rich regions are stained by prodan and PVPVA-rich regions are stained by R6G. The yellow arrows point towards the specific phase separation behavior where circular drug-rich domains have smaller polymer-rich domains inside them in addition to the outer polymer-rich continuous phase. Scale bar is 50 μm.

3.5.6   Powder dissolution of nilvadipine and cilnidipine ASDs

Figure 3.13 shows the release behavior of nilvadipine from powdered Nil-PVPVA ASDs with drug loadings ranging from 5% to 20% at a nominal drug concentration of 100 μg/mL. It is evident that the powder dissolution results follow the same trend as the surface normalized dissolution, i.e., there is drastic decline in the drug release upon increasing the drug loading from 10% to 15%, indicative of a change in release mechanism for these systems. Low drug loadings (5% and 10%) dissolve rapidly giving rise to visibly turbid solutions, due to LLPS (confirmed by DLS, NTA and fluorescence spectroscopy: data not shown) while for high drug loadings (15% and 20%), the solution remains visibly clear apart from the presence of undissolved ASD particles. It should be noted that the difference in the drug release profiles between different drug loadings is not because

of crystallization and no crystallization was observed for the initial 2 hours of the experiment based on examination of the dissolution medium by polarized light microscopy.
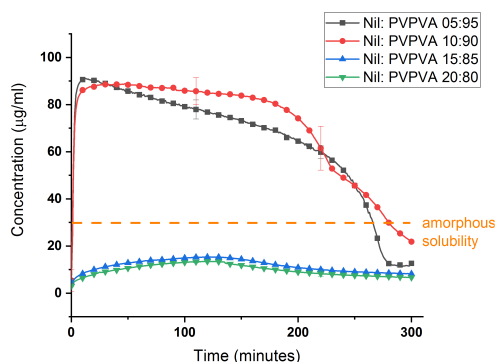
Figure 3.13 Nilvadipine dissolution profiles from powdered ASDs (mean±SD, n=3) at different drug loadings (5%-20% w/w). The dashed horizontal line represents amorphous solubility of nilvadipine. The ratios in the legend denote Nil: PVPVA weight ratio.

Figure 3.14 (a) shows the release behavior of cilnidipine from powdered Cil-PVPVA ASDs with drug loadings ranging from 5% to 20% at a nominal drug concentration of 100 µg/mL. Here, the drop-off in drug release occurs upon increasing the drug loading from 15% to 20%. Zoomed-in dissolution profiles of 20% and 25% drug loadings are given in Figure 3.14 (b) for clarity. For low drug loadings up to 15%, rapid and complete drug release is observed, while for high drug loading ASDs, only a very small extent of drug release was observed. Clear evidence of LLPS was found for ASDs with drug loadings up to 15% but was not observed for the higher drug loading ASDs. No crystallization was observed over the duration of the experiment.
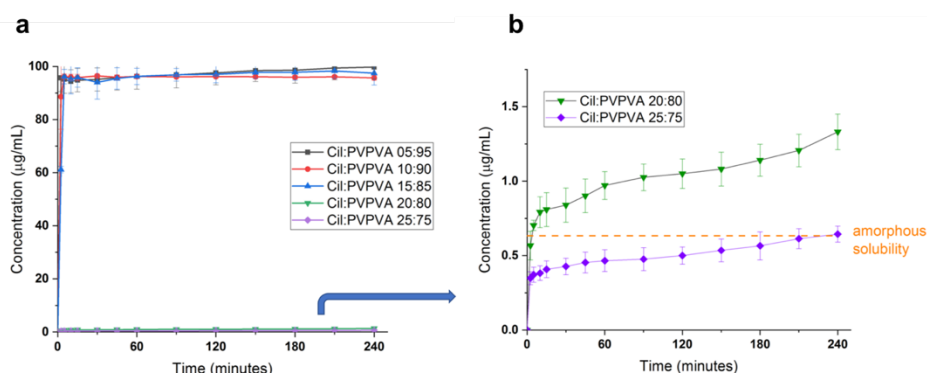
Figure 3.14 Cilnidipine dissolution profiles from ASDs (mean±SD, n=3) at different drug loadings (5%-25% w/w) (a). Zoomed in cilnidipine dissolution profiles for 20% and 25% drug loadings. The dashed horizontal line represents amorphous solubility of cilnidipine (b). The ratios in the legend denote Cil:PVPVA weight ratio.

3.6 Discussion

3.6.1 Link between LLPS occurrence and congruent release.

An important finding of this study is the observed link between LLPS with the formation of nano-sized drug-rich aggregates and the congruent release of ASD components. These nano-sized amorphous drug aggregates have a very rapid redissolution rate and thus can act as drug reservoir to replenish the depleted drug that has permeated through the biological membrane, thereby maintaining the maximum flux across the membrane for a longer duration of time.[66, 111] Another suggested *in-vivo* advantage of these drug-rich aggregates is their potential to decrease the diffusional resistance across the aqueous boundary layer (ABL) of the intestinal tract by acting as rapidly diffusing "shuttles" to transport the unbound drug to the membrane surface,[131] although clearly given their larger size, the diffusion rate of the nanodroplets is considerably slower than that of molecularly dissolved drug.

Considering the expected advantages of LLPS for bioavailability enhancement, it is important to develop a comprehensive understanding of drug, excipient and formulation factors that impact whether LLPS occurs or not. Traditionally, dissolution testing is restricted to measuring the drug release profile over the time period of interest. However, for controlled-release systems, emphasis has been given to measurement of polymer release profiles whereby various models have been developed to predict drug-dissolution based on polymer-dissolution profiles.[132-134] In the area of ASD dissolution, there have been a handful of studies that attempt to correlate drug and polymer release.[26, 118, 119, 127, 135] Herein, we have observed a clear link between the tendency of the system to undergo LLPS, and the congruency of drug and polymer release. Thus, LLPS is seen only for systems where simultaneous release of the drug and polymer occurs, which in turn is observed only at low drug loadings (Figure 3.15 and Tables 3.2-3.3).

Further, the remarkable drop in drug release rate observed when a certain drug loading is reached (Figure 3.15), and where components stop releasing congruently, has important implications for formulation development of ASDs. Thus, a small increase in drug loading for nilvadipine (from 10 to 15 wt.%) leads to a 60-fold decrease in the drug dissolution rate. A similar reduction is seen for cilnidipine formulations. A comparable trend in decreased release rate is seen with powder

dissolution. Clearly, if rapid release is required, drug loadings below this "drop-off" concentration, need to be selected for optimal performance.
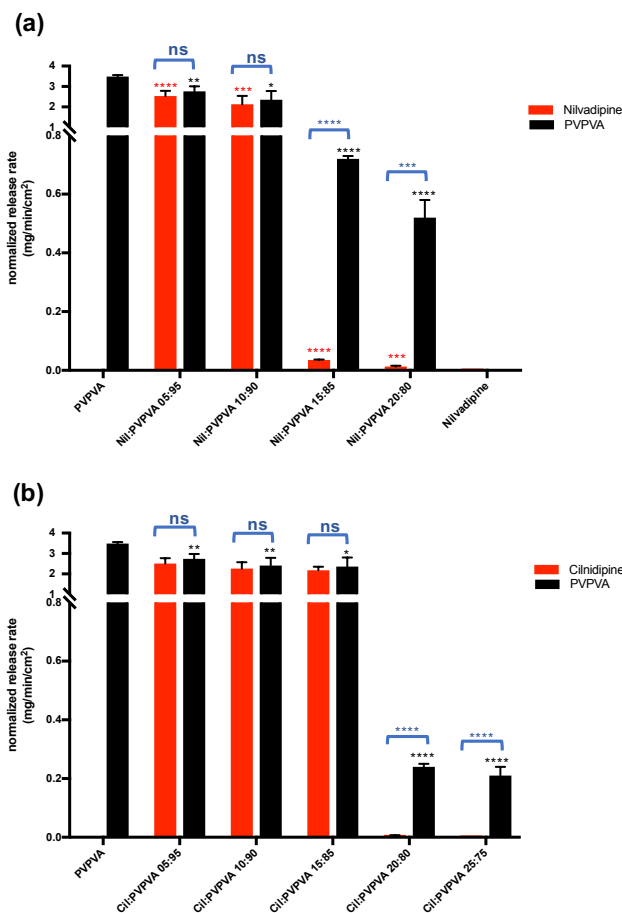
Figure 3.15 Surface normalized dissolution rates (mg/min/cm^2) of drug and polymer alone, and as part of nilvadipine ASDs at different drug loadings (5%-20% w/w) (a). Surface normalized dissolution rates (mg/min/cm^2) of polymer alone, and drug and polymer as part of cilnidipine ASDs at different drug loadings (5%-25% w/w) (b). The ratios in the legend denote drug:polymer weight ratios. ^{ns} p > 0.05, * p ≤ 0.05, ** p ≤ 0.01, *** p ≤ 0.001 and **** p ≤ 0.0001. Student's t-test performed between drug and polymer release rate for an ASD (blue asterisks), polymer release rate of an ASD and PVPVA alone release rate (black asterisks), and drug release rate of an ASD and drug alone release rate (red asterisks).

3.6.2 Switch between polymer-controlled (congruent) to drug-controlled (incongruent) release: effect of drug log P

A variety of factors linked to drug and polymer molecular properties is likely to play a role in determining the drug loading at which the switch from fast and congruent to slow and incongruent release occurs. When designing the current study, we hypothesized that a drug with a higher log P would result in an ASD with compromised dissolution behavior at a lower drug loading, relative

to a drug with a lower log P. The rationale behind the hypothesis was that the overall hydrophilicity of the ASD will depend on the properties of the drug and polymer, and the amount of each component. Thus, a more hydrophobic drug (based on the log P value), would more rapidly decrease the hydrophilicity of the drug-polymer blend as a function of composition, relative to a less hydrophobic drug, thereby negatively impacting dissolution performance. By judicious selection of structural analogs which have similar ability to hydrogen bond with the polymer (drug-polymer intermolecular interactions have been suggested to be important in drug dissolution from ASDs [118]), but vary in log P, we clearly see that our hypothesis is incorrect for the systems evaluated. Nilvadipine and cilnidipine ASDs switched from polymer-controlled to drug-controlled release at drug loadings above 10% and 15% respectively (~6-9% drug loading on a per mole basis), despite a log P differential of about 2.5 units. In a recent study with itraconazole (ClogP = 5.4) and PVPVA dispersions [26], the drop off in dissolution behavior was observed at greater than 20% drug loading, while for ritonavir (Clog P=4.5) and PVPVA dispersions, decreased dissolution occurred for drug loadings higher than 25%.[136] Simonelli and coworkers reported a notable decrease in the dissolution rate of sulfathiazole from PVP ASDs when the drug loading exceeded 25%.[137] These observations is particularly interesting because sulfathiazole is relatively more hydrophilic than the other compounds discussed with a Clog P of -0.5, although it is difficult to compare the results directly since the polymer used is not the same. Taken in concert, these observations further support the lack of correlation between molecular hydrophobicity and ASD dissolution performance in terms of the drug loading where drug release drops precipitously. Clearly, other factors need to be explored to better understand mechanisms involved in the change in release mechanism in ASDs formulated with PVPVA.

3.6.3 Potential role of amorphous-amorphous phase separation in degradation of dissolution performance

A striking difference in the morphology of the partially dissolved compact surface is observed between congruently and incongruently releasing systems. The former retain a smooth interface during dissolution, whereas for the latter, clear evidence of pit formation, and evolution of a porous interface is apparent. Given that we know from the dissolution results that the polymer leaves the ASD at a faster (normalized) rate than the drug, then the interface must become enriched in drug. This accounts for the porous nature of the surface given the low drug loading. The origin of the pit

formation can likely be attributed to rapid phase separation at the interface leading to drug-rich and polymer-rich areas, with subsequent dissolution of the polymer-rich regions. Evidence that this occurs is given by the confocal studies shown in Figure 3.12. Here, there is no loss of polymer because the phase separation is induced by exposure to high RH, rather than by contact with bulk water which will also dissolve the polymer. The microstructure which develops in the film exposed to high RH, in terms of the distribution of the drug into "donuts" is remarkably similar to surface topography observed in Figure 3.10, which shows similar drug-rich donut structures. Thus, the polymer-rich interior of the donut likely dissolves faster, leading to the observed pit-like structures initially observed at the interface (Figure 3.8b,d). Further evidence of the role of matrix phase separation is provided by the observation that a congruently releasing system can be converted into an incongruently system by exposing the system to high RH. Water vapor exposure induces phase separation at the compact surface, and changes the release profile such that drug release is minimal relative to the unexposed compact (Figure 3.3).   Thus, we can invoke a mechanism for dissolution where at low drug loadings, drug and polymer dissolution is faster than phase separation in the matrix. Hence, drug release is controlled by the polymer. Given that the polymer release rate is high, this translates to rapid drug release. In contrast, at higher drug loadings, it appears that phase separation occurs at a faster rate than drug release, leading to drug enrichment on the surface, and drug controlled release. For nilvadipine, the drug release rate from the amorphous form of the drug alone is more than 3 orders of magnitude slower than polymer release, explaining the precipitous drop in release rate when the dissolution mechanism changes with increased drug loading (Figure 3.15).

Our findings are different from the recently reported results of Chen et al,[138] wherein water-induced phase separation was found to have no impact on the dissolution rate of an amorphous solid dispersion. There are two possible explanations for discrepancy between the two studies. First, it should be considered that these authors studied ASDs containing a 40% drug loading. We would expect this high drug loading system to exhibit drug-controlled dissolution, as seen for the higher drug loading nilvadipine and cilnidipine dispersions. If phase separation within the matrix occurs rapidly during dissolution testing for the high drug loading systems, as postulated herein, then the lack of observable effect of amorphous phase separation can be readily explained. Second, there is difference between the intrinsic dissolution conditions employed in the two studies which

may have an impact on the relative dissolution rates of drug and polymer. Therefore, a direct comparison between the two studies may not be valid.

Overall, understanding ASD dissolution mechanisms and factors that contribute to the switch from polymer-controlled (congruent) to drug-controlled (incongruent) release, observed to occur when a given drug loading is exceeded for PVPVA dispersions, is likely to be important for formulation design. While we have observed that this switch occurs at different drug loadings for different drugs, the physicochemical factors that cause these differences are not well understood. While an improvement in dissolution rate would be anticipated by using an amorphous form of the drug, this rate increase is expected to be much smaller than that which can be achieved by formulating the ASD with a hydrophilic polymer such that the polymer release rate controls the drug release rate. Unfortunately, this appears to be possible only at relatively low drug loadings, which may not be desirable for commercial product formulation due to the large resultant dosage form size.

3.7 Conclusions

Low drug loading ASDs formulated with PVPVA show polymer-controlled drug release. Given that PVPVA is a hydrophilic polymer which releases rapidly from a compact, drug release is also rapid, and colloidal drug-rich species are formed in solution. The formation of colloidal drug-rich species occurs through the process of LLPS when the drug amorphous solubility is exceeded. Interestingly, an abrupt change in behavior is observed when the drug loading in the ASD exceeds a critical threshold. In this regime, drug release slows down by more than an order of magnitude, whereby drug and polymer release occurs at different rates. Characterization of the ASD interface after partial dissolution for these systems reveals enrichment of drug, explaining the slow-down in release, as well as the formation of a porous microstructure, consistent with the observed preferential polymer dissolution. In this regime, the amorphous solubility is not exceeded and LLPS does not occur. We suggest that there is a competition between phase separation in the hydrated matrix and dissolution. In the low drug loading regime, dissolution is faster than matrix phase separation, whereas for higher drug loadings, matrix phase separation, driven by water absorption, is fast, leading to a change in the dissolution mechanism. Further studies are clearly needed to probe dissolution mechanisms from ASDs.

CHAPTER 4. CONGRUENT RELEASE OF DRUG AND POLYMER FROM AMORPHOUS SOLID DISPERSIONS: INSIGHTS INTO THE ROLE OF DRUG-POLYMER HYDROGEN BONDING, SURFACE CRYSTALLIZATION AND GLASS TRANSITION

4.1 Abstract

Drug loading is an important parameter known to impact the release rate of a poorly soluble drug from an amorphous solid dispersion (ASD). Recent studies have shown that small increases in drug loading can dramatically reduce the drug release rate from ASDs prepared with poly (vinylpyrrolidone-co-vinyl acetate) (PVPVA). However, the link between drug physicochemical properties and the drug loading where release is abruptly compromised is not well understood. This study probes the role of three different factors on the relative dissolution rates of drug and polymer from PVPVA-based ASDs as a function of drug loading: 1) the impact of drug-polymer hydrogen bonding interactions on the initial dissolution rate of ASDs, investigated using two structural analogues, indomethacin (IND) and indomethacin methyl ester (INDester), 2) the influence of surface drug crystallization, observed for INDester ASDs, and 3) by changing temperature, the impact of 'wet' glass transition temperature (T_g). Scanning electron microscopy (SEM), with or without energy dispersive X-ray (EDX) analysis, Fourier transform infrared spectroscopy (FTIR) and powder X-ray diffraction (PXRD) were utilized to study the solid-state phase behavior and/or drug enrichment on the partially dissolved ASD tablet surfaces. Nanoparticle tracking analysis (NTA) was utilized to study the solution-state phase behavior. It was found that, contrary to expectations, ASDs with drug-polymer hydrogen bonding exhibited poorer initial release at moderate drug loadings (15-25%) as compared to the non-hydrogen bonding analog ASDs. Surface crystallization led to deterioration of dissolution performance. Lastly, T_g relative to experimental temperature also appeared to play a role in the observed dissolution behavior as a function of drug loading. These findings shed light on potential

mechanisms governing ASD dissolution performance and will aid in the development of optimized ASD formulations with enhanced dissolution performance.

4.2 Introduction

With advancements in high throughput screening assays, combinatorial chemistry, and target-based drug design, an increasing number of new chemical entities emerging from drug discovery pipelines are poorly water-soluble. Consequently, solubility enhancing formulations are often required to achieve the desired *in vivo* bioavailability.[2] Amorphous solid dispersions (ASDs), where the drug is molecularly dispersed in a polymeric matrix, are one of the most promising solubility enhancement strategies with several commercial products employing this approach.[112] However, the solubility and dissolution advantage accompanying ASDs is accompanied by certain risk factors, including drug crystallization and/or amorphous-amorphous phase separation (AAPS). Crystallization in the matrix, or from the supersaturated solution generated during dissolution, can reduce the amorphous solubility advantage.[18, 139, 140] AAPS is a likely precursor to matrix crystallization and may also impact ASD dissolution.[119, 140, 141]

The solid-state stability of ASDs has been an active topic of research for over two decades with reports of highly stable ASDs having "extraordinary" shelf lives providing evidence of the successful mitigation of crystallization risk through formulation with an appropriate polymer.[142, 143] However, drug release from ASDs is still poorly understood. It has been suggested that drug release from ASDs is polymer-controlled at low drug loadings, whereby both drug and polymer release at the same rate (congruently).[9, 118, 137] In contrast, when a higher drug loading is reached, which varies for different drug-polymer combinations, an abrupt decrease in drug release rate is observed, explained by a switch to drug-controlled release, whereby release of drug and polymer is incongruent.[136, 137, 141] It is intuitive that some interplay of drug and polymer properties plays an important role in this switch from polymer-controlled (congruent) to drug-controlled (incongruent) release as a function of drug loading. Unfortunately, the precise nature of this interplay and the associated factors have not been deciphered to date, hindering rational formulation design for optimized release.

The current study was designed to better understand how the drug properties impact the switch from congruent to incongruent release as a function of drug loading. The change in release mechanism and the drug loading at which it occurs is important. First, polymer-controlled release at low drug loadings typically results in drug concentrations higher than amorphous solubility, and as a result, liquid-liquid phase separation (LLPS) occurs.[63, 141] The drug-rich nanosized aggregates generated upon LLPS are thought to enhance *in vivo* drug absorption.[65, 66 144] Second, it is desirable to increase the drug loading in ASDs without compromising dissolution kinetics in order to minimize the pill burden; large oral solid dosage forms are undesirable for patients.

Previously, we studied the impact of drug log P on the limit of congruency (LoC, the highest drug loading at which drug and polymer release congruently[136]) for poly(vinylpyrrolidone-co-vinyl acetate) (PVPVA)-based ASDs. Somewhat counterintuitively, we found that the limit of congruency was the same for the two model compounds despite substantially different log P values.[141] Herein, we extend our studies to evaluate the impact of drug-polymer hydrogen bonding interactions on the limit of congruency. Drug-polymer hydrogen bonding interactions are generally considered advantageous to ASD physical stability.[61, 145, 146] However, the role of drug-polymer hydrogen bonding on drug release is poorly understood. PVPVA, also known as copovidone, was used as the model polymer. This polymer, which is widely used in marketed ASD formulations, is relatively hydrophilic and contains a strong hydrogen bond acceptor group, but no donors (Figure 4.1). Indomethacin (IND) and indomethacin methyl ester (INDester) were selected as model drugs, due to their differing hydrogen-bonding ability with PVPVA. The carboxylic acid group of IND can hydrogen bond with the vinylpyrrolidone carbonyl of PVPVA.[46, 147] However, the INDester lacks hydrogen bond donors and therefore cannot form specific interactions with the polymer. The primary hypothesis under evaluation was that drug-polymer hydrogen bonding interactions would be favorable in promoting drug release, leading to a higher limit of congruency for IND-PVPVA dispersions relative to those with INDester. Different drug loading ASDs were prepared, and surface area normalized dissolution was performed to monitor both drug and polymer release rates. Surface phase behavior and chemistry of partially dissolved ASD tablets were studied using different surface characterization techniques. Solution-state phase behavior, specifically, the formation of drug-rich nanosized aggregates, was monitored using nanoparticle tracking analysis (NTA).
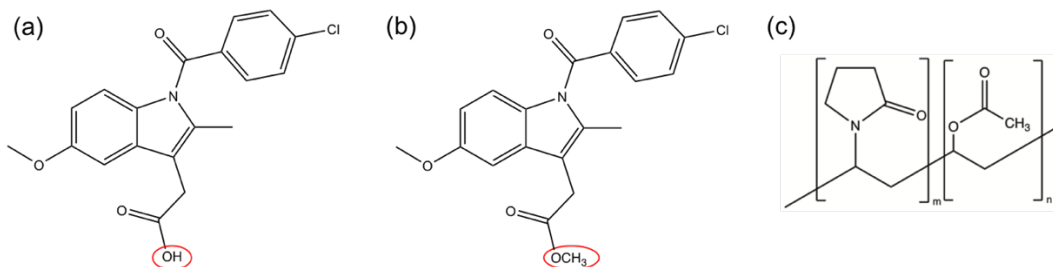
Figure 4.1 Structures of the model drugs and polymer used. Indomethacin (IND) (a), indomethacin methyl ester (INDester) (b), and poly(vinylpyrrolidone-co-vinyl acetate) (PVPVA) (c). Red circles highlight the difference in the structures of IND and INDester.

4.3   Materials

IND was purchased from ChemShuttle (Jiangsu, China). INDester was synthesized by substituting the carboxyl hydroxyl of IND by a methoxy (OCH$_3$) group as per the synthetic procedure described in the Appendix C, section C1. PVPVA (Kollidon VA 64) was supplied by the BASF Corporation (Ludwigshafen, Germany). Hydroxypropyl methylcellulose 606 (HPMC-606) was a gift from Shin-Etsu Chemical Co. (Tokyo, Japan). The medium for all solubility and dissolution studies of IND consisted of pH 2.1 100 mM phosphate buffer (so that IND remains in its un-ionized form), prepared by dissolving 7.8 g of sodium dihydrogen phosphate dihydrate and 3.4 mL of phosphoric acid (85%) to make up the volume to 1L in de-ionized water. The medium for all solubility and dissolution studies of INDester consisted of 100 mM, pH 6.8 phosphate buffer (to avoid hydrolysis of the ester), prepared by dissolving 6.96 g sodium phosphate dibasic anhydrous and 7.04 g of monosodium phosphate monohydrate in 1L of de-ionized water. Additionally, HPMC-606 was added into the medium up to a concentration of 200 µg/mL and 1000 µg/mL for all IND and INDester solubility and dissolution studies, respectively, to prevent crystallization for the duration of the experiment (a higher HPMC-606 concentration was utilized for INDester since it is a relatively fast crystallizer in comparison to IND).

4.4 Methods

4.4.1 Physicochemical properties of indomethacin (IND) and indomethacin methyl ester (INDester)

The physicochemical properties of indomethacin (IND) and indomethacin methyl ester (INDester) were measured as per the procedures mentioned in Appendix C, section C2, unless otherwise referenced to a literature source.

4.4.2 Crystalline and amorphous solubility determination

Crystalline solubility determination

The crystalline solubility of IND and INDester was determined in pH 2.1 and pH 6.8 phosphate buffer, respectively. Briefly, an excess amount of each drug was stirred in buffer at 37°C for 48 h. Then, the excess solid was separated from the solution by ultracentrifugation at 35 000 rpm for 30 min at 37 °C in an OptimaL-100 XP centrifuge (Beckman Coulter, Inc., Brea CA) equipped with a swinging-bucket rotor SW 41Ti. The concentration of the supernatant was determined by reverse-phase high performance liquid chromatography (RP-HPLC) system (Agilent Technologies, Santa Clara, CA) after appropriate dilution. Samples were analyzed in triplicate. For IND, a mobile phase of 50% acetonitrile and 50% acidified water (pH was adjusted to 2.0 by phosphoric acid) (v/v) at a flow rate of 1mL/min and ultraviolet (UV) detection wavelength of 254 nm was used. The separation column used was the Ascentis Express C18 column (15cm × 4.6 mm, 5 μm particle size). For INDester, a mobile phase of 50% acetonitrile and 50% water (v/v) at a flow rate of 1.25 mL/min was used, and the rest of the parameters were the same as above. The crystalline solubilities for IND and INDester were determined in the presence of 200 μg/mL and 1000 μg/mL of HPMC-606.

Amorphous solubility determination

For IND, a supersaturated solution was generated by adding 50 μL of 20 mg/mL of methanolic stock solution to 15 mL of pH 2.1 phosphate buffer (pre-equilibrated at 37°C) containing 200 μg/mL of HPMC-606. For INDester, 50 μL of 10 mg/mL of a methanolic stock solution was added to 15 mL of pH 6.8 buffer containing 1000 μg/mL of HPMC-606. The amorphous solubility was determined as the supernatant concentration obtained after the pelleting of amorphous drug-rich

aggregates by ultracentrifugation at 35 000 rpm in an OptimaL-100 XP centrifuge (Beckman Coulter, Inc., Brea CA) equipped with a swinging-bucket rotor SW 41Ti for 30 min at 37°C. The concentration of the supernatant was analyzed using the aforementioned HPLC methods.

4.4.3   Preparation of bulk ASDs by rotary evaporation

IND:PVPVA and INDester:PVPVA ASDs were prepared at 5%, 10%, 15%, 20% and 25% (w/w) drug loadings (DLs). A 1:1 v/v mixture of dichloromethane and methanol was used to dissolve solids for the preparation of IND ASDs, while tetrahydrofuran (THF) was used to prepare INDester ASDs, at a solid content of 50 mg/mL. The solvent was removed using a Buchi Rotavapor-R (Newcastle, Delaware) equipped with Yamato BM-200 water bath at 45 °C. The resultant ASD powders were kept under vacuum at room temperature overnight, cryo-milled and sieved (desired particle size of 106-250 μm). All ASDs were confirmed to be crystal-free by powder X-ray diffraction (PXRD) and polarized light microscopy (PLM).

4.4.4   Surface normalized dissolution of IND and INDester ASD tablets

Surface normalized dissolution of IND-PVPVA and INDester-PVPVA ASD tablets was carried out using a rotating-disk intrinsic dissolution rate apparatus (Agilent Technologies, Santa Clara, CA) to maintain a constant surface area throughout the release experiment and to minimize particle size and shape effects. Dissolution was carried out under non-sink conditions with respect to amorphous solubility, and a dissolution temperature of 37 °C was maintained unless otherwise specified. Briefly, 100 mg of the bulk ASD powder, milled and sieved to the desired particle size (106-250 μm), was compressed in an 8 mm tablet die (corresponding surface area of 0.5 cm^2) using a Carver press at a pressure of 1500 psi and held for a minute. After compression, the tablet die was coupled to a spindle rotating at 100 rpm with the exposed surface of the tablet matrix immersed into 100 mL of dissolution medium in a water-jacketed beaker maintained at 37 °C. The dissolution medium for IND-PVPVA ASD tablets was 100 mM pH 2.1 phosphate buffer, and for INDester-PVPVA ASD tablets, the dissolution medium was 100 mM pH 6.8 phosphate buffer. Two mL was removed at 1 min intervals from the dissolution medium for up to 5 min and replaced with fresh buffer. Then, 100 μL was used for drug analysis using HPLC, and the remaining sample was used for polymer analysis using the previously described HPLC-size exclusion

chromatography (SEC) method.[141] The surface normalized dissolution rate (R) is determined from linear regression analysis of the slope of the cumulative amount of dissolved drug/polymer as a function of time, and dividing the value of the slope times the volume of the dissolution medium, by the exposed surface area of the tablet matrix, and the fraction of the component of interest, as expressed by equation 20.

$$R = \frac{k \times V}{S \times x} \qquad (20.)$$

where k is the slope of the regression line (µg/mL.min), V is the volume of the dissolution medium (100 mL), S is the exposed surface area for tablet dissolution (0.5 cm²), and x is the fraction of each component.

Additionally, to explore the impact of drug glass transition temperature (T_g) on the dissolution performance of ASDs, surface normalized dissolution up to 5 min was also carried out at 10, 17, 25, and 57 °C for IND ASDs. Since the T_g of INDester is ~2°C, experimental constraints (freezing point of water), prevented sub-T_g studies being performed for this system. Dissolution for up to 30 min at 37°C was also performed for both IND and INDester ASDs in order to study the solution phase behavior, wherein the concentration of both drug and polymer was quantified at 5 min intervals. One additional dissolution experiment for the 25% DL INDester ASD was conducted for 60 min at 15°C in order to suppress crystallization and study the dissolution behavior in the absence of crystallization.

4.4.5   X-ray diffraction (XRD)

XRD analysis was performed on tablet surface initially and at the 5 min and 30 min dissolution time points to determine the presence or absence of crystallization. The tablet was loaded onto the glass XRD sample holder with an indented surface, such that the tablet surface of interest is up-facing and level with respect to the sample holder. The data were obtained with Cu K$_\alpha$ radiation using a Rigaku Smartlab diffractometer (Rigaku Americas, Texas) operating at 40 kV and 44 mV. Measurements were performed in the range of 5-40° 2θ with a scan rate of 4° 2θ/min and a step size of 0.02° using Bragg-Brentano mode. Compact surfaces were also examined using a polarized

light microscope (PLM) in reflection mode (Olympus BX-60, Olympus Corporation, Melville, NY) to probe the surface for birefringence.

4.4.6 Nanoparticle tracking analysis (NTA)

One mL of the dissolution medium was withdrawn after 30 min and injected into the flow-through cell stage of a NanoSight LM10 from Malvern Instruments (Westborough, MA) equipped with a 75 mW green laser (532 nm). The flow-through cell stage was maintained at 37 °C. A 20× magnification microscope objective was used to visualize the sample, and a video sequence of 30 s was recorded. The video was analyzed with a nanoparticle tracking analysis software to track the Brownian motion of individual particles, and the average particle size was then determined based on the Stokes-Einstein equation.

4.4.7 Fourier-transform infrared (FTIR) spectroscopy

IR spectra of fresh ASD tablet surfaces and partially dissolved tablet surfaces were collected in attenuated total reflectance (ATR) mode using a Bruker Vertex 70 FT-IR spectrophotometer (Bruker Corporation, MA, USA). To collect spectra from the partially dissolved tablet surface, the die was removed from the dissolution medium, followed by the removal of excess water using compressed air. The tablet was then taken out of the die and placed under a vacuum overnight (exposed surface upside). The scan range was set from 500 to 4000 cm^{-1} with a resolution of 4 cm^{-1}, and 64 scans were averaged. The detector and sample chamber were purged with dry, CO_2-free air to avoid interference from CO_2 and moisture.

4.4.8 Scanning electron microscopy (SEM)/ energy dispersive X-ray (EDX) analysis

SEM images of fresh and vacuum-dried partially dissolved ASD tablet surfaces were taken using a Nova nanoSEM field emission scanning electron microscope (FEI Company, Hillsboro, Oregon). ASD tablets were affixed to aluminum stubs (surface of interest exposed) using double-sided carbon tape and were coated with a platinum layer of 10 nm prior to analysis. For SEM imaging, a working distance of 5 mm was used with a 5 kV accelerating voltage and a 3 nm spot size.

EDX spectra were acquired at 5 kV using an Oxford EDX silicon drift detector (SDD, X-Max^N 80 mm^2) in combination with the AZtec software suite. Prior to EDX measurements, the EDX calibration was performed on pure carbon using carbon tape (Carbon Conductive Tape, Ted Pella Inc., Redding, CA). For EDX calibration and analysis, a spot size of 4 nm and a working distance of 10 mm was used. A total count of 500,000 was accumulated for each EDX spectrum, and a processing time of 6 s was utilized. The deadtime remained below 60%.

4.4.9   Film immersion studies

Preparation of ASD thin films

Thin films of IND:PVPVA and INDester:PVPVA (25% DL) were prepared using a spin coater (Chemat technologies Inc., Northridge, CA). For IND:PVPVA ASD films, the drug and polymer were dissolved in a 1:1 v/v methanol:dichloromethane mixture. For INDester:PVPVA ASD films, drug and polymer were dissolved in THF. The total solid (drug and polymer) concentration was 50 mg/mL. Stock solution (15 µL) was placed on a ZnS substrate (Model: SM-nIR2-Flat-5, Anasys Instruments Inc., SantaBarbara, CA), which was then spun for 6 s at 500 rpm, followed by 30 s at 3000 rpm. Spin coating was performed in a glovebox with a dry air purge at low RH conditions (~18% RH) to prevent water vapor induced phase separation during the preparation stage and obtain miscible ASD films.[19, 148] ASD films were dried under vacuum overnight afterwards to remove residual solvents.

Film immersion

To determine the evolution of morphology of film upon hydration, an IND:PVPVA 25:75 film was immersed in ~5 mL of pH 2.1 buffer and an INDester:PVPVA 25:75 film in ~5 mL of pH 6.8 buffer in a Petri dish for predetermined time intervals, followed by the removal of excess water with compressed air. The samples were further dried overnight inside a vacuum oven at room temperature.

Characterization of films via atomic force microscopy (AFM) coupled with nanoscale thermal analysis (nanoTA) and Lorentz contact resonance (LCR)

A nanoIR2 AFM-IR instrument (Anasys Instruments, Inc., Santa Barbara, CA) was used to study the evolved topographical features on the ASD films following buffer immersion. A Thermalever cantilever probe (Model: EXP-AN2-300, Anasys Instruments, Santa Barbara, CA) was used for topographical imaging. An x and y resolution of 256 points with a scan rate of 0.3 Hz was used. Topographical images were collected using the Analysis Studio software (Anasys Instruments, Inc., Santa Barbara, CA).

Nanoscale thermal analysis (nanoTA) was performed on the desired regions of the sample (based on topographical images). Briefly, the probe is heated linearly with time using a temperature ramp, and the extent of cantilever bending is recorded as the signal. A deflection in the signal is obtained when a thermal event occurs (typically, at the melting or glass transition temperature of the sample), and the sample surface becomes softened, followed by AFM tip penetration into the sample. Prior to data collection, a three-point calibration curve was established using three polymeric calibration standards with sharp melting points, namely, polycaprolactone (55°C), polyethylene (116°C), and poly(ethylene terephthalate) (235°C). A plot between deflection and heating voltage is generated by the software for each of the standards. Thereafter, a calibration curve is established between heating voltage and corresponding known melting points of the standards using a quadratic fit. The calibration curve is then loaded into the software to convert the voltage signal into the temperature for all further sample analyses. Next, the AFM tip is moved to a topographical feature of interest in an already acquired topographical image, and the temperature is ramped to locate the softening point, which, in this study, corresponds to glass transition temperature (T_g) of the feature. The probe was heated at a rate of 5 °C/s.

For collecting Lorentz contact resonance (LCR) spectra on the area of interest, a small LCR drive magnet was placed to generate oscillations in the cantilever. LCR sweeps were then conducted on the desired spots to generate LCR nanomechanical spectra, which are specific to the mechanical stiffness of the sample surface. The spectra were collected between 1 and 1000 kHz at 100 kHz/s scan rate. A drive strength of 50% was used for LCR sweeps.

4.5 Results

4.5.1 Physicochemical properties of indomethacin (IND) and indomethacin methyl ester (INDester)

The physicochemical properties of indomethacin (IND) and indomethacin methyl ester are summarized in Table 4.1.

Table 4.1 Comparison of physicochemical properties of indomethacin (IND) and indomethacin methyl ester (INDester)

Parameter	Indomethacin (IND)	Indomethacin methyl ester (INDester)
Molecular weight (g/mol)	357.8	371.8
pKa	4.5[*]	None
Charge	None at pH 2.1	None
logP	4.07	4.53
Melting temperature (°C)	160.7	91.4
T_g (onset) (°C)	43.5	1.7
Wet T_g (°C)[$]	29	-
Crystallization tendency[#]	Class III	Class II

* Value taken from ref. [149]
# Classification adapted from ref. [150]
$ Wet T_g (T_g of the amorphous drug saturated with water) was determined based on the total water content of the water-saturated amorphous drug estimated from the moisture sorption profile at an isothermal temperature of 37 °C, and assuming that T_g decreases by 10 °C for every 1% water sorbed.[59]
- Wet T_g of INDester could not be determined due to crystallization.

4.5.2 Crystalline and amorphous solubility

The crystalline and amorphous solubilities of IND in 100 mM pH 2.1 phosphate buffer in the presence of 200 µg/mL HPMC-606 were found to be 1.3 and 22.1 µg/mL, respectively (Table 4.2). The crystalline and amorphous solubilities of INDester in 100 mM pH 6.8 phosphate buffer in the presence of 1000 µg/mL HPMC-606 were found to be 0.6 and 3.9 µg/mL, respectively (Table 4.2). The corresponding amorphous:crystalline solubility ratios for IND and INDester were thus determined to be around 17 and 6.5, respectively. Control experiments performed to determine crystalline solubilities for both IND and INDester without pre-dissolved HPMC-606 and up to 1

mg/mL PVPVA (data not shown), indicated that neither polymer, at the concentrations used in this study, affected the equilibrium solubility values.

Table 4.2 Crystalline and amorphous solubility of indomethacin (IND) and indomethacin methyl ester (INDester). Values are given as the mean of 3 samples ± standard deviation.

Indomethacin	solubility (µg/mL)
crystalline	1.3±0.0
amorphous	22.1±0.5
Indomethacin methyl ester	solubility (µg/mL)
crystalline	0.6±0.0
amorphous	3.9±0.3

4.5.3   Surface normalized dissolution rates (initial 5 minutes)

Surface normalized dissolution profiles of drug alone, polymer alone, and drug and polymer from ASD tablets were determined. No crystallization of the dissolving ASD tablet surface was observed by either XRD or PLM for up to 5 min of dissolution for either IND or INDester ASD tablets. Figure 4.2 shows a comparison of surface normalized dissolution rates for both drug and polymer for IND-PVPVA and INDester-PVPVA ASDs and corresponding release versus time profiles are provided in Appendix C (Figure C2). The dissolution rate of amorphous IND alone was measured to be 0.002 mg/min/cm^2, while the dissolution rate of amorphous INDester alone could not be determined since solution concentrations obtained were below the HPLC detection limit. The dissolution rate of PVPVA alone was determined to be ~3.5 mg/min/cm^2, which is around 1700 times faster than that of amorphous IND alone. The surface normalized dissolution rates of drug and polymer from IND-PVPVA ASDs at low drug loadings (≤10% w/w) and INDester-PVPVA ASDs up to 25% (w/w) drug loading (DL) were found to be similar to the neat polymer release rate, indicating polymer-controlled dissolution, and congruent release of drug and polymer. For higher drug loading IND-PVPVA ASDs (≥15% w/w), drug release rates were more similar to the dissolution rate of amorphous IND alone, indicating a drug-controlled release mechanism. The PVPVA release rate from the higher drug loading IND-PVPVA ASDs (≥15% w/w) was found to be reduced, most likely due to the development of a drug-rich interface on the dissolving tablet front, which hinders the polymer release from subsurface regions. Thus, IND-

PVPVA dispersions show a limit of congruency of ~10% while INDester-PVPVA show initial congruent release up to 25% w/w drug.
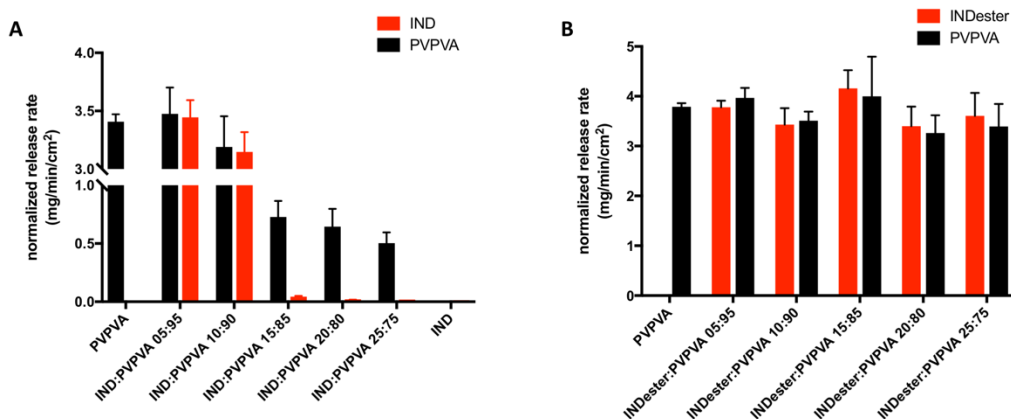
Figure 4.2 Surface normalized dissolution rates for amorphous IND alone, PVPVA alone and when incorporated into an ASD (A). Surface normalized dissolution rates for PVPVA alone and INDester and PVPVA when incorporated into an ASD (B). The ratios in the legend represent drug:polymer weight ratios in the ASDs. Errors bars represent standard deviations, n=3.

4.5.4 Surface normalized dissolution rates (extended times)

Because exceeding the amorphous solubility of the drug during dissolution, with the subsequent occurrence of LLPS, is a desirable dissolution outcome for ASDs, longer dissolution experiments (up to 30 min) were performed. Figures 4.3 and 4.4 show the release versus time profiles for both drug and polymer as well as representative frames from NTA videos acquired on solutions obtained after ASD tablet dissolution. The presence of scattering centers in the NTA images suggests that drug-rich nanosized aggregates formed during dissolution. Notably, congruently releasing low drug loading IND-PVPVA ASDs (5% and 10% w/w drug loadings) exceeded the amorphous solubility of the drug, leading to the appearance of scattering centers, while drug concentrations for higher drug loading IND-PVPVA ASDs (≥15% w/w) remained below the amorphous solubility. Similarly, all congruently releasing INDester-PVPVA ASDs led to solution concentrations exceeding the amorphous solubility, with the occurrence of LLPS. However, congruency of drug and polymer was lost at a later time point for INDester dispersions with drug loadings >5%. Drug release ceased, and the polymer release rate was reduced when this occurred. The change in the release behavior was attributed to drug crystallization at the compact surface, as supported by XRD analysis and PLM imaging of the partially dissolved tablet surface (Figure C3).

To investigate further, an additional dissolution experiment was performed at 15 °C with the 25% DL INDester-PVPVA ASD, with the goal of suppressing drug crystallization. This system showed congruent release of drug and polymer over the 60 min period of the experiment (Figure C4). None of the IND-PVPVA ASDs showed any signs of crystallization up to 30 min of dissolution (Figure C5). Visual observation of samples (Figure C6) also indicated that the solutions obtained from the dissolution of congruently releasing ASDs were turbid. It should be noted that no birefringence was observed, suggesting that the turbidity is due to LLPS rather than solution crystallization. The size of the nanosized drug-rich aggregates formed upon dissolution, as determined by NTA, was in the range of 250-350 nm.
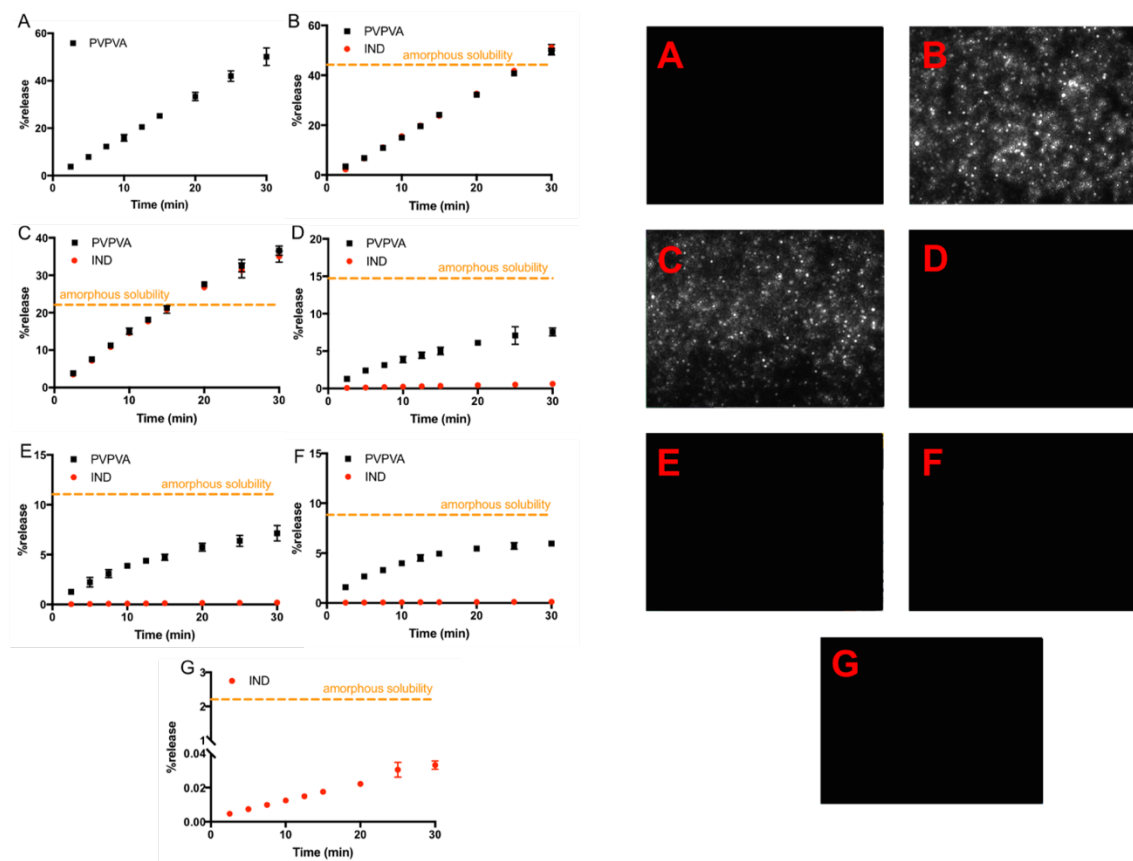
Figure 4.3 Percent release versus time profile (left) and NTA scattering images of solutions obtained after dissolution (right) of PVPVA alone (A) and amorphous IND alone (G) and when incorporated into an ASD (IND:PVPVA 05:95 (B), IND:PVPVA 10:90 (C), IND:PVPVA 15:85 (D), IND:PVPVA 20:80 (E), IND:PVPVA 25:75 (F)). The ratios represent drug:polymer weight ratios. Error bars represent standard deviations, n=3.
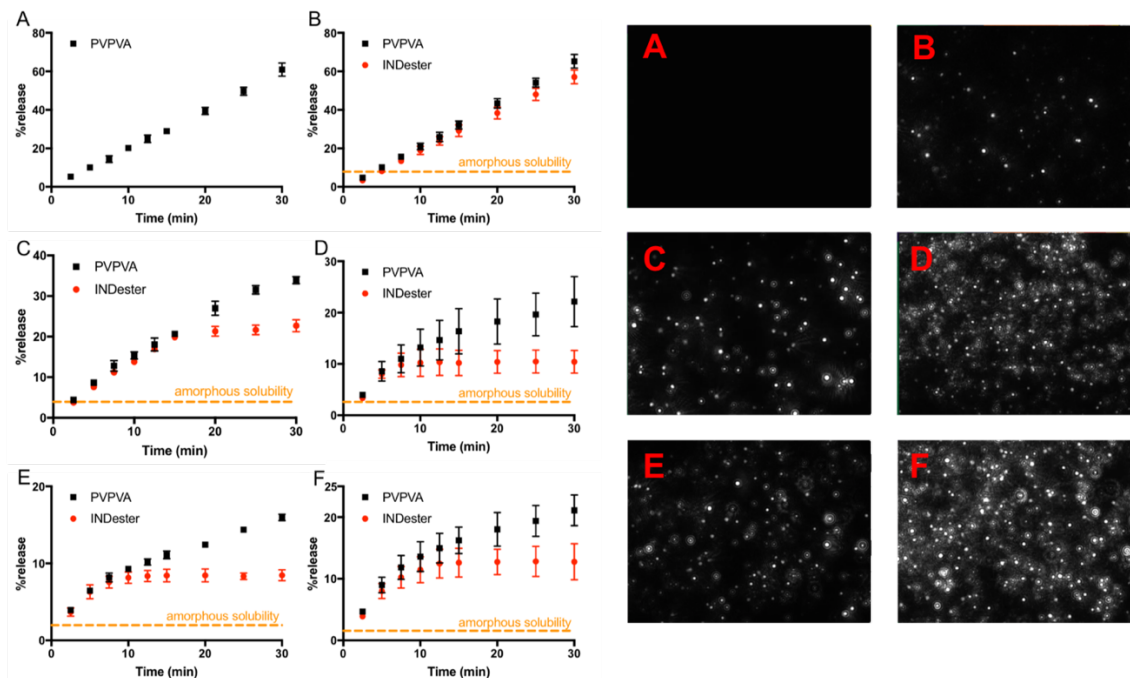
Figure 4.4 Percent release versus time profile (left) and NTA scattering images of solutions obtained after dissolution (right) of PVPVA alone (A) and INDester and PVPVA incorporated into an ASD (INDester:PVPVA 05:95 (B), INDester:PVPVA 10:90 (C), INDester:PVPVA 15:85 (D), INDester:PVPVA 20:80 (E), INDester:PVPVA 25:75 (F)). The ratios represent drug:polymer weight ratios. Error bars represent standard deviations, n=3.

4.5.5 FTIR spectroscopy

Attenuated total reflectance-FTIR (ATR-FTIR) spectroscopy was used to characterize the presence and extent of drug-polymer hydrogen bonding interaction between drug and polymer before and after dissolution and to potentially determine the occurrence of matrix crystallization (if present). It can be seen from Figure 4.1 that IND contains a carboxylic acid group, a potential H-bond donor, while PVPVA contains carbonyl groups, potential H-bond acceptors; hence, IND and PVPVA can interact with each other through H-bonding. In contrast, a similar H-bonding interaction is not possible between INDester and PVPVA due to the absence of a donor hydrogen group.

The reference normalized IR spectra of pure amorphous IND and PVPVA are shown in Figure 4.5A over the specific wavenumber region of interest, i.e., 1500-1850 cm^{-1}. Amorphous IND has three peaks at 1734, 1705 and 1678 cm^{-1} in the carbonyl region, which have been assigned to the free acid carbonyl, acid carbonyl in a cyclic dimer and amide carbonyl, respectively.[46] PVPVA

shows two peaks in the carbonyl region, one at 1730 cm^{-1} belonging to the vinyl acetate (VA) carbonyl and another at 1668 cm^{-1} which belongs to the vinylpyrrolidone (VP) carbonyl. The peak at 1591 cm^{-1} is specific to IND and corresponds to aromatic C-C stretching. The carbonyl region is of specific interest to study the H-bonding interaction between IND and PVPVA as shown in Figure 4.5B. For IND:PVPVA ASDs with drug loadings between 10 and 70%, the peak at 1705 cm^{-1} disappeared, and new peak appeared at 1634 cm^{-1} (previously assigned to hydrogen-bonded PVP carbonyl[46]) with an increase in intensity as a function of drug loading, indicating an increase in the number of H-bonding interactions between IND and PVPVA. The drug-specific peak at 1591 cm^{-1} continuously increased in intensity with an increase in drug loading, and thus is a useful indicator to evaluate potential drug enrichment on the IND-PVPVA ASD tablet surface during dissolution.
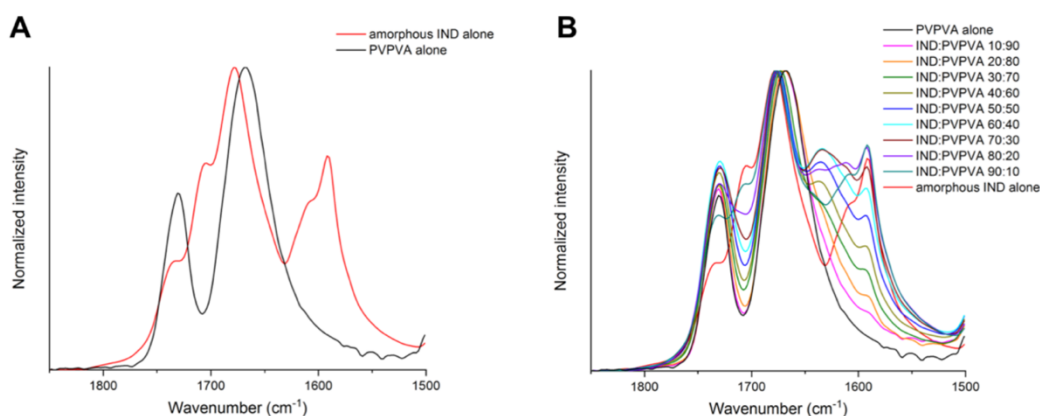
Figure 4.5 Comparison of normalized IR spectra of amorphous IND alone and PVPVA alone (A). Normalized IR spectra of IND-PVPVA ASD tablets at different drug loadings along with amorphous IND alone and PVPVA alone (B). The ratios in the legend represent drug-polymer weight ratios.

After dissolution, spectral changes were observed for high ($\geq$15%), but not low drug loading ($\leq$10%) ASDs. As can be seen in Figure C7A (Appendix C), for the 10% DL IND:PVPVA ASD, which is a congruently releasing formulation, the IR spectrum before and after dissolution is essentially unchanged. In contrast, the 15% DL ASD (Figure C7B, Appendix C) showed an increase in intensity for peaks at both 1634 and 1591 cm^{-1}, consistent with surface drug enrichment. Changes to these peaks were even more pronounced for the 25% drug loading compacts (Figure 4.6). Successive increases in intensity were observed at both 1634 and 1591 cm^{-1}, indicative of drug enrichment as a function of time, which in turn leads to an increase in the proportion of

polymer carbonyl groups that interact with the drug. Since the dimer peak at 1705 cm^{-1}, which is characteristic of drug-drug interactions, was absent in all spectra, it is reasonable to assume that the ASD becomes concentrated in drug at the surface, but that some polymer is still present. This is also supported by the presence of the hydrogen-bonded polymer carbonyl peak at 1634 cm^{-1}. The surface composition following partial dissolution was estimated using a curve fitting approach (Figure C8, Appendix C), using the spectra in Figure 4.5B as the reference systems, with results summarized in Table 4.3.
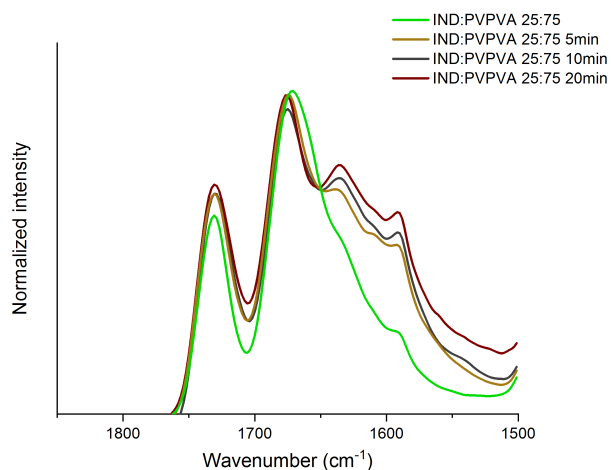
Figure 4.6 Normalized IR spectra of IND-PVPVA 25:75 ASD tablet surface before dissolution and at successive time points after dissolution (5, 10, and 20 min time points).

Table 4.3 Estimated composition of the partially dissolved tablet surface of IND:PVPVA 25:75 ASD following dissolution for 5, 10, or 20 min.

Time (min)	Estimated drug percentage at tablet surface (%)
5	~40-50
10	~50
20	~60

The INDester:PVPVA ASDs show no evidence of drug-polymer hydrogen bonding, with no changes to the PVP carbonyl region (Figure C9, Appendix C). Given that spectral differences exist between crystalline and amorphous INDester (Figure C9, Appendix C), the IR spectra can also be used to confirm crystallization at the compact surface during dissolution. The crystalline form has a characteristic absorption band at 1607 cm^{-1}. No discernable differences in spectra were

found between 0 and 5 min dissolution (Figure C10, Appendix C). However, after 20 min, a characteristic band at 1607 cm^{-1} was observed (Figure C10, Appendix C), consistent with drug crystallization, in good agreement with PXRD observations.

4.5.6 SEM/EDX analysis

SEM images of freshly prepared tablet surfaces for both IND and INDester ASDs had smooth surface topography (data not shown). For IND ASDs (Figure 4.7), the surface topography that evolved after dissolution remained smooth for congruently releasing formulation (10% DL) but became rough for incongruently releasing formulation (15% DL), presumably due to faster polymer release, resulting in a drug-rich porous interface on the dissolving tablet surface, a phenomenon previously observed for other compounds.[141] A similar rough tablet surface evolved for 25% DL, at the 5 min time point.

IND:PVPVA 10:90   IND:PVPVA 15:85   IND:PVPVA 25:75
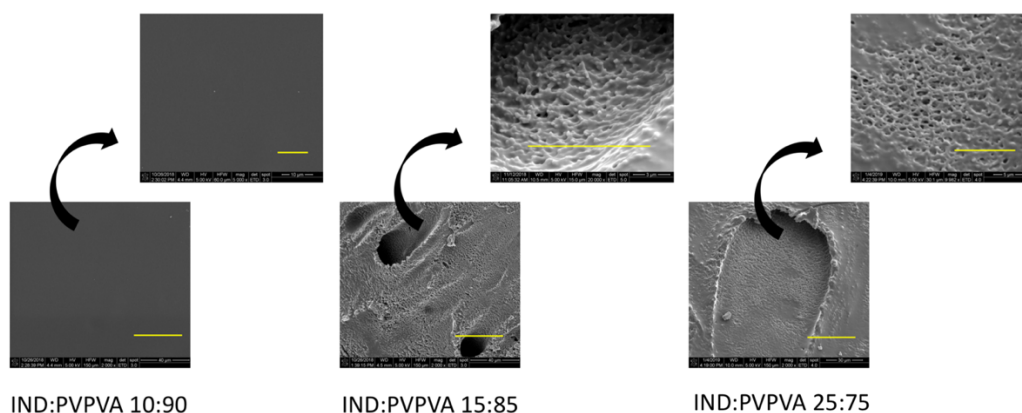
Figure 4.7 SEM images of dissolving tablet surface (5 min time point) for IND:PVPVA 10:90, IND:PVPVA 15:85 and IND:PVPVA 25:75 ASD tablets at low magnification (2000X, lower panel, scale bar is 40 μm) and at high magnification (10000-20000X, upper panel, scale bar is 10 μm). The ratios in the legend represent drug-polymer weight ratios.

To investigate the drug-polymer composition of the partially dissolved IND:PVPVA 25:75 ASD tablet surface, EDX spectroscopy was employed, and the chlorine: nitrogen atomic ratio was calculated. The molecular formula of IND is $C_{19}H_{16}ClNO_4$; thus, the Cl/N atomic ratio is 1, while PVPVA is a copolymer of N-vinyl-2-pyrrolidone and vinyl acetate with a molecular formula of $C_{10}H_{15}NO_3$ for the two monomers, and thus, Cl/N atomic ratio is 0. Since, there is single atom of both Cl and N in a drug molecule and one N atom per copolymer unit of PVPVA, the percent Cl/N

atomic ratio should be proportional to the mole percent of drug in the ASD as per equation 21. This can then be converted to the weight percent of drug using the drug MW and the MW of an idealized monomer of the polymer.

$$\% \frac{Cl}{N} \, atomic \, ratio \propto \left(\frac{number \, of \, moles \, of \, drug}{number \, of \, moles \, of \, drug + number \, of \, moles \, of \, polymer} \right) \times 100 \quad (21.)$$
$$= mole\% \, of \, drug \, in \, ASD$$

The % Cl/N atomic ratio was experimentally determined on ASDs of known composition (10, 30, 50, 70, and 90 wt. % drug loading) and a linear relationship was established between % Cl/N atomic ratio and mole % drug (Appendix C, section C3). Using this calibration curve, the surface composition of partially dissolved IND:PVPVA 25:75 ASD tablet surfaces after 5, 10, and 20 min of dissolution was estimated with results shown in Table 4.4.

Table 4.4 Experimentally determined % Cl/N atomic ratio and corresponding estimated % DL (by weight) of IND-PVPVA 25:75 ASD tablets before dissolution and at successive dissolution time points of 5, 10, and 20 min.[*]

Dissolution time point (min)	% Cl/N atomic ratio	wt. % drug loading
0 (initial tablet)	17±1	25±2
5	29±2	41±3
10	42±11	55±11
20	60±11	72±9

[*]Values are given as the mean of 3 samples ± standard deviation.

The INDester:PVPVA (25% DL) tablet showed smooth topography at the end of 5 min of dissolution as shown in Figure 4.8A, consistent with the initial congruent release of drug and polymer. At later time points, surface crystallization was observed as early as 10 min after dissolution as shown in Figure 4.8B, and by 20 min the surface was extensively covered with crystals (Figure 4.8C).
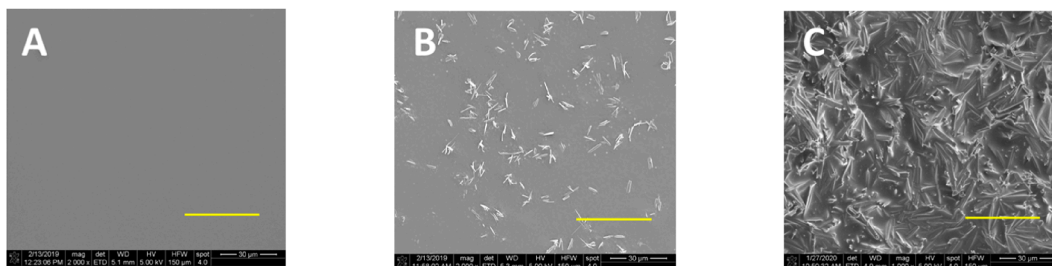
Figure 4.8 SEM images of dissolving tablet surface for INDester:PVPVA 25:75 ASD at the 5 min time point (A), 10 min time point (B) and 20 min time point (C). Images A and B are taken at 2000× magnification, and the image C is taken at 1000× magnification. The scale bar is 40 μm.

4.5.7   Film immersion studies

Visual observation

Miscible films of 25% DL ASDs were prepared by spin coating and immersed in pH 2.1 (IND) and pH 6.8 (INDester) buffer solutions. Representative images for initial, 2 s, 15 s, 1 min, 2 min, 5 min, 10 min, and 20 min time points are presented in Appendix C, Figure C12. No visual changes were observed for the IND:PVPVA 25:75 film (Appendix C, Figure C12A). For the INDester:PVPVA 25:75 ASD film, clear evidence of a cloudy solution developing around the films can be observed (Appendix C, Figure C12B). This observation of cloudiness is consistent with the generation of supersaturated drug solution in the vicinity of the ASD film and the presence of small scattering species in solution, as observed using NTA (Figure 4.4).

Topographical imaging

The AFM height images for IND:PVPVA and INDester:PVPVA ASD films (25% DL) after buffer immersion and drying were acquired. Uneven dissolution of IND:PVPVA ASD films is quite evident from the rough topographies of films which evolve as early as 2 sec (Figure 4.9). With time, the roughness of the film increased and the height features became larger, from 15 nm at 2 sec to about 150 nm at 20 min. The topography evolution can be explained by the faster polymer release, leaving behind an uneven drug-rich phase. In contrast, INDester:PVPVA ASD films (25% DL) showed smooth surfaces with few topographical features for up to 2 minutes of immersion (Appendix C, Figure C13) consistent with congruent drug and polymer release. Beyond this time, the film had dissolved completely (Appendix C, section C4).

127
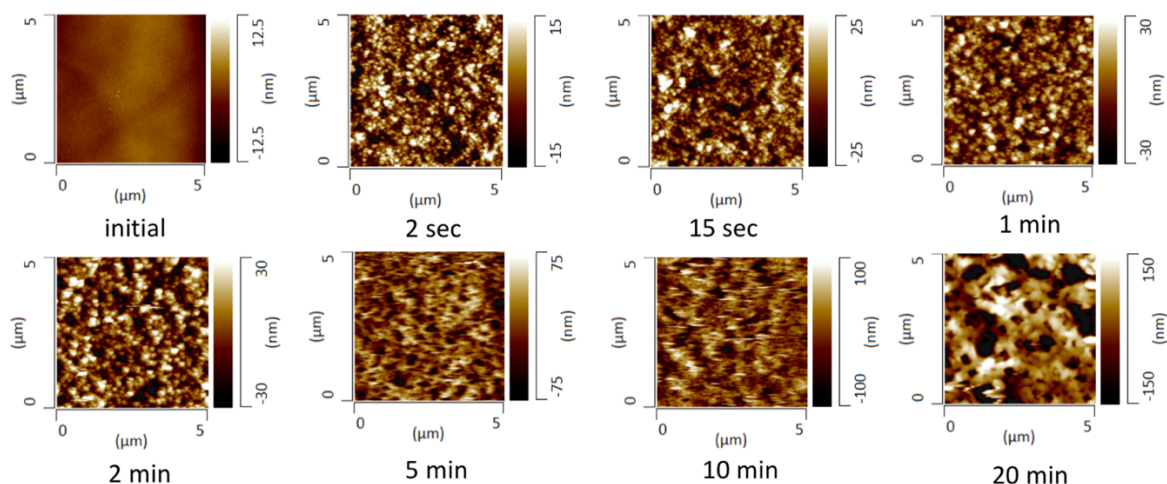
Figure 4.9 AFM topographical images of spin coated films of IND:PVPVA 25:75 ASD after buffer immersion for different time intervals.

Nanoscale thermal analysis (nano-TA)

To quantify drug and polymer composition of remnants of IND:PVPVA 25:75 ASD film at various timepoints after buffer immersion, a calibration curve for T_g as a function of drug loading was obtained. Specifically, T_gs of homogeneous films of IND alone, PVPVA alone and miscible ASDs at five different drug loadings were measured and fitted to the Gordon-Taylor equation (Figure C15 of Appendix C, equation 22):

$$T_{g,mix} = \frac{w_1 T_{g1} + k w_2 T_{g2}}{w_1 + k w_2} \tag{22.}$$

where $T_{g,mix}$ is the glass transition of the homogeneous film, w_1 and T_{g1} are the weight fraction and glass transition temperature of IND, w_2 and T_{g2} are the weight fraction and glass transition temperature of PVPVA. The T_gs of drug alone (T_{g1}) and polymer alone (T_{g2}) film were determined to be 53 and 130 °C by nanoTA, respectively. It should to be noted that the T_g values obtained from nanoTA for amorphous IND and PVPVA are comparatively higher than the reported calorimetric values,[46, 145, 151] likely due to differences in the measurement techniques. As expected, the T_gs of the homogeneous films increased as the polymer loading increased. The value of k, the fitting parameter in the Gordon-Taylor equation was determined to be 0.91, by partial least squares regression fitting of the experimentally determined T_gs of the homogeneous films.

Subsequently, the drug loading of the remnants of IND:PVPVA 25:75 ASD films were calculated based on the Gordon Taylor equation from T_g values determined experimentally using nanoTA. The T_g decreased after buffer immersion (Figure 4.10A), with sequential decreases seen with increasing immersion time (Figure 4.10B). The decreasing trend in the average T_g as a function of immersion time is consistent with drug enrichment, with estimates of the increase in drug loading given in Table 4.5.
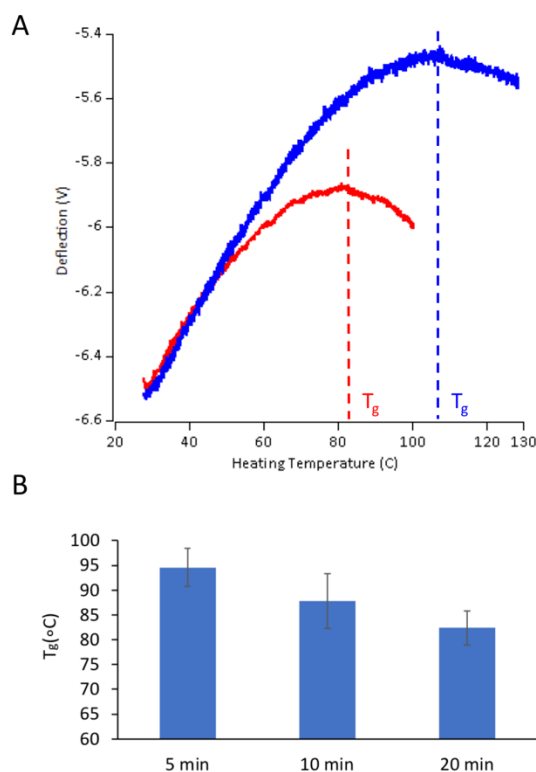
Figure 4.10 Representative nanoTA thermograms showing the local glass transition temperatures. The blue curve is from the freshly prepared IND:PVPVA 25:75 ASD film and the red curve is from the film remnants after 20 min of dissolution (A). Mean local glass transition temperatures of remnants of IND:PVPVA 25:75 ASD film at different time points after buffer immersion followed by film drying. Error bars represent standard deviations, n=3 (B).

Table 4.5 Experimentally determined local glass transition temperatures (mean ± standard deviation, n=3) using nanoTA for IND:PVPVA 25:75 ASD film initially and at different time points after buffer immersion followed by film drying and corresponding % DL (by weight) estimated using the Gordon-Taylor equation.

Dissolution time point (min)	Local T_g (°C)	Wt. % DL
0 (initial tablet)	111± 6	23 ± 7
5	95 ± 4	44 ± 5
10	88 ± 6	52 ± 7
20	82 ± 3	60 ± 5

4.5.8 Surface normalized dissolution rates (up to 5 min) 10, 17, 25, and 57 °C

In order to study the impact of dissolution temperature relative to T_g on the dissolution behavior of ASDs, especially in the context of congruent versus incongruent release of drug and polymer as a function of drug loading, the surface normalized dissolution rates of drug and polymer from ASD tablets of IND-PVPVA were additionally determined up to 5 min at dissolution temperatures of 10, 17, 25, and 57 °C to cover temperature ranges both above and below T_g. The wet T_g of neat IND was estimated to be 29 °C, after considering the water content at 37 °C. In addition, we also determined the wet T_g of the estimated drug-enriched composition of the incongruently releasing IND-PVPVA tablets post dissolution (~70% DL) to be 18 °C (Appendix C, section C5). This may be the more relevant T_g to determine since our studies show that when phase separation occurs, the drug-rich phase contains a non-negligible amount of polymer. Hence, at 25, 37, and 57 °C, the water-saturated IND-rich phase is present in the supercooled liquid state, while at 17°C, the drug-rich phase is slightly below the onset of the calorimetrically measured glass transition event and at 10°C, the drug-enriched composition is expected to be glass. The drug loading threshold at which dissolution changes from being congruent to incongruent remained unchanged (LoC~10% DL) at 25 and 57°C relative to 37°C as shown in Figure 4.11. However, at 17°C, the drug loading threshold where the dissolution behavior showed a "falling off the cliff" effect[136] decreased and

130

was found to be 5% DL, i.e. at a lower drug loading than for 37 °C (Figure 4.11). To ensure a glassy state of the drug-enriched composition with respect to the dissolution temperature, we additionally studied the IND:PVPVA 05:95 ASD tablet dissolution at 10°C. Interestingly, the previously (at 17°C) congruently releasing IND-PVPVA 05:95 ASD tablet was found to be incongruent at 10 °C. Thus, the limit of congruency for the IND-PVPVA ASD tablet at 10 °C is <5% DL (Figure 4.11). No matrix crystallization occurred during the experiments as confirmed by XRD and PLM performed on partially dissolved tablets after dissolution.
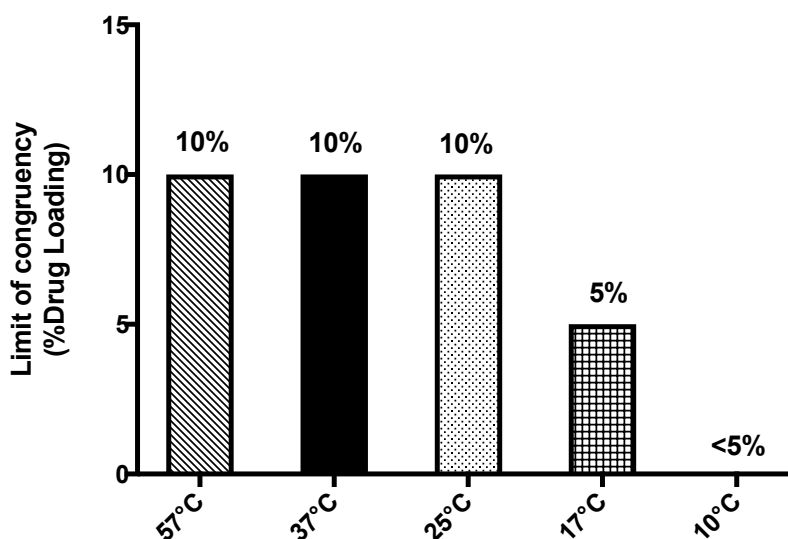
Figure 4.11 Limit of congruency (% drug loading by weight) for IND-PVPVA ASDs at 57, 37, 25, 17, and 10°C.

4.6 Discussion

4.6.1 Mechanisms of incongruent release

Herein, we observe different patterns of drug and polymer release from amorphous solid dispersions of IND-PVPVA and INDester-PVPVA, which are dependent on both compound and drug loading. At low drug loadings, the release of each drug and polymer occurs congruently (i.e., simultaneously) and appears to be controlled by the polymer since the release rate is similar to that of the neat polymer, at least for short time frames, as seen from Figure 4.2. In contrast, for higher drug loads and/or longer time periods, a polymer releases faster than a drug (Figures 4.3 and 4.4). However, the origins of the change in dissolution mechanism are quite different for each compound and subsequently have varying consequences on the release patterns.

131

The INDester-PVPVA dispersion release behavior is relatively straightforward to explain. Initially, the drug is able to release at the same rate as the polymer, for all drug loadings tested (up to 25% DL), but subsequently, crystallization occurs at the solid-liquid interface (for drug loadings > 10%). When crystallization commences, the drug release rate will depend on the interplay between the dissolution rate of the drug from the portion of the surface that remains amorphous and the surface crystal nucleation and growth rates. When the surface becomes covered in crystals, a plateau in solution drug concentration is achieved; this concentration exceeds both the amorphous and crystalline solubility in all cases. Minimal drug release can occur after extensive surface drug crystallization because the solution is supersaturated with respect to the crystalline form at this point, and hence there is no dissolution driving force. The reduction in polymer release can be attributed to the impeding effect of the drug surface layer. It is interesting that the crystallization of the drug at the interface does not result in measurable net desupersaturation over the time frame of the experiment, indicating a low ability of these crystals to grow beyond a certain threshold and consume the ambient supersaturation. Further, it is apparent that crystallization is not triggered by the evolving supersaturation and hence is not occurring from the solution phase. Rather, the polymer is unable to prevent crystallization at the compact interface following hydration. The observed susceptibility to crystallization may arise, in part, due to the low T_g of INDester. Thus, the release is controlled by the chemical composition and solid-state forms present at the compact solid-water interface, which change as a function of dissolution time. Ultimately, there is a competition between drug release, which is quite rapid, since it is controlled by polymer release, and matrix crystallization, which appears to show a dependency on drug loading, being more rapid at higher drug loadings. The phase behavior of IND-ester ASDs is summarized in the schematic, Figure 4.12A. An alternate explanation for the release profiles of the higher drug loading INDester-PVPVA ASDs could be a loss of congruency of drug and polymer at later time points, leading to the insufficient polymer at the interface to inhibit matrix crystallization. However, the congruent release observed when the temperature was lowered and crystallization was prevented (Appendix C, Figure C4), lends support to the mechanism described in Figure 4.12A.

IND-PVPVA ASDs show a quite different pattern of behavior. For these systems, the drug release switches from being fast and polymer-controlled at low drug loadings, to showing almost no release when the drug loading increases by a small increment (from 10 to 15% DL). This "falling off the cliff" effect has been observed for other systems[119, 136, 141] and has been explained by a competition between the kinetics of drug release and amorphous-amorphous phase separation (AAPS) occurring in the matrix. For AAPS, the formation of a drug-rich and a polymer-rich phase would be expected to lead to a more rapid release of the polymer (at least immediately after phase separation), leading to polymer depletion at the interface. Drug release would then be controlled by the properties of the drug-rich phase and slower due to the lower dissolution rate of the amorphous drug relative to that of the polymer (neat polymer dissolves 3 orders of magnitude faster than neat amorphous drug). Further, due to polymer depletion at the interface, mass balance considerations require that the drug becomes correspondingly enriched. This, in turn, leads to the formation of a barrier through which polymer must diffuse, ultimately reducing the polymer release rate. This likely explains why the polymer release is non-linear with time, becoming slower (Figure 4.3). An alternative explanation to AAPS would be differential loss of polymer from the interface, without the occurrence of AAPS as a precursor. However, the change in surface roughness, occurring over a length scale of ~500 nm (Figures 4.7 and 4.9), for incongruently releasing IND-PVPVA ASDs, is more supportive of the phase separation mechanism; systematic loss of polymer from the interface without phase separation would not be anticipated to change surface topography to the extent observed. Figure 4.12B summarizes the proposed changes in the interface composition as a function of dissolution time for IND-PVPVA ASDs at low and high drug loadings. No change in morphology or composition occurs for low drug-loading, congruently releasing ASDs. High drug loading and incongruently releasing ASDs become increasingly surface drug-enriched as a function of time. Compelling evidence for enrichment of drug at the interface is provided by several orthogonal techniques with results summarized in Table 4.6. Although these techniques work by different principles and have varying surface sensitivities (Appendix C, section C6), good agreement about the extent of surface and near-surface drug-enrichment as a function of dissolution time is readily apparent.
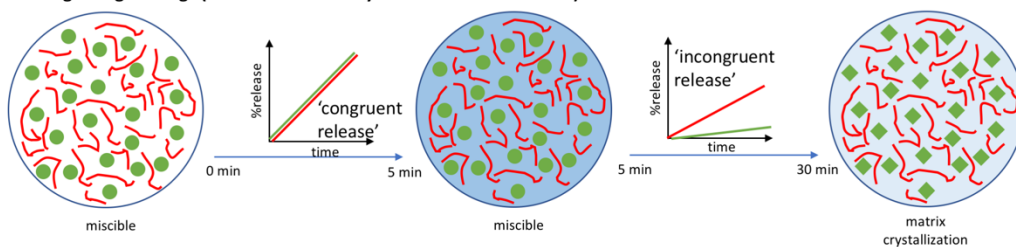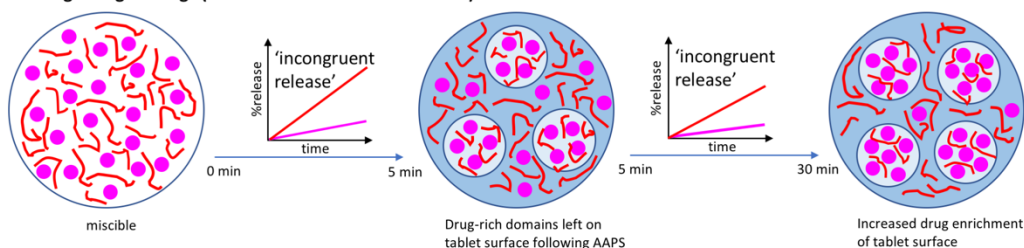
Figure 4.12 A schematic showing change in the composition of the ASD matrix for INDester-PVPVA ASDs (A) and IND-PVPVA ASDs (B) at low and high drug loadings. The different shades of background color (blue) are meant to represent the different extent of hydration within the ASD matrix at different time points or for different phases at a single time point.

There is abundance of literature where crystallization within the ASD matrix has been shown to have deleterious effect on ASD dissolution performance.[66, 140, 152, 153] However, when comparing INDester to IND dispersions, it should be noted that crystallization is actually less detrimental to release than AAPS in this instance, since a higher level of drug release is achieved at a given time point and drug loading for the INDester versus the IND ASDs (Figures 4.3 and 4.4). This highlights the extremely deleterious effects of drug surface enrichment. The large differential in the dissolution rate of the neat amorphous drug and polymer (Figure 4.2A) readily explains why enrichment of the surface with amorphous drug needs to be avoided through appropriate formulation design. The key role of the polymer in driving drug release is also apparent, given that the drug releases at essentially the same rate as the neat polymer dissolution rate for the congruent dissolution regimen.

Table 4.6 A comparison of the surface composition (wt. % drug) estimated using various analytical techniques for the IND:PVPVA 25:75 ASD at different time points of dissolution for ASD tablets and buffer immersion for ASD films.

IND:PVPVA 25:75 dissolution/buffer immersion time point	FTIR (tablets)	EDX analysis (tablets)*	AFM-nanoTA (films)*
5 min	~40-50	41 ± 3	44 ± 5
10 min	~50	55 ± 11	52 ± 7
20 min	~60	72 ± 9	60 ± 5

*Values represent mean ± standard deviation, n=3.

4.6.2 Role of drug-polymer hydrogen bonding interactions

AAPS appears to be the precursor to subsequent incongruent release of drug and polymer for higher drug loading ASDs[119, 136, 141] and literature studies have shown ASDs with stronger drug-polymer hydrogen bonding interactions appear to be more resistant to water-induced AAPS when stored under high humidity conditions.[61, 154] Therefore, we anticipated that the IND-PVPVA ASDs, which are well documented to have extensive drug-polymer hydrogen bonding interactions,[46, 147] would outperform the corresponding INDester ASDs which lack drug-polymer hydrogen bonds. In other words, the hypothesis was that IND ASDs would be more resistant to AAPS during dissolution relative to the INDester ASDs and would show the congruent release of drug and

polymer up to high drug loadings. Analysis of release profiles over short time frames (Figure 4.2) and at lower temperatures (Appendix C, Figure C4) clearly demonstrate that our hypothesis appears to be incorrect, whereby the IND ASDs have a much lower limit of congruency than the INDester dispersions. Thus, the presence of drug-polymer hydrogen bonding interactions in dry IND-PVPVA ASDs did not have a positive impact on the LoC relative to the structural analogue with no hydrogen bonding. To determine if there is a general trend between drug-polymer hydrogen bonding interactions and the LoC boundary, additional compounds with different hydrogen bonding abilities need to be studied.

4.6.3   Impact of glass transition temperature relative to the dissolution temperature

The most discernable difference between the IND and INDester ASDs is the presence or absence of hydrogen bonding, both within the neat amorphous material, and with the polymer. As discussed above, drug-polymer hydrogen bonding does not appear to contribute favorably to the limit of congruency. However, beyond impacting the potential for drug-polymer hydrogen bonding, the replacement of the hydroxyl group with a methoxy group also leads to substantial differences in melting point and T_g between the two compounds (Table 4.1). Given that the T_g is an important characteristic of amorphous systems,[123, 155, 156] it is of interest to consider if the T_g variation between the two compounds contributed to the observed differences in release profiles. The variable temperature dissolution studies on IND-PVPVA dispersions provide some insight. At 17°C (a temperature below the wet T_g of IND), when the mobility of the drug is reduced, the LoC is reduced from 10 to 5% DL. This suggests that there may be some impact of the drug T_g on the LoC, whereby drugs in the glassy state may achieve lower limits of congruency, relative to those in the supercooled liquid state. However, we have to consider that the drug-rich phase contains a considerable amount of polymer (estimated to be around 30% after drug-enrichment at the surface has occurred, Table 4.6), and the wet T_g of this phase (determined as 18°C for the IND-PVPVA 70% DL ASD) may be more relevant. Indeed, the release study at 10°C, a temperature which ensures a glassy state, showed a further reduction in LoC, to <5% DL (Figure 4.11). Thus, plausibly, a T_g effect on the LoC might be better linked to the wet T_g of the drug-rich ASD surface layer (~70% drug in this instance) rather than that of the neat, water-saturated drug T_g. In terms of deconvoluting the effect of temperature on dissolution *per se*, versus the role of T_g, it should be noted that the LoC (~10% DL) did not change as a function of temperature for temperatures above

the wet T_g, spanning a > 30 °C variation (25, 37, and 57°C), and only showed a change when decreasing from 25 to 17°C, transversing the T_g.

In considering the role of T_g, it is worth briefly reviewing polymer dissolution mechanisms. Polymer dissolution in an aqueous medium, involves two transport processes, solvent diffusion into the polymer, and chain disentanglement. The kinetics of the latter process are faster when the polymer is plasticized and in the rubbery state, above T_g. Under these conditions, polymer dissolution is typically accompanied by the formation of a gel layer at the dissolving interface from which the polymer chain disentangles and diffuses into the solution.[157] Below T_g, the gel layer thickness reduces or diminishes, resulting in change of dissolution mechanism from "chain disentanglement" to "cracking", releasing small blocks of the polymer via an eruption process.[158] In the case of ASDs, the "ease" of chain disentanglement, and hence the rate of polymer dissolution is expected to depend on: (1) the amount of water absorbed by the glassy matrix to form the gel layer. This will decrease with an increase in drug loading[159] and may explain the polymer-controlled dissolution at low drug loadings, where substantial amounts of water are absorbed because the hydrophilic polymer is the major component, and (2) the T_g of the hydrated ASD matrix/gel layer relative to the experimental temperature (which may change if the composition of the interface alters with time). By lowering the experimental temperature, the mobility and disentanglement of polymer chains are impeded. This may explain the reduction in the LoC for IND-PVPVA ASDs with decreasing experimental temperatures. A recent study by Que et al. reported the LoC of PVPVA ASDs formed with a high T_g compound, ledipasvir (dry T_g ~ 160°C), to be ~5% DL in agreement with the findings of this study that ASDs with high T_gs relative to the experimental temperature may have a lower LoC.[160] As an alternate hypothesis, a reduction in temperature may simply change the relative kinetics of phase separation at the surface versus the dissolution rate, leading to the observed change in the limit of congruency, although this is not supported by lower temperature studies with INDester-PVPVA ASDs (Appendix C, Figure C4). Clearly, the role of T_g on release properties, if any, needs further investigation.

To put our research findings in perspective with the relevant literature data, here we summarize the limit of congruency reported for various PVPVA ASDs. The LoC is reported as 20% DL for itraconazole[26] (T_g ~ 60°C[34]), 25% DL for ritonavir[136] (T_g ~ 45°C[119]), 10% DL for nilvadipine[141]

($T_g \sim 49°C$[161]), 15% DL for cilnidipine[141] ($T_g \sim 27°C$[122]) and 5% DL for ledipasvir ($T_g \sim 160°C$). It should be noted that most of these drugs have hydrogen-bond donor groups (all with the exception of itraconazole) and dry T_g values that most likely result in the systems being in the supercooled liquid state at 37°C in an aqueous environment (with the exception of ledipasvir). Given preliminary observations of potential impacts of T_g and drug-polymer hydrogen bonding interactions, it is clearly of interest to evaluate a greater diversity of compounds including those with higher T_g values and different hydrogen bonding potential, to better understand the role of these factors.

4.7   Conclusion

Contrary to our initial hypothesis, hydrogen bonding between drug and polymer in PVPVA ASDs appears to be somewhat detrimental to dissolution performance, leading to an incongruent and/or slow release of components at lower drug loadings relative to an ASD that lacks specific drug-polymer interactions. Diminished dissolution performance was accompanied by enrichment of amorphous drug at the ASD surface. Less surprisingly, drug crystallization at the dissolving ASD surface was found to undermine dissolution performance. Thus, two failure mechanisms have been identified: drug enrichment at the surface due to crystallization and incongruent release of drug and polymer, whereby polymer release is faster, leading to a surface drug-rich amorphous phase with a slow dissolution rate. This study thus provides mechanistic insights into the various factors that impact the dissolution of ASDs. Future studies will focus on exploring the generalities of these observations using other drug-polymer combinations, with the ultimate aim of developing strategies to design amorphous solid dispersions with optimal release performance at higher drug loadings.

CHAPTER 5. PATTERNS OF DRUG RELEASE AS A FUNCTION OF DRUG LOADING FROM AMORPHOUS SOLID DISPERSIONS: A COMPARISON OF FIVE DIFFERENT POLYMERS

5.1 Abstract

To reduce the pill burden associated with amorphous solid dispersions (ASDs), which arises from the large quantity of polymer used in the formulation, it is of interest to understand the relationship between drug loading and release properties. The aim of this study was to comprehensively evaluate drug release mechanisms from ASDs with polymers of varying hydrophobicity as a function of drug loading. Surface normalized dissolution rates of drug and polymer were studied for felodipine ASDs with polyvinylpyrrolidone (PVP), polyvinylpyrrolidone/vinyl acetate (PVPVA), Eudragit® S 100 (EUDS), hydroxypropylmethylcellulose (HPMC), and hydroxypropylmethylcellulose acetate succinate (HPMCAS), as a function of drug loading. The moisture sorption profiles and water contact angle measurements suggested the following rank order for hydrophobicity of the different polymers: HPMCAS $\simeq$ EUDS > HPMC > PVPVA > PVP. For ASDs with relatively hydrophilic polymers, viz., PVP, PVPVA and HPMC, dissolution rates were polymer-controlled at low drug loadings ($\leq 15\%$), whereas dissolution rates were controlled by that of the amorphous drug at high drug loadings, with a drastic decline in drug release rates. The sudden decline in the dissolution performance above a certain drug loading, termed the limit of congruency, in case of hydrophilic polymers was attributed to water-induced phase separation. For ASDs with more hydrophobic polymers, namely, HPMCAS and EUDS, the dissolution rate of both drug and polymer remained congruent (i.e., similar) for drug loadings as high as 50%, with a gradual decline in drug release rates at higher drug loadings. Notably, at low drug loadings and across the different polymers, when drug and polymer released congruently, the polymer dictated the drug release rate, such that ASDs prepared with the most hydrophilic polymers showed the fastest drug release rates. This suggested a 'trade-off' in choosing between higher dissolution rates with more hydrophilic polymers at low drug loadings and higher drug loadings achievable with more hydrophobic polymers at the expense of lower dissolution rates. The findings described herein have significant implications for rational selection of polymers for formulation of ASDs with high drug loading and enhanced dissolution performance.

5.2 Introduction

An increasing number of drug candidates in discovery and development pipelines are poorly water soluble. Consequently, there is a pressing need for solubility and dissolution enhancement strategies to formulate these drugs into oral drug products, which are preferable from a patient compliance perspective.[2] Drug amorphization is often an effective approach to temporarily improve the drug solubility relative to the crystalline counterpart.[162] However, amorphous drugs are metastable and tend to crystallize, with a loss of solubility advantage. An amorphous solid dispersion, where the drug is molecularly dispersed in a hydrophilic polymer matrix, can be used to circumvent drug crystallization.[163]

An amorphous drug typically shows a solubility advantage of 2-20 fold[64] over the crystalline form and therefore, an equivalent dissolution rate advantage can be anticipated as per the Noyes-Whitney equation (eq 23).[47]

$$\frac{dC}{dt} = k\ (C_s - C_t) \tag{23.}$$

where dC/dt is the dissolution rate, that is the change in solution concentration (C) with time (t), k is the dissolution rate constant, C_s is the saturation solubility of the solid form (crystalline or amorphous depending on the solid state form used in the dosage form) in the dissolution medium and C_t is the bulk concentration of the solute in the dissolution medium, at time t. Equation 23 also predicts that the maximum solution concentration achievable upon dissolution of the amorphous form of the drug should be equivalent to amorphous solubility at which the passive membrane transport rate of the drug is maximized.[65]

For exceptionally insoluble compounds, which are increasing in prevalence,[64] an increase in dissolution rate of 2-20 fold due to amorphization is likely still insufficient for adequate oral absorption. Fortunately, formulating the drug as an amorphous solid dispersion changes the dissolution behavior, whereby the dissolution rate of each component depends on the composition and interactions as previously described by Higuchi and coworkers.[48, 137] Corrigan presented an extensive review of multicomponent systems and noted potential limitations of Higuchi's

diffusion-controlled dissolution models for non-disintegrating systems with a large relative solubility difference between the components.[9] At high drug loadings, diffusion models are thought to adequately describe the drug release rates, where initially both drug and polymer release independently (polymer faster than the drug), followed by the formation of a drug-rich barrier layer at the dissolution front which then controls the dissolution in accordance with equation 23. At low drug loadings, there is insufficient drug to form an intact drug-rich layer. The drug release is then controlled by the dissolution of the polymer. In other words, at low drug loadings, both drug and polymer release congruently, i.e., at the same rate. In the congruent regimen, the drug dissolution rate $(\frac{dC}{dt})_{drug}$ is dependent on the polymer dissolution rate $(\frac{dC}{dt})_{polymer}$ and the weight fraction of the drug present as shown in equation 24:

$$(\frac{dC}{dt})_{drug} = \frac{(\frac{dC}{dt})_{polymer} \cdot N_{drug}}{N_{polymer}} \qquad (24.)$$

where N is the weight fraction of the component. Since the polymer dissolution rate, in general, is orders of magnitude higher than the drug dissolution rate, a viable formulation strategy for poorly soluble drugs is to formulate ASDs at drug loadings such that the dissolution of drug and polymer is congruent in order to achieve complete and rapid drug release. An additional advantage of polymer-controlled release is that drug concentrations surpassing the amorphous solubility of the drug can be obtained. For concentrations above the amorphous solubility, the solution undergoes liquid-liquid phase separation (LLPS) with the formation of drug-rich nano-sized amorphous aggregates. The drug-rich phase, has been shown to act as an effective drug reservoir, replenishing the dissolved drug to sustain the maximum flux during an *in vitro* membrane transport study.[164] Some *in vivo* studies have also shown bioavailability enhancement due to the presence of amorphous drug-rich nano-aggregates.[66, 165, 166]

Unfortunately, the congruent release mechanism has only been observed for low drug loadings (DLs) (≤25% w/w), with the primary focus of most studies being polyvinylpyrrolidone/vinyl acetate (PVPVA)-based ASDs.[26, 136, 141, 160] The drug loading boundary where the release mechanism switches from congruent to incongruent, with a concomitant steep decline in drug

dissolution rate, has been termed the limit of congruency (LoC). The low LoC, typically seen for PVPVA-based ASDs, poses a major formulation challenge for high dose drugs, and is an impediment to achieving a final dosage form size amenable from a patient compliance perspective. The LoC for PVPVA ASDs is thought to depend on drug properties and drug-polymer interactions, ranging from as low as 5% DL for ledipasvir-PVPVA ASDs to a high of 25% DL for ritonavir-PVPVA ASDs.[136, 160] While PVPVA is one of the most commonly used polymers in commercial ASD formulations,[167] there are other polymers either currently utilized or being investigated for ASD formulations.[168] Drug loading dependent dissolution performance with poor drug release at higher drug loadings also has been observed with other polymers,[117, 119, 169] but no correlation has yet been established between polymer properties and LoC.

The aim of the current study was to probe the mechanism of drug release from ASDs prepared with different polymers as a function of drug loading, and to decipher the role of polymer hydrophobicity on the dissolution mechanism. Different drug loading felodipine (Fel) ASDs were prepared with five diverse polymers, namely, polyvinylpyrrolidone (PVP), PVPVA, Eudragit® S 100 (EUDS), hydroxypropylmethylcellulose (HPMC), and hydroxypropylmethylcellulose acetate succinate (HPMCAS), which cover a range of polymer hydrophobicities and chemistries. Wood's intrinsic dissolution rate (IDR) apparatus was used to minimize surface area variations across different ASD formulations. Both drug and polymer release rates were monitored. Solid-state phase behavior and/or surface chemistry of partially dissolved ASD tablets were studied using microcomputed tomography (microCT) and scanning electron microscopy (SEM) with energy dispersive X-ray analysis (EDX). Fel-polymer ASD films were prepared and Fourier-transform infrared (FTIR) spectroscopy was employed to study drug-polymer interactions; ASD films were also monitored for phase behavior under high RH storage using confocal fluorescence imaging.

5.3 Materials

Felodipine (Fel) and nilvadipine (Nil) were purchased from Chemshuttle (Jiangsu, China). Cilnidipine (Cil) was purchased from Euroasia Chemicals Pvt. Lt. (Mumbai, India). PVPVA 64 was supplied by the BASF Corporation (Ludwigshafen, Germany). PVP (K29/32) was obtained from ISP technologies Inc. (Wayne, NJ). HPMCAS (MF grade) was from SE Tylose USA, Inc. (Totowa, NJ). EUDS was supplied by Evonik Corporation (Piscataway, NJ). HPMC (Methocel™

E5 Premium LV) was from the Dow Chemical Company (Midland, MI). The chemical structures of the model drug and polymers are given in Fig. 5.1. All buffer salts, formic acid (FA), as well as organic solvents (HPLC grade methanol, acetonitrile and dichloromethane), were obtained from Fisher Scientific (Pittsburgh, PA).

A total amount of 7.057 g of monosodium phosphate monohydrate and 6.936 g sodium phosphate dibasic anhydrous was dissolved in water to obtain a final volume of 1L to prepare 100 mM pH 6.8 phosphate buffer. This pH 6.8 buffer was used for all solubility and dissolution studies except for EUDS, for which a pH 7.4 100 mM phosphate buffer was used (EUDS is soluble only above pH 7[170]). The amounts of monosodium phosphate monohydrate and sodium phosphate dibasic anhydrous dissolved in 1 L of water to obtain pH 7.4 buffer were 2.872 g and 11.241 g, respectively.
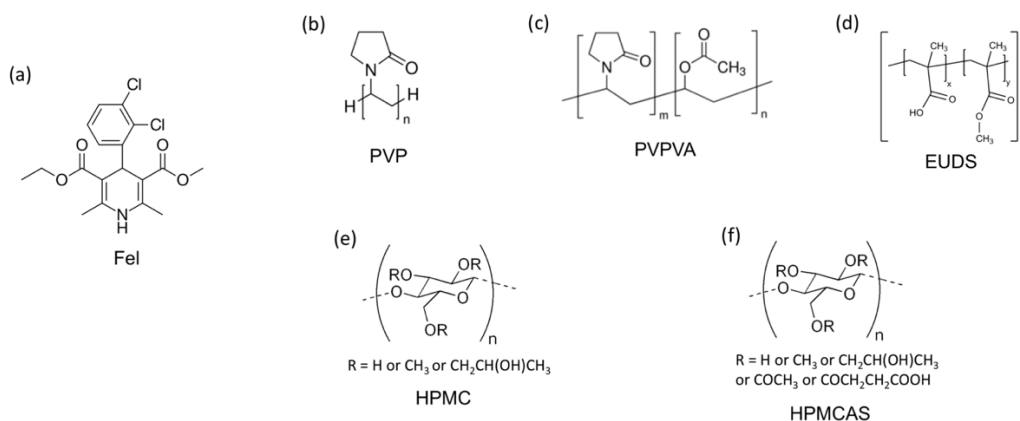
Figure 5.1 Chemical structures of (a) Felodipine (Fel), (b) Polyvinylpyrrolidone (PVP), (c) Polyvinylpyrrolidone/vinyl acetate (PVPVA), (d) Eudragit® S 100 (EUDS), (e) Hydroxypropylmethylcellulose (HPMC) and (f) Hydroxypropylmethylcellulose acetate succinate (HPMCAS).

5.4   Materials

5.4.1   Solubility determination

Crystalline solubility

The crystalline solubility of felodipine was determined in pH 6.8 phosphate buffer in the absence or presence of 1000 μg/mL of each polymer (pH 7.4 phosphate buffer was used for EUDS). An excess amount of drug was added to each solution of interest and the solutions were stirred at 37°C

for 48 h. All samples were prepared in triplicate. Excess solids were separated by ultracentrifugation using a swinging bucket rotor (SW 41Ti) in an Optima L-100XP ultracentrifuge (Beckman Coulter Inc., Brea, CA). Samples were spun at 35000 rpm and 37°C for 30 minutes. The supernatant was analyzed by a reverse phase high performance liquid chromatography (RP-HPLC) system (Agilent Technologies, Santa Clara, CA) after appropriate dilution. A mobile phase of 70% acetonitrile and 30% water (v/v) at a flow rate of 0.5 mL/min with an injection volume of 80 µL and ultraviolet (UV) detection wavelength of 360 nm was used. An Ascentis Express C18 column (15 cm x 4.6 mm, 5µm particle size) was used.

Amorphous solubility

The amorphous solubility of felodipine was determined by ultracentrifugation in the presence of 100 µg/mL of HPMC (to prevent crystallization during the experiment). Briefly, a felodipine methanolic stock solution of 3 mg/mL was added into 15 mL of pH 6.8 phosphate buffer solution. The solution was pre-equilibrated at 37°C and stirred at 300 rpm. The supersaturated solution thus generated was then ultracentrifuged and the supernatant concentration was analyzed using the procedures described above. Experiments were conducted in triplicate.

5.4.2 Water sorption analysis

An SGA-100 symmetrical gravimetric analyzer (TA Instrument, New Castle, DE) was used to measure water sorption profiles of polymers of interest. Briefly, in the initial drying step, a small amount of polymer (~20 mg) was dried at 60°C and 0% RH for 60 minutes. Afterwards, samples were exposed to stepwise increases in relative humidity (RH) starting from 5% up to 95% RH with a step size of 10% RH and a maximum equilibration time of 180 min at an isothermal temperature of 37°C. The equilibrium criterion was less than 0.01% weight change in 5 minutes. Nitrogen was used as the purge gas.

5.4.3 Contact angle measurement

Polymer films were prepared on a quartz slide using spin coating. Briefly, each polymer was dissolved in a 1:1 v/v mixture of methanol and dichloromethane at a solids content of 50 mg/mL. A 100 µL aliquot was taken from each solution and spun onto a quartz slide at 3000 rpm for 60 s

using a KW-4A spin coater (Chemat Technology Inc. Northridge, CA). The resultant polymer thin films were vacuum dried for 24 h before being used for contact angle measurements. The contact angle of each polymer film was measured using the static sessile drop method with a Rame-Hart Model 500 Standard goniometer (Succasunna, NJ). A drop (~ 1.5 µL) of dissolution buffer (pH 6.8 phosphate buffer with the exception of EUDS, where pH 7.4 phosphate buffer was used) was gently dropped on the surface of the polymer film using a 200 µL pipette tip. Once the drop was stabilized on the polymer surface as visualized through an optical camera in conjunction with the DROPimage advanced software, the contact angle was immediately measured. The angle formed between the liquid-solid interface and the liquid-air interface was reported as the contact angle (Appendix D, Figure D1). Contact angle measurements were performed on triplicate films for each polymer.

5.4.4   Preparation of powdered ASDs

Stock solutions of drug, polymer and drug-polymer mixtures were prepared at a total solid content of 50 mg/mL in 1:1 v/v of methanol:dichloromethane. ASDs of different drug loadings (wt. %) were prepared by solvent evaporation using a rotary evaporator (Buchi Rotavapor-R, New Castle, DE) equipped with a water bath set at a temperature of 45 °C. The neat amorphous drug and polymer were also obtained by this method. The resultant ASDs were dried in a vacuum oven overnight. ASD powders were cryo-milled and sieved to obtain a desired particle size of 106-250 µm prior to tableting and dissolution.

5.4.5   Surface normalized dissolution of ASD tablets

Intrinsic dissolution rates (IDR) for neat amorphous drug and polymers, or surface area normalized dissolution rates for drug and polymer from ASDs were determined. The dissolution was carried out under non-sink conditions w.r.t. the drug amorphous solubility using a Wood's IDR measurement apparatus (Agilent Technologies, Santa Clara, CA). Briefly, 100 mg of the sieved ASD powder was tableted in an 8 mm circular intrinsic die (tablet surface area of ~0.5 cm^2) at a compression pressure of 1500 psi held for a minute in a hydraulic press (Carver Inc., Wabash, IN). The die was then mounted on an overhead rotating paddle and immersed into 100 mL of 100 mM pH 6.8 phosphate buffer maintained at 37 °C. A rotation speed of 100 rpm was used. A total of 9

samples were collected with 2 mL of sample collected at each timepoint during the course of a 1 h experiment. The samples were collected at 5 min intervals up to 30 min and every 10 min thereafter. Fresh media was added at each timepoint to replace the volume sampled. Out of the 2 mL sample, 100 μL was used for drug analysis, and was diluted with 100 μL of acetonitrile prior to high performance liquid chromatography (HPLC) analysis. The remaining 1.9 mL of the sample was filtered through a 0.2 μm nylon syringe filter, and the initial 1 mL was discarded. For PVP and PVPVA analysis, 400 μL of the remaining filtrate was diluted with 100 μL of methanol. For EUDS analysis, 0.75 mL of filtrate was diluted with 0.25 mL of acetonitrile. For HPMC and HPMCAS analysis, 0.5 mL of filtrate was diluted with an equivalent volume of methanol.

5.4.6 HPLC analysis of drug and polymer

A 1260 Infinity HPLC system (Agilent, Santa Clara, CA) equipped with a UV detector (G1314F Variable Wavelength Detector, Agilent) and an evaporative light scattering detector (ELSD) (G4260B, Agilent) was used. The RP-HPLC method for felodipine quantification was as discussed above. RP-HPLC methods for nilvadipine and cilnidipine quantification were as described previously.[141]

For PVP and PVPVA quantification, a HPLC-size exclusion chromatography (SEC) method with UV detection was used.[141] The column was an A2500, Aqueous GPC/SEC column (300 x 8.0 mm) (P/N CLM3016, Malvern Panalytical, Worcestershire, UK) and the mobile phase consisted of a 80:20 v/v mixture of pH 7.4 phosphate buffer saline (PBS) solution and methanol. A single PBS tablet (SKU No. P32080-100T, Research Products International, Mt. Prospect, IL) per 100 mL of purified water was dissolved to prepare pH 7.4 PBS solution. A flow rate of 0.5 mL/min, an injection volume of 50 μL and a UV detection wavelength of 205 nm was utilized for the method. Separate calibration curves for PVP and PVPVA were prepared between 5-1000 μg/mL ($r^2 >$ 0.998).

For EUDS analysis, a HPLC-SEC method with UV detection was utilized.[171] The column was a Shodex OHpak SB-804 HQ column (300 x 8.0 mm) maintained at 40°C. A 1:3 v/v mixture of acetonitrile and 30 mM sodium phosphate buffer (pH 8.3) was used as the mobile phase. A flow

rate of 1 mL/min, an injection volume of 50 μL and a UV detection wavelength of 210 nm was utilized for the method. A calibration curve was prepared between 0.5-250 μg/mL ($r^2 > 0.999$).

For HPMC and HPMCAS analysis, HPLC with ELSD detection was used as described previously,[121, 172] with a Shodex RS pak DS-413 polystyrene gel column (150 x 4.6 mm, 3.5 μm particle size). A gradient HPLC method with acidified water (0.1% FA) and acidified acetonitrile (0.1% FA) was utilized. A flow rate of 0.5 mL/min and an injection volume of 80 μL was utilized. ELSD settings included gas flow rate of 1.5 SLM (standard liter per minute), nebulizer and evaporator temperature of 80°C and 85°C, respectively. Separate ELSD standard curves (log scale) were established for HPMC and HPMCAS between polymer concentration and ELSD scattering intensity for the concentration range between 2-250 μg/mL ($r^2 > 0.999$).

5.4.7   Microstructural characterization and/or surface elemental composition analysis of partially dissolved tablets

Microcomputed tomography (micro-CT)

Partially dissolved tablets (10 minute timepoint), after overnight vacuum drying, were examined using a SKYSCAN 1272 high resolution X-ray micro-CT scanner (Bruker, Billerica, MA). An X-ray tube voltage of 60 kV and tube current of 167 μA was utilized; the X-ray beam was filtered through a 0.25 mm aluminum filter. The sample was mounted on a Styrofoam holder on a rotating stage and scanned over 180° with a rotation step of 0.1°. The spatial resolution was 3 μm/pixel. NRECON software (v1.6.9.8, Bruker) was utilized for image reconstruction. Appropriate post processing corrections, namely, beam hardening, ring artifact reduction, misalignment compensation and smoothing were applied. After image reconstruction, individual 2D slices were viewed and documented using *Dataviewer* software (Bruker).

Scanning electron microscopy (SEM)

Initial, as well as partially dissolved, tablet surfaces (10 minute timepoint) were analyzed using an FEI Nova NanoSEM (FEI Company, Hillsboro, Oregan) equipped with an Everhart-Thorney detector. Tablets were placed on SEM aluminum stubs (exposed surface upside) using double

sided carbon tape and sputter-coated with platinum before imaging. Scanning was performed at beam spot size of 5, with 10 mm working distance and at an accelerating voltage of 5 kV.

In order to determine the differences in the elemental composition of tablet surfaces before and after dissolution, energy dispersive X-ray (EDX) analysis was also performed with the aforementioned Nova NanoSEM and an X-Max EDX silicon drift detector (80 mm^2, Oxford Instruments, Abingdon, UK). EDX calibration was performed with carbon as the calibration element using a carbon tape (Ted Pella Inc., Redding, CA) attached to the edge of the sample. Point and ID function was used to calculate elemental composition (atomic %). A total count of 100,000 was accumulated for each EDX spectrum with a processing time of 6 seconds. EDX data were analyzed using AZtec software (Oxford Instruments).

5.4.8 Phase behavior of high-RH exposed ASD films by confocal fluorescence microscopy

ASD films of felodipine with different polymers, containing 0.2 wt. % prodan were exposed to 97% RH for 24 hours. The use of prodan as an environment sensitive fluorescent probe to study the phase behavior of ASDs has been described previously.[18, 19] The expectation is that a hydrophobic probe, such as prodan, will partition into drug-rich phase in the event of water-induced phase separation enabling the direct visualization of phase separation under a confocal fluorescence microscope (CFM). ASD films at 30:70 drug:polymer ratio (by weight) were prepared by spin coating on quartz slides in a glove box under a dry air purge (~18%RH) to eliminate water vapor induced phase separation during preparation. CFM imaging of the ASD films before and after high RH exposure was performed using a Nikon A1 confocal microscope (Melville, NY) with excitation at 407 nm and emission over 425-475 nm.

5.4.9 Infrared (IR) spectroscopy

Spin-coated ASD films of felodipine with different polymers at 30:70 drug:polymer ratio (by weight) were prepared on a KRS-5 substrate (Harrick Scientific Corporation, Ossining, NY). IR spectra were measured in transmission mode using a Bruker Vertex 70 FTIR spectrometer (Bruker Corporation, Billerica, MA) with detector and sample chamber purged with dry, CO_2-free air. A

total of 64 scans were averaged for both the background and the sample spectra. The spectra were collected at a resolution of 4 cm^{-1}.

5.4.10 Statistical analysis

Statistical analysis was conducted using student's t-test or one-way ANOVA with the Tukey's multiple comparison test using GraphPad Prism 7.0. A p value ≤ 0.05 was used to assess the statistical significance.

5.4.11 Log P

Log P values of nilvadipine (Nil) and cilnidipine (Cil) were measured as per the procedures mentioned in Appendix D, section D1. The experimental log P of felodipine was taken from the literature.[173]

5.5 Results

5.5.1 Solubility

Felodipine has a crystalline solubility of about 1.3 µg/mL and an amorphous solubility of 8 µg/mL at 37°C (Table 5.1) in pH 6.8 phosphate buffer. In the presence of 1000 µg/mL of polymer, the crystalline solubility values of felodipine were the same within experimental error (Appendix D, Table D1).

Table 5.1 Crystalline and amorphous solubility of felodipine. Values are given as the mean of 3 samples ± standard deviation.

Felodipine	solubility (µg/mL)
crystalline	1.3 ± 0.3
amorphous	8 ± 1

5.5.2 Rank ordering of polymer hydrophobicity

Water sorption analysis

The water sorption profiles of the 5 polymers and amorphous felodipine are shown in Fig. 5.2. PVP is the most hydrophilic polymer, absorbing the highest amount of water at all RH values. Felodipine is the most hydrophobic compound based on the mass of water absorbed. HPMCAS and EUDS are the most hydrophobic polymers. Based on the water sorption profiles, the ordering of the polymers from most to least hydrophobic is:

HPMCAS ≥ EUDS > HPMC > PVPVA > PVP.
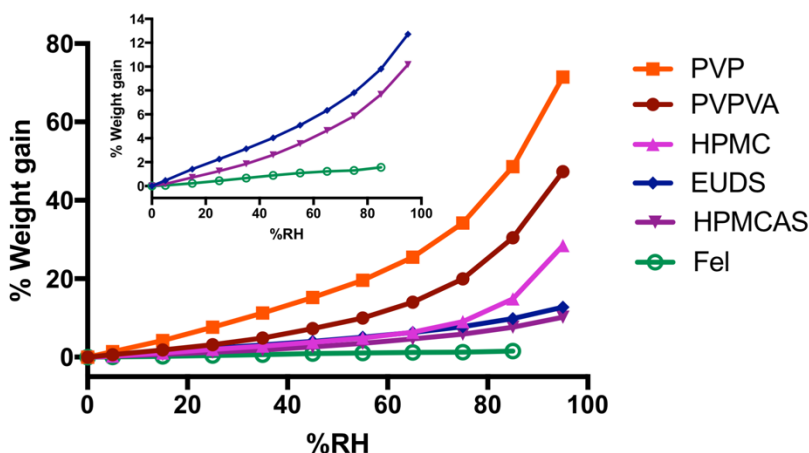
Figure 5.2 Water sorption profiles of the amorphous drug and polymers used in the study at 37°C. The less hygroscopic systems are shown in the inset with an expanded y-axis.

Contact angle measurements

Table 5.2 shows the measured static contact angle of buffer on the surface of different polymer films. A higher contact angle value indicates poorer wetting, consistent with higher surface hydrophobicity and vice versa. The rank ordering of different polymers based on the contact angles is in agreement with that obtained from the water sorption analysis: HPMCAS = EUDS > HPMC > PVPVA > PVP (most hydrophobic to least hydrophobic).

Table 5.2 Contact angle of dissolution buffer on different polymer surfaces.

Polymer	Contact angle (°)
PVP	11.9 ± 0.9
PVPVA	14.6 ± 0.4
HPMC	26 ± 1
EUDS	45.9 ± 1.6
HPMCAS	46.8 ± 5.7

5.5.3   Surface normalized release profiles of felodipine ASDs

The release profiles of felodipine-PVP and felodipine-HPMCAS ASDs at different drug loadings, as well as for neat amorphous drug and neat polymer are summarized in Figures 5.3 and 5.4, respectively. For PVP ASDs with 5% and 10% DLs, drug and polymer released congruently (i.e., at the same rate) and rapidly, quickly exceeding the amorphous solubility of felodipine (Fig. 5.5). For 15% DL and above, drug and polymer released incongruently with slow and negligible drug release. The LoC boundary for the Fel-PVP system was thus determined to be 10% DL. In contrast, Fel-HPMCAS ASDs, showed congruent release of both components for all DLs tested, and the amorphous solubility was exceeded for all systems (Fig. 5.6). For higher drug loadings, notably 50% DL, a lag period was observed, which was subsequently followed by congruent release of ASD components. The release profiles of felodipine ASDs with PVPVA, HPMC and EUDS are shown in Figure D2-D4 (Appendix D). The release behavior of the ASDs with the more hydrophilic polymers followed a similar pattern to that of PVP with LoCs of 15% and 10% DL observed for PVPVA and HPMC respectively. ASDs with EUDS were similar to HPMCAS systems, showing congruent release up to 50% DL, albeit with a slower release rate. No drug crystallization, either in solution or on the dissolving tablet surface, was observed for any system based on powder X-ray diffraction (PXRD) and/or polarized light microscopy (PLM).
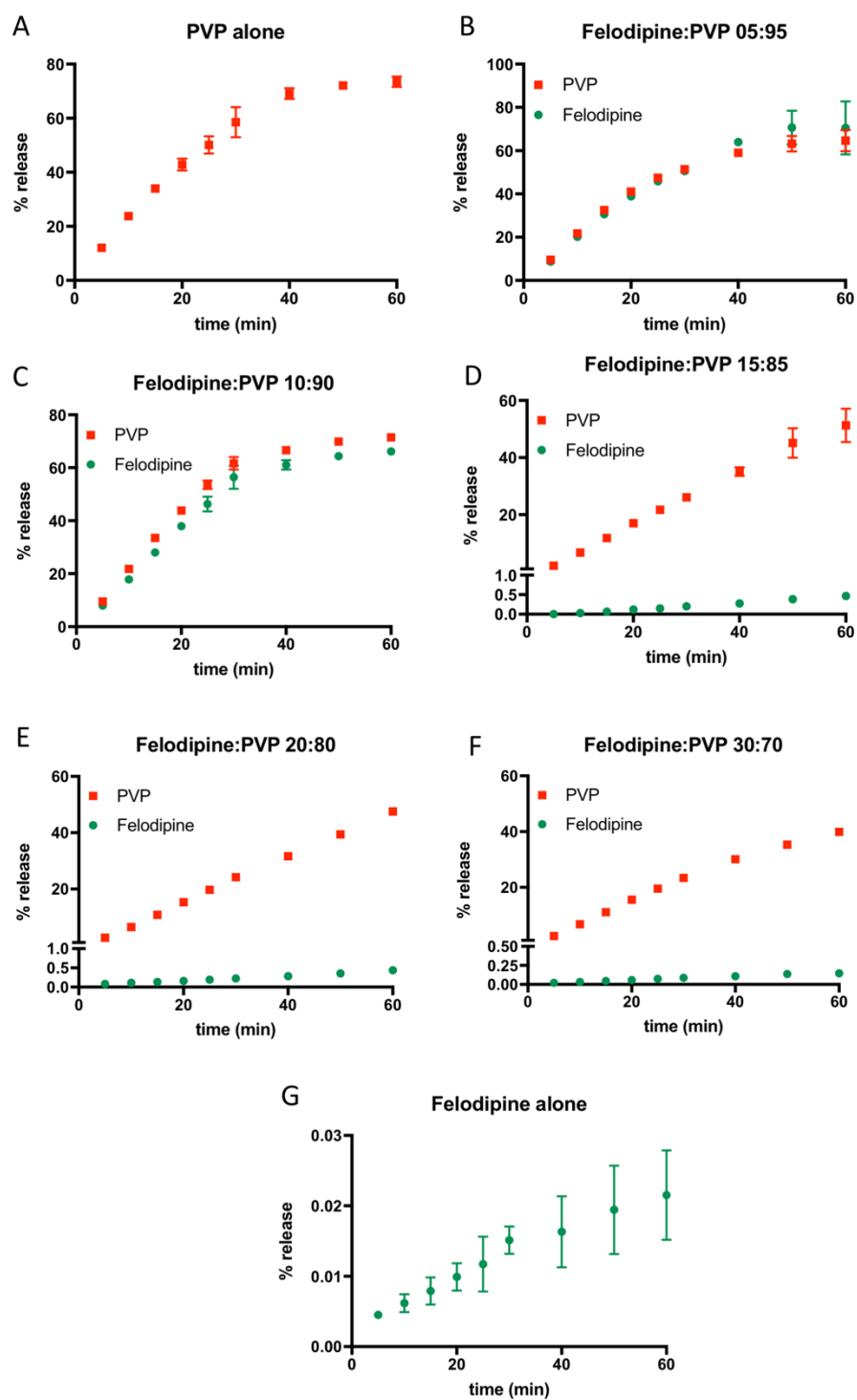
Figure 5.3 Percent release versus time profiles for amorphous Fel, PVP and Fel-PVP ASDs. The ratios in the legend represent drug:polymer weight ratios in the ASDs. Both polymer (red squares) and drug (green circles) release rates are shown for the ASDs. Error bars represent standard deviations, n=3.
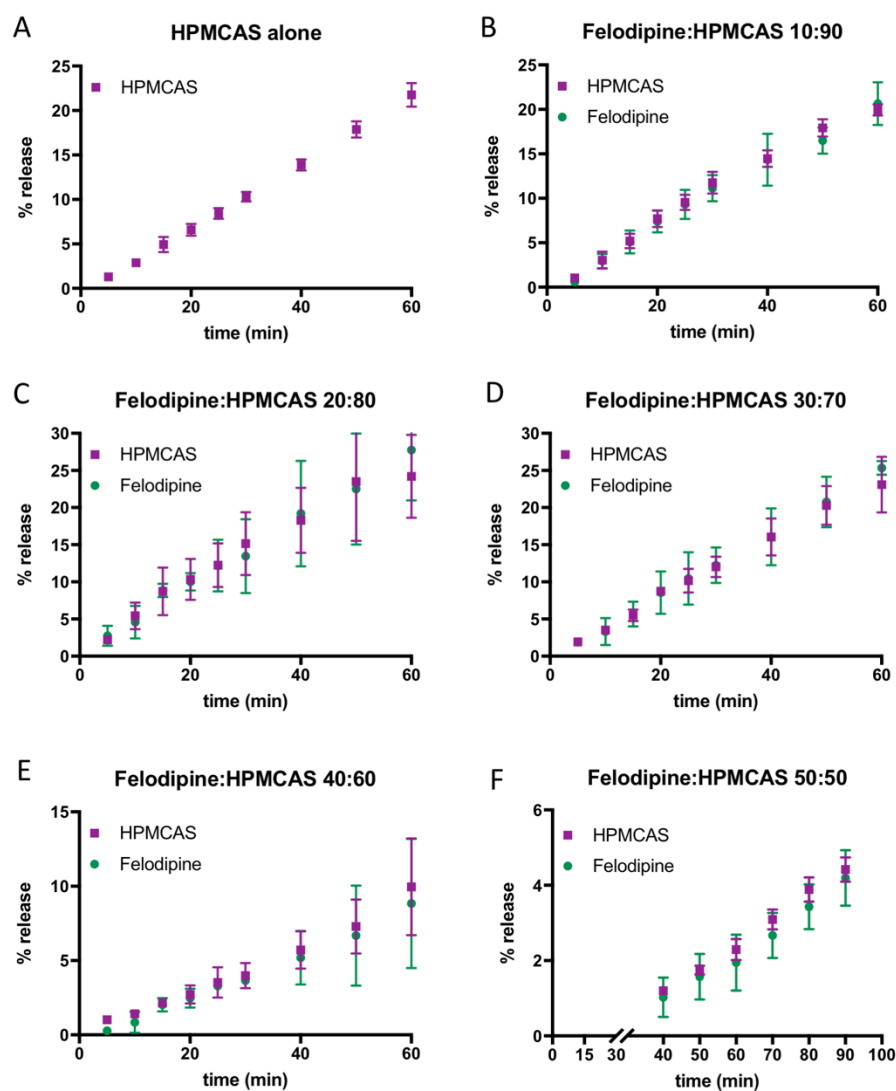
Figure 5.4 Percent release versus time profile for HPMCAS alone and Fel-HPMCAS ASDs at different drug loadings. The ratios in the legend represent drug:polymer weight ratios in the ASDs. Both polymer (purple squares) and drug (green circles) release rates are shown for the ASDs. Error bars represent standard deviations, n=3.
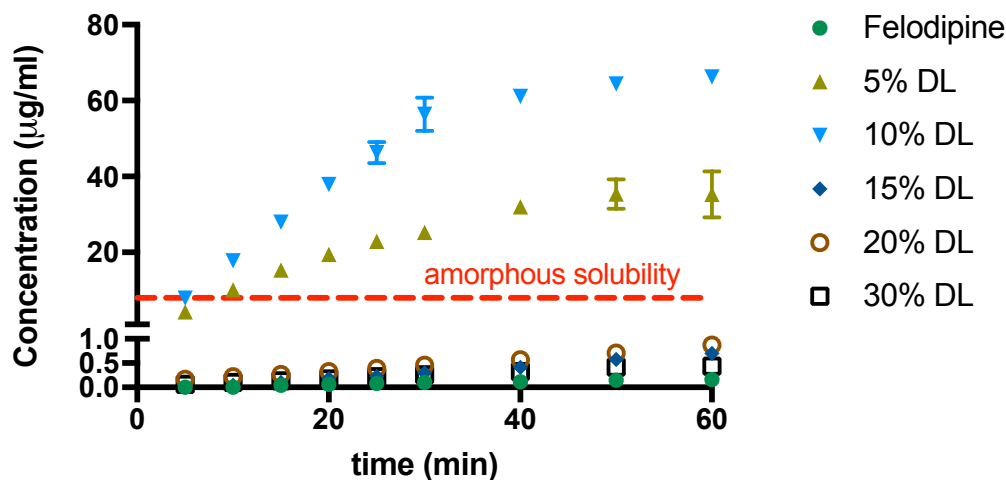
Figure 5.5 Concentration versus time profile for felodipine from amorphous drug alone and when incorporated into PVP ASDs. The legends represent drug loadings (by weight) in the ASDs. Error bars represent standard deviations, n=3.
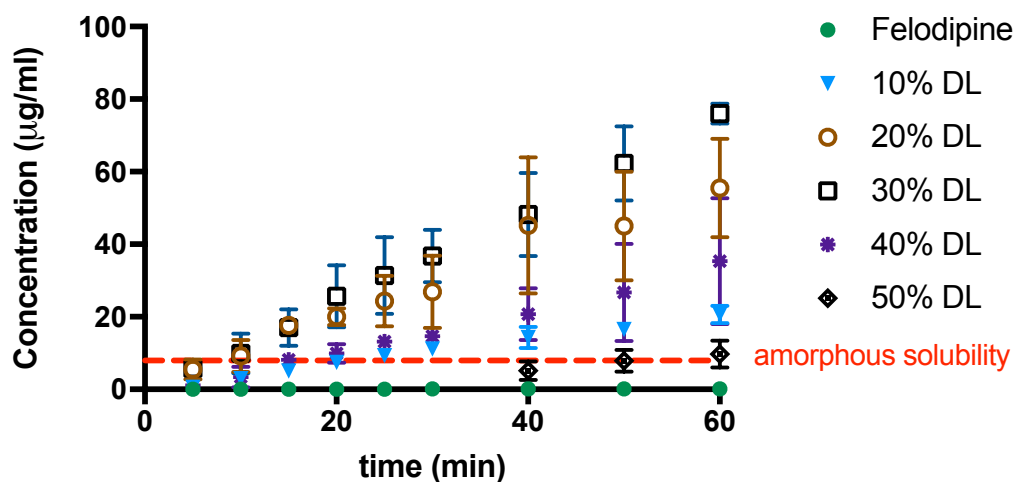
Figure 5.6 Concentration versus time profile for felodipine from amorphous drug alone and when incorporated into HPMCAS ASDs. The legends represent drug loadings (by weight) in the ASDs. Error bars represent standard deviations, n=3.

5.5.4 Comparison of surface normalized release rates of drug and polymer from ASDs

The dissolution rate (A, mg/min.cm^2) of drug or polymer from single component or ASD dissolution profiles, was calculated using equation 25:

$$A = \frac{k \times V}{S \times N} \tag{25.}$$

154

where k is the slope of the regression line (mg/mL.min) not including the origin, V is the volume of dissolution medium (100 mL), S is the tablet surface area (0.5 cm^2), and N is the weight fraction of each component (weight fraction is used on the assumption that the densities of each component are similar). The dissolution rates of amorphous felodipine and the different polymers are summarized in Fig. 5.7A. PVP and PVPVA, show the highest release rates, while EUDS dissolves more than an order of magnitude more slowly. The dissolution rates of the polymers do not show the same order as the hydrophobicity rankings. However, all polymers showed much higher dissolution rate as compared to amorphous drug alone.

The dissolution rates of drug and polymer from the ASDs as a function of drug loading are plotted in Fig. 5.7B-F. PVP, PVPVA and HPMC ASDs showed two distinct dissolution regimens as a function of drug loading, wherein at low drug loading, polymer and drug release simultaneously at a rate similar to that of the pure polymer, suggesting that the polymer properties control the drug release rate. Once a certain drug loading is exceeded, congruent release is lost and drug release diminishes dramatically ("falls off the cliff"). In contrast, HPMCAS and EUDS ASDs showed congruent release of components across all drug loadings studied (up to 50% DL). Up to 30% DL, the drug release rate was found similar to the neat polymer release rate, however, at higher drug loadings (≥40% DL), and most notably with HPMCAS, a decline in both drug and polymer release rates was observed. Thus, the presence of a high amount of hydrophobic drug impacts the polymer release rate even though congruency is maintained; this has been observed previously for HPMCAS ASDs.[118]
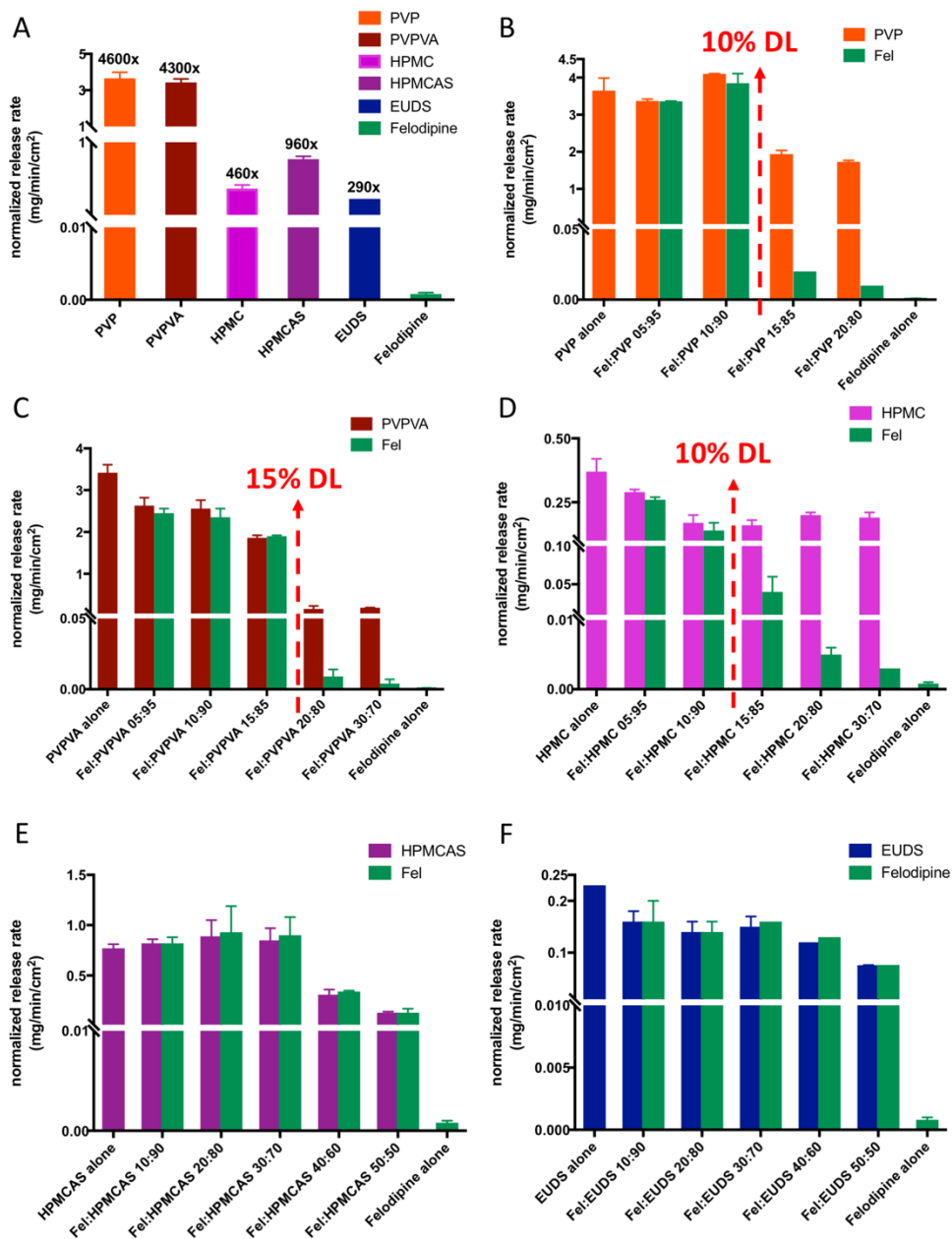
Figure 5.7 Comparison of intrinsic dissolution rates of different polymers and amorphous felodipine. Numbers on the bars in panel A indicate the ratio of the polymer dissolution rate to the drug dissolution rate (A). Surface normalized dissolution rates of drug alone, polymer alone, and ASDs at different drug:polymer weight ratios with PVP (B), PVPVA (C), HPMC (D), HPMCAS (E) and EUDS (F). Red arrow represents LoC wherever applicable. Error bars represent standard deviations, n=3.

5.5.5 Impact of drug hydrophobicity

To investigate the role of drug hydrophobicity on polymer release, HPMCAS ASDs were evaluated with two structural analogs of felodipine, with different log P values, at a 40% DL.

Nilvadipine (log P=4.06) and cilnidipine (log P=5.40), have log P values lower and higher than felodipine (log P=4.46), respectively. The hypothesis was that the component release rates, while remaining congruent, will be reduced relative to that of neat polymer to an extent that depends on the drug log P (used as a measure of compound lipophilicity). Results are summarized in Fig.5.8. Congruent release was observed for all systems. Both polymer and drug released more slowly than neat polymer, and the release rate decreased with an increase in drug hydrophobicity, nilvadipine > felodipine > cilnidipine. The difference in release rates for these three ASDs was statistically significant (ANOVA test, Appendix D, Table D2).
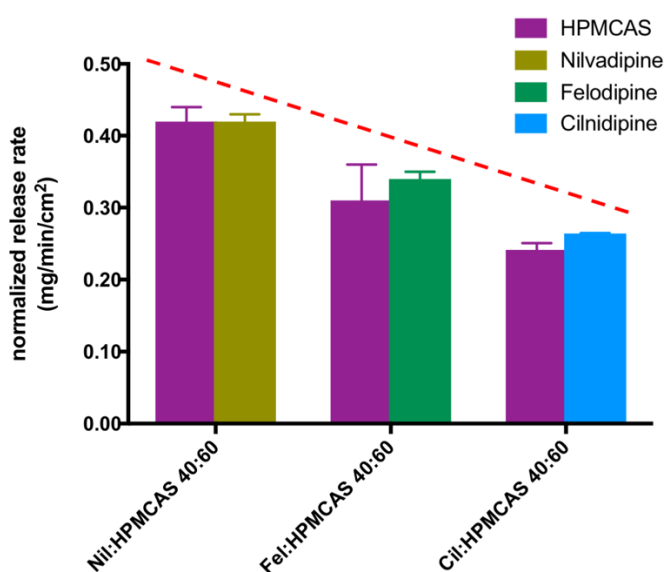
Figure 5.8 Surface normalized dissolution rates of HPMCAS ASDs at 40% DL with nilvadipine (Nil), felodipine (Fel) and cilnidipine (Cil). Error bars represent standard deviations, n=3. Red dashed line is meant to be a guide for the eyes to see the trend in ASD release rate as a function of drug log P.

5.5.6   Microcomputed tomography (micro-CT) images

Fig. 5.9 shows the micro-CT cross-sectional images of the partially dissolved felodipine ASD tablets (10 min timepoint) at 30% DL with different polymers. For ASDs with PVP, PVPVA and HPMC (Fig. 5.9A-C), a porous interface (as marked by double-headed yellow arrow) was formed after 10 min of dissolution, consistent with the faster polymer release observed for these systems (Fig. 5.7). For HPMCAS and EUDS ASDs (Fig. 5.9D,E), no discernable interface was observed and the tablet surface remained homogeneous with the bulk. Thus, no change in surface morphology is observed for congruently releasing ASDs with the more hydrophobic polymers.
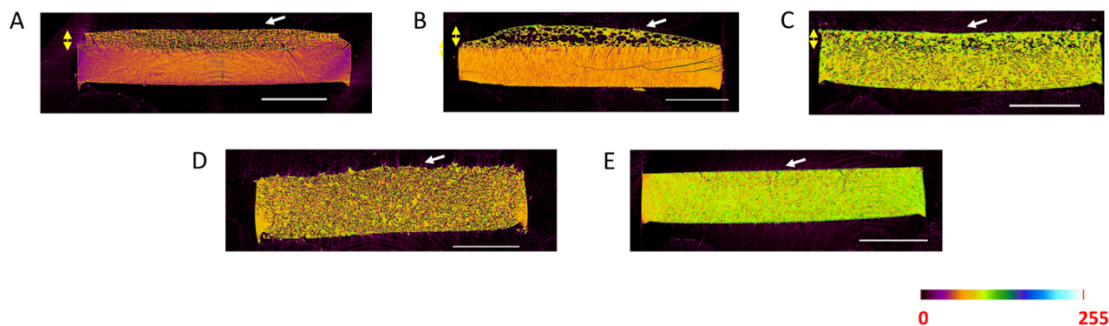
Figure 5.9 x-y cross-section images of partially dissolved tablets (10 minute timepoint) for Fel-PVP (A) Fel-PVPVA (B), Fel-HPMC (C), Fel-HPMCAS (D) and Fel-EUDS (E) at 30% drug loading. The white arrow on the images indicates the dissolving face of the tablet. Scale bar (in white) is 2 mm. The color scale bar represents the range of density measurement with zero representing the lowest density and 255 representing the highest density measured. The color contrast differences between different formulations is likely due to different individual densities of the formulations with different polymers.

5.5.7   Scanning electron microscopy (SEM) and Energy-dispersive X-ray (EDX) analysis

SEM images of the initial tablet surfaces for felodipine ASDs at 30% DL with different polymers showed smooth topography (Appendix D, Fig. D5). After 10 minutes of dissolution, surfaces were in general rougher. The partially dissolved tablet surfaces of PVP and PVPVA ASDs had characteristic 'pores' or 'pits' present, consistent with the porous interface observed for these tablets in micro-CT images (Figure 5.10).
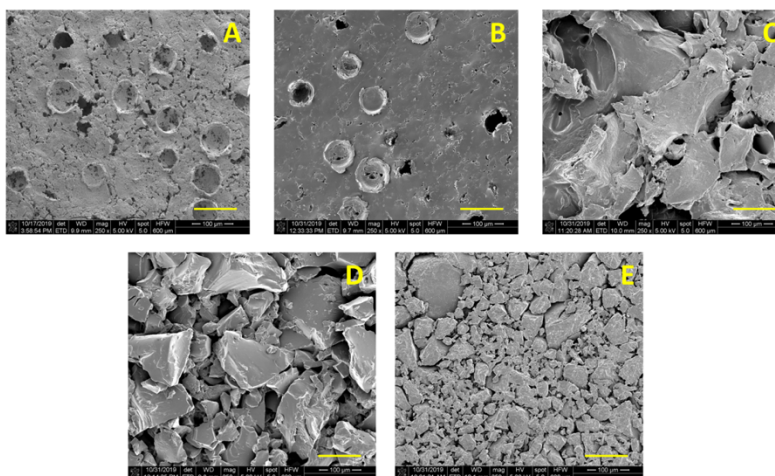
Figure 5.10 SEM images of partially dissolved tablets (10 minute time point) for Fel-PVP (A) Fel-PVPVA (B), Fel-HPMC (C), Fel-HPMCAS (D) and Fel-EUDS (E) at 30% drug loading. Scale bar is 100 µm.

EDX analysis was conducted to determine changes in the elemental composition and, in turn, drug-polymer composition at the surface after partial dissolution. The incongruently releasing ASD tablet compositions (PVP, PVPVA and HPMC ASDs at 30% DL) showed drug enrichment based on an increased chlorine content on the tablet surfaces after dissolution (Fig. 5.11); chlorine is present only in felodipine (Fig. 5.1). In contrast 30% DL ASDs with HPMCAS or EUDS, which showed congruent release, had the same surface chlorine content before and after dissolution (Fig. 5.11).
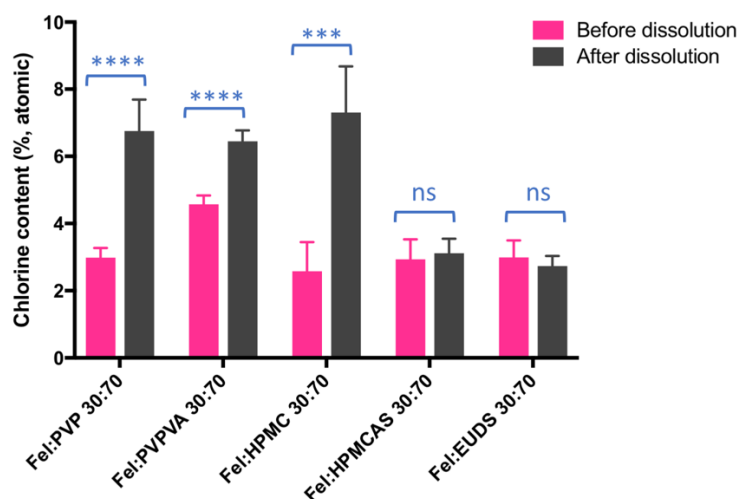
Figure 5.11 Chlorine content found on the ASD tablet surface, before and after dissolution (10 minute timepoint), using energy-dispersive X-ray (EDX) analysis. The ratios in the legend denotes drug:polymer weight ratios. Student's t-test performed between chlorine content before and after dissolution ($^{ns}p>0.05$, $^{***}p\leq0.001$ and $^{****}p\leq0.0001$)

5.5.8 Confocal fluorescence microscopy imaging of ASD films

Confocal fluorescence microscopy was carried out on ASD films to understand the tendency for phase separation to occur in the ASD matrix in the presence of water. Prodan, a fluorescent probe, should preferentially partition into the drug-rich phase in the event of phase separation, leading to inhomogeneous fluorescence in the film. Films initially showed homogeneous fluorescence, with a uniform blue color prior to high RH exposure, indicating initially miscible ASDs (data not shown). After 24 hours of high RH exposure, 30% DL ASD films with PVP, PVPVA and HPMC showed discrete domains of intense blue color (Fig. 5.12), consistent with phase separation. On the other hand, HPMCAS and EUDS ASDs remained homogeneous, showing uniform fluorescence intensity, suggesting minimal or no phase separation in these films.

159
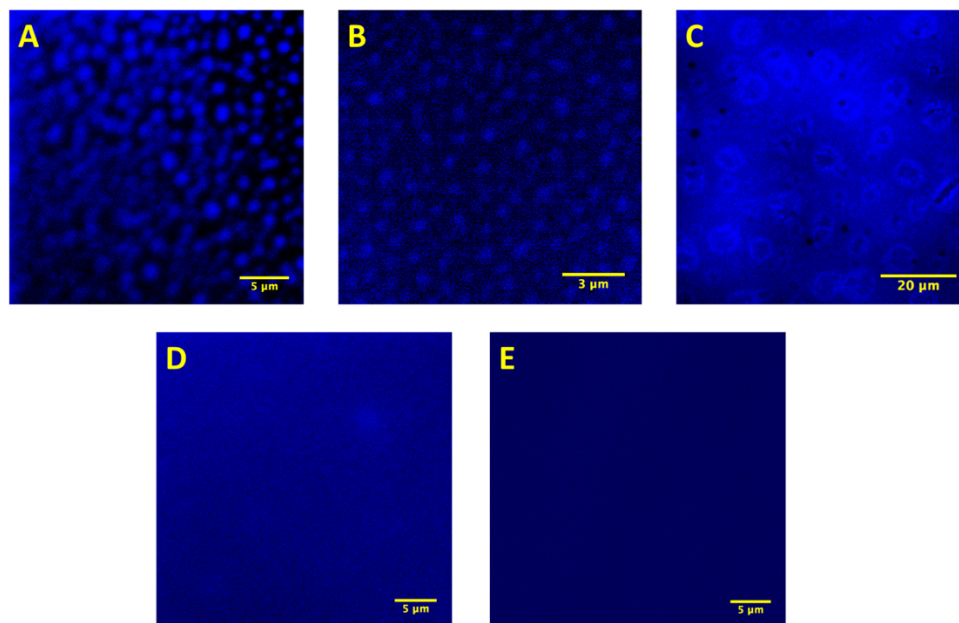
Figure 5.12 Representative confocal fluorescence microscopy images of 30% DL felodipine ASDs after exposure to water: PVP (A), PVPVA (B), HPMC (C), HPMCAS (D) and EUDS (E). Images were taken at an appropriate magnification based on the size of domains, if present, such as in case of A, B and C. For images without any specific features, such as D and E, both high magnification (shown here) and low magnification (shown in Fig. D6, Appendix D) images were taken.

5.5.9   IR spectroscopy

The polymers used in this study have different functional groups, and therefore, may vary in their ability to interact with the model compound. IR spectroscopy was employed to study hydrogen bonding between drug and polymer. Felodipine has an NH group which is an H-bond donor, whereby the peak position has been shown to vary with the strength of the intermolecular interaction.[17, 146, 174] The NH group of felodipine forms a hydrogen bond with the carbonyl function of another drug molecule in neat amorphous drug, therefore, shifts in the NH peak position reflect disruption of drug-drug interactions and the potential formation of interactions between drug and polymer.

The infrared spectra of spin-coated films of felodipine and ASDs at 30% DL are shown in Fig. 5.13. Amorphous felodipine shows a NH stretch peak at 3342 cm^{-1},[17] whereas none of the polymers have any significant peaks in this region (data not shown). In PVP and PVPVA ASDs, the NH peak position shifts downward, consistent with stronger hydrogen bonds between the drug and polymer in these ASDs relative to those present in amorphous felodipine. In contrast, the NH peak

position increases to higher wavenumbers in EUDS and HPMCAS ASDs suggesting weaker interactions than in amorphous felodipine. For HPMC ASD, no spectral shift was observed in the NH region; either there is no specific interaction between felodipine and HPMC or the strength of drug-polymer interaction is similar to that found in neat amorphous felodipine. Based on changes in the peak position of the drug carbonyl peaks, the latter scenario appears to be the case (Appendix D, Fig. D7). NH peak positions are summarized in Table 5.3. Based on variations in the NH peak position, the order of drug-polymer hydrogen bonding strength is: PVP $\cong$ PVPVA > HPMC > HPMCAS > EUDS. However, it should be noted that a shoulder or a second peak was still present at 3342 cm^{-1} for most ASDs, indicative of residual drug-drug hydrogen bonding interactions and quantitative information about the extent of the drug-polymer hydrogen bonding interactions cannot be extracted from these data.
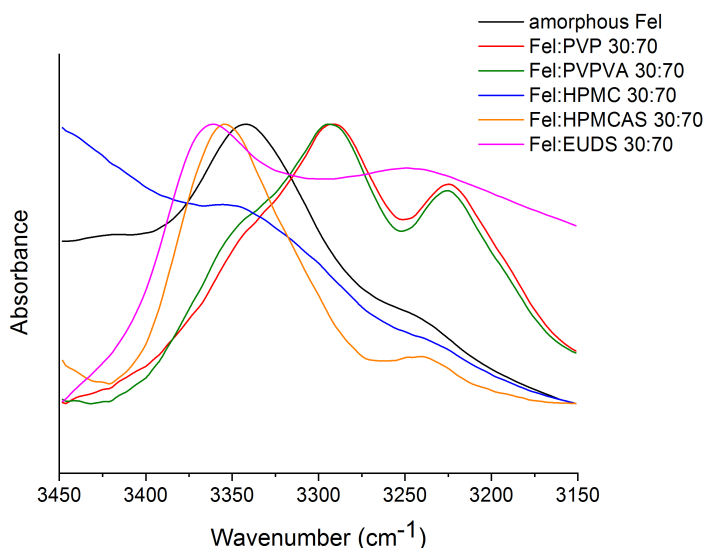
Figure 5.13 Normalized infrared absorbance spectra showing the NH stretching region (3150-3450 cm^{-1}) for amorphous felodipine and felodipine ASDs with different polymers at 30% drug loading. The ratios in the legend represent drug:polymer weight ratios in the ASDs.

Table 5.3 NH stretch peak position in amorphous felodipine alone and felodipine ASDs at 30%DL.

Hydrogen bond	Peak position (cm^{-1})
Felodipine-felodipine	3342
Felodipine-PVP	3292
Felodipine-PVPVA	3293
Felodipine-HPMC	3344
Felodipine-EUDS	3354
Felodipine-HPMCAS	3362

5.6 Discussion

5.6.1 Drug loading impact on normalized dissolution rate

Felodipine has an amorphous solubility about 6 times higher than its crystalline solubility. This translates to a relatively modest solubility enhancement, given the low crystalline solubility (1µg/mL). In turn, the dissolution rate advantage derived from amorphous drug-controlled dissolution, is expected to be modest (eq. 23), and it can be seen that the IDR of amorphous felodipine is indeed extremely low (Figure 5.3G and 5.7A). This reinforces the concept that simply rendering an extremely poorly water soluble drug amorphous is unlikely to yield sufficient dissolution rate advantages to adequately increase bioavailability, in particular for high dose drugs. Thus, the *in vivo* advantage of ASDs most likely stems in large part from the presence of a hydrophilic polymer, which, in combination with molecular dispersion of the drug, can lead to polymer-controlled drug release.[26, 136, 141, 160] Given that the neat polymer can dissolve several hundred-fold faster than a lipophilic amorphous drug (Fig. 5.7A), exploiting polymer-controlled ASD dissolution is likely essential to maximize drug absorption for systems exhibiting solubility and dissolution rate limited absorption. However, drug loading plays a critical role in determining if polymer-controlled release can be achieved. Interestingly, we see two patterns of behavior for the relationship between drug loading and drug/polymer release rates, depending on the polymer. Three polymeric systems (ASDs with PVP, PVPVA and HPMC) show polymer-controlled drug release only at low drug loadings, followed by a dramatic decline in drug release when the drug loading exceeds a certain value (LoC). This "falling off the cliff" in terms of drug release rate is

accompanied by a loss of congruent release of drug and polymer. Thus, at DLs higher than the LoC, polymer releases faster than drug, leading to drug enrichment at the dissolving interface, and reduced drug release rate. In contrast, ASDs with HPMCAS or EUDS, showed congruent release for all drug loadings (as reported previously with EUDS).[175] However, increasing the DL still imposes a "penalty" in terms of drug release rate, notably for ≥30% DL because the presence of greater quantities of drug impacts the polymer release rate. The HPMCAS ASDs, in particular, show more of a negative "slope" in the drug release rate, rather than the "cliff" seen with PVP, PVPVA and HPMC ASDs.

In terms of understanding the differences in the patterns of behavior, we note that the polymers showing a distinct LoC boundary are 1) more hydrophilic and 2) neutral. In contrast, HPMCAS and EUDS are more hydrophobic and need to ionize in order to dissolve. As such, their ability to interact with both water and the drug is different in the dry versus the hydrated state (where pH >> pKa).

Role of drug hydrophobicity

For systems maintaining congruency up to high drug loadings, as noted above, the presence of increasing amounts of felodipine retards HPMCAS dissolution. This previously observed effect has been attributed to a variety of factors, such as, effects on binding and polymer swelling,[9] the presence of strong drug-polymer interactions,[118, 176] as well as an increase in the hydrophobicity of ASD due to the presence of drug.[118] By choosing three structural analogues with different log P values, but similar ability to form intermolecular interactions with the polymer, the role of drug lipophilicity becomes clearer. Thus, the observation that both polymer and drug release rates reduce with an increase in drug log P (Fig. 5.8) substantiates the supposition that drug hydrophobicity plays a role in influencing component release rates, at least for congruently releasing systems at high drug loading. In contrast, a previous study demonstrated that at low drug loadings, polymer properties appear to dominate and no correlation with drug log P could be observed.[141] Therefore, it seems likely that there is a cutover drug loading where the drug properties start to substantially impact release rates, as the overall hydrophobicity of the system becomes dominated by the drug (Appendix D, section D2).

5.6.2 Mechanistic explanation for occurrence of a LoC

LoC and diffusion-based theoretical models

According to Higuchi's diffusion-based dissolution models for two-component systems,[137] such as an ASD, a congruent release scenario is only feasible at a critical mixture ratio calculated based on equation 26:

$$\frac{N_{drug}}{N_{polymer}} = \frac{D_{drug} \cdot C_{s(drug)}}{D_{polymer} \cdot C_{s(polymer)}} \qquad (26.)$$

where *N* is the weight fraction, *D* is the diffusion coefficient and C_s is the saturation solubility of the component. However, for an ASD system, a large disparity exists between the solubilities of the two components and therefore, for all practical purposes, the drug loading in the ASD always will be higher than critical mixture ratio as calculated using equation 26 (≥1% DL, section D3, Appendix D). In such cases, the initial release of each component should be diffusion-controlled and governed by equation 23, eventually leading to the formation of a drug-rich porous layer at the dissolving surface (due to differences in the dissolution rate of each component), which then governs the subsequent dissolution rate. Higuchi's model may adequately describe high drug loading ASDs, but fails to model the release behavior of low drug loading ASDs, whereby congruent release of ASD components is often seen over a range of (low) drug loadings, whereby the solid-liquid boundary of each ASD component recedes at a similar pace.[23, 136, 141, 160] This behavior is observed in this study for up to 10% DL for PVP and HPMC ASDs, and up to 15% DL for PVPVA ASDs. It has been argued that amount of drug present at such low drug loadings is insufficient to form and support an intact porous drug-rich layer,[9] resulting in polymer-controlled release at drug loadings higher than those predicted by the theoretical approach described by eq. 26. Based on both the current study, and other published work, the argument that the amount of drug present in the dispersion is the sole reason for this sudden change in dissolution performance at the LoC, doesn't seem hold true for the following two reasons. First, the LoC for a given polymer (PVPVA) varies with drug from 5-25%.[26, 136, 141, 160] Second, ASDs with HPMCAS and EUDS, were found to show congruent release up to 50% DL. Thus, evaluating only the drug:polymer ratio, as per the Higuchi model, is clearly an over simplification, and other factors

including the role of water in inducing phase separation at the solid-liquid interface should be considered.

LoC and AAPS

Water is known to be detrimental to the miscibility of some ASDs and it has been suggested that ASDs can undergo phase separation upon matrix hydration during dissolution.[18, 61, 71, 119, 154] This is referred as water-induced amorphous-amorphous phase separation (AAPS), and is expected to have deleterious effect on ASD dissolution.[119, 136, 140, 141] For a given drug, the thermodynamic favorability for the occurrence of water-induced AAPS will depend on the drug loading, polymer type, the relative affinity of the polymer and drug for the solvent and the amount of water absorbed by the ASD matrix, which in turn depends on the extent and strength of drug-polymer interactions.[18, 61, 159, 177] The kinetics of water-induced AAPS is also important, considering that this is a competing process to dissolution. In an earlier study, we established that the occurrence of water-induced AAPS changes the release behavior of an originally congruently releasing ASD to the incongruent regime.[141] Thus, competition between AAPS and dissolution rate may be key in determining the observed ASD dissolution regime, namely polymer-controlled and congruent, or incongruent. If dissolution is faster than AAPS, thought to be the case for the low drug loading ASDs (≤10% DL) in this study, irrespective of polymer type, drug and polymer release congruently with the dissolving tablet surface retaining its initial composition during the dissolution process. However, if AAPS occurs faster than dissolution, phase separated drug- and polymer-rich domains will form and dissolve at a rate dictated by the composition of each phase. Faster release of the polymer will render the surface drug-rich, reducing the rate of drug release. At low drug loadings, insufficient drug is present to form a contiguous drug-rich layer on the surface, and there may also be a lower tendency for AAPS and/or slower phase separation kinetics, and these factors likely help maintain the congruent release of ASD components. At higher drug loadings, there is increased tendency and/or rate of AAPS leading to surface drug-enrichment, which acts both as a physical barrier to polymer release from subsurface layers, and reduces the drug release rate towards that seen for neat amorphous drug. Thus, water-induced AAPS is likely the cause for the observed LoC and associated loss in dissolution performance for high drug loading PVP, PVPVA and HPMC ASDs. Since the thermodynamics and kinetics of water-induced AAPS during dissolution, depend not only on the drug loading, but also on the amount of water absorbed,

polymer hygroscopicity likely also plays a role in defining the ASD dissolution regimen. The congruent release mechanism for high drug loading ASDs with HPMCAS and EUDS, which were less hygroscopic, conceivably can be explained by absorption of lower amounts of water (Figure 5.2) that are insufficient to induce AAPS. Support for the conjecture is provided by Figure 5.12, where no discernable signs of AAPS were observed for ASDs with these less hygroscopic polymer following storage at high RH. In contrast, fluorescence microscopy images for PVP, PVPVA and HPMCAS ASDs are consistent with the occurrence of phase separation. The micro-CT (Figure 5.9) and SEM/EDX data (Figures 5.10 and 5.11) also support the occurrence of AAPS followed by formation of a porous drug-rich layer (due to preferential loss of polymer) at the solid-solution interface for ASD tablets with the more hygroscopic polymers, after partial dissolution.

5.6.3 Drug-polymer interactions and ASD dissolution

Intermolecular interactions (e.g. hydrogen bonds, van der Waals) exist between drug and polymer in miscible ASDs. It has been suggested that ASDs with strong drug-polymer interactions may resist water-induced AAPS, especially, during high RH storage conditions.[61, 154] Herein, we observe no positive correlation between drug polymer hydrogen bonding interaction strength and the LoC boundary. Indeed, the polymers that have stronger hydrogen bonding interactions with felodipine (PVP, PVPVA and HPMC) show low LoC boundaries, while more consistent dissolution rates as a function of drug loading are seen with HPMCAS and EUDS, which appear to form weaker interactions with the drug. Thus, the role of drug-polymer interactions, if any, in determining the LoC boundary, clearly needs further evaluation.

5.6.4 "Trade-off" between high dissolution rate and high LoC

In this study, we observe different patterns of drug and polymer release from amorphous solid dispersions as a function of drug loading that appear to depend on polymer hydrophobicity. Drug release from ASDs with relatively hydrophilic polymers, PVP, PVPVA and HPMC, showed extremely different dissolution behavior on either side of the LoC boundary, which itself occurred at a relatively low drug loading (10-15% DL). Below the LoC boundary, dissolution is rapid, complete and polymer-controlled (congruent) with achieved drug concentrations exceeding the drug amorphous solubility leading to LLPS. In contrast, a dramatic decline in release is seen at

drug loadings higher than the LoC boundary, producing a "falling off a cliff" effect,[136] wherein both drug and polymer release becomes minimal. This is clearly illustrated in Figure 5.14 for the PVPVA dispersions. Thus, it is crucial to keep the drug loading at or below LoC for these ASDs to avert the risk of severely compromised dissolution performance and bioavailability. This pattern of behavior for PVPVA-based ASDs may underlie the outcomes noted for human PK studies of grazoprevir-PVPVA ASD formulations.[178] The tablet with the 30% DL ASD intermediate showed the highest bioavailability, where an increase in drug loading from 30% to 40% resulted in a halving of the bioavailability. The neat amorphous drug had less than one fourth of the bioavailability seen for the 30% DL ASD. The observed drug loading dependent bioavailability was attributed to a decline in the dissolution rate with DL.[167]
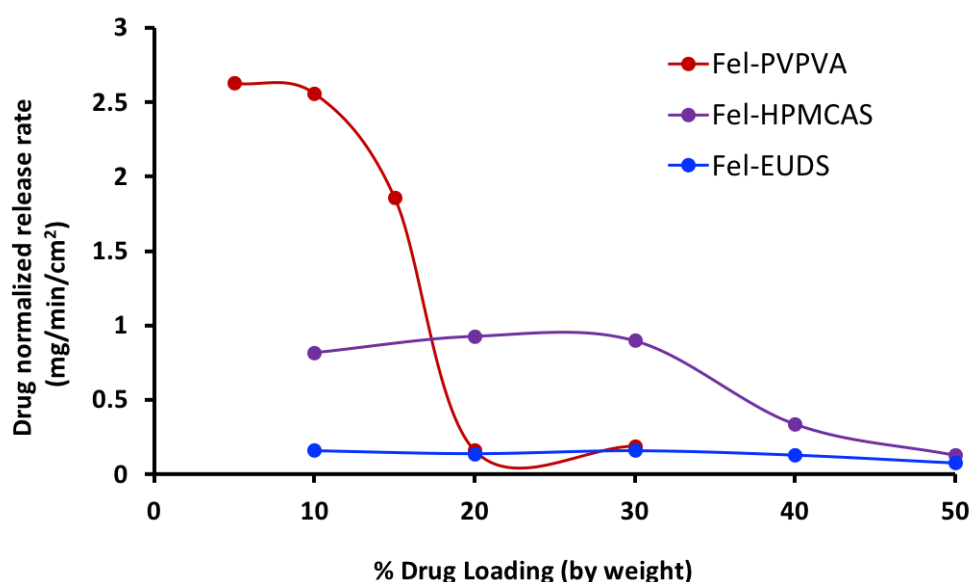
Figure 5.14 Normalized release rate of drug from felodipine ASDs as a function of drug loading (wt. %) with three different polymers: PVPVA, HPMCAS and EUDS.

For HPMCAS and EUDS-based ASDs, no LoC was observed up to 50% DL. However, given that these polymers have intrinsically slower dissolution (Figure 5.7A), it is apparent that they have release disadvantages relative to PVPVA ASDs for the low drug loadings regimen (≤15% DL). However, HPMCAS provides relatively better release at higher drug loadings (>15% DL), although the release does decline, above 30% DL. Figure 5.14 clearly shows the crossover between PVPVA and HPMCAS ASD performance, where HPMCAS shows improved release for DLs of 20-40%. Drug release from EUDS ASDs is low, albeit consistent, across all drug loadings. Thus,

more hydrophilic polymers may be a better choice at low drug loadings (below LoC) owing to their faster dissolution rate, while a more hydrophobic polymer may allow for improved release rates at somewhat higher DLs. Consequently, the choice of an appropriate polymer for an amorphous solid dispersion will depend on the trade-off between the higher dissolution rate derived from a more hydrophilic polymer and the more consistent release with increasing DL, achievable with a more hydrophobic polymer. This balance will be ultimately dictated by the required dissolution profile to achieve adequate exposure *in vivo*, and the dose to be delivered. Fig. 5.15 summarizes this trade-off in case of felodipine via comparison between individual dissolution rates of different polymers, reflective of dissolution rate advantage achievable with polymer-controlled dissolution and corresponding drug loading limitations (LoCs) for gaining such an advantage.
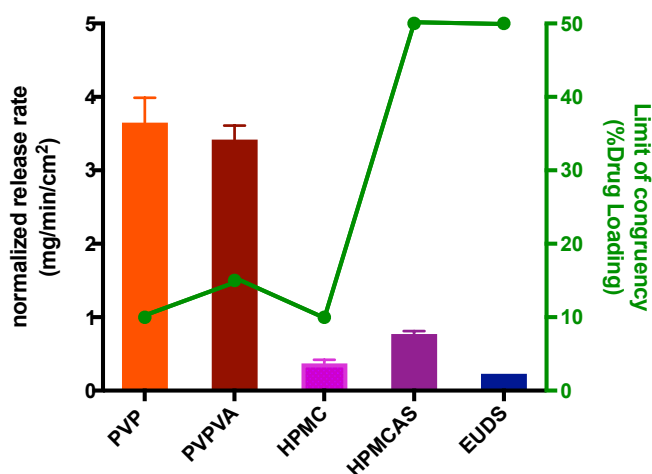
Figure 5.15 Comparison of individual intrinsic dissolution rates of different polymers Error bars represent standard deviations, n=3. (left y-axis) Limit of congruency (% drug loading by weight) of felodipine ASDs with different polymers (right y-axis).

5.7   Conclusion
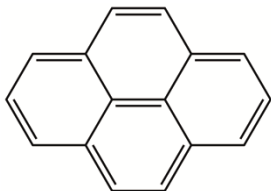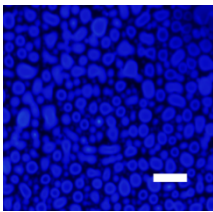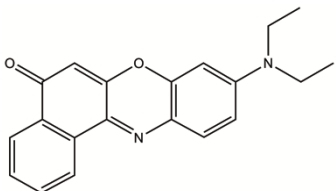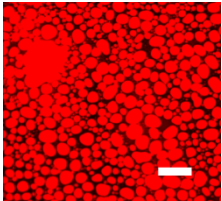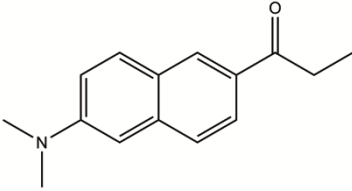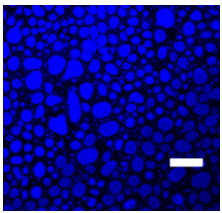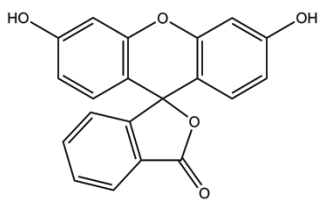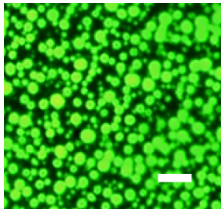
We have identified different drug loading dependent dissolution mechanisms of ASDs based on polymer hydrophobicity. For relatively hydrophilic, non-ionizing polymers, the dissolution rate of each component from the ASDs is rapid and polymer-controlled at low drug loadings, while at higher drug loadings, the drug release rate is markedly reduced. For more hydrophobic polymers that require ionization to dissolve, the dissolution rate is more consistent as a function of drug loading. However, some decline in the release rate of both drug and polymer is seen at higher drug

loadings, whereby both components continue to release at comparable rates. Water-induced AAPS is likely the cause for the dramatic decline in release rate observed with the more hydrophilic polymers at higher drug loadings. Because the hydrophilic polymers show faster dissolution rates as compared to hydrophobic polymers for the polymer-controlled dissolution regimen, ASDs prepared with these polymers provide advantages in terms of release rates for the low drug loading regimen. In contrast, more slowly dissolving polymers may yield improved drug release rates at higher drug loadings. The mechanistic understanding gained in this study will help formulators make rational polymer choices for ASDs, and provides insight into the trade-off between using hydrophilic versus hydrophobic polymers, particularly at higher drug loadings.
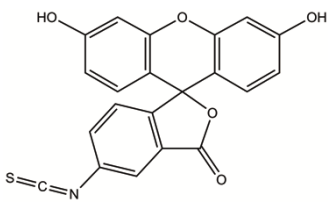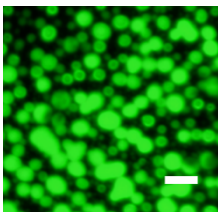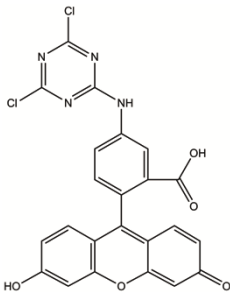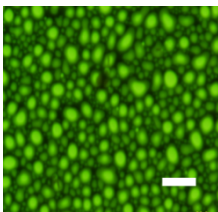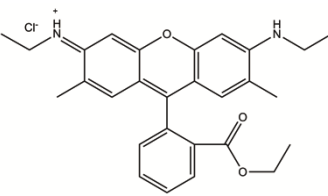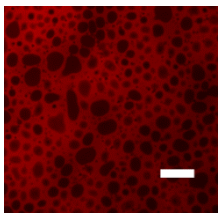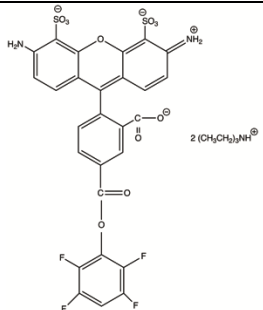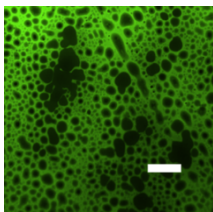
APPENDIX A

Supporting information for Chapter 2

Table A1: Chemical structure, drug/polymer specificity, ionic/neutral nature and log D of fluorescent probes evaluated

Fluorescence probe	Chemical structure$	Fluorescence image¶ for drug/polymer specificity	Ionic/ Neutral	Log D*
Pyrene			Neutral	3.45
Nile red			Neutral	2.98
Prodan			Neutral	3.28
Fluorescein			Neutral but ionizable[#]	-1.30[179]

FITC			Neutral but ionizable[#]	0.85[180]
5-DTAF			Neutral but ionizable[#]	Not available
R6G			cationic[96]	2.1[181]
Alexa Fluor®488			anionic[96]	-10.48[182]

[$]Chemical structures were drawn by ChemDraw®16

[¶]Fluorescence images were taken using a wide field fluorescence microscope (Olympus BX- 51, Olympus, NY) (Scale bar is 20 μm)

[*]For neutral/ un-ionizable compounds, log P = log D at any pH. Therefore, for pyrene, nile red and prodan, log P has been taken as such from ChemDraw®16 and log D as has been taken for other probes at pH 7.4 from references as stated.

[#] Fluorescein and its derivatives (FITC and 5-DTAF) are water soluble and considered easily ionizable due to the presence of an ionizable carboxylate group [94, 95].

Supporting information for Chapter 3
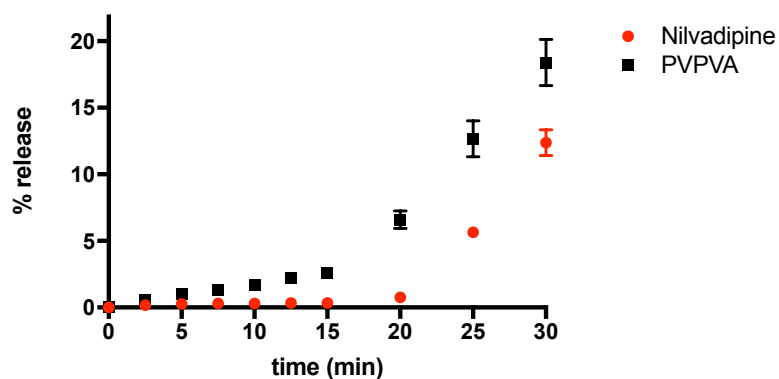
Figure B1. Dissolution rates (mean±SD, n=3) of drug and polymer for Nil:PVPVA 10:90 ASD from a tablet surface exposed to 97% RH for 12 hours.

(e.)
Mean: 339.9 ± 1.5 nm
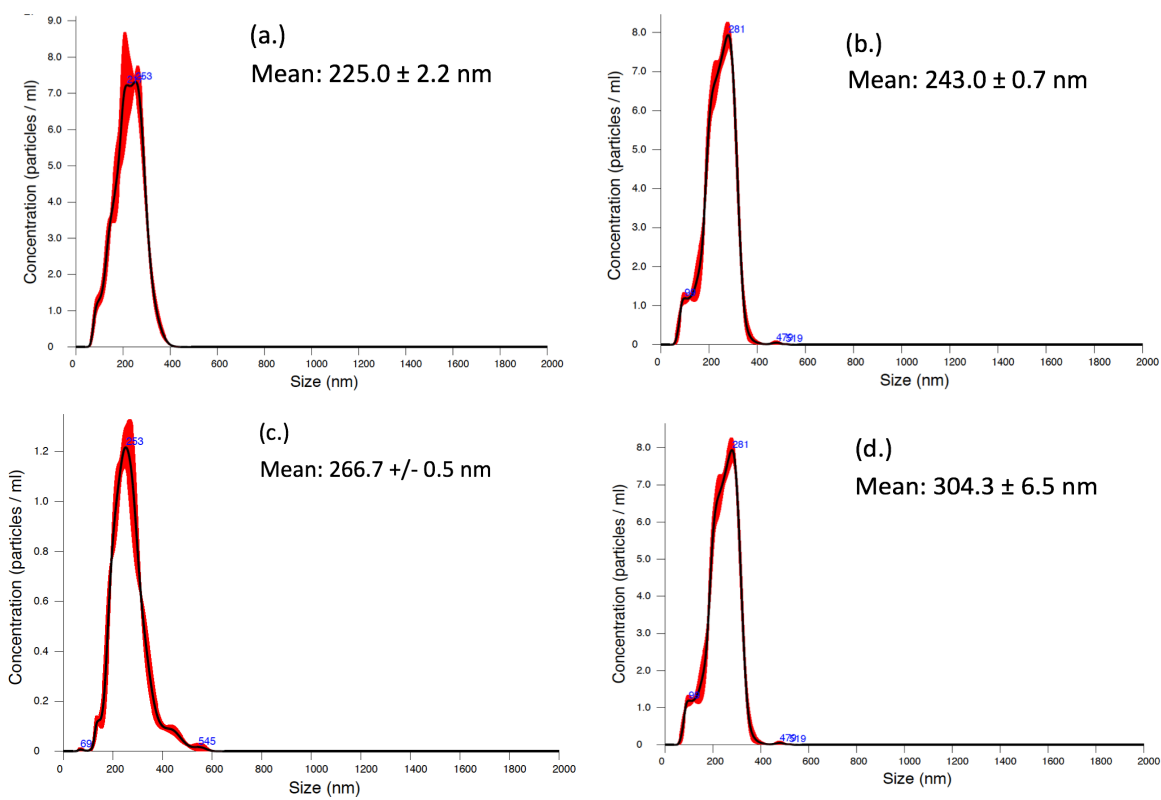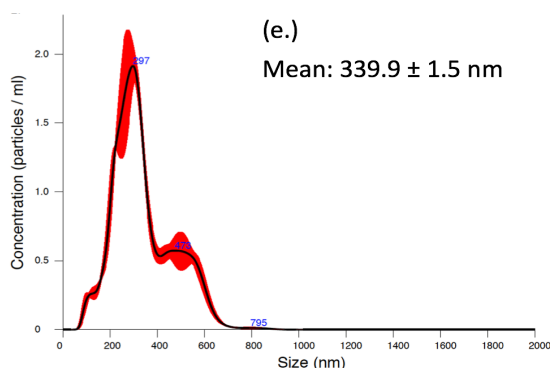
Figure B2. NTA size distributions of solutions obtained after dissolution of Nil: PVPVA and Cil:PVPVA ASDs with different drug:polymer weight ratios. Nil:PVPVA 05:95 (a), Nil:PVPVA 10:90 (b), Cil:PVPVA 05:95 (c), Cil:PVPVA 10:90 (d) and Cil:PVPVA 15:85. Error bars (in red) indicate +/- 1 standard error of the mean.
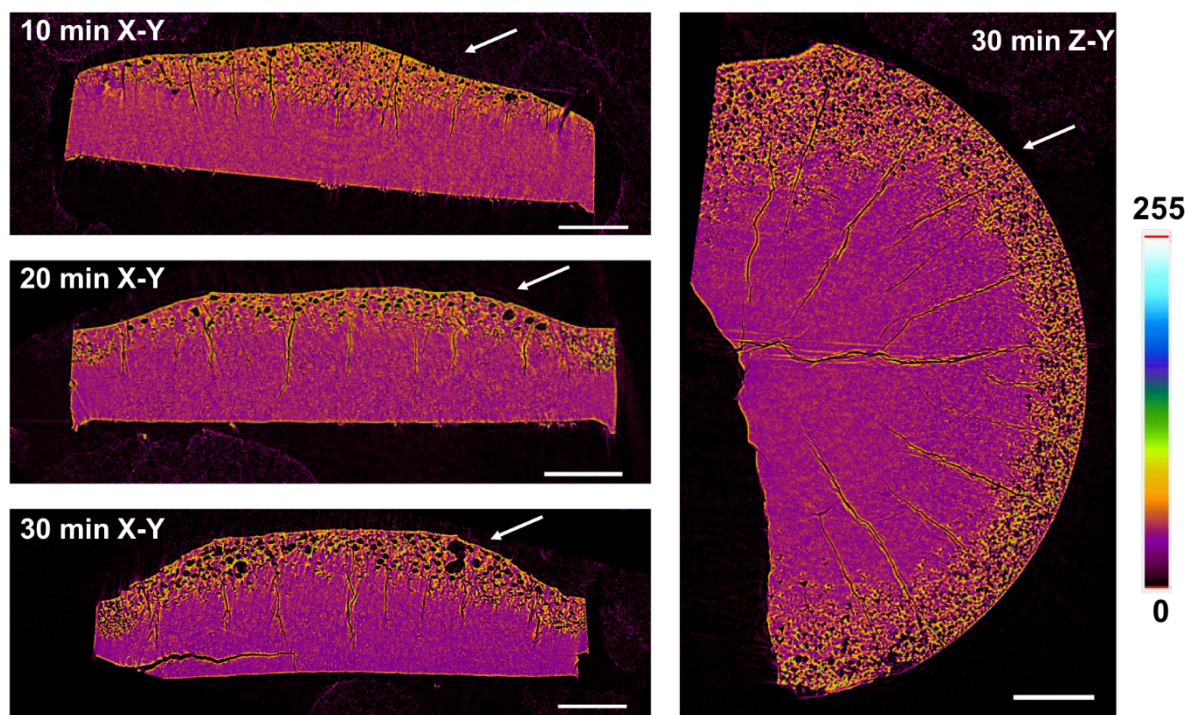
Figure B3. x-y cross-section images of partially dissolved tablets of Nil:PVPVA 15:85 (by weight) at 10, 20 and 30 minute time points (left panel). Note the increase in porosity of the interface with time and the appearance of a network of "channels" in the tablet matrix at longer times. The right panel shows a representative z-y cross section of half a tablet of partially dissolved Nil:PVPVA 15:85 ASD after 30 minutes of dissolution showing the porous interface and the progression of "channels" across the z-y plane. The arrow on the images is pointing towards the dissolving face of the tablet. The color scale bar represents the range of density measurement with zero representing the lowest density and 255 representing the highest density measured. Scale bar (in white) is 1 mm.
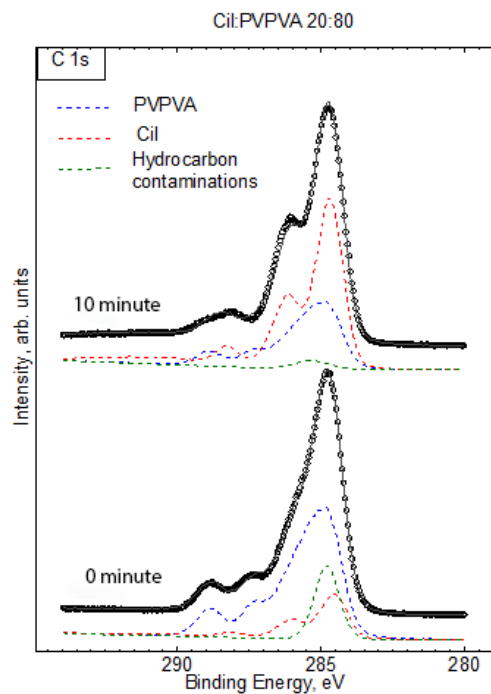
Figure B4. The C 1s spectra of initial Cil:PVPVA 20:80 tablet surface at 0 minute time point (the bottom spectrum) compared with partially dissolved tablet at 10 minute time point (the top spectrum).
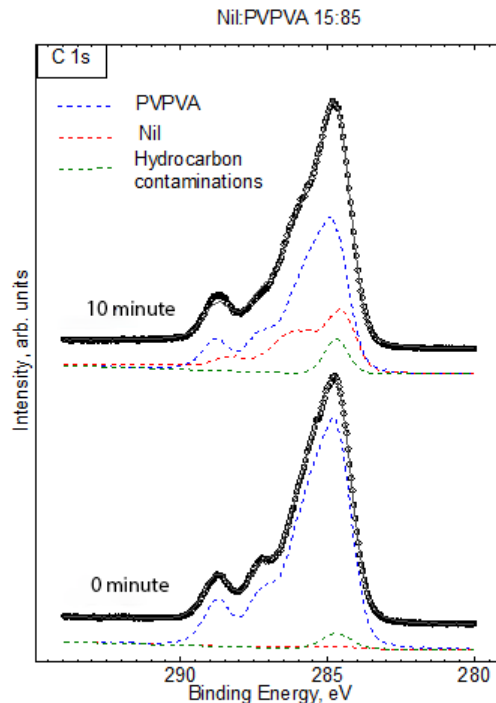
Figure B5. The C 1s spectra of initial Nil:PVPVA 15:85 tablet surface at 0 minute time point (the bottom spectrum) compared with partially dissolved tablet at 10 minute time point (the top spectrum).

174

Table B1. Surface compositions as measured by XPS (mean±SD, n≥3) of congruently releasing ASD tablet formulations (Nil:PVPVA 10:90 and Cil:PVPVA 15:85) before and after dissolution (partially dissolved surface at 10 minute dissolution time point)

ASD tablet composition (dissolution time point)	% surface composition based on XPS (C1s spectra, weight ratio)	
	Drug	PVPVA
Nil:PVPVA 10:90 (0 minute time point)	1±1	99±1
Nil:PVPVA 10:90 (10 minute time point)	1±0^{ns}	99±0^{ns}
Cil:PVPVA 15:85 (0 minute time point)	13±0	87±0
Cil:PVPVA 15:85 (10 minute time point)	13±3^{ns}	87±3^{ns}

^{ns} not significantly different from corresponding 0 minute time point %drug (or %polymer) surface composition ($p > 0.05$)

Supporting information for Chapter 4

Section C1: *Synthesis of indomethacin methyl ester (INDester)*

Indomethacin and anhydrous benzenesulfonic acid (1:2 molar ratio) were dissolved in methanol with heating (ca. 50°C). Indomethacin methyl ester crystals precipitated out after cooling the solution to room temperature. The crystals obtained were immediately isolated and dried.[183] NMR confirmed the correct structure with additional 1H and 13C NMR signals for methyl ester at δ 3.70 ppm and 52.11 ppm, respectively, as shown in Figure S1. The purity of the product obtained was >95%.
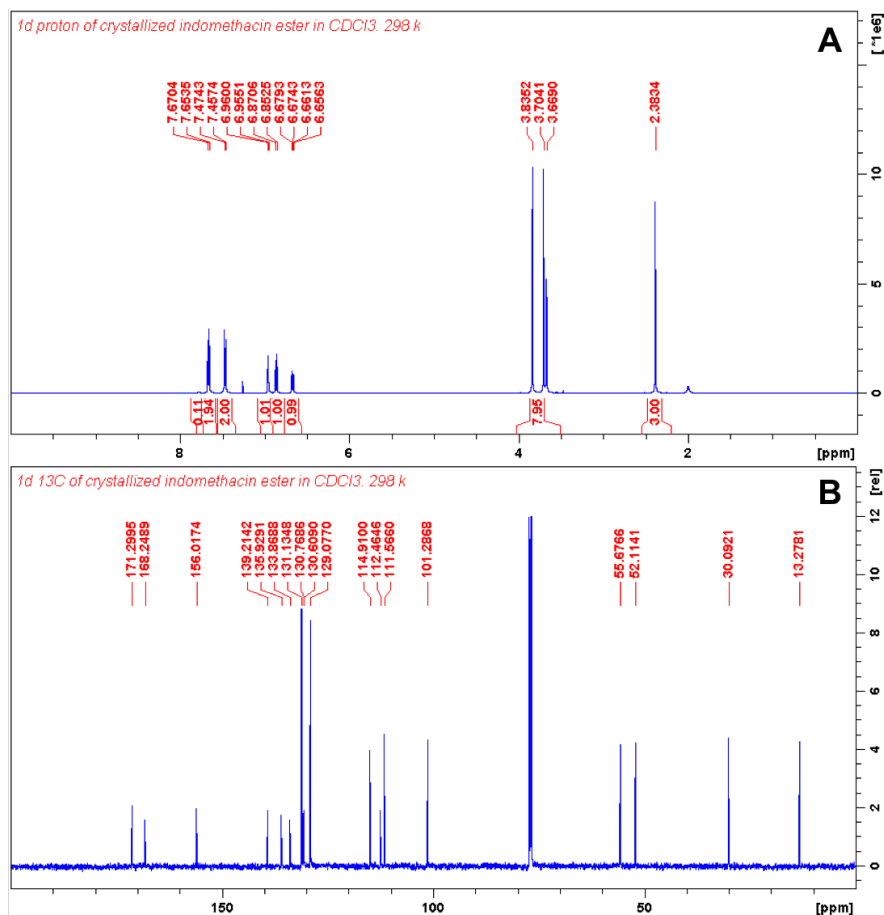
Figure C1. 1H (A) and 13C NMR (B) spectrum for synthesized indomethacin methyl ester (INDester) in deuterated chloroform (500 MHz Bruker NMR spectrometer; 298 K).

Section C2: *Physicochemical properties of indomethacin (IND) and indomethacin methyl ester (INDester)*

Thermal analysis (melting point, dry glass transition temperature (dry T_g) and crystallization tendency). Crystalline IND and INDester samples were analyzed using a differential scanning calorimeter (DSC) model Q2000 (TA Instruments, New Castle, DE). The instrument was calibrated for temperature using indium and tin, and for enthalpy using indium. Dry nitrogen at 50 mL/min was used as the purge gas. Around 5 mg of individual drug sample was placed in the sealed Tzero aluminum sample pan. The sample was heated to 20-30°C above melting point (~180°C for IND and ~120°C for INDester) to determine the melting temperature (T_m) from the melting endotherm, and thereafter the sample was cooled at 20°C/min to -40°C and then reheated at a 2°C/min underlying heating rate with a modulation amplitude of 1°C and a 60 seconds modulation period to determine the glass transition temperature (T_g). To determine and classify the crystallization tendency of the drug, a previously developed protocol was utilized,[150] wherein samples were prepared in a hermetically sealed pans, heated at 10°C/min to about 20°C above the melting temperature, cooled at a rate of 20°C/min to -75°C, and reheated at 10°C/min to just above the melting temperature. Thereafter, depending on the observed crystallization behavior, drugs were classified as per the below classification:

Class	Behavior
Class 1	Crystallization observed during cooling of the melt at 20°C/min
Class 2	No crystallization on cooling but crystallization observed upon heating at 10°C/min
Class 3	No crystallization observed on cooling as well as upon subsequent heating at 10°C/min

Octanol-water partition coefficient (log P). To measure the partition coefficient (log P), the pH of the aqueous phase was adjusted such that the predominant form of the drug is un-ionized and pH was kept close to the dissolution medium pH used for both IND and INDester individually. The aqueous phase used for determining IND log P consisted of 0.01N HCl pH 2.0 and for INDester, a phosphate buffer solution of pH 6.5 was used (both saturated with 1-Octanol). For individual log P determination of IND and INDester, a bi-phasic medium consisting of equal volume ratios of

octanol and aforementioned respective aqueous medium for both IND and INDester was used. A predefined drug concentration was dissolved into the organic phase from a solid and the two phases were vigorously mixed together for 24 hours. Afterwards, both phases were separated and drug was quantified in both phases using LC-MS. Log P was then determined using the equation C1:

$$\mathrm{logP} = \log \frac{[\text{drug concentration}]_{\text{octanol}}}{[\text{drug concentration}]_{\text{aqueous buffer}}} \qquad\qquad (\text{C1})$$

Wet T_g of indomethacin. The amorphous IND was prepared by melting at 180°C followed by quench cooling with liquid nitrogen. Next, moisture sorption profile of the amorphous drug was obtained using a SGA-100 symmetric vapor sorption analyzer (VTI corp, Hialeah, FL) at the desired temperature of interest (37°C) with a stepwise increase in relative humidity from 5% to 95% with a 10% increment at each step. A plot of weight gain as a function of RH was then used to estimate the total amount of water present in amorphous drug after saturation by extrapolating the data to 100%RH. The wet T_g (T_g of the water-saturated amorphous drug) was then estimated using the previously determined dry T_g value (obtained from the DSC), total estimated water content of water-saturated amorphous drug, and from the experimental observation that, T_g decreases by 10°C for each 1% of water sorbed.[59]
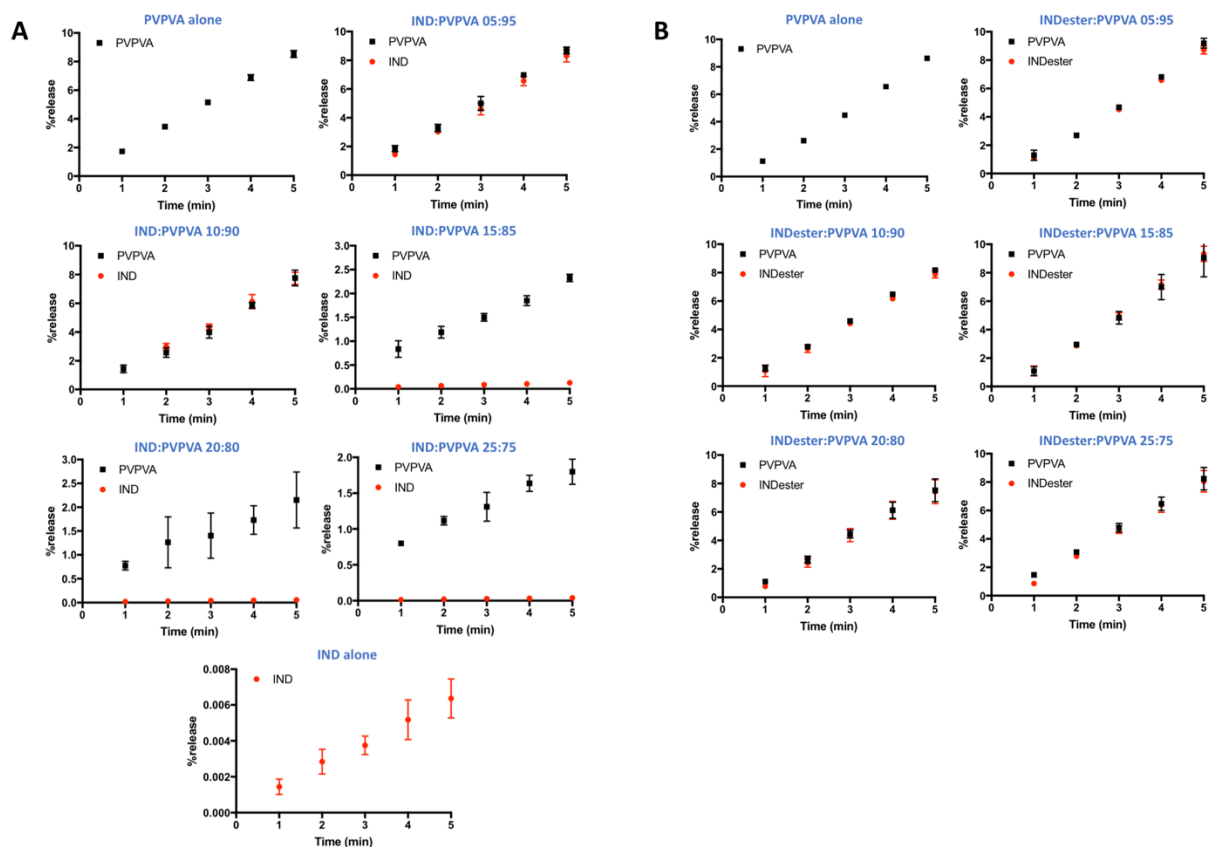
Figure C2. Percent release versus time profiles for amorphous IND alone, PVPVA alone and when incorporated into an ASD (A). Percent release versus time profiles for PVPVA alone, and INDester and PVPVA when incorporated into an ASD (B). The ratios in the legend represent drug:polymer weight ratios in the ASDs. Error bars represent standard deviations, n=3.

179

A.

INDester:PVPVA 05:95   INDester:PVPVA 10:90   INDester:PVPVA 15:85

INDester:PVPVA 20:80   INDester:PVPVA 25:75

B.
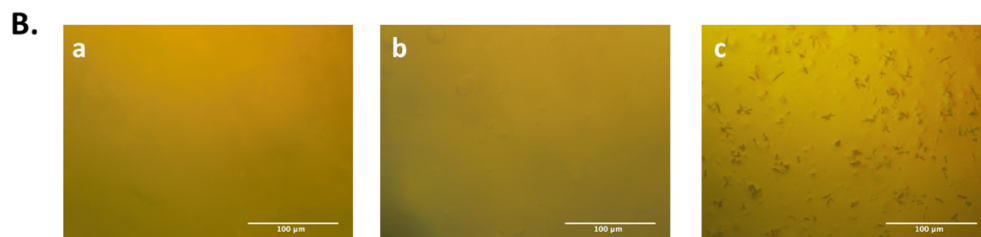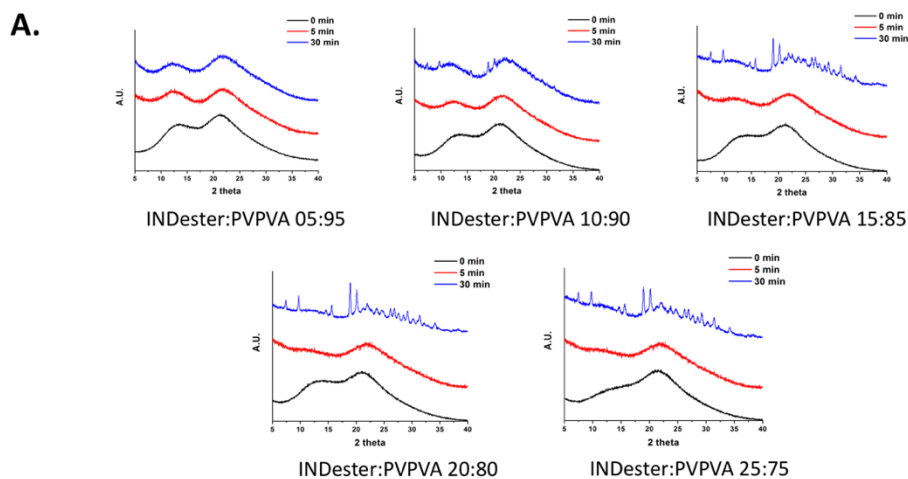
Figure C3. X-ray diffraction (XRD) patterns of INDester:PVPVA ASD tablet surfaces at 0, 5 and 30 min dissolution time points. The ratios in the legend represent drug-polymer weight ratios (A). Representative reflective polarized light microscopy images of ASD tablet surface of INDester:PVPVA 25:75 at 0 min (a), 5 min (b) and 10 min (c) time points. Notice the appearance of needle-like crystals on tablet surface at 10 min dissolution time point (B).
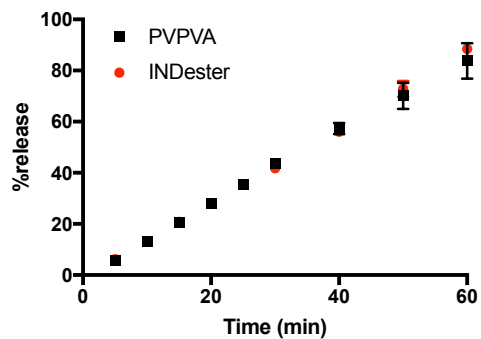
Figure C4. Percent release versus time profile of INDester and PVPVA obtained after dissolution of 25% DL (by weight) ASD at an experimental temperature of 15°C. Error bars represent standard deviations, n=3. Note that all the data points, as early as 5 minutes, are above the amorphous solubility of INDester.
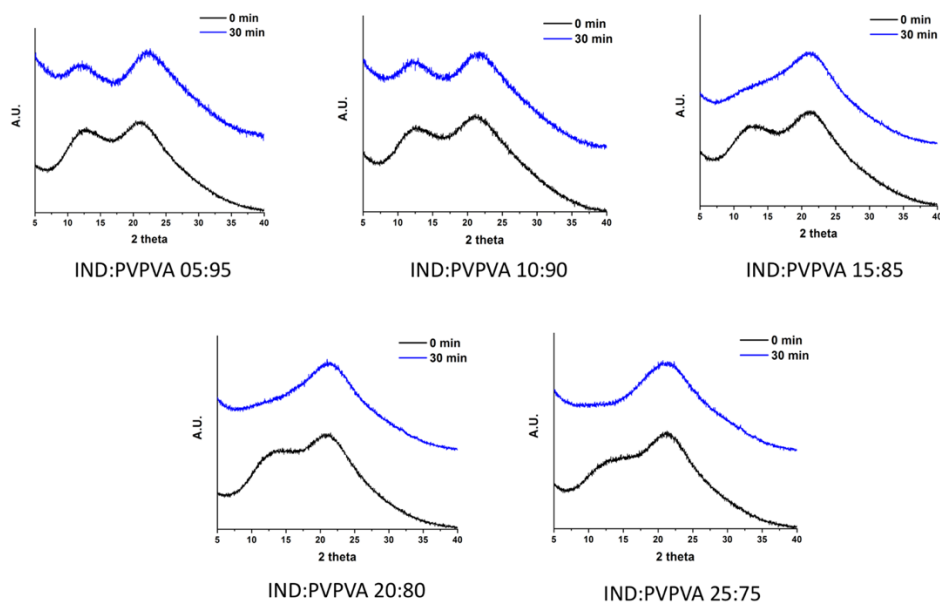
Figure C5. XRD patterns of IND:PVPVA ASD tablet surfaces at 0 and 30 min dissolution timepoint. The ratios in the legend represent drug-polymer weight ratios.
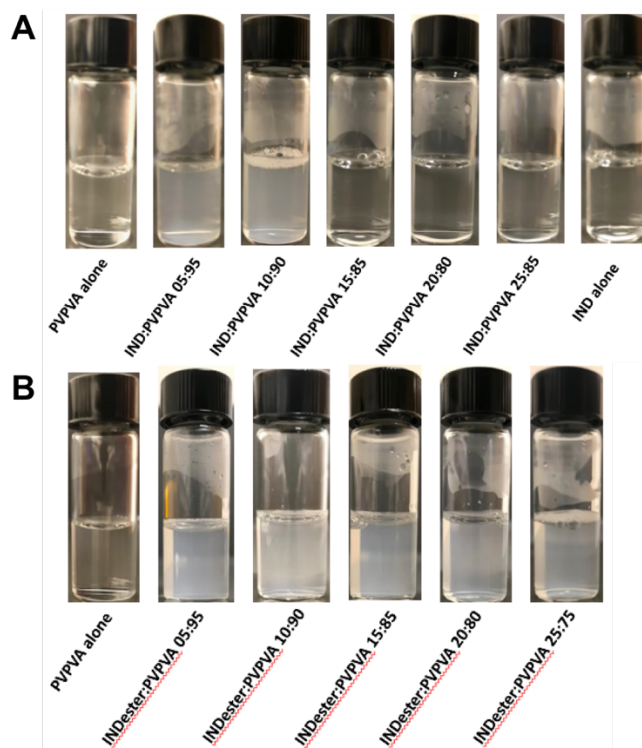
Figure C6. Appearance of the solutions obtained from the dissolution of tablets: PVPVA alone, amorphous IND alone and IND:PVPVA ASDs at different drug loadings (A) and PVPVA alone and INDester:PVPVA ASDs at different drug loadings (B). The ratios in the legend represent drug:polymer weight ratios.
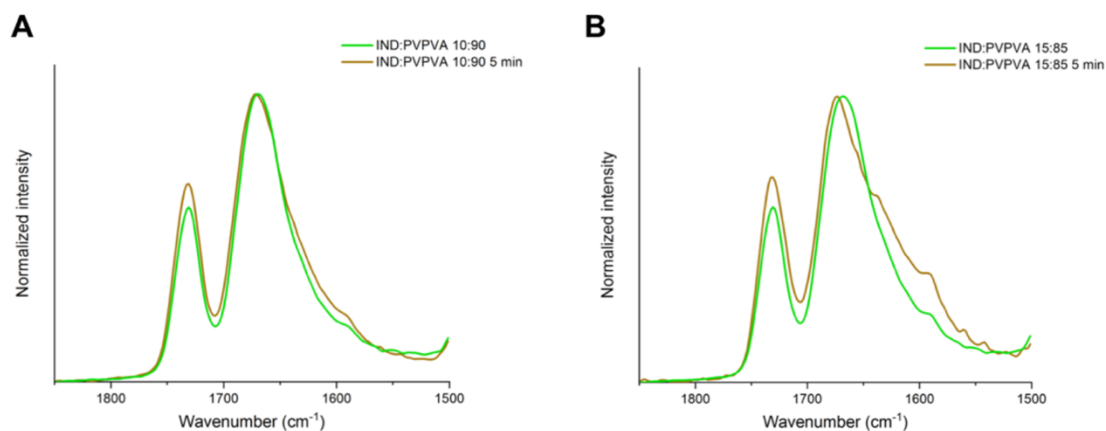
Figure C7. Normalized IR spectra of IND-PVPVA 10:90 ASD tablet surface before and after dissolution (5 min time point) (A). Normalized IR spectra of IND-PVPVA 15:85 ASD tablet surface before and after dissolution (5 min time point) (B).
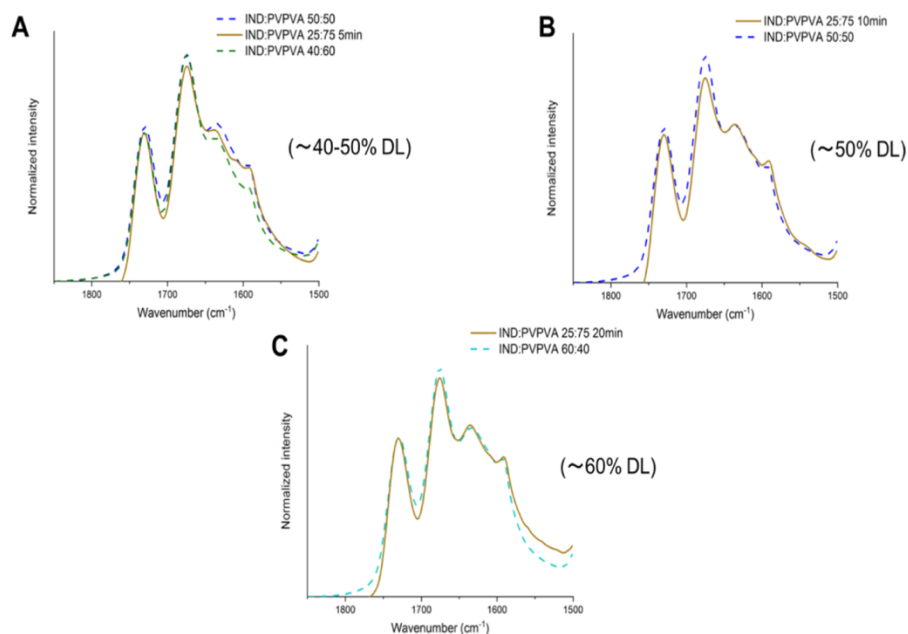
Figure C8. Best-fitted IR spectra from partially dissolved IND:PVPVA 25:75 ASD tablets at successive time points of 5 min (A), 10 min (B) and 20 min (C), represented by the solid lines. The reference curves are the IR spectra from ASD standards of known drug loadings represented by dashed lines. The drug loadings (DLs) in the brackets are the best estimated values for the partially dissolved ASD tablet surface obtained by curve fitting method. The ratios in the legend represents drug:polymer weight ratios.
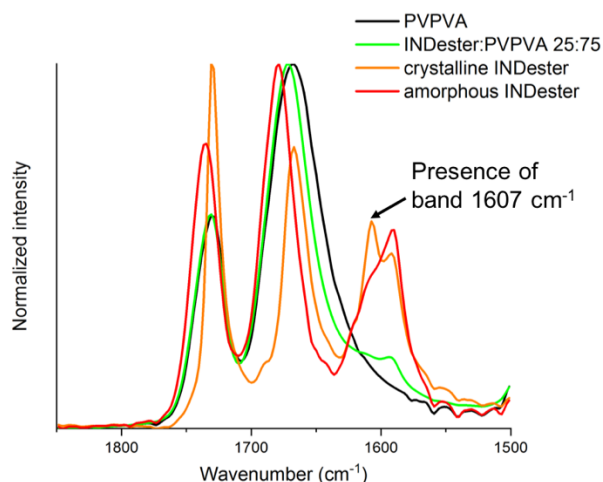
Figure C9. Normalized IR spectra of PVPVA alone, crystalline INDester alone, amorphous INDester alone and INDester-PVPVA 25:75 (w:w) ASD tablet.
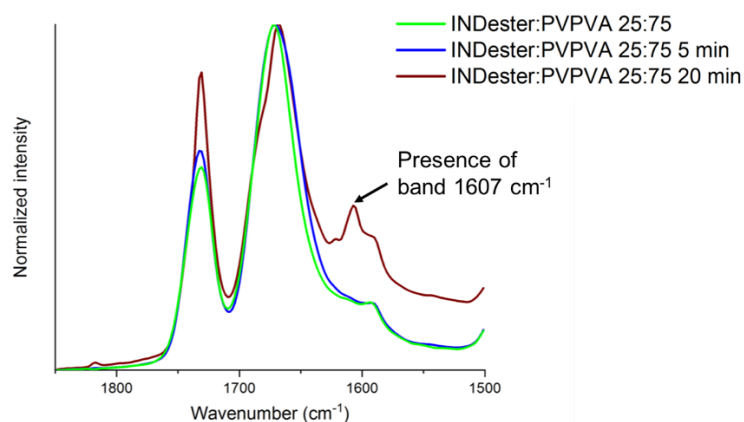
Figure C10. Normalized IR spectra of INDester-PVPVA 25:75 ASD tablet surface before dissolution and at successive time points after dissolution (5 and 20 min time points).

Section C3: *EDX analysis: linear regression model*

% Cl/N atomic ratio corresponding to IND alone and PVPVA alone tablets, and standard drug loading (by weight) ASD tablets (10, 20, 30, 40, and 50 %), are provided in Table C1. A linear regression model was established between % drug loading (by moles) and experimentally determined % Cl/N atomic ratio as provided in Figure C11.

Table C1: Experimentally determined % Cl/N atomic ratio corresponding to IND alone, PVPVA alone and IND:PVPVA ASD tablets of standard drug loadings (as prepared, by weight).

IND:PVPVA weight ratio for ASD tablet	Theoretical %drug loading as prepared (by weight)	Theoretical %drug loading (by moles)*	Experimental %Cl/N atomic ratio
IND alone	0	0	0±0
IND:PVPVA 10:90	10	6.1	6.6±0.8
IND:PVPVA 30:70	30	20.0	21.3±1.4
IND:PVPVA 50:50	50	36.9	33.8±1.9
IND:PVPVA 70:30	70	57.7	58.2±5.4
IND:PVPVA 90:10	90	84.0	84.7±4.3
PVPVA alone	100	100	99.2±6.8

* % drug loading (by weight) was converted to % drug loading (by moles) by an appropriate conversion factor after considering average molecular weight for single unit of IND and PVPVA.

$$y = 0.9955x + 0.1056$$
$$R^2 = 0.9986$$
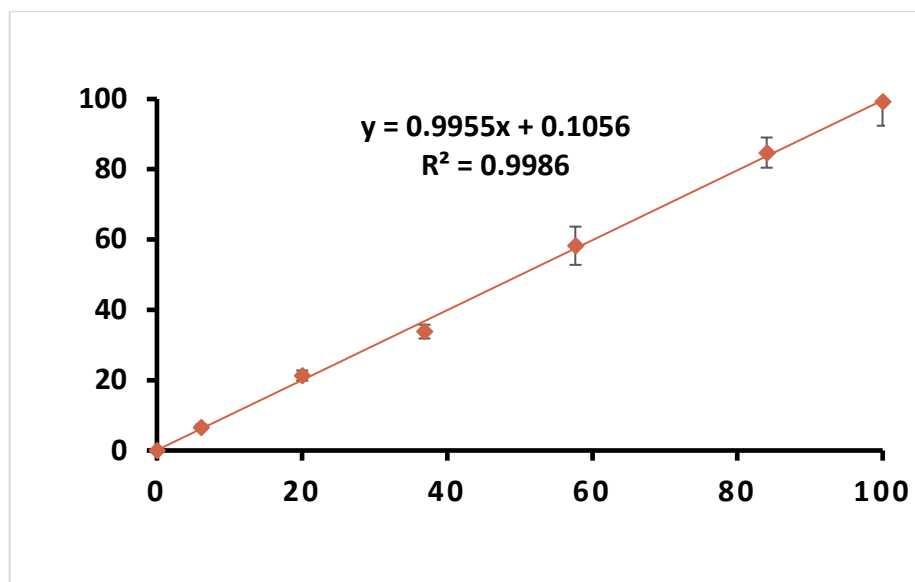
Figure C11. Linear regression model between experimentally determined % Cl/N atomic ratio via SEM/ EDX analysis and corresponding % drug loading (by moles) for IND alone, PVPVA alone and standard drug loading ASD tablets (as prepared).
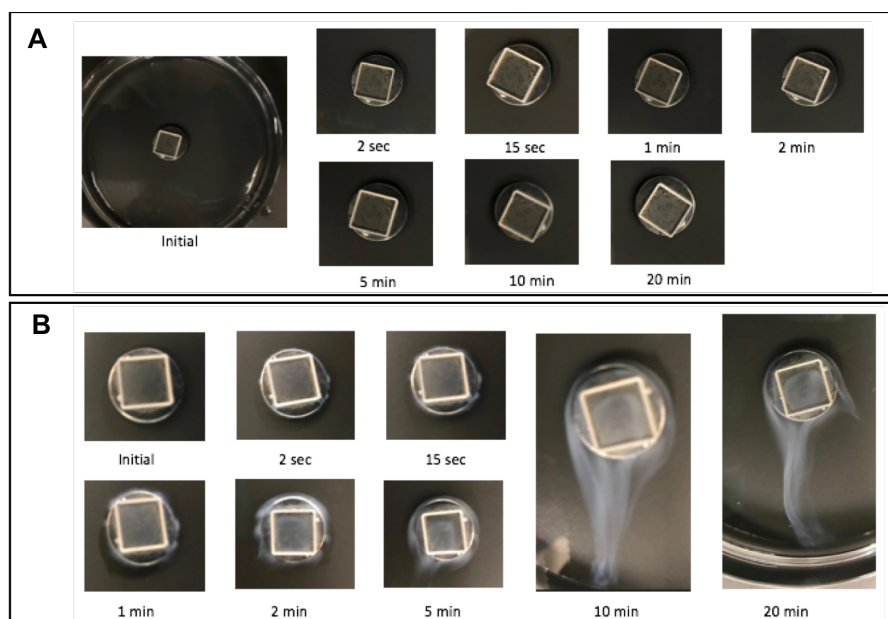
Figure C12. Representative images of IND:PVPVA 25:75 ASD film (Panel A) and INDester:PVPVA 25:75 ASD film (Panel B) at different time points after immersing in the buffer solution in a Petri dish.
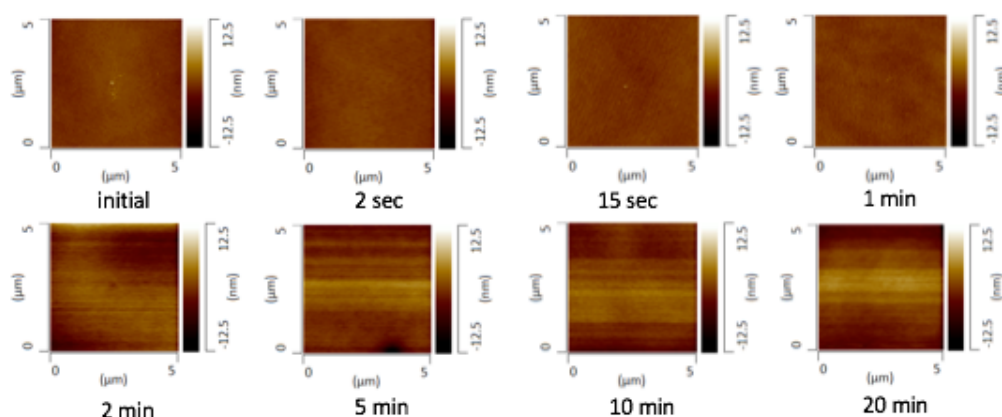
Figure C13. AFM topographical images of spin coated films of INDester:PVPVA 25:75 ASD after buffer immersion for different time intervals.

Section C4: *Lorentz contact resonance (LCR) spectroscopy*

To determine the endpoint (if exists) of INDester:ASD 25:75 ASD film dissolution, the first flexural resonance peak of LCR spectrum (the first and usually the largest peak) from the sample surface was chosen to differentiate between a substrate with a residual ASD film versus a bare substrate. As shown in Figure C14(A), the first flexural resonance peak for an ASD film has a lower frequency than a bare ZnS substrate, indicating that the substrate is stiffer than the ASD film,

thereby enabling the use of LCR spectroscopy to determine the dissolution endpoint, i.e., when the film has completely dissolved after a certain time of buffer immersion. As shown in Figure C14(B) and C14(C), the first flexural resonance peak of the mechanical spectra taken from the sample surface shifted towards higher frequency as a function of buffer immersion time, subsequently plateauing at a value corresponding to the bare substrate, indicating thinning of the ASD film due to dissolution until the complete film dissolved, which is at about 2 minutes in this case. It is worth noting that although LCR is strictly a surface sensitive technique, when the ASD film thickness is in the range of 10 s of nanometers (from an originally ~100-200 nm thick film) due to thinning upon dissolution, the resultant resonance peak may be a combination of the stiffness of ASD film and underlying substrate, giving intermediate resonance frequencies between the ASD film and ZnS substrate at intermediate dissolution timepoints.[184]
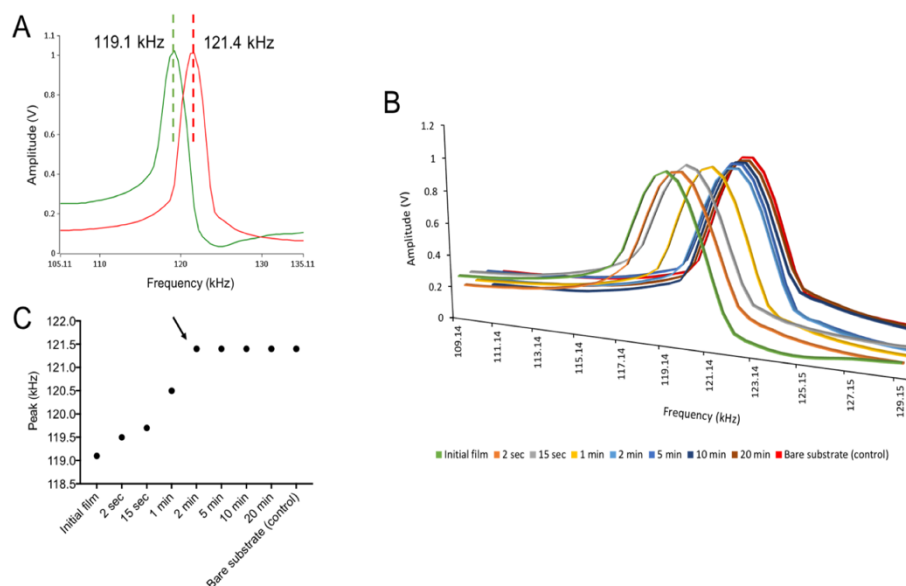
Figure C14. Reference mechanical spectra of INDester:PVPVA 25:75 ASD film and a bare substrate (control) (A). Mechanical spectra obtained from the ASD film initially and at various time points (corresponding to legends in the figure) after buffer immersion (B). The first flexural resonance peak of LCR spectrum as a function of time elapsed after buffer immersion of the ASD film (C).
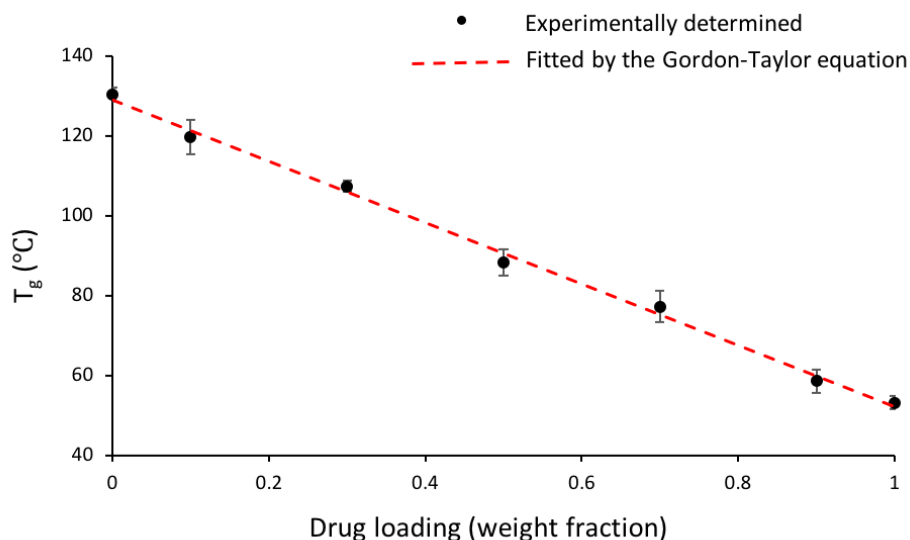
Figure C15. T_g of IND alone, PVPVA alone and IND:PVPVA ASD films of different drug loadings as determined by nanoTA. The dashed line represents the T_g fitted by the Gordon-Taylor equation and the data points represent the experimentally determined T_g. Error bars represent standard deviations, n=3.

Section C5: *T_g measurement of the water-saturated IND-PVPVA 70:30 ASD (Wet T_g)*

The T_g of the water-saturated 70% DL IND-PVPVA ASD was determined by placing the ASD in a 100% RH chamber at 37°C and periodically weighing the sample to the nearest 0.01 mg. Samples were weighed every 30 minutes until a constant mass was achieved between two consecutive readings (less than 0.1% weight change), whereupon the sample was considered 'water-saturated'. This occurred by the 4 hour timepoint and T_g of this water-saturated ASD, also designated as 'the wet T_g', was determined by differential scanning calorimeter (DSC) in modulation mode with a refrigerated cooling accessory (TA Instruments, New Castle, DE) in a hermetically sealed pan. The temperature was increased at a rate of 2°C/min with a modulation frequency of ±1°C every 60 seconds and a nitrogen flow of 50 mL/min. The wet T_g of water-saturated IND-PVPVA 70:30 ASD was determined to have an onset of 18°C, which is about 45°C lower than the initial ASD which had a dry T_g of 63°C. An overlay of the DSC thermograms showing the wet and dry T_gs of IND-PVPVA 70:30 ASD is shown in Figure C16. Note that the water sorbed by the water-saturated IND-PVPVA ASD at 100% RH was approximately 6% based on the weight gained in the 100% RH chamber upon equilibration. This value was in good agreement with the one obtained by extrapolation of the moisture sorption isotherm of the IND:PVPVA 70:30 ASD (37°C) to 100% RH (isotherm is shown in Figure C17). The moisture sorption profile was obtained using a

symmetric vapor sorption analyzer SGA-100 (VTI Instrument, Irvine, CA) with a 5% step increase in the relative humidity (RH) from 5% to 95%.
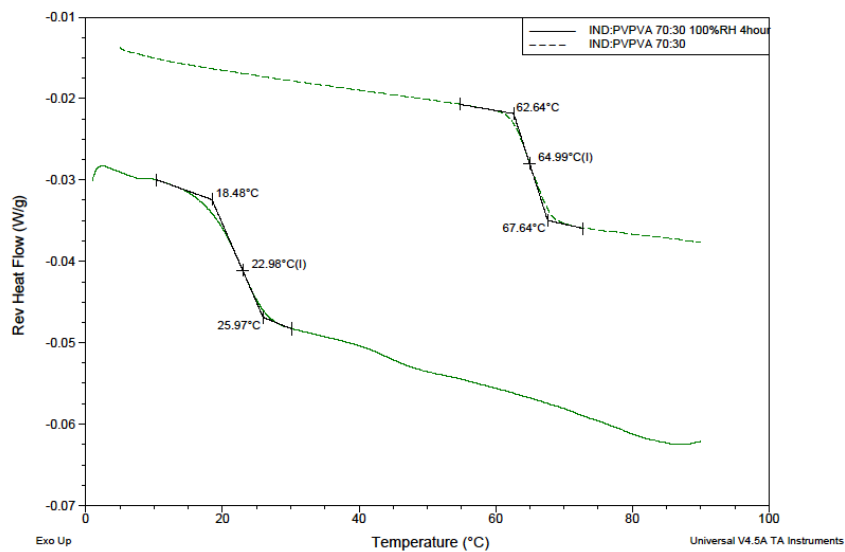
Figure C16. Representative mDSC reverse heat flow curves indicating the dry T_g of IND:PVPVA 70:30 ASD (upper curve) and wet Tg of water-saturated IND:PVPVA 70:30 ASD after equilibration at 100%RH for 4 hours at 37°C (lower curve).
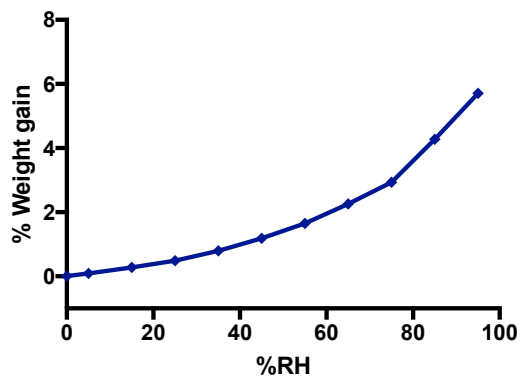
Figure C17. Water sorption profile of the IND:PVPVA 70:30 ASD at 37°C.

Section S6: *Information depth of the three analytical techniques used for elemental composition quantitation in this study*

Attenuated total reflectance-Fourier transform infrared (ATR-FTIR) spectroscopy:

ATR-FTIR penetration depth (d_p) depends on the wavelength of interest (λ), refractive indices of ATR crystal (n_1) and sample (n_2) and the angle of the entering light beam (θ) as given by the following equation C2:[185]

$$d_p = \frac{\lambda}{2\pi(n_1^2 Sin^2\theta - n_2^2)^{1/2}} \qquad (C2)$$

In this study, diamond crystal was utilized as the ATR crystal with a refractive index of 2.4 (n_1 = 2.4) and the angle of the entering light beam for the spectrometer used was 45°. Typical values of refractive indices for organic substances range from ca. 1.2 to 1.5 (n_2 = 1.2-1.5). The two wavelengths of interest for this study, 1591 cm^{-1} and 1634 cm^{-1}, were then fit into equation C2 to determine penetration depth as shown in table C2.

Table C2: Penetration depth (d_p) (μ) of ATR-FTIR for reasonably assumed range of refractive indices for the sample (1.2-1.5) and wavelengths of interest (1591 cm^{-1} and 1634 cm^{-1}) for this study:

	n_2 = 1.2	n_2 = 1.5
λ = 1634 cm^{-1}	2.17	1.22
λ = 1591 cm^{-1}	2.11	1.25

SEM/EDX analysis

The size of the microvolume affected by the electron beam and thus the information depth of the SEM/EDX analysis was determined using Monte-Carlo-based simulation software Win X-ray,[186] and found to be 600 nm for indomethacin and 800 nm for PVPVA. The information depth for ASDs is anticipated to lie between these two extremes, i.e., 600-800 nm based on the drug loading.

The parameters used for Win X-ray simulation were kept same as the parameters used for EDX data collection, i.e, 5 keV of accelerating voltage and a spot size of 4 nm. A representative graphic of the simulated electron trajectories obtained using Win X-ray for indomethacin sample is shown in Figure C18.
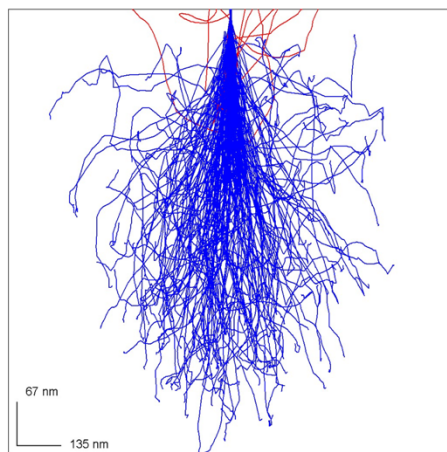
Figure C18. A representative graphic of the simulated electron trajectories obtained using Win X-ray for indomethacin sample for an accelerating voltage of 5 keV and a spot size of 4 nm.

AFM nanoTA

AFM-based thermal analysis (nanoTA) technique is a highly surface sensitive technique for which the depth sensitivity varies depending on the thermomechanical properties of the material but has been found in the order of 50 nm for pharmaceutical materials. [184]

APPENDIX D

Supporting information for Chapter 5
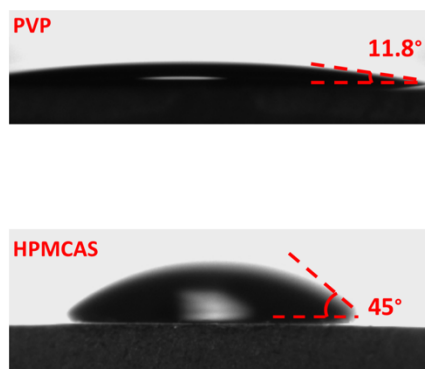
Figure D1. Representative optical images of pH 6.8 buffer drops on polyvinylpyrrolidone (PVP) and hydroxypropylmethylcellulose acetate succinate (HPMCAS) films showing the range of contact angle measurements.

Section D1: *Octanol-water partition coefficient (logP)*

To measure the partition coefficient (LogP), the aqueous phase was a phosphate buffer solution of pH 6.5 (saturated with 1-Octanol). Note that all compounds used in this study are predominantly un-ionized across the pH range. A bi-phasic medium consisting of equal volume ratios of octanol and aforementioned aqueous medium was used for the experiment. A predefined drug concentration was dissolved into the organic phase from a solid and the two phases were vigorously mixed together for 24 hours. Afterwards, both phases were separated and drug was quantified in both phases using LC-MS. Log P was then determined using the equation D1:

$$\text{logP} = \log \frac{[\text{drug concentration}]_{\text{octanol}}}{[\text{drug concentration}]_{\text{aqueous buffer}}} \qquad (D1)$$

Table D1: Crystalline solubility values of felodipine in the presence of 1000 µg/mL of polymers at 37°C in pH 6.8 phosphate buffer. Values are given as the mean of 3 samples ± standard deviation.

Felodipine	solubility (µg/mL)
w/PVP	1.2 ± 0.2
w/PVPVA	1.1 ± 0.0
w/HPMC	1.3 ± 0.1
w/HPMCAS	0.9 ± 0.3
w/EUDS*	1.4 ± 0.1

*pH 7.4 phosphate buffer was used for EUDS
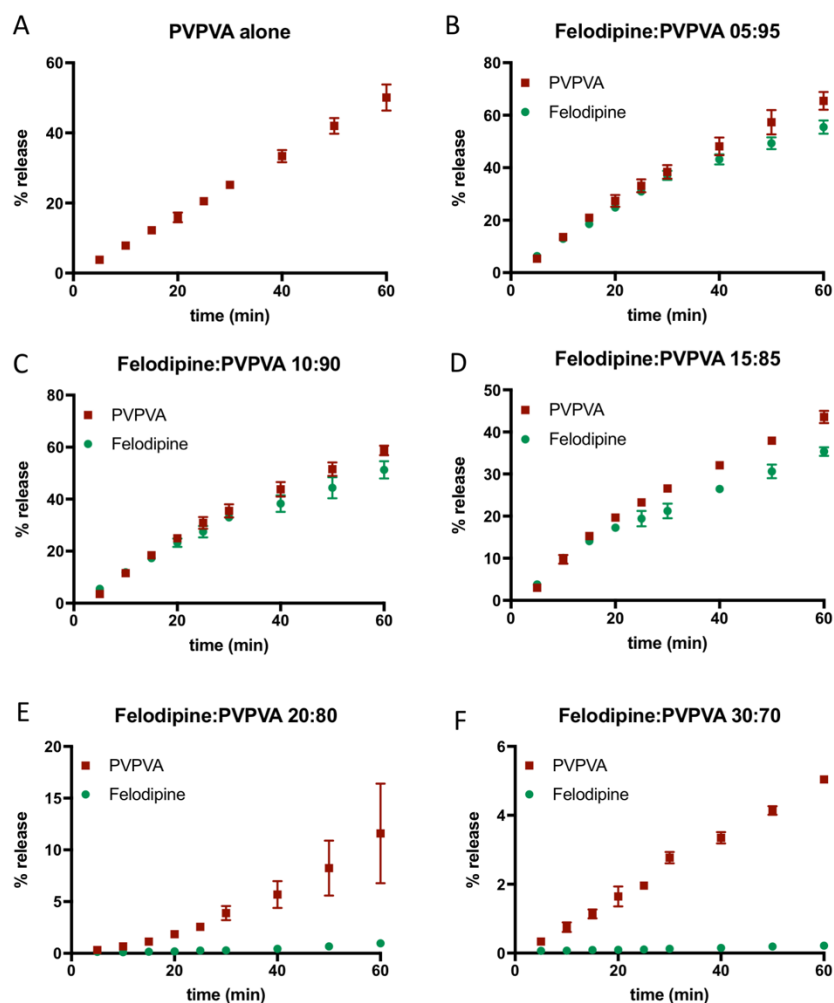
Figure D2. Percent release versus time profiles for PVPVA alone and Fel-PVPVA ASDs at different drug loadings. The ratios in the legend represent drug:polymer weight ratios in the ASDs. Error bars represent standard deviations, n=3.
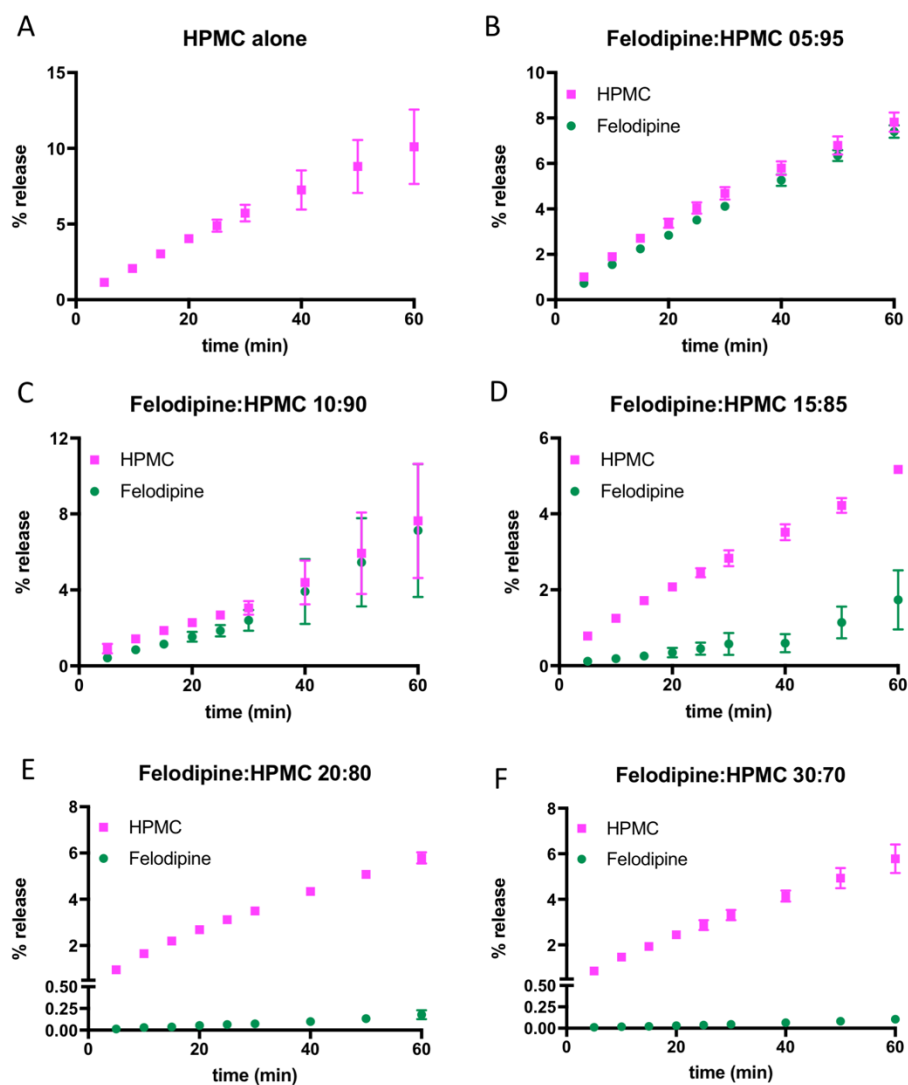
Figure D3. Percent release versus time profiles for HPMC alone and Fel-HPMC ASDs at different drug loadings. The ratios in the legend represent drug:polymer weight ratios in the ASDs. Error bars represent standard deviations, n=3.
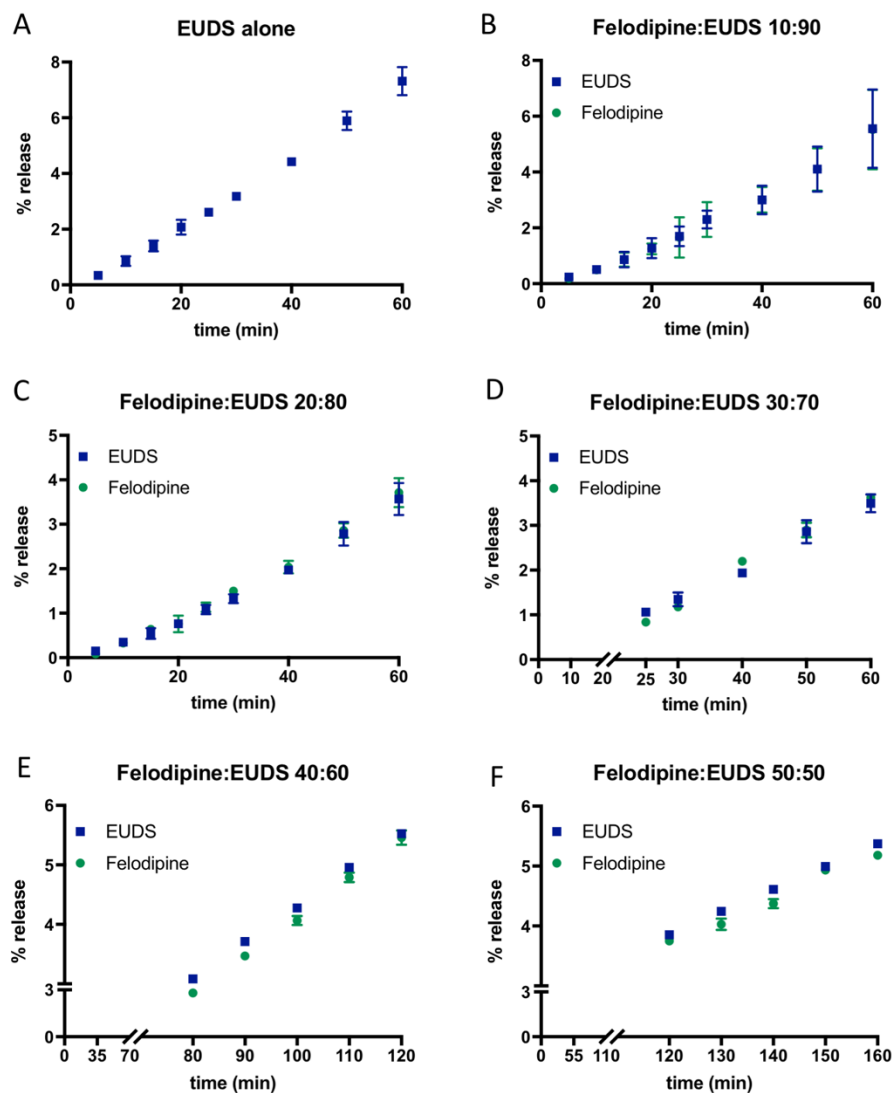
Figure D4. Percent release versus time profiles for EUDS alone and Fel-EUDS ASDs at different drug loadings. The ratios in the legend represent drug:polymer weight ratios in the ASDs. Error bars represent standard deviations, n=3.
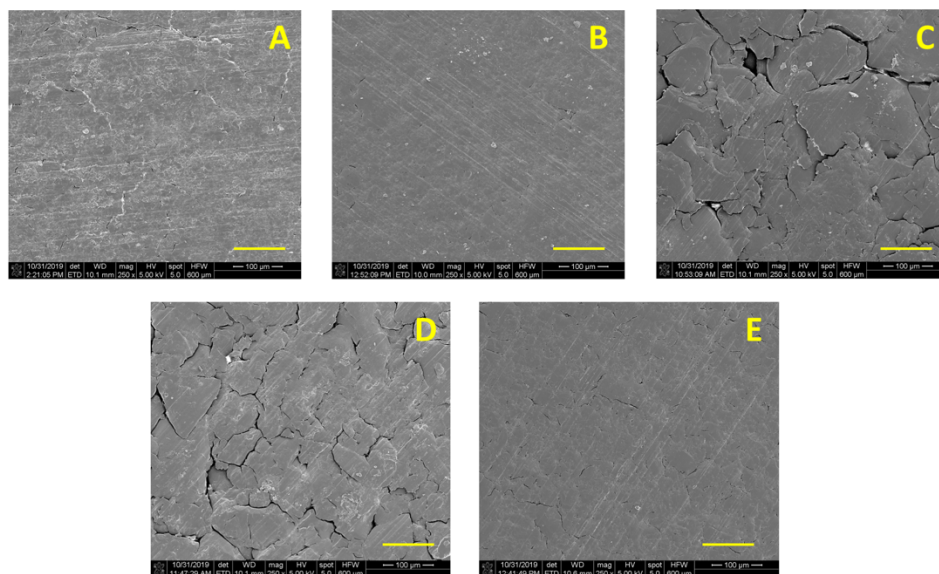
Figure D5. SEM images of initial ASD tablet surfaces (before dissolution) for Fel-PVP (A), Fel-PVPVA (B), Fel-HPMC (C), Fel-HPMCAS (D) and Fel-EUDS (E) at 30% DL. Scale bar is 100 μm.
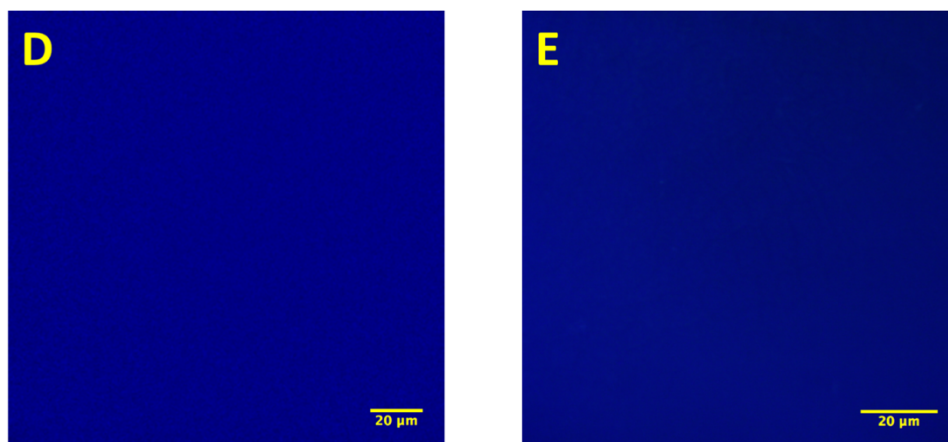
Figure D6. Representative confocal fluorescence microscopy images (at low magnification) of 30% DL felodipine ASDs after exposure to moisture with polymers: HPMCAS (D) and EUDS (E). Nomenclature has been matched with Fig. 12 of the main article.
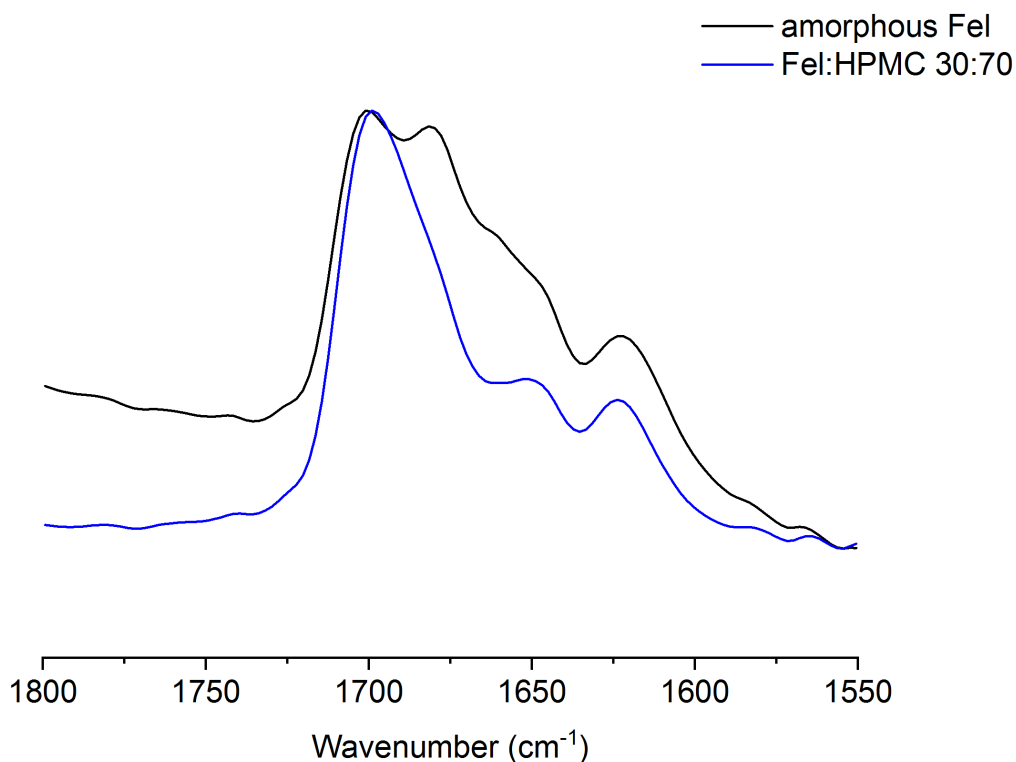
Figure D7. Infrared spectra showing the carbonyl stretching region (1550-1800 cm^{-1}) for amorphous felodipine and felodipine-HPMC ASD at 30% drug loading. Amorphous felodipine shows a doublet at 1701 cm^{-1} and 1682 cm^{-1}; while for felodipine-HPMC ASD, the peak at 1682 cm^{-1} is not discernable, and a single slightly broader peak is located at 1699 cm^{-1}.

Section D2: *Estimated water sorption (wt%) of the water-saturated HPMCAS ASDs with different drugs*

The water sorbed (% wt gain) by the water-saturated 40% DL HPMCAS ASDs of nilvadipine (Nil), felodipine (Fel) and cilnidipine (Cil) at 100% RH based on extrapolation from the moisture sorption isotherm of the respective ASDs at 37°C (Figure D8). The moisture sorption profile was obtained using a dynamic vapor sorption analyzer DVS Resolution (Surface Measurement Systems, Allentown, PA) with a 5% step increase in the relative humidity (RH) from 5% to 95%.
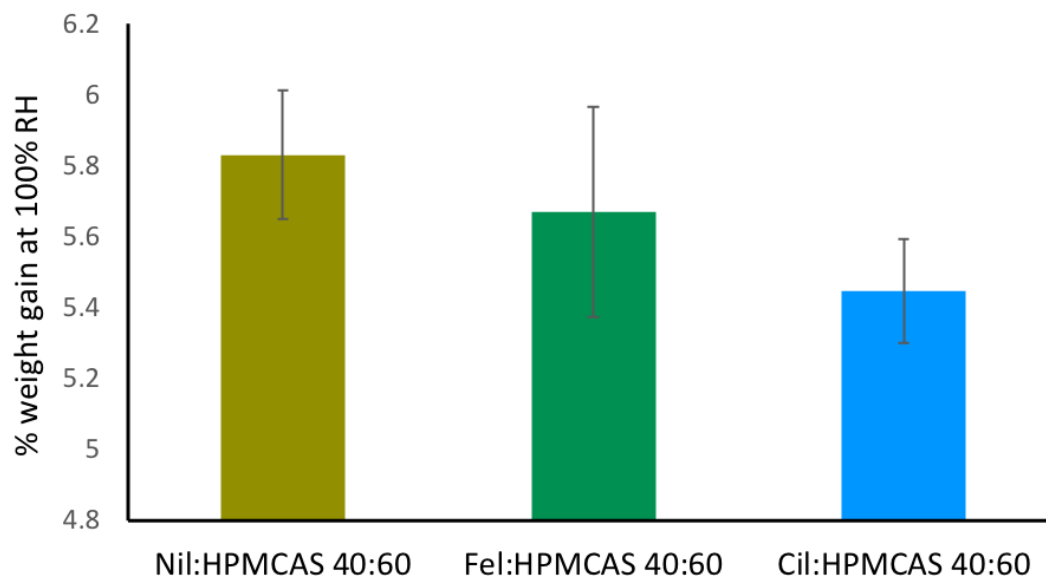
Figure D8. Estimated water sorbed (% weight gain) at 100 %RH based on the extrapolation from the water sorption profiles of 40% DL HPMCAS ASDs of: nilvadipine (Nil), felodipine (Fel) and cilnidipine (Cil) at 37°C. The ratios in the legend represent drug:polymer weight ratios.

Section D3. *Exemplary calculation for critical mixture ratio of Fel-PVPVA ASD*

Critical mixture ratio of Fel-PVPVA ASDs was calculated based on equation 25 of chapter 5. Amorphous solubility of felodipine was taken as the value of $C_{s(drug)}$, i.e., 8 µg/mL. $C_{s(polymer)}$ was the solubility value of PVPVA in 100 mM pH 6.8 phosphate buffer, i.e., 46 mg/ml taken from a literature reference source.[139] The ratio of the diffusion coefficients was estimated based on the Stokes-Einstein equation and following assumptions: (1) The medium through which the drug and the polymer diffuses has similar viscosity; (2) the drug molecule is about 1 nm in size and the polymer's hydrodynamic radius is about 10 nm. Thus, $D_{drug}/D_{polymer}$ was assumed to be 10. Then, based on the equation 25, the critical mixture ratio ($N_{drug}/N_{polymer}$) was estimated to be an extremely low number, 1.7×10^{-6}.

REFERENCES

1. Di, L.; Fish, P. V.; Mano, T. Bridging solubility between drug discovery and development. *Drug Discovery Today* 2012, *17*, (9), 486-495.

2. Williams, H. D.; Trevaskis, N. L.; Charman, S. A.; Shanker, R. M.; Charman, W. N.; Pouton, C. W.; Porter, C. J. Strategies to address low drug solubility in discovery and development. *Pharmacol Rev* 2013, *65*, (1), 315-499.

3. Rangel-Yagui, C. O.; Pessoa, A., Jr.; Tavares, L. C. Micellar solubilization of drugs. *J Pharm Pharm Sci* 2005, *8*, (2), 147-65.

4. Leuner, C.; Dressman, J. Improving drug solubility for oral delivery using solid dispersions. *Eur J Pharm Biopharm* 2000, *50*, (1), 47-60.

5. Anby, M. U.; Williams, H. D.; McIntosh, M.; Benameur, H.; Edwards, G. A.; Pouton, C. W.; Porter, C. J. Lipid digestion as a trigger for supersaturation: evaluation of the impact of supersaturation stabilization on the in vitro and in vivo performance of self-emulsifying drug delivery systems. *Mol Pharm* 2012, *9*, (7), 2063-79.

6. Huang, Y.; Dai, W.-G. Fundamental aspects of solid dispersion technology for poorly soluble drugs. *Acta Pharmaceutica Sinica. B* 2014, *4*, (1), 18-25.

7. Craig, D. Q. The mechanisms of drug release from solid dispersions in water-soluble polymers. *Int J Pharm* 2002, *231*, (2), 131-44.

8. Friesen, D. T.; Shanker, R.; Crew, M.; Smithey, D. T.; Curatolo, W. J.; Nightingale, J. A. Hydroxypropyl methylcellulose acetate succinate-based spray-dried dispersions: an overview. *Mol Pharm* 2008, *5*, (6), 1003-19.

9. Corrigan, O. I. Mechanisms of dissolution of fast release solid dispersions. *Drug Development and Industrial Pharmacy* 1985, *11*, (2-3), 697-724.

10. Corrigan, O. I. Retardation of polymeric carrier dissolution by dispersed drugs: factors influencing the dissolution of solid dispersions containing polyethlene glycols. *Drug Development and Industrial Pharmacy* 1986, *12*, (11-13), 1777-1793.

11. Dubois, J. L.; Ford, J. L. Similarities in the release rates of different drugs from polyethylene glycol 6000 solid dispersions. *J Pharm Pharmacol* 1985, *37*, (7), 494-5.

12. Craig, D. Q. M.; Newton, J. M. The dissolution of nortriptyline HCl from polyethylene glycol solid dispersions. *International Journal of Pharmaceutics* 1992, *78*, (1), 175-182.

13. Saers, E. S.; Craig, D. Q. M. An investigation into the mechanisms of dissolution of alkyl p-aminobenzoates from polyethylene glycol solid dispersions. *International Journal of Pharmaceutics* 1992, 83, (1), 211-219.

14. Sjökvist, E.; Nyström, C. Physicochemical aspects of drug release. VI. Drug dissolution rate from solid particulate dispersions and the importance of carrier and drug particle properties. *International Journal of Pharmaceutics* 1988, 47, (1), 51-66.

15. Alonzo, D. E.; Zhang, G. G.; Zhou, D.; Gao, Y.; Taylor, L. S. Understanding the behavior of amorphous pharmaceutical systems during dissolution. *Pharm Res* 2010, 27, (4), 608-18.

16. Ilevbare, G. A.; Liu, H. Y.; Edgar, K. J.; Taylor, L. S. Inhibition of solution crystal growth of ritonavir by cellulose polymers - factors influencing polymer effectiveness. *Crystengcomm* 2012, 14, (20), 6503-6514.

17. Konno, H.; Taylor, L. S. Influence of different polymers on the crystallization tendency of molecularly dispersed amorphous felodipine. *J Pharm Sci* 2006, 95, (12), 2692-705.

18. Purohit, H. S.; Taylor, L. S. Phase separation kinetics in amorphous solid dispersions upon exposure to water. *Mol Pharm* 2015, 12, (5), 1623-35.

19. Saboo, S.; Taylor, L. S. Water-induced phase separation of miconazole-poly (vinylpyrrolidone-co-vinyl acetate) amorphous solid dispersions: Insights with confocal fluorescence microscopy. *Int J Pharm* 2017, 529, (1-2), 654-666.

20. Hoff, J. H. v. t.; Ewan, T.; Cohen, E., Studies in chemical dynamics. The Chemical publishing company: Easton, Pa., 1896; p vi, 286 p.

21. Koshari, S. H. S.; Ross, J. L.; Nayak, P. K.; Zarraga, I. E.; Rajagopal, K.; Wagner, N. J.; Lenhoff, A. M. Characterization of protein–excipient microheterogeneity in biopharmaceutical solid-state formulations by confocal fluorescence microscopy. *Molecular Pharmaceutics* 2017, 14, (2), 546-553.

22. Almeida e Sousa, L.; Reutzel-Edens, S. M.; Stephenson, G. A.; Taylor, L. S. Assessment of the amorphous "solubility" of a group of diverse drugs using new experimental and theoretical approaches. *Mol Pharm* 2015, 12, (2), 484-95.

23. Chiou, W. L.; Riegelman, S. Pharmaceutical applications of solid dispersion systems. *J Pharm Sci* 1971, 60, (9), 1281-302.

24. Deneau, E.; Steele, G. An In-Line Study of Oiling Out and Crystallization. *Organic Process Research & Development* 2005, 9, (6), 943-950.

25. Special Applications. In Crystallization of Organic Compounds.

26. Bhardwaj, V.; Trasi, N. S.; Zemlyanov, D. Y.; Taylor, L. S. Surface area normalized dissolution to study differences in itraconazole-copovidone solid dispersions prepared by spray-drying and hot melt extrusion. *Int J Pharm* 2018, 540, (1-2), 106-119.

27. Granados, E. G.; González-Benito, J.; Baselga, J.; Dibbern-Brunelli, D.; Atvars, T. D. Z.; Esteban, I.; Piérola, I. F. Phase-separated polymer blends: Complementary studies between scanning electron microscopy, epifluorescence microscopy, and fluorescence microspectroscopy. *Journal of Applied Polymer Science* 2001, 80, (7), 949-955.

28. Ha Chang, S.; Ki Lee, W.; Cho Won, J. Δχ effects on the miscibility of polymer blends. *Macromolecular Symposia* 2011, 84, (1), 279-288.

29. Robard, A.; Patterson, D.; Delmas, G. The "Δη effect" and polystyrene-poly(vinyl methyl ether) compatibility in solution. *Macromolecules* 1977, 10, (3), 706-708.

30. Al-Obaidi, H.; Brocchini, S.; Buckton, G. Anomalous properties of spray dried solid dispersions. *Journal of Pharmaceutical Sciences* 2009, 98, (12), 4724-4737.

31. Vehring, R.; Foss, W. R.; Lechuga-Ballesteros, D. Particle formation in spray drying. *Journal of Aerosol Science* 2007, 38, (7), 728-746.

32. Zhu, L.; Wong, L.; Yu, L. Surface-enhanced crystallization of amorphous nifedipine. *Mol Pharm* 2008, 5, (6), 921-6.

33. Rowan, S. M.; Newton, M. I.; Driewer, F. W.; McHale, G. Evaporation of Microdroplets of Azeotropic Liquids. *The Journal of Physical Chemistry B* 2000, 104, (34), 8217-8220.

34. Purohit, H. S.; Taylor, L. S. Miscibility of itraconazole-hydroxypropyl methylcellulose blends: insights with high resolution analytical methodologies. *Mol Pharm* 2015, 12, (12), 4542-53.

35. Pethrick, R. Polymer physics. Edited by Michael Rubinstein and Ralph H Colby Oxford University Press, Oxford, 2003. ISBN 019852059X. pp 440. Polymer International 2004, 53, (9), 1394-1395.

36. Murdande, S. B.; Pikal, M. J.; Shanker, R. M.; Bogner, R. H. Solubility advantage of amorphous pharmaceuticals: I. A thermodynamic analysis. *Journal of Pharmaceutical Sciences* 99, (3), 1254-1264.

37. Brouwers, J.; Brewster, M. E.; Augustijns, P. Supersaturating drug delivery systems: the answer to solubility-limited oral bioavailability? *J Pharm Sci* 2009, 98, (8), 2549-72.

38. Dahan, A.; Beig, A.; Ioffe-Dahan, V.; Agbaria, R.; Miller, J. M. The twofold advantage of the amorphous form as an oral drug delivery practice for lipophilic compounds: increased apparent solubility and drug flux through the intestinal membrane. *AAPS J* 2013, 15, (2), 347-53.

39. Newman, A.; Knipp, G.; Zografi, G. Assessing the performance of amorphous solid dispersions. *J Pharm Sci* 2012, 101, (4), 1355-77.

40. Paul, H. L., L.; Patrick, M.; Craig, M.; Narayan, V.; Wei, X.; Wei, X. Amorphous Solid Dispersions: Analytical challenges and Opportunities. *AAPS Newsmagazine* September 2009.

41. Van den Mooter, G.; Wuyts, M.; Blaton, N.; Busson, R.; Grobet, P.; Augustijns, P.; Kinget, R. Physical stabilisation of amorphous ketoconazole in solid dispersions with polyvinylpyrrolidone K25. *Eur J Pharm Sci* 2001, 12, (3), 261-9.

42. Hancock, B. C.; Zografi, G. The Relationship Between the Glass Transition Temperature and the Water Content of Amorphous Pharmaceutical Solids. *Pharmaceutical Research* 1994, 11, (4), 471-477.

43. Aso, Y.; Yoshioka, S. Molecular mobility of nifedipine-PVP and phenobarbital-PVP solid dispersions as measured by 13C-NMR spin-lattice relaxation time. *J Pharm Sci* 2006, 95, (2), 318-25.

44. Marsac, P. J.; Shamblin, S. L.; Taylor, L. S. Theoretical and practical approaches for prediction of drug-polymer miscibility and solubility. *Pharm Res* 2006, 23, (10), 2417-26.

45. Khougaz, K.; Clas, S. D. Crystallization inhibition in solid dispersions of MK-0591 and poly(vinylpyrrolidone) polymers. *J Pharm Sci* 2000, 89, (10), 1325-34.

46. Taylor, L. S.; Zografi, G. Spectroscopic characterization of interactions between PVP and indomethacin in amorphous molecular dispersions. *Pharm Res* 1997, 14, (12), 1691-8.

47. Noyes, A. A.; Whitney, W. R. The rate of solution of solid substances in their own solutions. *Journal of the American Chemical Society* 1897, 19, (12), 930-934.

48. Higuchi, W. I.; Mir, N. A.; Desai, S. J. Dissolution rates of polyphase mixtures. *J Pharm Sci* 1965, 54, (10), 1405-10.

49. Rumondor, A. C. F.; Jackson, M. J.; Taylor, L. S. Effects of Moisture on the Growth Rate of Felodipine Crystals in the Presence and Absence of Polymers. *Crystal Growth & Design* 2010, 10, (2), 747-753.

50. Rumondor, A. C.; Ivanisevic, I.; Bates, S.; Alonzo, D. E.; Taylor, L. S. Evaluation of drug-polymer miscibility in amorphous solid dispersion systems. *Pharm Res* 2009, 26, (11), 2523-34.

51. Karthika, S.; Radhakrishnan, T. K.; Kalaichelvi, P. A Review of classical and nonclassical nucleation theories. *Crystal Growth & Design* 2016, 16, (11), 6663-6681.

52. Mullin, J. W., Crystallization. 4th ed.. ed.; Oxford ; Boston : Butterworth-Heinemann: Oxford ; Boston, 2001.

53. Erdemir, D.; Lee, A. Y.; Myerson, A. S. Nucleation of crystals from solution: classical and two-step models. *Accounts of Chemical Research* 2009, 42, (5), 621-629.

54. Jackson, K. A. On the theory of crystal growth: The fundamental rate equation. *Journal of Crystal Growth* 1969, 5, (1), 13-18.

55. Sun, Y.; Zhu, L.; Wu, T.; Cai, T.; Gunn, E. M.; Yu, L. Stability of amorphous pharmaceutical solids: crystal growth mechanisms and effect of polymer additives. *AAPS J* 2012, 14, (3), 380-8.

56. Physical Stability and Crystallization Inhibition. In Pharmaceutical Sciences Encyclopedia.

57. Newman, A., Pharmaceutical amorphous solid dispersions. Hoboken, New Jersey : Wiley: 2015.

58. Masayasu, S.; Hiroshi, S.; Syûzô, S. Calorimetric Study of the Glassy State. IV. Heat capacities of glassy water and cubic ice. *Bulletin of the Chemical Society of Japan* 1968, 41, (11), 2591-2599.

59. Andronis, V.; Yoshioka, M.; Zografi, G. Effects of sorbed water on the crystallization of indomethacin from the amorphous state. *J Pharm Sci* 1997, 86, (3), 346-51.

60. Indulkar, A. S.; Waters, J. E.; Mo, H.; Gao, Y.; Raina, S. A.; Zhang, G. G. Z.; Taylor, L. S. Origin of nanodroplet formation upon dissolution of an amorphous solid dispersion: A mechanistic isotope scrambling study. *Journal of Pharmaceutical Sciences* 106, (8), 1998-2008.

61. Rumondor, A. C.; Wikstrom, H.; Van Eerdenbrugh, B.; Taylor, L. S. Understanding the tendency of amorphous solid dispersions to undergo amorphous-amorphous phase separation in the presence of absorbed moisture. *AAPS PharmSciTech* 2011, 12, (4), 1209-19.

62. Tung, H.-H., Crystallization of organic compounds an industrial perspective. Hoboken, N.J. : Wiley: Hoboken, N.J., 2009.

63. Ilevbare, G. A.; Taylor, L. S. Liquid-liquid phase separation in highly supersaturated aqueous solutions of poorly water-soluble drugs: implications for solubility enhancing formulations. *Crystal Growth & Design* 2013, 13, (4), 1497-1509.

64. Taylor, L. S.; Zhang, G. G. Z. Physical chemistry of supersaturated solutions and implications for oral absorption. *Adv Drug Deliv Rev* 2016, 101, 122-142.

65. Raina, S. A.; Zhang, G. G. Z.; Alonzo, D. E.; Wu, J.; Zhu, D.; Catron, N. D.; Gao, Y.; Taylor, L. S. Enhancements and limits in drug membrane transport using supersaturated solutions of poorly water soluble drugs. *J Pharm Sci* 2014, 103, (9), 2736-2748.

66. Wilson, V.; Lou, X.; Osterling, D. J.; Stolarik, D. F.; Jenkins, G.; Gao, W.; Zhang, G. G. Z.; Taylor, L. S. Relationship between amorphous solid dispersion in vivo absorption and in vitro dissolution: phase behavior during dissolution, speciation, and membrane mass transport. *J Control Release* 2018, 292, 172-182.

67. Thayer, A. M. Finding Solutions. Chem. Eng. News 2010, 88, (22), 13-18.

68. Rumondor, A. C.; Stanford, L. A.; Taylor, L. S. Effects of polymer type and storage relative humidity on the kinetics of felodipine crystallization from amorphous solid dispersions. *Pharm Res* 2009, 26, (12), 2599-606.

69. Yu, L. Amorphous pharmaceutical solids: preparation, characterization and stabilization. *Adv Drug Deliv Rev* 2001, 48, (1), 27-42.

70. Qian, F.; Huang, J.; Zhu, Q.; Haddadin, R.; Gawel, J.; Garmise, R.; Hussain, M. Is a distinctive single Tg a reliable indicator for the homogeneity of amorphous solid dispersion? *Int J Pharm* 2010, 395, (1-2), 232-5.

71. Marsac, P. J.; Rumondor, A. C.; Nivens, D. E.; Kestur, U. S.; Stanciu, L.; Taylor, L. S. Effect of temperature and moisture on the miscibility of amorphous dispersions of felodipine and poly(vinyl pyrrolidone). *J Pharm Sci* 2010, 99, (1), 169-85.

72. Newman, A.; Engers, D.; Bates, S.; Ivanisevic, I.; Kelly, R. C.; Zografi, G. Characterization of amorphous API:Polymer mixtures using X-ray powder diffraction. *J Pharm Sci* 2008, 97, (11), 4840-56.

73. Lauer, M. E.; Siam, M.; Tardio, J.; Page, S.; Kindt, J. H.; Grassmann, O. Rapid assessment of homogeneity and stability of amorphous solid dispersions by atomic force microscopy--from bench to batch. *Pharm Res* 2013, 30, (8), 2010-22.

74. Karavas, E.; Georgarakis, M.; Docoslis, A.; Bikiaris, D. Combining SEM, TEM, and micro-Raman techniques to differentiate between the amorphous molecular level dispersions and nanodispersions of a poorly water-soluble drug within a polymer matrix. *Int J Pharm* 2007, 340, (1-2), 76-83.

75. Keratichewanun, S.; Yoshihashi, Y.; Sutanthavibul, N.; Terada, K.; Chatchawalsaisin, J. An investigation of nifedipine miscibility in solid dispersions using Raman spectroscopy. *Pharm Res* 2015, 32, (7), 2458-73.

76. Vogt, F. G., Solid-State Characterization of Amorphous Dispersions. In Pharmaceutical Sciences Encyclopedia, John Wiley & Sons, Inc.: 2010.

77. Li, N.; Taylor, L. S. Nanoscale infrared, thermal, and mechanical characterization of telaprevir-polymer miscibility in amorphous solid dispersions prepared by solvent evaporation. *Mol Pharm* 2016, 13, (3), 1123-36.

78. Tian, B.; Tang, X.; Taylor, L. S. Investigating the correlation between miscibility and physical stability of amorphous solid dispersions using fluorescence-based techniques. *Mol Pharm* 2016, 13, (11), 3988-4000.

79. Purohit, H. S.; Ormes, J. D.; Saboo, S.; Su, Y.; Lamm, M. S.; Mann, A. K. P.; Taylor, L. S. Insights into nano- and micron-scale phase separation in amorphous solid dispersions using fluorescence-based techniques in combination with solid state nuclear magnetic resonance spectroscopy. *Pharm Res* 2017, 34, (7), 1364-1377.

80. Singh, A.; De Bisschop, C.; Schut, H.; Van Humbeeck, J.; Van Den Mooter, G. Compression effects on the phase behaviour of miconazole-poly (1-vinylpyrrolidone-co-vinyl acetate) solid dispersions-role of pressure, dwell time, and preparation method. *J Pharm Sci* 2015, 104, (10), 3366-76.

81. Singh, A.; Van Humbeeck, J.; Van den Mooter, G. A new twist in the old story-can compression induce mixing of phase separated solid dispersions? A case study of spray-dried miconazole-PVP VA64 solid dispersions. *Pharm Res* 2014, 31, (11), 3191-200.

82. Worku, Z. A.; Aarts, J.; Singh, A.; Van den Mooter, G. Drug-polymer miscibility across a spray dryer: a case study of naproxen and miconazole solid dispersions. *Mol Pharm* 2014, 11, (4), 1094-101.

83. Marcott, C.; Lo, M.; Kjoller, K.; Prater, C.; Noda, I. Spatial differentiation of sub-micrometer domains in a poly(hydroxyalkanoate) copolymer using instrumentation that combines atomic force microscopy (AFM) and infrared (IR) spectroscopy. *Appl Spectrosc* 2011, 65, (10), 1145-50.

84. Khanal, D.; Dillon, E.; Hau, H.; Fu, D.; Ramzan, I.; Chrzanowski, W. Lorentz contact resonance spectroscopy for nanoscale characterisation of structural and mechanical properties of biological, dental and pharmaceutical materials. *J Mater Sci Mater Med* 2015, 26, (12), 272.

85. Somnath, S.; Liu, J. O.; Bakir, M.; Prater, C. B.; King, W. P. Multifunctional atomic force microscope cantilevers with Lorentz force actuation and self-heating capability. *Nanotechnology* 2014, 25, (39), 395501.

86. Lee, B.; Prater, C. B.; King, W. P. Lorentz force actuation of a heated atomic force microscope cantilever. *Nanotechnology* 2012, 23, (5), 055709.

87. Van Eerdenbrugh, B.; Taylor, L. S. Application of mid-IR spectroscopy for the characterization of pharmaceutical systems. *Int J Pharm* 2011, 417, (1-2), 3-16.

88. Lauer, M. E.; Grassmann, O.; Siam, M.; Tardio, J.; Jacob, L.; Page, S.; Kindt, J. H.; Engel, A.; Alsenz, J. Atomic force microscopy-based screening of drug-excipient miscibility and stability of solid dispersions. *Pharmaceutical Research* 2011, 28, (3), 572-584.

89. Coates, J., Interpretation of Infrared Spectra, A Practical Approach. In Encyclopedia of Analytical Chemistry, John Wiley & Sons, Ltd: 2006.

90. Harrison, A. J.; Bilgili, E. A.; Beaudoin, S. P.; Taylor, L. S. Atomic Force Microscope Infrared Spectroscopy of Griseofulvin Nanocrystals. *Analytical Chemistry* 2013, 85, (23), 11449-11455.

91. Van Eerdenbrugh, B.; Lo, M.; Kjoller, K.; Marcott, C.; Taylor, L. S. Nanoscale mid-infrared imaging of phase separation in a drug-polymer blend. *J Pharm Sci* 2012, 101, (6), 2066-73.

92. Dillon, E.; Kjoller, K.; Prater, C. Lorentz contact resonance imaging for atomic force microscopes: probing mechanical and thermal properties on the nanoscale. *Microscopy Today* 2013, 21, (6), 18-24.

93. Li, N.; Gilpin, C. J.; Taylor, L. S. Understanding the impact of water on the miscibility and microstructure of amorphous solid dispersions: An AFM–LCR and TEM–EDX study. *Molecular Pharmaceutics* 2017, 14, (5), 1691-1705.

94. Brelje, T. C.; Wessendorf, M. W.; Sorenson, R. L. Multicolor laser scanning confocal immunofluorescence microscopy: practical application and limitations. *Methods Cell Biol* 2002, 70, 165-244.

95. Margulies, D.; Melman, G.; Shanzer, A. Fluorescein as a model molecular calculator with reset capability. *Nat Mater* 2005, 4, (10), 768-771.

96. Milanova, D.; Chambers, R. D.; Bahga, S. S.; Santiago, J. G. Electrophoretic mobility measurements of fluorescent dyes using on-chip capillary electrophoresis. *Electrophoresis* 2011, 32, (22), 3286-94.

97. Diaspro, A.; Chirico, G.; Usai, C.; Ramoino, P.; Dobrucki, J., Photobleaching. In handbook of biological confocal microscopy, Pawley, J. B., Ed. Springer US: Boston, MA, 2006; pp 690-702.

98. Tsien, R. Y.; Ernst, L.; Waggoner, A., Fluorophores for confocal microscopy: photophysics and photochemistry. In Handbook Of Biological Confocal Microscopy, Pawley, J. B., Ed. Springer US: Boston, MA, 2006; pp 338-352.

99. Castleman, K. R. Digital image color compensation with unequal integration periods. Bioimaging 1994, 2, (3), 160-162.

100. Hellmann, E. H.; Hellmann, G. P.; Rennie, A. R. Solvent-induced phase separation in polycarbonate blends PC/TMPC. *Colloid and Polymer Science* 1991, 269, (4), 343-352.

101. Pouchlý, J.; Patterson, D. Polymers in Mixed Solvents. *Macromolecules* 1976, 9, (4), 574-579.

102. Rumondor, A. C. F.; Taylor, L. S. Effect of polymer hygroscopicity on the phase behavior of amorphous solid dispersions in the presence of moisture. *Molecular Pharmaceutics* 2010, 7, (2), 477-490.

103. Rumondor, A. C. F.; Marsac, P. J.; Stanford, L. A.; Taylor, L. S. Phase behavior of Poly(vinylpyrrolidone) Containing Amorphous Solid Dispersions in the Presence of Moisture. *Molecular Pharmaceutics* 2009, 6, (5), 1492-1505.

104. Vasanthavada, M.; Tong, W. Q.; Joshi, Y.; Kislalioglu, M. S. Phase behavior of amorphous molecular dispersions II: Role of hydrogen bonding in solid solubility and phase separation kinetics. *Pharm Res* 2005, 22, (3), 440-8.

105. Dibbern-Brunelli, D.; Atvars, T. D. Z.; Joekes, I.; Barbosa, V. C. Mapping phases of poly(vinyl alcohol) and poly(vinyl acetate) blends by FTIR microspectroscopy and optical fluorescence microscopy. *Journal of Applied Polymer Science* 1998, 69, (4), 645-655.

106. Johnson, I., The Molecular Probes Handbook: A Guide to Fluorescent Probes and Labeling Technologies, 11th Edition. Life Technologies Corporation: 2010.

107. Abbe, E. Beiträge zur Theorie des Mikroskops und der mikroskopischen Wahrnehmung. *Archiv für mikroskopische Anatomie* 1873, 9, (1), 413-418.

108. Purohit, H. S.; Ormes, J. D.; Saboo, S.; Su, Y.; Lamm, M. S.; Mann, A. K. P.; Taylor, L. S. Insights into nano- and micron-scale phase separation in amorphous solid dispersions using fluorescence-based techniques in combination with solid state nuclear magnetic resonance spectroscopy. *Pharmaceutical Research* 2017, 1-14.

109. Sagui, C.; Grant, M. Theory of nucleation and growth during phase separation. *Physical Review E* 1999, 59, (4), 4175-4187.

110. Tres, F.; Posada, M. M.; Hall, S. D.; Mohutsky, M. A.; Taylor, L. S. Mechanistic understanding of the phase behavior of supersaturated solutions of poorly water-soluble drugs. *Int J Pharm* 2018, 543, (1-2), 29-37.

111. Indulkar, A. S.; Gao, Y.; Raina, S. A.; Zhang, G. G. Z.; Taylor, L. S. Exploiting the phenomenon of liquid–liquid phase separation for enhanced and sustained Membrane Transport of a Poorly Water-Soluble Drug. *Molecular Pharmaceutics* 2016, 13, (6), 2059-2069.

112. Jermain, S. V.; Brough, C.; Williams, R. O., 3rd. Amorphous solid dispersions and nanocrystal technologies for poorly water-soluble drug delivery - An update. *Int J Pharm* 2018, 535, (1-2), 379-392.

113. Dubois, J. L.; Ford, J. L. Similarities in the release rates of different drugs from polyethylene glycol 6000 solid dispersions. *Journal of Pharmacy and Pharmacology* 1985, 37, (7), 494-495.

114. Craig, D. Q. M.; Newton, J. M. The dissolution of nortriptyline hcl from polyethylene-glycol solid dispersions. *International Journal of Pharmaceutics* 1992, 78, (2-3), 175-182.

115. Saers, E. S.; Craig, D. Q. M. An investigation into the mechanisms of dissolution of alkyl p-aminobenzoates from polyethylene glycol solid dispersions. *International Journal of Pharmaceutics* 1992, 83, (1-3), 211-219.

116. Mosquera-Giraldo, L. I.; Li, N.; Wilson, V. R.; Nichols, B. L. B.; Edgar, K. J.; Taylor, L. S. Influence of polymer and drug loading on the release profile and membrane transport of telaprevir. *Molecular Pharmaceutics* 2018.

117. Jackson, M. J.; Kestur, U. S.; Hussain, M. A.; Taylor, L. S. Dissolution of danazol amorphous solid dispersions: supersaturation and phase behavior as a function of drug loading and polymer type. *Mol Pharm* 2016, 13, (1), 223-31.

118. Chen, Y.; Wang, S.; Wang, S.; Liu, C.; Su, C.; Hageman, M.; Hussain, M.; Haskell, R.; Stefanski, K.; Qian, F. Initial drug dissolution from amorphous solid dispersions controlled by polymer dissolution and drug-polymer interaction. *Pharm Res* 2016, 33, (10), 2445-58.

119. Purohit, H. S.; Taylor, L. S. Phase behavior of ritonavir amorphous solid dispersions during hydration and dissolution. *Pharm Res* 2017, 34, (12), 2842-2861.

120. Xie, T.; Taylor, L. S. Dissolution performance of high drug loading celecoxib amorphous solid dispersions formulated with polymer combinations. *Pharmaceutical Research* 2016, 33, (3), 739-750.

121. Chen, Y.; Liu, C.; Chen, Z.; Su, C.; Hageman, M.; Hussain, M.; Haskell, R.; Stefanski, K.; Qian, F. Drug-polymer-water interaction and its implication for the dissolution performance of amorphous solid dispersions. *Mol Pharm* 2015, 12, (2), 576-89.

122. Raina, S. A.; Van Eerdenbrugh, B.; Alonzo, D. E.; Mo, H.; Zhang, G. G. Z.; Gao, Y.; Taylor, L. S. Trends in the precipitation and crystallization behavior of supersaturated aqueous solutions of poorly water-soluble drugs assessed using synchrotron radiation. *J Pharm Sci* 2015, 104, (6), 1981-1992.

123. Mosquera-Giraldo, L. I.; Taylor, L. S. Glass-liquid phase separation in highly supersaturated aqueous solutions of telaprevir. *Mol Pharm* 2015, 12, (2), 496-503.

124. Rumondor, A. C. F.; Wikström, H.; Van Eerdenbrugh, B.; Taylor, L. S. Understanding the tendency of amorphous solid dispersions to undergo amorphous–amorphous phase separation in the presence of absorbed moisture. *AAPS PharmSciTech* 2011, 12, (4), 1209-1219.

125. Hate, S. S.; Reutzel-Edens, S. M.; Taylor, L. S. Insight into amorphous solid dispersion performance by coupled dissolution and membrane mass transfer measurements. *Molecular Pharmaceutics* 2018.

126. Stewart, A. M.; Grass, M. E.; Brodeur, T. J.; Goodwin, A. K.; Morgen, M. M.; Friesen, D. T.; Vodak, D. T. Impact of drug-rich colloids of itraconazole and HPMCAS on membrane flux in vitro and oral bioavailability in rats. *Molecular Pharmaceutics* 2017, 14, (7), 2437-2449.

127. Harmon, P.; Galipeau, K.; Xu, W.; Brown, C.; Wuelfing, W. P. Mechanism of dissolution-induced nanoparticle formation from a copovidone-based amorphous solid dispersion. *Molecular Pharmaceutics* 2016, 13, (5), 1467-1481.

128. Wagner, J. M., X-ray photoelectron spectroscopy. New York : Nova Science Publishers: New York, 2011.

129. Bhujbal, S. V.; Zemlyanov, D. Y.; Cavallaro, A.; Mangal, S.; Taylor, L. S.; Zhou, Q. T. Qualitative and quantitative characterization of composition heterogeneity on the surface of spray dried amorphous solid dispersion particles by an advanced surface analysis platform with high surface sensitivity and superior spatial resolution. *Mol Pharm* 2018, 15, (5), 2045-2053.

130. Mahlin, D.; Berggren, J.; Gelius, U.; Engstrom, S.; Alderborn, G. The influence of PVP incorporation on moisture-induced surface crystallization of amorphous spray-dried lactose particles. *Int J Pharm* 2006, 321, (1-2), 78-85.

131. Stewart, A. M.; Grass, M. E.; Mudie, D. M.; Morgen, M. M.; Friesen, D. T.; Vodak, D. T. Development of a biorelevant, material-sparing membrane flux test for rapid screening of bioavailability-enhancing drug product formulations. *Molecular Pharmaceutics* 2017, 14, (6), 2032-2046.

132. Lee, P. I.; Peppas, N. A. Prediction of polymer dissolution in swellable controlled-release systems. *Journal of Controlled Release* 1987, 6, (1), 207-215.

133. Borgquist, P.; Körner, A.; Piculell, L.; Larsson, A.; Axelsson, A. A model for the drug release from a polymer matrix tablet—effects of swelling and dissolution. *Journal of Controlled Release* 2006, 113, (3), 216-225.

134. Vrentas, J. S.; Vrentas, C. M. Diffusion-controlled polymer dissolution and drug release. *Journal of Applied Polymer Science* 2004, 93, (1), 92-99.

135. Simonelli, A. P.; Mehta, S. C.; Higuchi, W. I. Dissolution rates of high energy polyvinylpyrrolidone (pvp)-sulfathiazole coprecipitates. *Journal of Pharmaceutical Sciences* 1969, 58, (5), 538-549.

136. Indulkar, A. S.; Lou, X.; Zhang, G. G. Z.; Taylor, L. S. Insights into the dissolution mechanism of ritonavir-copovidone amorphous solid dispersions: importance of congruent release for enhanced performance. *Mol Pharm* 2019, 16, (3), 1327-1339.

137. Simonelli, A. P.; Mehta, S. C.; Higuchi, W. I. Dissolution rates of high energy polyvinylpyrrolidone (PVP)-sulfathiazole coprecipitates. *J Pharm Sci* 1969, 58, (5), 538-49.

138. Chen, H.; Pui, Y.; Liu, C.; Chen, Z.; Su, C. C.; Hageman, M.; Hussain, M.; Haskell, R.; Stefanski, K.; Foster, K.; Gudmundsson, O.; Qian, F. Moisture-induced amorphous phase separation of amorphous solid dispersions: molecular mechanism, microstructure, and its impact on dissolution performance. *J Pharm Sci* 2018, 107, (1), 317-326.

139. Mosquera-Giraldo, L. I.; Li, N.; Wilson, V. R.; Nichols, B. L. B.; Edgar, K. J.; Taylor, L. S. Influence of polymer and drug loading on the release profile and membrane transport of telaprevir. *Mol Pharm* 2018, 15, (4), 1700-1713.

140. Knopp, M. M.; Wendelboe, J.; Holm, R.; Rades, T. Effect of amorphous phase separation and crystallization on the in vitro and in vivo performance of an amorphous solid dispersion. *Eur J Pharm Biopharm* 2018, 130, 290-295.

141. Saboo, S.; Mugheirbi, N. A.; Zemlyanov, D. Y.; Kestur, U. S.; Taylor, L. S. Congruent release of drug and polymer: a "sweet spot" in the dissolution of amorphous solid dispersions. *J Control Release* 2019, 298, 68-82.

142. Theil, F.; Milsmann, J.; Kyeremateng, S. O.; Anantharaman, S.; Rosenberg, J.; van Lishaut, H. Extraordinary long-term-stability in kinetically stabilized amorphous solid dispersions of fenofibrate. *Mol Pharm* 2017, 14, (12), 4636-4647.

143. Theil, F.; Anantharaman, S.; Kyeremateng, S. O.; van Lishaut, H.; Dreis-Kuhne, S. H.; Rosenberg, J.; Magerlein, M.; Woehrle, G. H. Frozen in time: kinetically stabilized amorphous solid dispersions of nifedipine stable after a quarter century of storage. *Mol Pharm* 2017, 14, (1), 183-192.

144. Stewart, A. M.; Grass, M. E.; Mudie, D. M.; Morgen, M. M.; Friesen, D. T.; Vodak, D. T. Development of a biorelevant, material-sparing membrane flux test for rapid screening of bioavailability-enhancing drug product formulations. *Mol Pharm* 2017, 14, (6), 2032-2046.

145. Matsumoto, T.; Zografi, G. Physical properties of solid molecular dispersions of indomethacin with poly(vinylpyrrolidone) and poly(vinylpyrrolidone-co-vinyl-acetate) in relation to indomethacin crystallization. *Pharm Res* 1999, 16, (11), 1722-8.

146. Kothari, K.; Ragoonanan, V.; Suryanarayanan, R. The role of drug-polymer hydrogen bonding interactions on the molecular mobility and physical stability of nifedipine solid dispersions. *Mol Pharm* 2015, 12, (1), 162-70.

147. Yuan, X.; Xiang, T. X.; Anderson, B. D.; Munson, E. J. Hydrogen bonding interactions in amorphous indomethacin and its amorphous solid dispersions with poly(vinylpyrrolidone) and poly(vinylpyrrolidone-co-vinyl acetate) studied using (13)C solid-state NMR. *Mol Pharm* 2015, 12, (12), 4518-28.

148. Li, N.; Gilpin, C. J.; Taylor, L. S. Understanding the impact of water on the miscibility and microstructure of amorphous solid dispersions: An AFM-LCR and TEM-EDX study. *Mol Pharm* 2017, 14, (5), 1691-1705.

149. Nerurkar, J.; Beach, J. W.; Park, M. O.; Jun, H. W.   Solubility of (+/-)-ibuprofen and S (+)-ibuprofen in the presence of cosolvents and cyclodextrins. *Pharm Dev Technol* 2005, 10, (3), 413-21.

150. Baird, J. A.; Van Eerdenbrugh, B.; Taylor, L. S.   A classification system to assess the crystallization tendency of organic molecules from undercooled melts. *J Pharm Sci* 2010, 99, (9), 3787-806.

151. Chokshi, R. J.; Shah, N. H.; Sandhu, H. K.; Malick, A. W.; Zia, H.   Stabilization of low glass transition temperature indomethacin formulations: impact of polymer-type and its concentration. *J Pharm Sci* 2008, 97, (6), 2286-98.

152. Theil, F.; Milsmann, J.; Anantharaman, S.; van Lishaut, H.   Manufacturing amorphous solid dispersions with a tailored amount of crystallized api for biopharmaceutical testing. *Mol Pharm* 2018, 15, (5), 1870-1877.

153. Purohit, H. S.; Trasi, N. S.; Sun, D. D.; Chow, E. C. Y.; Wen, H.; Zhang, X.; Gao, Y.; Taylor, L. S.   Investigating the impact of drug crystallinity in amorphous tacrolimus capsules on pharmacokinetics and bioequivalence using discriminatory in vitro dissolution testing and physiologically based pharmacokinetic modeling and simulation. *J Pharm Sci* 2018, 107, (5), 1330-1341.

154. Rumondor, A. C.; Marsac, P. J.; Stanford, L. A.; Taylor, L. S.   Phase behavior of poly(vinylpyrrolidone) containing amorphous solid dispersions in the presence of moisture. *Mol Pharm* 2009, 6, (5), 1492-505.

155. Kothari, K.; Ragoonanan, V.; Suryanarayanan, R.   Influence of molecular mobility on the physical stability of amorphous pharmaceuticals in the supercooled and glassy States. *Mol Pharm* 2014, 11, (9), 3048-55.

156. Hancock, B. C.; Shamblin, S. L.; Zografi, G.   Molecular mobility of amorphous pharmaceutical solids below their glass transition temperatures. *Pharm Res* 1995, 12, (6), 799-806.

157. Miller-Chou, B. A.; Koenig, J. L.   A review of polymer dissolution. *Progress in Polymer Science* 2003, 28, (8), 1223-1270.

158. Raptis, G., Auflsungsmechanismus von glasig amorphen Polymeren. Freie Universitẽ, B., Ed. Berlin West: Berlin [West], 1969.

159. Crowley, K. J.; Zografi, G.   Water vapor absorption into amorphous hydrophobic drug/poly(vinylpyrrolidone) dispersions. *Journal of Pharmaceutical Sciences* 2002, 91, (10), 2150-2165.

160.Que, C.; Lou, X.; Zemlyanov, D. Y.; Mo, H.; Indulkar, A. S.; Gao, Y.; Zhang, G. G. Z.; Taylor, L. S. Insights into the dissolution behavior of ledipasvir-copovidone amorphous solid dispersions: role of drug loading and intermolecular interactions. *Mol Pharm* 2019, 16, (12), 5054-5067.

161.Miyazaki, T.; Yoshioka, S.; Aso, Y.; Kawanishi, T. Crystallization rate of amorphous nifedipine analogues unrelated to the glass transition temperature. *Int J Pharm* 2007, 336, (1), 191-5.

162.Hancock, B. C.; Parks, M. What is the true solubility advantage for amorphous pharmaceuticals? *Pharm Res* 2000, 17, (4), 397-404.

163.Van den Mooter, G. The use of amorphous solid dispersions: A formulation strategy to overcome poor solubility and dissolution rate. *Drug Discov Today Technol* 2012, 9, (2), e71-e174.

164.Indulkar, A. S.; Gao, Y.; Raina, S. A.; Zhang, G. G.; Taylor, L. S. Exploiting the phenomenon of liquid-liquid phase separation for enhanced and sustained membrane transport of a poorly water-soluble drug. *Mol Pharm* 2016, 13, (6), 2059-69.

165.Stewart, A. M.; Grass, M. E.; Brodeur, T. J.; Goodwin, A. K.; Morgen, M. M.; Friesen, D. T.; Vodak, D. T. Impact of drug-rich colloids of itraconazole and HPMCAS on membrane flux in vitro and oral bioavailability in rats. *Mol Pharm* 2017, 14, (7), 2437-2449.

166.Kesisoglou, F.; Wang, M.; Galipeau, K.; Harmon, P.; Okoh, G.; Xu, W. Effect of amorphous nanoparticle size on bioavailability of anacetrapib in dogs. *J Pharm Sci* 2019, 108, (9), 2917-2925.

167.McKelvey, C. A.; Kesisoglou, F. Enabling an HCV treatment revolution and the frontiers of solid solution formulation. *J Pharm Sci* 2019, 108, (1), 50-57.

168. Developing Solid Oral Dosage Forms: Pharmaceutical Theory and Practice, 2nd Edition. Developing Solid Oral Dosage Forms: Pharmaceutical Theory and Practice, 2nd Edition 2017, 1-1160.

169.Davis, M. T.; Potter, C. B.; Mohammadpour, M.; Albadarin, A. B.; Walker, G. M. Design of spray dried ternary solid dispersions comprising itraconazole, soluplus and HPMCP: Effect of constituent compositions. *Int J Pharm* 2017, 519, (1-2), 365-372.

170.Thakral, S.; Thakral, N. K.; Majumdar, D. K. Eudragit®: a technology evaluation. *Expert Opinion on Drug Delivery* 2013, 10, (1), 131-149.

171.Ueda, K.; Yamazoe, C.; Yasuda, Y.; Higashi, K.; Kawakami, K.; Moribe, K. Mechanism of enhanced nifedipine dissolution by polymer-blended solid dispersion through molecular-level characterization. *Mol Pharm* 2018, 15, (9), 4099-4109.

172. Wang, S.; Liu, C.; Chen, Y.; Zhang, Z.; Zhu, A.; Qian, F. A high-sensitivity HPLC-ELSD method for HPMC-AS quantification and its application in elucidating the release mechanism of HPMC-AS based amorphous solid dispersions. *Eur J Pharm Sci* 2018, 122, 303-310.

173. Van Der Lee, R.; Pfaffendorf, M.; Koopmans, R. P.; Van Lieshout, J. J.; Van Montfrans, G. A.; Van Zwieten, P. A. Comparison of the time courses and potencies of the vasodilator effects of nifedipine and felodipine in the human forearm. *Blood Pressure* 2001, 10, (4), 217-222.

174. Tang, X. C.; Pikal, M. J.; Taylor, L. S. A spectroscopic investigation of hydrogen bond patterns in crystalline and amorphous phases in dihydropyridine calcium channel blockers. *Pharm Res* 2002, 19, (4), 477-83.

175. Higashi, K.; Hayashi, H.; Yamamoto, K.; Moribe, K. The effect of drug and EUDRAGIT(R) S 100 miscibility in solid dispersions on the drug and polymer dissolution rate. *Int J Pharm* 2015, 494, (1), 9-16.

176. Merkel, H. P., Proceedings of the International Symposium on Povidone. College of Pharmacy, University of Kentucky: Lexington, Ky., 1983.

177. Rumondor, A. C. F.; Konno, H.; Marsac, P. J.; Taylor, L. S. Analysis of the moisture sorption behavior of amorphous drug–polymer blends. *Journal of Applied Polymer Science* 2010, 117, (2), 1055-1063.

178. Patent Application Titled "Pharmaceutical Composition of Selective Hcv Ns3/4a Inhibitors" Published Online (USPTO 20160339074). Pharma Business Week 2016, 159.

179. Tres, F.; Treacher, K.; Booth, J.; Hughes, L. P.; Wren, S. A.; Aylott, J. W.; Burley, J. C. Real time Raman imaging to understand dissolution performance of amorphous solid dispersions. *J Control Release* 2014, 188, 53-60.

180. Gomaa, Y. A.; Garland, M. J.; McInnes, F. J.; Donnelly, R. F.; El-Khordagui, L. K.; Wilson, C. G. Flux of ionic dyes across microneedle-treated skin: effect of molecular characteristics. *Int J Pharm* 2012, 438, (1-2), 140-9.

181. Mottram, L. F.; Forbes, S.; Ackley, B. D.; Peterson, B. R. Hydrophobic analogues of rhodamine B and rhodamine 101: potent fluorescent probes of mitochondria in living C. elegans. *Beilstein J Org Chem* 2012, 8, 2156-65.

182. Hughes, L. D.; Rawle, R. J.; Boxer, S. G. Choose Your Label Wisely: Water-Soluble Fluorophores Often Interact with Lipid Bilayers. *PLoS ONE* 2014, 9, (2), e87649.

183. Trask, A. V.; Shan, N.; Jones, W.; Motherwell, W. D. S. Indomethacin methyl ester. Acta Crystallographica Section E-Structure Reports Online 2004, 60, (4), 508-509.

184. Li, N.; Taylor, L. S. Nanoscale infrared, thermal, and mechanical characterization of telaprevir–polymer miscibility in amorphous solid dispersions prepared by solvent evaporation. *Molecular Pharmaceutics* 2016, 13, (3), 1123-1136.

185. Griffiths, P. R.; De Haseth, J. A., Fourier transform infrared spectrometry. John Wiley & Sons: 2007; Vol. 171.

186. Gauvin, R.; Lifshin, E.; Demers, H.; Horny, P.; Campbell, H. Win X-ray: A new Monte Carlo program that computes X-ray spectra obtained with a scanning electron microscope. *Microscopy and Microanalysis* 2006, *12*, (1), 49-64.

VITA

Sugandha Saboo received her Bachelors in Pharmacy (Hons.) and Masters in Pharmacy (with specialization in Pharmaceutics) from Birla Institute of Technology and Science, Pilani, India. During her Masters, she came to the States for six months for her Master's dissertation work at University of New Mexico, Albuquerque. After that she worked for one year in Formulation R&D at Dr. Reddy's Laboratories, Hyderabad, India. In the fall of 2015, Sugandha joined the department of Industrial and Physical Pharmacy at Purdue University, West Lafayette, Indiana.